



HAL
open science

AGuIX, a theranostic nanoparticle to improve image-guided radiation therapy : a proof ofconcept in pancreatic cancer

Alexandre Detappe

► **To cite this version:**

Alexandre Detappe. AGuIX, a theranostic nanoparticle to improve image-guided radiation therapy : a proof ofconcept in pancreatic cancer. Radiochemistry. Université de Lyon, 2017. English. NNT : 2017LYSE1032 . tel-01590727

HAL Id: tel-01590727

<https://theses.hal.science/tel-01590727>

Submitted on 20 Sep 2017

HAL is a multi-disciplinary open access archive for the deposit and dissemination of scientific research documents, whether they are published or not. The documents may come from teaching and research institutions in France or abroad, or from public or private research centers.

L'archive ouverte pluridisciplinaire **HAL**, est destinée au dépôt et à la diffusion de documents scientifiques de niveau recherche, publiés ou non, émanant des établissements d'enseignement et de recherche français ou étrangers, des laboratoires publics ou privés.



N° d'ordre NNT : 2017LYSE1032

THÈSE DE DOCTORAT DE L'UNIVERSITÉ DE LYON
opérée au sein de
l'Université Claude Bernard Lyon 1

Ecole Doctorale ED 206
Chimie, Procédés, Environnement

Spécialité de doctorat : Physique Médicale
Discipline : Nanomédecine

Soutenue publiquement le 07/02/2017 par :
Alexandre DETAPPE

**AGuIX, une nanoparticule théranostique pour
améliorer la radiothérapie guidée par l'image:
preuve de concept appliquée au cancer du
pancréas**

Devant le jury composé de :

RODRIGUEZ-LAFRASSE Claire, Prof., Université de Lyon	Examinatrice	Président(e)
GIRAUD Jean-Yves, PhD, HdR, CHU de Grenoble		Rapporteur
PRISE Kevin, Prof., Queen's University, Belfast		Rapporteur
LE DUC Géraldine, PhD, CEO, NH TherAguix		Examinatrice
TILLEMENT Olivier, Prof., UMR 5306		Directeur de thèse
BERBECO Ross, Associate Prof., Harvard Med. School		Invité

RÉSUMÉ

Les travaux menés au cours de cette thèse ont pour but de démontrer l'efficacité d'une nanoparticule de polysiloxane boostée par la présence d'atomes de gadolinium afin d'agir comme agent théranostique en radiothérapie pour améliorer le traitement du cancer du pancréas. Commercialisée sous le nom d'AGuIX (acronyme d'Activation et Guidage de l'Irradiation par rayonnement X), ces nanoparticules s'utilisent comme agents de contraste IRM et radiosensibilisants sous irradiation. Un ciblage passif est utilisé pour cibler la tumeur, aussi connu sous le nom de « enhanced permeability and retention (EPR-) effect ». De par leur composition chimique permettant d'empêcher la fuite de gadolinium libre dans le corps, et de par leur taille (5 nm), les nanoparticules AGuIX sont reconnues pour leur bénignité après injection intraveineuse.

Jusqu'à présent, l'efficacité des nanoparticules AGuIX a été démontré avec des irradiations pré-cliniques ou monoénergétiques pour les cancers du cerveau (glioblastome, métastases cérébrales), tête et cou, et poumon. L'irradiation préclinique de faible énergie (220 kV), et l'irradiation clinique (6 MV) sont adaptées pour activer les nanoparticules. L'effet radiosensibilisant des nanoparticules métalliques étant principalement causé par effet photoélectrique, il est nécessaire d'utiliser des photons d'énergie proche de la raie K du gadolinium (50.2 keV) afin de créer une interaction avec les électrons de l'atome dans le but d'amplifier localement la dose autour des nanoparticules aboutissant à des effets biologiques menant à une augmentation de la mort cellulaire. Ainsi, en théorie, le passage de l'irradiation préclinique (220 kV) à l'irradiation clinique (6 MV) devrait permettre une diminution de l'effet de dose induit par les nanoparticules dû à la diminution du nombre de photons de basse énergies.

Dans le cadre de cette thèse, nous avons réalisé une preuve de concept sur le cancer du pancréas, connu pour son faible taux de survie, avec machines précliniques et cliniques. Afin de relever le défi du passage en clinique, nous avons proposé une méthode pour créer un « adoucissement du faisceau d'irradiation » et démontré la possibilité d'utiliser les nanoparticules AGuIX pour un essai clinique de phase I. Les travaux de recherche ont été réalisés en trois temps : une étape de calcul analytique permettant d'obtenir une information sur l'influence des différents paramètres d'irradiation, une confirmation de l'efficacité des nanoparticules avec faisceaux précliniques, et enfin une preuve de concept avec faisceaux cliniques. Notre étude avec faisceaux cliniques est la première étude réalisée démontrant l'efficacité de nanoparticules de gadolinium passivement ciblées vers la tumeur, et démontre qu'il est possible d'obtenir des résultats cliniques similaires à ceux obtenus en préclinique.

MOTS-CLÉS

AGuIX; Nanoparticule; Radiothérapie; Imagerie par Résonance Magnétique

**AGuIX, a theranostic nanoparticle to improve
image-guided radiation therapy: a proof of
concept in pancreatic cancer**

ABSTRACT

The PhD research performed aimed to demonstrate the efficacy of a polysiloxane-based gadolinium nanoparticle to act as a theranostic agent (positive MRI contrast agent and radiosensitizer) on a pancreatic cancer model. Known under the acronym AGuIX (Activation and Guidance by Irradiation X), the nanoparticle led to a better MR signal than current FDA-approved contrast agents and to a significant dose enhancement while irradiated with external radiation beams. AGuIX is a non-toxic nanoparticle thanks to its chemical composition (gadolinium entrapped in DOTA), that clears rapidly through the kidneys due to its small size (sub-5nm). The nanoparticle reaches the tumor by passive targeting through the enhanced permeability and retention (EPR-) effect.

Previous studies demonstrated AGuIX ability to act as an efficient radiosensitizer under the presence of preclinical radiations or monoenergetic radiation beams for multiple cancer models. The preclinical irradiation (220 kV) has been shown effective in activating high atomic number (Z) nanoparticles. The energy peak is close to the k-edge of the different high-Z elements used (50.2 keV for the gadolinium), leading to a strong photoelectric effect. Auger electrons generation and biological effects occur afterwards creating a local dose enhancement. However, clinical treatments use a higher energy beam (>6 MV). At these energy ranges, the photoelectric probability is less important, decreasing the direct interaction of the nanoparticles with the incoming photons. Theoretically, the radiation dose escalation should hence be less important than observed with the preclinical irradiation beams (220 kV).

We performed a proof of concept on a pancreatic tumor model, known for its low survival rates, with preclinical and clinical radiation beams to evaluate the efficacy of the AGuIX nanoparticles. To increase the efficacy of the clinical radiation beam without modifying the nanoparticle structure in order to obtain a dose enhancement close to the one observed with the preclinical beam, we evaluated key clinical beam parameters to understand and increase the mechanisms of interaction between the incident photons and the high-Z nanoparticles. Hence, we evaluated by analytical calculation the impact of the radiation beam under different conditions of irradiation, confirming the potential of the nanoparticles with a preclinical beam, and finally shown their significant efficacy under a clinical setup. This study is the first to evaluate the potential of a high-Z nanoparticle to act as radiosensitizer following low dose intravenous injections.

KEYWORDS

AGuIX; Nanoparticle; Radiation Therapy; Magnetic Resonance Imaging

RÉSUMÉ SUBSTANTIEL

L'objectif principal de la radiothérapie est de détruire les cellules cancéreuses tout en préservant les tissus sains. Une augmentation locale de la dose délivrée par radiothérapie est cependant nécessaire pour certaines tumeurs radiorésistantes comme celle du pancréas. Une telle situation demande alors de trouver un compromis entre la dose de radiation délivrable à la tumeur et celle reçue par les cellules saines avoisinantes de manière à ne pas dépasser leur seuil de tolérance. Les cliniques utilisent à l'heure actuelle des méthodes de radiothérapie de précision comme la radiothérapie conformationnelle par modulation d'intensité (RCMI) comprenant les méthodes d'irradiation step and shoot et intensity modulated arc therapy (VMAT), et dans une moindre mesure la protonthérapie, la hadronthérapie ou des irradiations synchrotrons. Des méthodes alternatives sont cependant proposées pour augmenter le contrôle local de la radiothérapie, comme l'utilisation d'agents radiosensibilisants.

A l'opposé des agents chimiques radiosensibilisants comme la Tirapazamine ou la Crocétine, nous avons utilisé une nanoparticule comprenant des éléments de haut numéro atomique (e.g., le gadolinium) dans le but d'amplifier localement l'effet thérapeutique de la radiothérapie. De part leur numéro atomique, ces atomes bénéficient d'une forte capacité d'absorption par effet photoélectrique des photons de faible énergie (<100 keV) afin de générer un dépôt local de dose par l'émission de photoélectrons et d'électrons Auger. En plus de créer un effet physique, l'activation de la nanoparticule par les photons incidents crée des substances chimiques contribuant à la formation de lésions simples et double brins de l'ADN, mais permet également d'endommager la membrane cellulaire et certains organites du cytoplasme conduisant à la mort cellulaire. Cette approche a mené au développement de nombreuses nanoparticules comme celles à base d'argent ($Z=47$), gadolinium ($Z=64$), hafnium ($Z=72$), or ($Z=79$), et bismuth ($Z=84$).

A l'heure actuelle, le couplage scanographie – IRM est couramment utilisé pour la délimitation tumorale des tissus mous (prostate, tumeurs cérébrales, pancréas). De nombreux développements s'orientent vers la conception de machines couplant une IRM à l'accélérateur linéaire à la place des imageurs embarqués sur les accélérateurs linéaires (CBCT) pour guider les traitements en temps réel, et ainsi bénéficier d'une meilleure qualité de visualisation des tissus mous grâce à l'IRM.

Les nanoparticules comprenant du gadolinium sont particulièrement adaptées pour une utilisation en clinique. Elles possèdent des propriétés magnétiques attrayantes pour l'IRM ainsi que des propriétés d'agent radiosensibilisant pour la radiothérapie. Dans ce cadre, notre équipe a développé un nouveau type de nanoparticules à base de gadolinium pouvant être suivies par IRM après injection intraveineuse et servant d'agents radiosensibilisants à haute efficacité: les nanoparticules AGuIX. Ces nanoparticules sont composées d'un coeur de polysiloxane entouré de ligands cycliques dérivés du DOTA (acide 1,4,7,10-tétra-azacyclododécane - 1,4,7,10-tétra-acétique) greffés de manière covalente à la matrice de polysiloxane. Elles présentent un diamètre hydrodynamique de 3 ± 1 nm et une masse d'environ 10 kDa.

Basé sur l'étude des nanoparticules AGuIX, cette thèse présente au sein de ces 3 chapitres: 1) une évaluation analytique de l'importance du choix du faisceau d'irradiation et de l'impact des différents paramètres d'irradiation (taille de champ d'irradiation, profondeur d'irradiation, modalité d'irradiation (6 MV et 6 MV-FFF), 2) une évaluation *in vitro* pour comparer l'efficacité du faisceau 6 MV-FFF par rapport au faisceau clinique 6 MV ainsi qu'une évaluation des paramètres d'irradiation décrits précédemment, 3) une évaluation toxicologique après injection intraveineuse des nanoparticules, leur propriété de contraste IRM et de ciblage tumoral, et leur efficacité radiosensibilisante avec irradiation clinique 6 MV et 6 MV-FFF.

APPROCHE ANALYTIQUE

La première partie de la thèse a pour but d'évaluer de manière analytique l'efficacité des nanoparticules durant une irradiation clinique et d'optimiser les paramètres d'irradiations physiques pour assurer une efficacité optimale des nanoparticules. L'avantage du calcul analytique par rapport au calcul Monte-Carlo est sa rapidité d'exécution. Bien que moins précis que le calcul Monte-Carlo, le calcul analytique a l'avantage d'offrir en quelques minutes une idée rapide de l'impact de la modification du paramètre étudié.

Jusqu'à présent, pour obtenir un meilleur effet radiosensibilisant, le challenge était d'augmenter la concentration de nanoparticules dans la tumeur, de diminuer la taille de la nanoparticule, ou de la modifier chimiquement pour augmenter son temps de circulation dans le sang. Dans notre étude, nous nous sommes concentrés sur les méthodes d'irradiation qui augmentent l'effet biophysique des nanoparticules. Il est convenu que l'augmentation de photons de faible énergie (<250 keV) permet une activation des nanoparticules par effet photoélectrique, menant à des cascades d'électrons Auger et à la génération de dérivés actifs de l'oxygène (ROS). Ce phénomène permet aux nanoparticules d'être efficaces avec des faisceaux d'irradiation préclinique (220 kV). Cependant, la majorité des patients sont traités avec des irradiations de l'ordre du mega-electronvolt (6 MV dans 90% des cas). Ces faisceaux sont composés d'un spectre d'énergie avec une énergie moyenne de 1.25 MeV, et une très faible part de photons basse énergie.

Nous avons ainsi évalué l'effet de la profondeur d'irradiation, de la taille de champ, mais également l'impact du faisceau d'irradiation sur la création d'un adoucissement de faisceau (diminuer l'énergie moyenne du spectre d'énergie pour augmenter les photons de faible énergie). Une fois les paramètres validés, nous avons comparé différents faisceaux d'irradiation clinique pour activer AGuIX. Nous avons comparé l'efficacité théorique d'un faisceau 6 MV avec un faisceau 6 MV-FFF essentiellement utilisé en radiation stéréotaxique et connu pour sa capacité à augmenter les électrons de contamination. Enfin, nous avons effectué un calcul prenant en compte la modification de la cible permettant de générer les photons. Généralement, cette cible est composée de cuivre/tungstène. Nous avons proposé de la remplacer par une cible de carbone qui permet une augmentation de la génération de photons de faible énergie avec une énergie maximum de 2.5 MeV.

L'ensemble des résultats obtenus confirme que l'adoucissement de faisceau permet d'augmenter l'effet de dose induit par les nanoparticules AGuIX. Cependant, pour de faibles tailles de champ ($< 3\text{cm} \times 3\text{cm}$), ce phénomène n'est plus observé. En effet, un phénomène de durcissement de faisceau (absorption des photons de faible énergie et augmentation de l'énergie moyenne du spectre d'énergie) est observé dans les profondeurs étudiées (> 10 cm), menant à une diminution de l'effet des nanoparticules. Enfin, à paramètres d'irradiations identiques, une augmentation de l'effet radiosensibilisant de 20-35% est attendue avec l'utilisation du faisceau 6 MV-FFF comparé au faisceau 6 MV. La modification théorique de la cible cuivre/tungstène par du cuivre permettrait quant à elle une augmentation de plus d'un facteur 10 de l'effet des nanoparticules par rapport au faisceau 6 MV-FFF.

Ces résultats encourageants ont donné lieu à une investigation préclinique pour valider les résultats analytiques avec dans un premier temps une évaluation *in vitro*, puis *in vivo*.

AGuIX, UN AGENT RADIOSENSIBILISANT EFFICACE: PREUVE DE CONCEPT IN VITRO

Les tests *in vitro* nous ont permis d'évaluer et de comparer l'efficacité des nanoparticules AGuIX avec irradiations précliniques (220 kV) et cliniques (6 MV, 6 MV-FFF) mais également de quantifier l'impact de l'internalisation des nanoparticules sur leur efficacité radiosensibilisante. Les nanoparticules AGuIX étant principalement constituées d'atomes de gadolinium, leur internalisation au sein des cellules pancréatiques s'est quantifiée par IRM et les résultats obtenus ont ensuite été comparés aux

résultats ICP-MS. Nous avons observé qu'après 1h environ, la cellule est saturée d'AGuIX avec une concentration de l'ordre de 1,5 pg/cellule de gadolinium. Au sein même de la cellule, les nanoparticules sont concentrées sous la forme de cluster de nanoparticules.

Nous avons évalué l'efficacité des nanoparticules AGuIX dans les conditions optimales d'irradiation: 1h d'incubation et irradiation préclinique (220 kV). Nous observons une augmentation significative des cassures d'ADN double brins, une augmentation de mort apoptotique, et une diminution significative de la vie cellulaire sur le long terme évaluée par essai clonogénique dans la condition de traitement AGuIX + irradiation préclinique. Après avoir confirmé l'efficacité des nanoparticules AGuIX pour une lignée cellulaire pancréatique capan-1, nous avons évalué l'impact des paramètres d'irradiations cliniques sur l'efficacité de la nanoparticule. Nous avons démontré l'influence de l'adoucissement du faisceau clinique sur l'augmentation de l'efficacité des nanoparticules, mais également confirmé l'augmentation de la mort cellulaire lorsque AGuIX est couplée à l'irradiation 6 MV-FFF.

Nous avons démontré lors de ces irradiations *in vitro* que l'utilisation des AGuIX permet une escalade de dose même lorsque celles-ci ne sont pas internalisées dans la cellule, confirmant les différentes hypothèses d'effets biologiques tel que la création de dérivés actifs de l'oxygène.

Ces résultats nous ont permis d'avancer à l'étape *in vivo* où nous avons réalisé une étude de toxicologie sur souris ainsi qu'une évaluation de l'efficacité des nanoparticules AGuIX avec irradiation préclinique et clinique après leur injection intraveineuse.

AGuIX, UNE NANOPARTICULE THÉRANOSTIQUE POUR LA RADIOTHÉRAPIE GUIDÉE PAR L'IMAGE

Après la preuve réalisée *in vitro*, nous nous sommes penchés sur l'étude d'AGuIX *in vivo*. Grâce à l'effet théranostique des nanoparticules (thérapeutique et diagnostique), nous avons pu évaluer leur biodistribution par IRM. De part leur diamètre hydrodynamique (inférieur à 5 nm), les nanoparticules AGuIX ont ciblé notre modèle sous-cutané de tumeur pancréatique dans les 30 minutes après injection avant de s'éliminer sans toxicité ou effets secondaires par les reins. Cette étude de biodistribution a été validée par ICP-MS qui est considéré comme le gold standard pour mesurer la quantité de métal dans un organe.

Cette étude de biodistribution nous a permis de déterminer le moment propice pour assurer que l'irradiation soit réalisée au moment où le plus grand nombre de nanoparticules soient présentes dans la tumeur. Nous avons ainsi quantifié l'effet des nanoparticules dans 3 conditions distinctes d'irradiation: une irradiation préclinique ; une irradiation 6 MV clinique ; une irradiation 6 MV-FFF clinique. Chacun de ces traitements a été réalisé avec une irradiation unique de 10 Gy. L'irradiation préclinique s'est déroulée avec 2 faisceaux orthogonaux (0 et 90 degrés) tandis que les irradiations cliniques ont été réalisées avec un seul faisceau à 180 degrés. Dans le cas des irradiations cliniques, la souris est placée en position ventrale sur 10 cm de solide de densité équivalente à l'eau (PMMA) avec 2 cm de bolus sur le dos pour couvrir la tumeur. Pour chaque étude réalisée, un effet significatif a été observé par rapport à l'irradiation contrôle de 10 Gy avec une augmentation de la survie de plus de 55 jours pour le faisceau préclinique, 45 jours pour le 6 MV et 62 jours pour le 6 MV-FFF. Aucune toxicité directement liée à la présence des nanoparticules dans les organes sains n'a été observée.

Ces études *in vivo* ont permis de confirmer la non-toxicité des AGuIX et leur efficacité d'utilisation comme agent diagnostique, leur non-interaction durant l'irradiation dans les tissus sains, et leur efficacité avec des faisceaux d'irradiation clinique.

CONCLUSION

En plus des paramètres d'irradiation, d'autres facteurs cliniques affectent également l'impact des

nanoparticules sur l'augmentation de la dose locale. La vascularisation de la tumeur, sa perméabilité, et d'autres facteurs biologiques impactent l'internalisation, la biodistribution, et l'efficacité thérapeutique des nanoparticules. La localisation de la tumeur, sa visibilité par les modalités d'imageries, le suivi de son mouvement créé par la respiration du patient, ainsi que d'autres phénomènes physiologiques sont des challenges couramment rencontrés en clinique. L'utilisation de produits de contraste ayant des caractéristiques similaires à celles de la nanoparticule AGuIX permet d'adresser ces challenges. L'utilisation pré-traitement et durant le traitement de l'IRM en radiothérapie représentent de nouvelles modalités en clinique indiquant un besoin important d'agents servant à la fois de produit de contraste et de radiosensibilisant. La nanoparticule AGuIX répond à ce besoin en permettant une meilleure précision de la radiothérapie en condition clinique tout en augmentant son efficacité.

L'efficacité des AGuIX à la fois comme agent diagnostique et thérapeutique a été démontrée la suite d'une injection intraveineuse de faible concentration sur un modèle sous-cutané d'adénocarcinome pancréatique. Grâce au mécanisme d'activation des nanoparticules, les résultats obtenus peuvent être étendus à tout autre modèle tumoral correctement vascularisé dans le but de permettre l'accumulation des AGuIX par effet passif dans la tumeur.

L'utilisation d'une machine de type flattening filter free permet une augmentation significative de l'amplification de dose induite par les nanoparticules AGuIX tout en diminuant les durées d'irradiation du patient. Un traitement plus précis est ainsi obtenu pour des sites mobiles comme le pancréas ou le poumon. Même avec un irradiateur clinique standard, ce phénomène d'activation reste significatif comparé à une irradiation simple. L'ensemble de ces résultats permet de confirmer l'efficacité de cette nanoparticule dans des conditions d'irradiations cliniques.

Contents

1	INTRODUCTION	17
1.1	State of art	17
1.1.1	Positioning of the thesis	19
1.1.2	Presentation of the nanoparticle	19
1.2	On demand nanoparticle activation	20
1.2.1	Physical activation	21
1.2.2	Biological reaction	24
1.3	Cancer site targeting processes	24
1.3.1	Passive targeting	24
1.3.2	Active targeting	25
1.4	Publication	25
2	ANALYTICAL APPROACH	29
2.1	Motivations	29
2.2	Beam modeling and dose deposition calculation	30
2.2.1	Monte-Carlo simulation	30
2.2.2	Analytical calculation	30
2.2.3	Probability of photon-nanoparticle interaction	32
2.3	Impact of the clinical setup on nanoparticle activation	33
2.3.1	Depth and field size dependency	33
2.3.2	Impact of the radiation beam for radiation dose enhancement	34
2.4	Conclusion	35
2.5	Publications	36
3	AGUIX, AN EFFECTIVE RADIOSENSITIZER : <i>in vitro</i> PROOF OF CONCEPT	49
3.1	Motivations	49
3.2	Nanoparticle uptake by cells	50
3.2.1	MRI quantification	50
3.2.2	Inductively coupled plasma mass spectrometry validation	50
3.3	In vitro proof of concept	52
3.3.1	Proof of concept with preclinical radiation beam	52
3.3.2	Proof of concept with clinical radiation beam	54
3.4	Conclusion	56
3.5	Publication	56
4	THERANOSTIC NANOPARTICLES FOR IMAGE-GUIDED RADIATION THERAPY	67
4.1	Motivations	67
4.2	Animal model	68
4.3	Pharmacokinetics and biodistribution studies	68
4.3.1	Biodistribution in mice	68
4.3.2	Laser Induced Breakdown Spectroscopy (LIBS) imaging	69
4.4	Non-human primates: biodistribution and pharmacokinetics study	70
4.4.1	Biodistribution study in non-human primates	70

4.4.2	Pharmacokinetics study in non-human primates	70
4.5	In vivo radiation studies	72
4.5.1	Preclinical radiations	72
4.5.2	Clinical radiations	75
4.5.3	Enhanced in vivo clinical outcomes with nanoparticles and flattening filter free beams	78
4.6	Conclusion	78
4.7	Publications	80
5	CONCLUSION	101
5.1	Publication	103

Listing of figures

1.1	Number of publications related to the use of nanoparticles in biology and radiation oncology	18
1.2	Top-down process of AGuIX	20
1.3	Different imaging abilities of AGuIX	20
1.5	Photoelectric effect	21
1.4	Photon-matter interaction	21
1.7	Compton effect	22
1.6	Mass energy absorption coefficient comparison for soft tissue and heavy elements . .	23
1.8	Passive targeting process	25
2.1	Schematic representation for our analytical calculation	30
2.2	Fluency comparison	31
2.3	The sphere of interaction represents the range of photoelectrons generated by NPs .	32
2.4	Depth and field size dependence for a 5 nm diameter size nanoparticle irradiated by a 6 MV clinical radiation beam.	34
2.5	The percentage of low energy photons (25–150 keV) for a standard (Cu/W target) beam, a FFF (Cu/W target) beam, and a carbon target beam.	35
2.6	Endothelial dose enhancement factor calculation in function of the irradiation beam	35
3.1	MRI phantom studies and cellular uptake studies	51
3.2	<i>In vitro</i> uptake study	51
3.3	<i>In vitro</i> radiation studies: 53BP-1, FACS, clonogenic assay	53
3.4	PDD comparison between preclinical and clinical radiation beams	54
3.5	Energy dependence for radiosensitization with clinical radiation beam	55
3.6	<i>In vitro</i> radiation comparison between 6 MV and 6 MV-FFF clinical beams	57
4.1	Magnetic resonance biodistribution study	69
4.2	LIBS imaging for intratumoral AGuIX localization	69
4.3	Biodistribution studies in cynomolgus monkeys	70
4.4	Zoom of the nanoparticles accumulation in the kidneys	71
4.5	Pharmacokinetic study in cynomolgus monkeys	71
4.6	Histological H&E staining on the organs excised from monkeys after administration of AGuIX	72
4.7	Non-human primate pharmacokinetic study	73
4.8	MR-guided radiation therapy dosimetry	74
4.9	Radiation effect in mice muscle tissue	74
4.10	Tumor survival studies and radiation damage assessment	75
4.11	Preclinical tumor survival studies and radiation damage assessment	76
4.12	Dosimetry study performed with clinical settings	77
4.13	Clinical tumor survival studies and radiation damage assessment	77
4.14	Clinical tumor growth and survival studies comparison between 6 MV and 6 MV-FFF combined with nanoparticles	78
4.15	6 MV vs. 6 MV-FFF clinical radiation damage assessment	79

5.1 Schematic representation of LINAC and MR-LINAC 102

ACKNOWLEDGEMENTS/REMERCIEMENTS

Prof. Dr. Olivier Tillement, directeur de l'équipe FENNEC de l'Institut Lumière Matière: Je remercie tout particulièrement Olivier Tillement, de m'avoir accueilli dans son équipe, d'avoir encadré ce travail de thèse, ainsi que pour ses nombreuses idées et son dynamisme.

Prof. Dr. Ross Berbeco: I would like to thank Ross Berbeco for giving me the opportunity to perform my dissertation research in his group at the Dana-Farber Cancer Institute, as well as for his friendly advice and academic support.

Dr. Cédric Louis, CEO de Nano-H: Je remercie Cédric Louis de m'avoir accueilli au sein de son entreprise et de m'avoir financé mes 3 années de recherche.

I also thank Sijumon Kunjachan, Olivia Kelada, Chen Haijian, Yibin Liu, Salomon Manier, Thibaud Coroller, and Pascal Drané, for their great friendships as well as their academic and non-academic support.

Je tiens à remercier l'ensemble du groupe de Lyon (Francois Lux, Eloise Thomas, Fabien Rossetti, Mahmoud Ould Metidji, Shady Kotb) que j'ai appris à connaître pendant NanoHybride et à travers nos nombreux échanges par email.

Je tiens à remercier tout particulièrement Lucie Sancey qui m'a aidé à comprendre l'imagerie LIBS et qui m'a apporté de précieux conseils en biologie.

Jennifer Hayashi, Armel Doulasséf: I would like to thank Jennifer and Armel for challenging me to explain the use of nanoparticles in radiation oncology as well as for their motivation to learn and making office life more fun.

Et enfin, un grand merci à Tiphonie Maier qui m'aura supporté et motivé tout au long de mes études supérieures, et particulièrement durant ces 3 années de thèse. Bien évidemment, je remercie également ma famille pour leur soutien avec une pensée spéciale pour ma mère.

1

Introduction

Contents

1.1	State of art	17
1.1.1	Positioning of the thesis	19
1.1.2	Presentation of the nanoparticle	19
1.2	On demand nanoparticle activation	20
1.2.1	Physical activation	21
1.2.2	Biological reaction	24
1.3	Cancer site targeting processes	24
1.3.1	Passive targeting	24
1.3.2	Active targeting	25
1.4	Publication	25

1.1 STATE OF ART

While radiation is effective in killing cancer cells, the dose safely deliverable to the target volume is often limited by the possibility of collateral damages to surrounding healthy tissues. However, for some cancer sites, it has been shown that a dose escalation in the tumor could significantly improve local control and patient survival [1]. While recently developed methods such as intensity-modulated radiation therapy (IMRT), volumetric modulated arc therapy (VMAT), and image-guided radiation therapy (IGRT) have improved the delivered radiation dose conformality, dose escalation remains an important clinical challenge that needs to be addressed to improve the efficacy of radiation therapy [2].

Nanoparticles design is a rising landscape in the era of modern oncology offering new perspectives as shown by the increase of scientific publications related to their use in radiation oncology (Fig. 1.1).

The enhancement of radiation effect induced by radiosensitizing nanoparticles is probably one of the most translational aspects. Radiosensitizing nanoparticles increase the radiobiological effects within the site of disease while maintaining the current clinical constraints on dose delivered to healthy organs. The photoelectric interaction increases strongly as a function of the atomic number of the nanoparticle (proportional to $Z^4 - Z^3$), giving these particles a high interaction probability

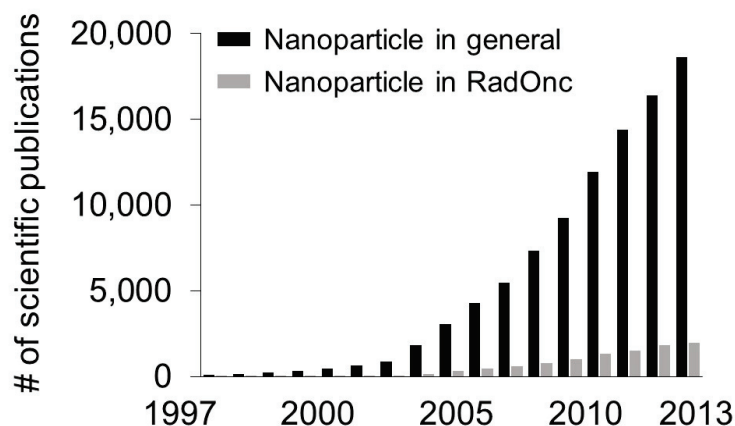


Figure 1.1: Number of publications related to the use of nanoparticles in biology (dark) and radiation oncology (grey) between 1997 and 2013 [3].

with low energy photons and allowing the formation of additional diffused photons, photoelectrons, Auger electrons and reactive oxygen species (ROS) that have the potential to amplify the biological damage. Even under high-energy photon irradiation, high-Z nanoparticles can interact with primary or secondary species permitting a highly efficient nanoscale dose deposition around the nanoparticles [4]. Consequently, the differential effect between healthy tissue and tumor tissue is improved.

The efficacy of nanoparticles as radiosensitizers has been demonstrated at the preclinical level for multiple high-Z nanoparticles since Hainfeld *et al.* demonstrated the potential of gold nanoparticles after systemic injection [5], and at the clinical level for hafnium nanoparticles [6]. However, because of the injection method (intratumoral injection) and because of their size (50 nm), the hafnium nanoparticles applications are mainly limited to easy-to-access tumor sites, such as sarcoma, head and neck, and prostate cancers. For the majority of other cancer sites, intravenous injection remains an obligation and does not modify the standard clinical practices. To address these limitations while still ensuring low toxicity to the healthy tissues, theranostic nanoparticles were created, combining diagnostic and therapeutic properties.

Gadolinium is a well-known element for biomedical applications. Its use in medicine is directly correlated with the development of contrast agents for MRI, a non-invasive and non-ionizing method for acquiring volumetric images with high spatial resolution and excellent soft-tissue contrast. Some clinics have begun to replace CT simulation with MRI simulation for radiation treatment planning purposes, and future MR-LINAC and MR-based real-time tumor tracking techniques are under development [7, 8]. Besides their use for imaging applications, gadolinium based compounds are also envisaged for therapeutic applications. Gadolinium displays high capture cross-section due to its relatively high atomic number ($Z = 64$) and can interact with high energies irradiations, making gadolinium-based nanoparticles effective radiosensitizers.

AGuIX (Activation and Guidance of Irradiation by X-ray) is a sub-5nm nanoparticle based on a polysiloxane network surrounded by gadolinium chelates designed to be an effective MRI contrast agent and radiosensitizer [9, 10]. Because of the vascular endothelial growth factor (VEGF) produced by tumor cells to stimulate the tumor angiogenesis and of the lack of effective lymphatic drainage in the tumor tissues, AGuIX can penetrate the tumor after a systemic injection thanks to the enhanced permeability and retention (EPR-) effect. The nanoparticle stay inside the tumor for a significant

period of time, while the nanoparticles which are not uptaken by the tumor are cleared by the kidneys, avoiding toxicity issues by limiting the nanoparticles exposition to healthy organs. Preclinical studies conducted in various tumor models have demonstrated that low concentrations of nanoparticles injected intravenously were attractive radiosensitizers with a significant therapeutic effect, while confirming that the nanoparticle is non-toxic [11]. In addition, the high longitudinal relaxivity of AGuIX ($11.9 \pm 1 \text{ s}^{-1} \cdot \text{mM}^{-1}$ per Gd at 60 MHz) allows for better contrast properties than current FDA-approved gadolinium chelates, creating a potential for future use in MR-guided radiation therapy, notably with the upcoming MR-LINAC technology [12, 13].

The logical step after demonstrating the potential of the AGuIX at the preclinical level for several tumor localizations is to continue the nanoparticle development to the clinical step. A current good manufacturing practice (cGMP) process has been developed and the regulatory toxicity tests on two animal models (rodents and monkeys) have shown no evidence of toxicity. Currently, the nanoparticle AGuIX has been validated by the Agence Nationale de la Santé et du Médicament (ANSM) to start a clinical phase I trial on brain metastasis at the Grenoble Hospital (France). A clinical phase I will be performed by our group in close collaboration with NH TherAguix SAS in order to a) determine the safety of the nanoparticle and its maximum tolerated dose in patients concurrently treated with standard chemoradiation; b) define the recommended phase II dose of the nanoparticle; and c) define the biodistribution of a single intravenous injection as well as multiple injections in order to provide a rationale of dosing administration. These results will demonstrate the translationality of using nanoparticles as image-guided radiation therapy agents. The proof of concept of using the AGuIX as a theranostic agent in human will be a breakthrough approach for patient benefit.

1.1.1 POSITIONING OF THE THESIS

This thesis research work has been completed through a partnership between the Institut Lumière-Matière, Lyon 1 (France), supervised by Prof. Olivier Tillement, the Nano-RadOnc group from the department of Radiation Oncology, Dana-Farber Cancer Institute (DFCI), Boston MA (USA), supervised by Dr. Ross Berbeco, Associate Professor at the Harvard Medical School, and the company Nano-H, a French company specialized in designing nanoparticles. The main goal of this thesis is to demonstrate that the use of AGuIX nanoparticles can improve the treatment of pancreatic cancer when combined to a clinical irradiation, without having to modify the current clinical workflow.

The synthesis of the AGuIX nanoparticles was performed in the Institut Lumière Matière, while the proof of concept was performed at the Dana-Farber Cancer Institute.

1.1.2 PRESENTATION OF THE NANOPARTICLE

AGuIX is a sub-5 nm nanoparticle synthesized by a top-down process (Fig. 1.2). A polysiloxane shell is formed around the lanthanide core and chelating molecules (e.g. DOTA) are grafted on the outside. Using a top-down process, the lanthanide oxide core is dissolved and the Gd^{3+} are chelated to empty DOTA sites [14]. The resulting nanoparticle ($\text{Gd}_{10}\text{Si}_{40}\text{C}_{200}\text{N}_{50}\text{O}_{150}\text{H}_x$) has a polysiloxane core supporting approximately 10 chelating sites that for the majority contain Gd^{3+} . The remaining DOTA can be chelated in order to attach PET and SPECT tracers or a combination thereof, while fluorescent probes can be attached on the surface of the nanoparticles, depending on the desired application (Fig. 1.3) [15]. This original structure entrapping the free gadolinium atoms into the chelates allows the nanoparticle to be nontoxic at high concentration, stable over time, and cleared through the kidneys without accumulation in other organs.

In this thesis research work, we used AGuIX nanoparticles composed by 10 chelates of gadolinium only. Using gadolinium atoms allows the nanoparticles to act as a theranostic agent.

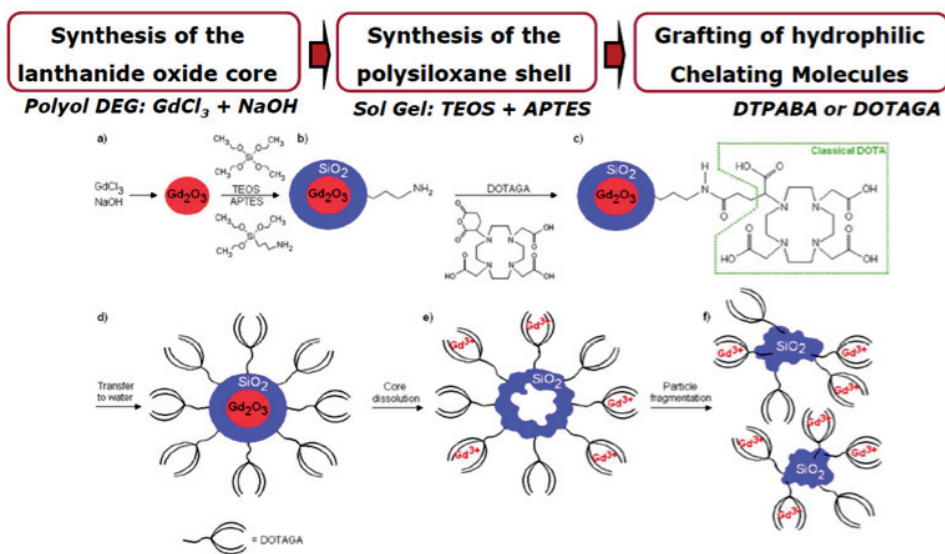


Figure 1.2: Scheme of SRP synthesis: a) core synthesis, b) polysiloxane shell synthesis, c) DOTAGA grafting, d) transfer to water, e) core dissolution, f) polysiloxane fragmentation. Image courtesy of Mignot *et al.* [13]

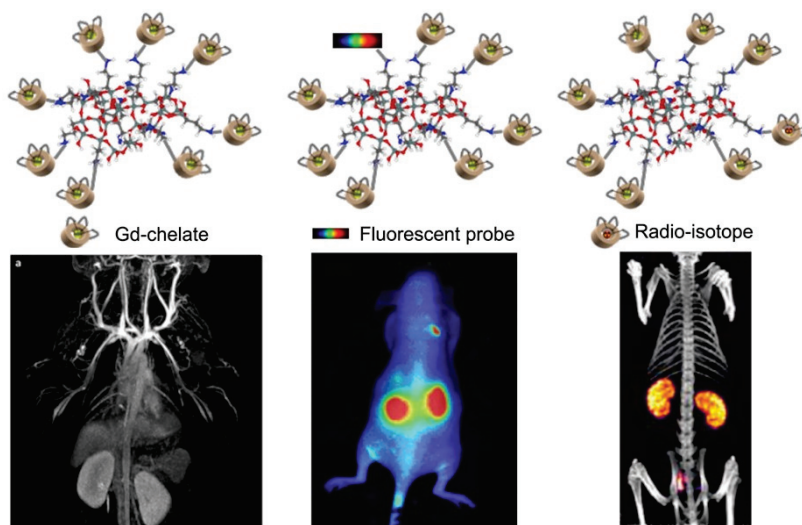


Figure 1.3: The AGuIX can be used as MR contrast agent, and as a fluorescent probe or SPECT/PET tracer.

1.2 ON DEMAND NANOPARTICLE ACTIVATION

Radiosensitizing nanoparticles made of high-Z atoms, such as AGuIX, have for goal to create a differential effect between the tumor and the surrounding healthy organs. The process of high-Z nanoparticles, such as AGuIX, is based on physical interactions and biological reactions.

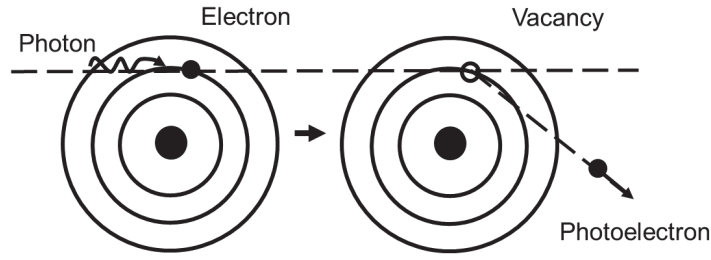


Figure 1.5: Schematic representation of the Photoelectric effect

1.2.1 PHYSICAL ACTIVATION

Photons can interact with the nanoparticles via absorption, inelastic diffusion, or elastic diffusion. These interactions may happen with the electrons localized around the nucleus, the nucleus itself, or the electromagnetic field of the nucleus. We focus on the interactions relating to the radiation therapy field applied in nanomedicine: Photoelectric effect and Compton effect.

PREDOMINANCE OF PHOTON INTERACTIONS

The different interactions processes are determined by the cross-section value. In function of the energy and the atomic number, 3 specific regions can be observed: Low energy / High Z: Photoelectric effect; Moderate energy / Moderate Z : Compton effect ; High energy / High Z : Pair production (Fig. 1.4).

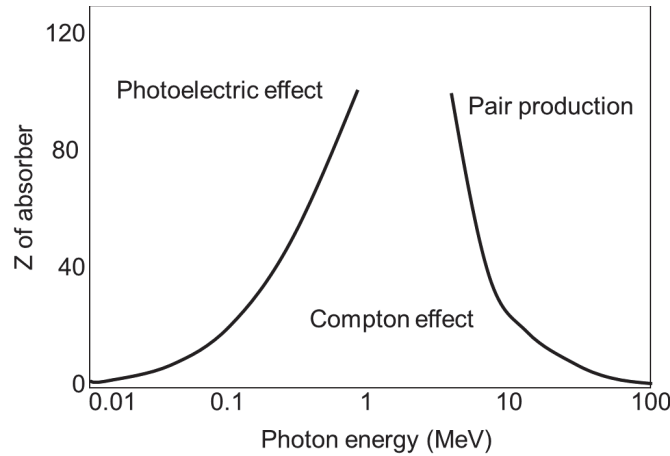


Figure 1.4: Regions where one of the three photon-matter interactions dominates.

PHOTOELECTRIC EFFECT

In a photoelectric effect (Fig. 1.5), an incident photon with an energy equal to the initial photon ($h\nu_0$) releases the totality of its energy to an atomic electron.



where γ is the incident photon, X is the atom with a mass A, ${}^A X^+$ is the same ionized atom, and e^- is a free electron.

The photon is absorbed while the photoelectron is ejected outside the atom with an energy equal to:

$$T_e = h\mu_o - E_b \quad (1.2)$$

where T_e is the photoelectron energy, $h\mu_o$ the initial photon energy, and E_b the binding energy needed to extract the electron from the nucleus attraction.

EFFECT OF THE INCIDENT PHOTON ENERGY

To create a photoelectric effect, the incident photon energy has to be higher or equal to the binding energy E_b . The probability of interaction is maximal when $h\mu_o = E_b$. When $h\mu_o$ increases, the probability of interaction decreases. Thus, a low energy photon will interact with the peripheral electron while a high energy photon will be able to interact with a higher shell of the atom. However, it is noteworthy that the probability of interaction is not linear.

ATOMIC NUMBER DEPENDENCY

The probability of interaction is increased by the atomic number (Z) by a factor $Z^{4.5}$. For this reason, high- Z nanoparticles such as gold ($Z = 79$) are mainly used as radiosensitizers (Fig. 1.6) [17].

SECONDARY EFFECT

The photoelectron generation creates an excitation in the inner shell leading to an atom with an energy above its ground state. This atom can relax and lose its energy in different ways. Two phenomena are in competition to fill this space: the characteristic radiation and the generation of Auger electron. Both phenomena start with the outer electron jumping in to fill the vacancy created in the inner shell. The characteristic X-ray radiation is depicted by an energy given off as a single X-ray photon while for the Auger electrons, the energy is given off by one of the outer electrons leaving carrying a characteristic kinetic energy.

COMPTON INTERACTION

The Compton scattering is the result of the collision between a high-energy photon and a target. This interaction releases bound electrons from the outer shell of the atom. When a Compton effect occurs, the incident photon ($h\mu_o$) interacts with an almost-free electron at rest in the form of kinetic energy. The remaining energy creates a scattered photon ($h\mu'$).

$${}^A X + \gamma = e^- + \gamma' + {}^A X^+ \quad (1.3)$$

A photon may create multiple Compton diffusions, losing progressively its energy. Usually, the generated photon will finish its interaction process by a photoelectric effect. The Compton effect is dependent of the atomic number Z (Fig. 1.7).

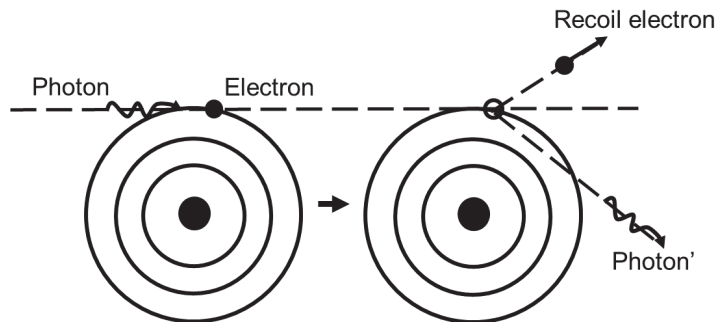


Figure 1.7: Schematic representation of the Compton effect

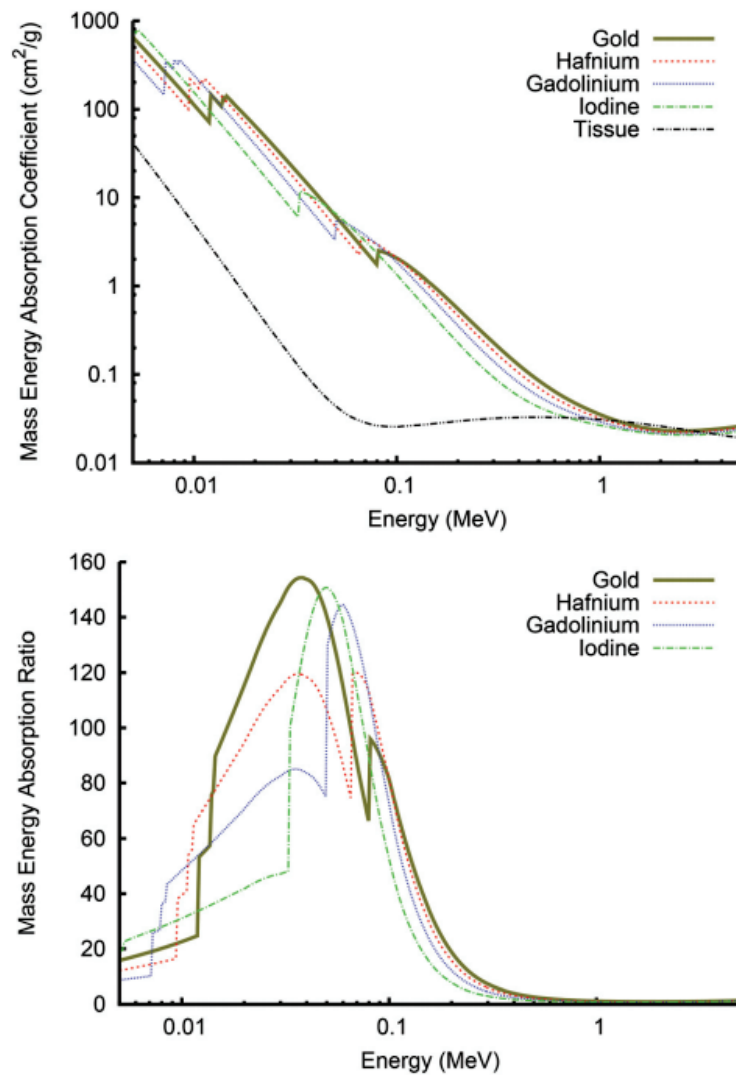


Figure 1.6: Comparison of mass energy absorption coefficients for soft tissue and a range of heavy elements (top). Although higher-Z metals generally have the highest absorption coefficient, this is not always the case, with edge structure introducing significant variation. This is similarly apparent in the ratio of metal absorption to soft tissue (bottom), which shows gold's absorption is surpassed by other metals over a wide range of the kilovoltage region. Image courtesy of SJ McMahon [17].

1.2.2 BIOLOGICAL REACTION

In addition to the physical dose enhancement induced by high-Z nanoparticles, radiation-induced biochemical reactions may also contribute to the overall tumor damages. However, the essential mechanism is still under investigation [18]. The radiosensitizing potential of gold (Au), gadolinium (Gd), hafnium (Hf), and bismuth (Bi) has been investigated preclinically [19, 20-23]. Until recently, analytical simulations and Monte-Carlo calculations were describing the dose enhancement observed inside the cells by a physical dose increase. However, the results did not match with the larger dose enhancement observed. More recently, interest has been growing around the biological response induced by the presence of the nanoparticles in the cells under radiation. One of the hypothesis to explain the higher dose enhancement observed *in vitro/in vivo* compared to the one predicted by simulation would be attributed to a local increase of reactive oxygen species (ROS) upon X-rays irradiation, resulting by an enhancement of the generation of H_2O_2 , OH^\bullet [24]. The generation of reactive oxygen species may lead to an increase of DNA double strand breaks and thus to an increase of cytotoxicity. This explanation is currently under investigation by many research groups and seems to be one explanation among others (bystander effect, abscopal effect, mitochondrial dysfunction, etc.) explanation of the discrepancy between the theory and the experiments.

1.3 CANCER SITE TARGETING PROCESSES

Nanomedicine is a rising field evolving as fast as the deployment of new nanotechnologies. With a size ranging from 1 to 100 nm, high-Z nanoparticles offer the means to aim radiation therapy selectively at cancerous cells. Nanoparticles can be used as radiosensitizers to increase locally the radiation. There are two different approaches to target the nanoparticles inside the tumor.

1.3.1 PASSIVE TARGETING

Passive targeting relies on the permeability of the tumor vasculature: leaky blood vessels due to endothelial gaps and non-aligned vascular endothelium [25]. Because of the size of the nanoparticles and their surface properties, nanoparticles can escape through blood vessel walls into tissues. In addition, the dysfunctional lymphatic drainage results in the retention of the nanoparticles within the tumor tissues. These two specific physiopathological phenomena are called enhanced permeability and retention (EPR-) effect (Fig. 1.8). This effect is vessel, tumor, and patient dependent. The phenomenon is increased with the fast growing and high vascularization of the tumor. Thus, for a slow growing tumor, a less pronounced effect is expected. Nanoparticles are relevant for tumor targeting using the EPR-effect due to their longer circulation time.

The EPR-effect is largely dependent of the tumor biological features, such as the level of angiogenesis tissue and lymphatic drainage, the neovascularization of the tumor, the density of the stromal response, and the intratumoral response.

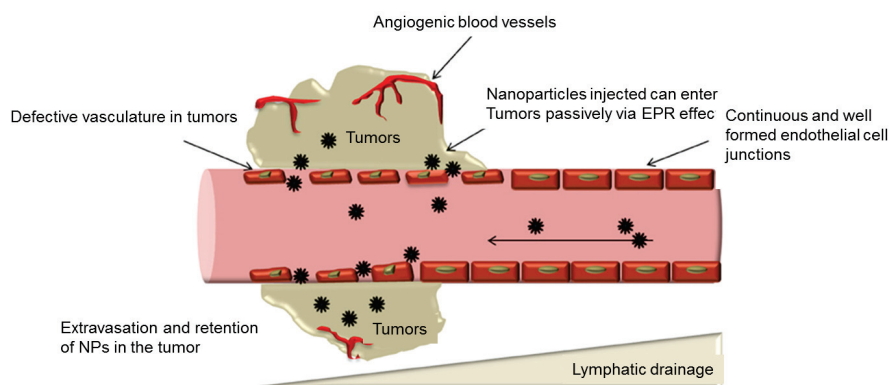


Figure 1.8: Schematic representation of the passive targeting process. Image adapted from Dan Peer *et al.* [26]

1.3.2 ACTIVE TARGETING

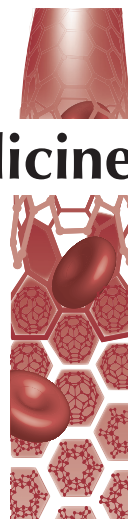
The active targeting is based on the incorporation of specific agents within the nanoprobe formulation. Hence, antibodies, aptamers, or peptides are mainly used as targeting ligands. These entities aim to specifically bind to cell surfaces or molecules present in abundant quantity at the target site, which in case of tumors generally refers to receptors over-expressed either by the cancer cells themselves or by tumor endothelial cells. The efficacy of an active tumor targeting nanoparticle is in most of the cases improved by the above-mentioned EPR-effect [27].

1.4 PUBLICATION

Editorial

For reprint orders, please contact: reprints@futuremedicine.com

Nanomedicine



Pushing radiation therapy limitations with theranostic nanoparticles

“Nanoparticles design is a rising landscape in the era of modern oncology offering new perspectives.”

First draft submitted: 2 March 2016; Accepted for publication: 10 March 2016; Published online: 13 April 2016

Keywords: clinical trial • gadolinium • image-guided radiation therapy • radiosensitizer • theranostic nanoparticles

In radiation oncology, while radiation is effective in killing cancer cells, the dose safely deliverable to the target volume is often limited by the possibility of collateral damage to surrounding healthy tissues. However, for some cancer sites, it has been shown that a dose escalation in the tumor could significantly improve local control and patient survival [1]. While recently developed methods such as intensity-modulated radiation therapy, volumetric-modulated arc therapy and image-guided radiation therapy have improved the delivered radiation dose conformality, dose escalation remains an important clinical challenge that needs to be addressed to improve the efficacy of radiation therapy [2].

Nanoparticles design is a rising landscape in the era of modern oncology offering new perspectives. The enhancement of radiation effect induced by radiosensitizing nanoparticles is probably one of the most translational aspects. Radiosensitizing nanoparticles increase the radiobiological effects within the site of disease while maintaining the current clinical constraints on dose delivered to healthy organs. The photoelectric interaction increases strongly as a function of the atomic number of the nanoparticle (proportional to Z^4-Z^5), giving these particles a high interaction probability with low-energy photons and allowing the formation of additional diffused photons, photoelectrons, Auger electrons and reactive oxygen species that have the potential to amplify the biological damage. Even

under high-energy photon irradiation, high-Z nanoparticles can interact with primary or secondary species permitting a highly efficient nanoscale dose deposition around the nanoparticle [3]. Consequently, the differential effect between healthy tissue and tumor tissue is improved.

The efficacy of nanoparticles as radiosensitizers has been demonstrated at the preclinical level for multiple high-Z nanoparticles since Hainfeld *et al.* demonstrated the potential of gold nanoparticles after systemic injection [4], and at the clinical level for hafnium nanoparticles [5]. However, because of the injection method (intratumoral injection) and because of their size (50 nm), the hafnium nanoparticle applications are mainly limited to easy-to-access tumor sites, such as sarcoma, head and neck and prostate cancers. For the majority of other cancer sites, intravenous injection remains an obligation. To address these limitations while still ensuring low toxicity to the healthy tissues, theranostic nanoparticles were created, combining diagnostic and therapeutic properties.

Gadolinium is the most well-known element for biomedical applications. Its use in medicine is directly correlated with the development of contrast agents for MRI, a noninvasive and nonionizing method for acquiring volumetric images with high spatial resolution and excellent soft-tissue contrast. Some clinics have begun to replace CT simulation with MRI simulation for radiation treatment



Alexandre Detappe

Institut Lumiere Matière, UMR 5306 CNRS, Lyon 1 University, Lyon, France and

Department of Radiation Oncology, Dana-Farber Cancer Institute, Harvard Medical School, Boston, MA 02215, USA



Francois Lux

Institut Lumiere Matière, UMR 5306 CNRS, Lyon 1 University, Lyon, France



Olivier Tillement

Author for correspondence: Institut Lumiere Matière, UMR 5306 CNRS, Lyon 1 University, Lyon, France olivier.tillement@univ-lyon1.fr



planning purposes, and future MR-LINAC and MR-based real-time tumor tracking techniques are under development [6,7]. Besides their use for imaging applications, gadolinium-based compounds are also envisaged for therapeutic applications. Gadolinium displays high capture cross-section due to its relatively high atomic number ($Z = 64$) and can interact with high energies irradiations, making it an effective radiosensitizer.

“The enhancement of radiation effect induced by radiosensitizing nanoparticles is probably one of the most translational aspects.”

Our group developed AGuIX (Activation and Guidance of irradiation by x-ray), a sub-5 nm nanoparticle based on a polysiloxane network surrounded by gadolinium chelates [8,9], designed to be an effective MRI contrast agent and radiosensitizer. Because of the VEGF produced by tumor cells to stimulate the tumor angiogenesis and of the lack of effective lymphatic drainage in the tumor tissues, AGuIX can penetrate the tumor after a systemic injection thanks to the enhanced permeability and retention effect. The nanoparticles stay inside the tumor for a significant period of time, before being cleared by the kidneys, avoiding toxicity issues by limiting their exposition to healthy organs. Preclinical studies conducted in various tumor models have demonstrated that low concentrations of AGuIX injected intravenously were attractive radiosensitizers with a significant therapeutic effect, while confirming that the nanoparticle is nontoxic [10]. In addition, its high longitudinal relaxivity allows for better contrast properties than current US FDA-approved gadolinium chelates, creating a potential for future use in MRI-

guiding radiation therapy, notably with the upcoming MR-LINAC technology [11,12].

The logical step after demonstrating the potential of AGuIX at the preclinical level for several tumor localizations is to continue the nanoparticles development to the clinical step. A current GMP manufacturing process has been developed and the regulatory toxicity tests on two animal models (rodents and monkeys) have shown no evidence of toxicity. A clinical Phase I will be investigated in France by our group in close collaboration with NH TherAguix SAS in order to determine the safety of AGuIX and its maximum tolerated dose in patients concurrently treated with standard chemoradiation; define the recommended phase II dose of AGuIX; and define the biodistribution of a single intravenous injection as well as multiple AGuIX injections in order to provide a rationale of AGuIX dosing administration. These results will demonstrate the translationality of using nanoparticles as image-guided radiation therapy agents and further clinical trial will be performed to quantify the therapeutic benefits of AGuIX. The proof-of-concept of using AGuIX as a theranostic agent in human will be a breakthrough approach for patient benefit.

Financial & competing interests disclosure

F Lux, and O Tillement have one patent to disclose: WO2011135101. This patent protects some of the nanoparticles described in this publication: AGuIX. The authors have no other relevant affiliations or financial involvement with any organization or entity with a financial interest in or financial conflict with the subject matter or materials discussed in the manuscript apart from those disclosed.

No writing assistance was utilized in the production of this manuscript.

References

- Budiharto T, Haustermans K, Van Cutsem E *et al.* A Phase I radiation dose-escalation study to determine the maximal dose of radiotherapy in combination with weekly gemcitabine in patients with locally advanced pancreatic adenocarcinoma. *Radiat. Oncol.* 3, 30 (2008).
- Jaffray DA. Image-guided radiotherapy: from current concept to future perspectives. *Nat. Rev. Clin. Oncol.* 9(12), 688–699 (2012).
- Mcquaid HN, Muir MF, Taggart LE *et al.* Imaging and radiation effects of gold nanoparticles in tumour cells. *Sci. Rep.* 6, 19442 (2016).
- Hainfeld JF, Slatkin DN, Smilowitz HM. The use of gold nanoparticles to enhance radiotherapy in mice. *Phys. Med. Biol.* 49(18), N309–N315 (2004).
- Min Y, Caster JM, Eblan MJ, Wang AZ. Clinical translation of nanomedicine. *Chem. Rev.* 115(19), 11147–11190 (2015).
- (P015) Radiation Biological Responses of MRI-Linac vs Linac in Human Head and Neck and Lung Cancer Cells. *Oncology* 29(4 Suppl. 1), pii:205024 (2015) (Epub ahead of print).
- Keall PJ, Barton M, Crozier S *et al.* The Australian magnetic resonance imaging-linac program. *Semin. Radiat. Oncol.* 24(3), 203–206 (2014).
- Sancey L, Lux F, Kotb S *et al.* The use of theranostic gadolinium-based nanoprobe to improve radiotherapy efficacy. *Br. J. Radiol.* 87(1041), 20140134 (2014).
- Lux F, Sancey L, Bianchi A *et al.* Gadolinium-based nanoparticles for theranostic MRI-radiosensitization. *Nanomedicine (Lond.)* 10(11), 1801–1815 (2015).
- Sancey L, Kotb S, Truillet C *et al.* Long-term *in vivo* clearance of gadolinium-based AGuIX nanoparticles and their biocompatibility after systemic injection. *ACS Nano* 9(3), 2477–2488 (2015).

- 11 Detappe A, Kunjachan S, Rottmann J *et al.* AGuIX nanoparticles as a promising platform for image-guided radiation therapy. *Cancer Nanotechnol.* 6(1), 4 (2015).
- 12 Le Duc G, Miladi I, Alric C *et al.* Toward an image-guided microbeam radiation therapy using gadolinium-based nanoparticles. *ACS Nano* 5(12), 9566–9574 (2011).

2

Analytical approach

Contents

2.1	Motivations	29
2.2	Beam modeling and dose deposition calculation	30
2.2.1	Monte-Carlo simulation	30
2.2.2	Analytical calculation	30
2.2.3	Probability of photon-nanoparticle interaction	32
2.3	Impact of the clinical setup on nanoparticle activation	33
2.3.1	Depth and field size dependency	33
2.3.2	Impact of the radiation beam for radiation dose enhancement	34
2.4	Conclusion	35
2.5	Publications	36

2.1 MOTIVATIONS

While nanoparticle-based cancer therapy has been an active area of research for several years, current approaches are beset by significant challenges including inadequate diffusion of nanoparticles into the tumor and poor tissue penetration of the activating agent (optical, IR, UV, kV X-rays, etc.) [28, 29]. The treatment concept described overcomes these challenges and offers a simple clinical workflow for improving cancer therapy in combination with high energy external beam radiation therapy. The photoelectric interaction of low energy (<150 keV) photons with high atomic number atoms leads to the emission of short range electrons as detailed in Chapter 1. Auger interactions occur at very low energies and emitted Auger electrons are quickly absorbed before contributing to the dose enhancement around the nanoparticle [30-32]. Using Monte-Carlo techniques, it has been found that the nanoscopic photoelectric dose enhancement for a clinical 6 MV photon beam can be of many orders of magnitude [33-34]. Clinical radiation beams produced by a linear accelerator have substantial skin sparing and deep tissue penetration properties. However, an existing obstacle to high atomic number nanoparticle enhanced radiation therapy is the low proportion of low energy (<150 keV) photons in a clinical beam that will most strongly interact with the nanoparticle. In a nominal 6 MV beam, only 8% of the photon spectrum is comprised of photons with energies below 150 keV at

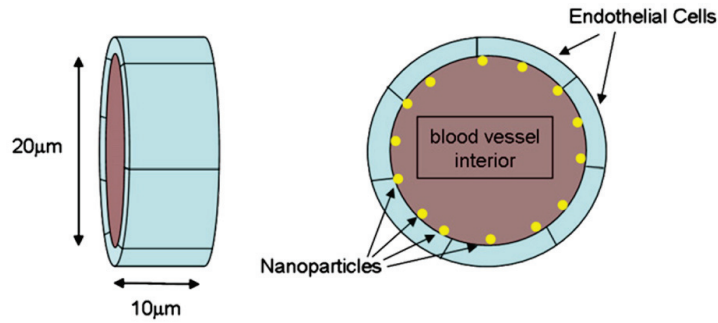


Figure 2.1: Simplified model of endothelial cell layer between intravascular cavity and tumor cells. The tumor is composed by 7 endothelial cells. The nanoparticles are attached to the vascular side of the endothelium. Image courtesy of R Berbeco *et al* [36].

10 cm depth in tissue. To overcome this obstacle, we have simulated by Monte-Carlo and calculated analytically the influence of the radiation beam modification and clinical setup modifications. The analytical calculation was performed with a polysiloxane-based gadolinium AGuIX nanoparticle (Si-GdNP).

2.2 BEAM MODELING AND DOSE DEPOSITION CALCULATION

2.2.1 MONTE-CARLO SIMULATION

Photon spectra were calculated for a Varian 6 MV linac using the EGSnrc Monte-Carlo (MC) computer mode. The accelerator head was simulated with flattening filter (STD) and without flattening filter (FFF) for different field sizes ($3 \times 3 \text{ cm}^2$ to $14 \times 28 \text{ cm}^2$), and depths (2 to 20 cm) (Fig. 2.2). For FFF linac simulations, flattening filter was removed from the simulation and a 2 mm copper plate was placed in the flattening filter position [35].

2.2.2 ANALYTICAL CALCULATION

THE MODEL

The analytical model is based on the dose deposition into an endothelial cell to create a vascular disruption [36]. The endothelial cell is simulated as a thin slab measuring $2 \mu\text{m}$ (thickness) \times $10 \mu\text{m}$ (length) \times $10 \mu\text{m}$ (width) (Fig. 2.1). It is surrounded on the four short sides by other similarly shaped cells. A spherical nanoparticle is simulated as attached to the vascular-side surface of the endothelial cell. The positioning of the nanoparticle along the endothelial cell exterior is not an important consideration. When the calculation is expanded to include multiple nanoparticles, evenly spread throughout the vasculature, photoelectrons released near the edge of an endothelial cell may deposit energy to the adjacent cell and vice versa, thereby providing lateral electron equilibrium. Self-absorption of photoelectrons within the nanoparticles is not considered, as it is negligible for MV beams. The nanoparticles size simulated was equal to 5 nm diameter. This size is relatively small in comparison to the endothelial cells but large enough not to be transmitted intracellularly or through the leaky vasculature. It is noteworthy that the size of the nanoparticles does not influence the calculation outcome for a given overall gadolinium level trapped in microvasculature.

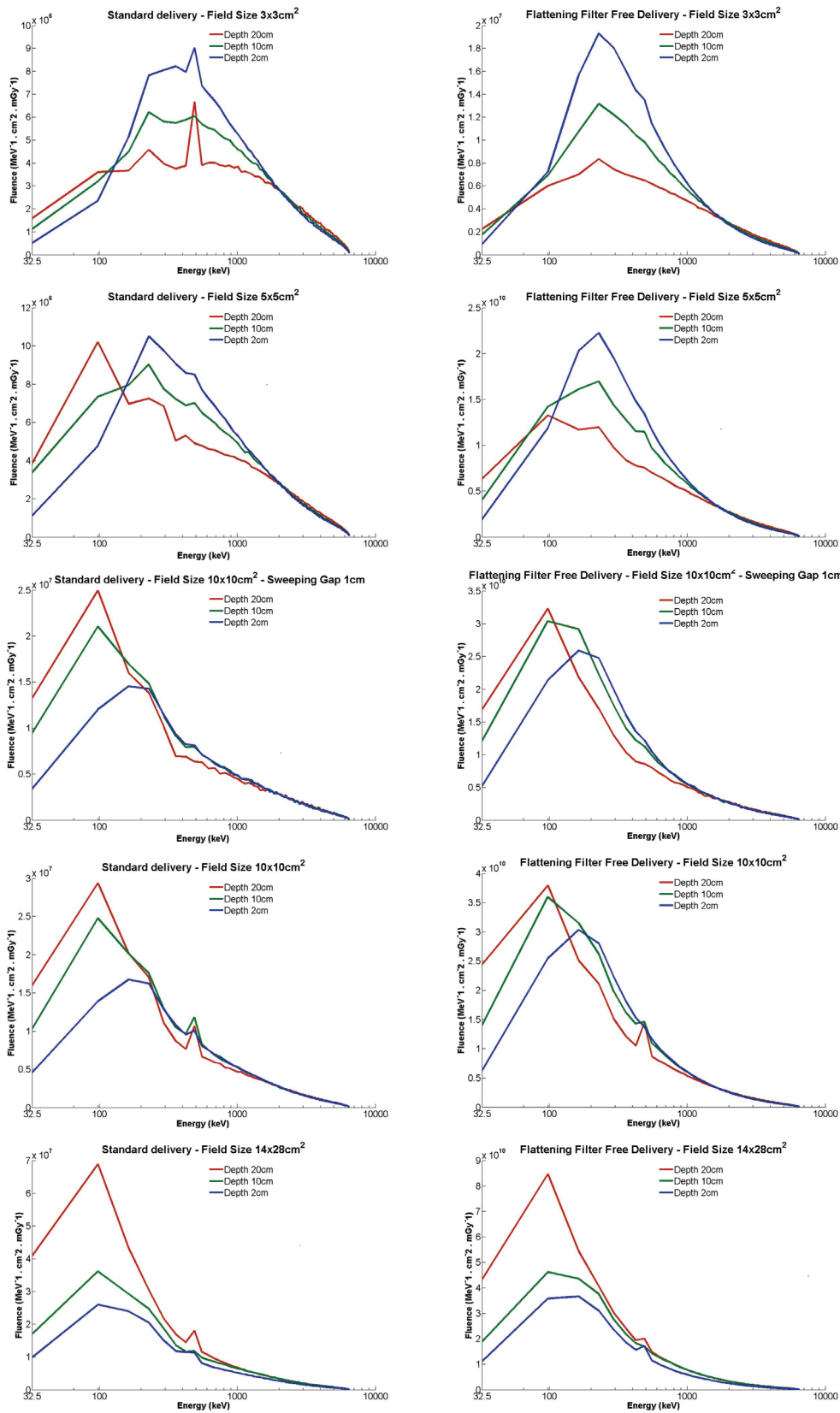


Figure 2.2: Comparison of the fluence in $\text{MeV}^{-1} \cdot \text{cm}^2 \cdot \text{mGy}^{-1}$ as a function of the energy in keV between the standard delivery method and the flattening filter free delivery method.

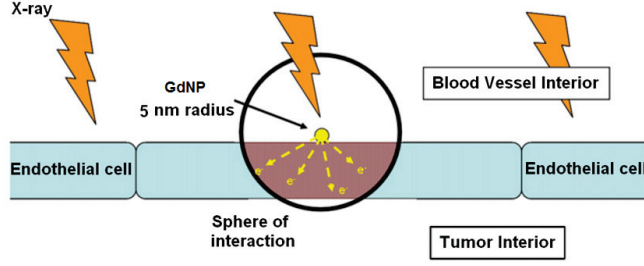


Figure 2.3: The sphere of interaction represents the range of photoelectrons generated by nanoparticles. The extra dose deposited in the nearest endothelial cell by the nanoparticle photoelectric emission is used to calculate the dose enhancement. Image courtesy of R Berbeco *et al* [36].

2.2.3 PROBABILITY OF PHOTON-NANOPARTICLE INTERACTION

The photoelectric effect is the principal effect modeling in this calculation. The dose deposited by Auger electrons is not taken into account in this simulation. The probability of interaction resulting in the emission of a photoelectron is calculated for each incident photon energy bin (Eq. 2.1). The figure 2.3 represents the simulation and where the dose enhancement is calculated.

$$\frac{N(x)}{N_0} = 1 - \exp\left(\left(\frac{\mu_{PE}}{\xi}\right)_{Metal} \cdot \xi_{NP} \cdot d_{NP}\right) \approx \left(\frac{\mu_{PE}}{\xi}\right)_{Metal} \times \xi_{NP} \times d_{NP} \quad (2.1)$$

- $(\mu_{PE}/\xi)_{Metal}$ is the photoelectric coefficient for gadolinium for a specific incident photon energy.
- d_{NP} is the average distance traversed by photons through a spherical 5 nm diameter nanoparticle.
- ξ_{NP} is the gadolinium density.

Each photoelectron emitted from a nanoparticle will deposit energy locally as a function of its initial kinetic energy. This kinetic energy can be found by subtracting the K-edge electron binding energy from the energy of the incident photon as sampled from the energy spectrum described previously. For example, an incoming 100-keV photon will release a K-edge electron with a kinetic energy of roughly 20 keV. The energy loss for a statistical sample of photoelectrons will occur in a sphere of interaction centered on the nanoparticle. For this first order analytic approximation, photoelectrons originate at the center of the nanoparticle and any increase in attenuation and scatter due to Z-material (rather than tissue) in the first 5 nm (i.e., within the nanoparticle) is ignored. Comparisons with macrodosimetry validate this approximation. In this study only the dose enhancement in the endothelial cells is being calculated, so the energy deposited in the sphere of interaction that lies outside the endothelial cells must be excluded.

In other words, we exclude half of the total energy deposited within the entire sphere and the energy deposited in the spherical cap present in the distal border of the cell. An adaptation of the calculation from Makrigiorgos *et al.* [37] was performed to determine the radiation dose from a spherical source to a slab geometry. The energy deposited within a volume is calculated by integration over the differential energy loss (dE/dr) from the surface of the AGuIX (R_n) to the distal side of the endothelial cell (D_E). Therefore the energy deposited within the endothelial cell is calculated as follow (Eq. 2.2):

$$E_{endothelial} = \int_{R_n}^{R_n+D_E} \frac{shell_{hemisphere} - shell_{cap}}{shell_{sphere}} \times \frac{dE}{dr} dr \quad (2.2)$$

where dE/dr is derived from the relationship expressed by Cole (Eq. 2.3) [38]:

$$\frac{dE}{dR} = 3.316 (R + 0.007)^{-0.435} + 0.0055R^{0.33} \quad (2.3)$$

and R is the residual range of the photoelectron at the point r , with $R = R_{tot} - r$, with R_{tot} the total range of the photoelectron for an energy E : $R_{tot} = 0.0431(E + 0.367)^{1.77} - 0.007$.

The absorbed dose is defined as the energy deposited in the endothelial cell divided by its mass. This calculation does not consider dose to endothelial cells from nanoparticles located on the opposite side of the blood vessel or those contained within the blood vessel (but not close to the wall). Given the energy of the emitted photoelectrons, the additional dose contribution from the former should not be significant because we are assuming an active targeting method and irradiation at the time point of fullest retention [39], we will also assume that no AGuIX are still flowing through the vessels at the time of irradiation. The energy bin with the largest contribution has a mean value of 97.5 keV. For this energy bin, the probability to create a photoelectron is equal to 6.1×10^{-4} per photon incident upon a gadolinium nanoparticle with a 5 nm diameter. The size is arbitrarily chosen for ease of comparison with the earlier work. As in that study, the nanoparticle size ends up canceling out when the overall local concentration is investigated. The additional dose deposited inside the adjacent endothelial cell by one AGuIX-photon interaction at this energy is 3.3×10^{-3} Gy.

2.3 IMPACT OF THE CLINICAL SETUP ON NANOPARTICLE ACTIVATION

2.3.1 DEPTH AND FIELD SIZE DEPENDENCY

With a local concentration of AGuIX nanoparticles equal to 30 mg/ml, a STD delivery method, at 2 cm depth, for a field size 10×10 cm², the endothelial dose enhancement factor (EDEF) is equal to 1.64 for the 97.5 keV energy bin. This result is similar to our previous study using a different source for the photon energy spectra. Summing all of the energy bins for this set-up, the total EDEF is 1.9. In general, EDEF increases with field size, going from 1.2 (3×3 cm², STD, 20 cm depth) to 3.5 (14×28 cm², STD, 20 cm depth). The total range in EDEF calculated is from 1.2 (3×3 cm², STD, 20 cm depth) to 4.2 (14×28 cm², FFF, 20 cm depth). The differences in EDEF for each configuration can be explained by the effects of field size, depth, and delivery mode, on the spectral content of the photon beam at the point of interaction. For field sizes greater than 5×5 cm², EDEF increases with increasing depth for both STD and FFF deliveries. For 5×5 cm² and below, EDEF is roughly constant with depth for STD delivery and decreases slightly with depth for FFF delivery.

In this study, we have calculated the dose enhancement due to photoelectric interactions only, excluding the contributions of Auger electrons as well as Compton interactions (Fig. 2.4). Auger production was not included because it has been shown that the impact of Auger electrons is most substantial below 20 keV incident photons. In addition, the very short range of Auger electrons necessitates close proximity of the source with the DNA target, something which is not included in our conservative model. The cross-section for Compton interactions has little dependence on the atomic number (Z) of the material and, therefore, is not expected to contribute substantially to the EDEF. It should be noted, however, that if our assumptions are incorrect and Auger and Compton interactions were left out in error, this would only lead to larger dose enhancement than is reported here. Therefore, our results can be taken as a conservative estimate on these grounds. Published experimental results in cell culture indicate similar findings albeit with less energy dependence than expected. Using fitted linear quadratic parameters, Chithrani *et al.* [40] showed dose enhancement factors of 1.66 (105 kVp), 1.43 (220 kVp), 1.18 (¹³⁷Cs), and 1.17 (6 MV). Jain *et al.* [41] found factors of 1.41 (160 kVp), 1.29 (6 MV), and 1.16 (15 MV) for MDAMB-231 cells and no significant effect for L132 or DU145 cells. Similar effects were seen by Liu *et al.* [42], but the published results are not easily comparable. While some of these differences may be due to nanoparticle formulation, cell line, experimental setup, dose calculation, and other experimental procedures, it is still possible that some other factor is limiting the efficacy of the kV beams. Speculation on this is beyond the scope of the current work, but it is something that should be investigated.

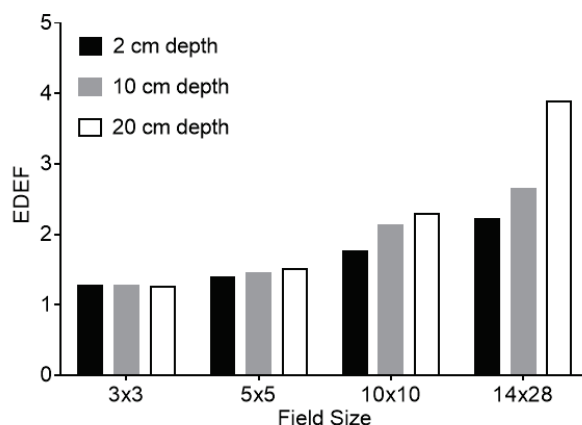


Figure 2.4: Depth and field size dependence for a 5 nm diameter size nanoparticle irradiated by a 6 MV clinical radiation beam.

2.3.2 IMPACT OF THE RADIATION BEAM FOR RADIATION DOSE ENHANCEMENT

An evaluation of 3 different clinical radiation beams was performed in order to compare their potential to increase the efficacy of the radiosensitizer AGuIX: 6 MV standard with a target Cu/W; 6 MV-FFF with a target Cu/W; and 6 MV with a target Carbon. Beam softening with a low Z target is expected to increase AGuIX therapeutic effectiveness. Our previous theoretical calculations combining Monte-Carlo with the analytical microdosimetry calculation described above predict a roughly 50%–150% increase in dose to the tumor endothelial cells for a 6 MV standard (Cu/W) beam. Factors that affect the therapeutic efficacy include depth in tissue, removal of the FFF, and the energy of the electron beam incident on the target. Due to the lack of any clear absolute metric of the consequences of endothelial dose enhancement, we report our results as relative endothelial dose enhancement, where the 6 MV standard Cu/W target is the reference. In this way, we are able to show the relative advantage of the lower atomic number linear accelerator target. The relative enhancement of each target is calculated at each depth, providing the increase in EDEF for the low Z target under the same treatment conditions as the conventional target. The explicit expression for the calculation of the relative improvement in EDEF is $EDEF_{new\ target}/EDEF_{standard\ flat(Cu/W)}$.

Figure 2.5 shows the percentage of low energy photons (25–150 keV) for each target and depth combination (2 cm, 10 cm, and 20 cm depth for a 10x10cm² field size). Relative to the 6 MV standard (Cu/W) beam, the 6 MV-FFF beam shows a substantial increase in low energy photons for all depths. At 10 cm depth, the 6 MV standard beam is composed of 8% low energy photons compared to 11% for the FFF beam. The 6 MV carbon target beam has a much larger proportion of low energy photons at all depths than either of the Cu/W beams (standard or FFF). At 10 cm depth, the 6 MV carbon target beam is composed of 28% low energy photons. This is nearly four times the low energy photon content of the standard 6 MV beam and more than two and a half times that of the 6 MV-FFF beam. Of note, the 6 MV carbon target beam becomes harder at greater depths whereas both 6 MV standard and FFF beams become softer at greater depths in tissue (Fig. 2.5).

As expected from the Monte-Carlo photon energy spectrum results, the relative improvement in EDEF for the carbon target beam is substantial at all depths. The calculation of relative increase in EDEF is made independently for each depth condition, using the entire photon energy spectrum. Figure 2.6 shows the relative EDEF for the carbon target beam compared to the 6 MV-FFF beam. At 2 cm depth, the carbon target beam provides 17.5 times the endothelial dose enhancement as a 6 MV standard beam. This reduces to 7.1 times at 10 cm depth and 3 times at 20 cm depth as the relative difference in the proportion of low energy photons decreases at the deepest depths. The 6 MV-FFF beam would supply more than twice as much endothelial dose at 2 cm, decreasing to 1.3

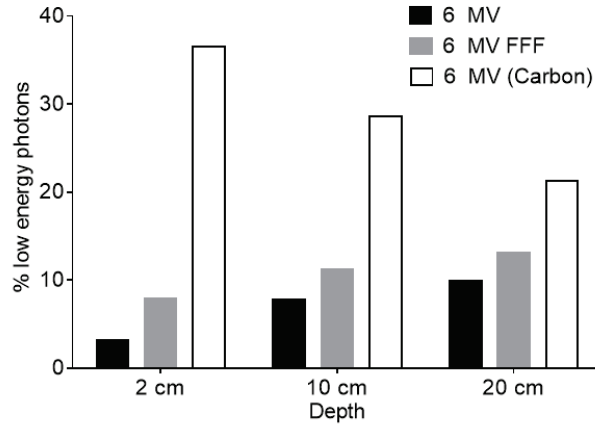


Figure 2.5: The percentage of low energy photons (25–150 keV) for a standard (Cu/W target) beam, a FFF (Cu/W target) beam, and a carbon target beam.

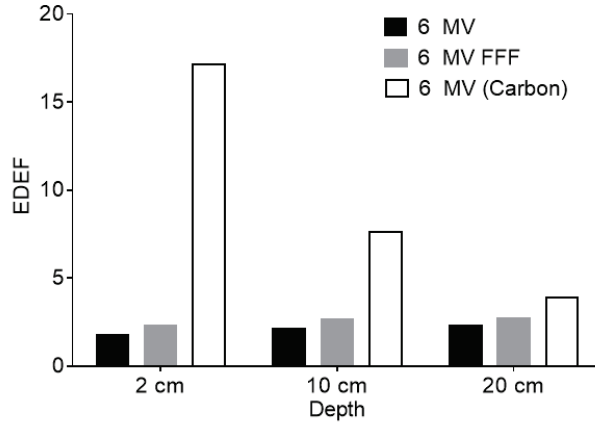


Figure 2.6: Endothelial dose enhancement factor calculation in function of the irradiation beam (6 MV beam, 6 MV-FFF, and 6 MV modified with a carbon target instead of copper) with a 5 nm diameter size gold nanoparticles.

times at 20 cm depth (Fig. 2.6).

2.4 CONCLUSION

Through this analytical calculation, we have shown that clinical beam parameters may be chosen to maximize the proportion of low energy photons incident on the nanoparticles, and thereby maximizing the therapeutic effect. When more scattering material (e.g., larger field sizes, depths in tissue, target) precedes the nanoparticle, the beam will be relatively softer than the primary, alone. The enhancement effect for every field size and depth investigated is amplified by the removal of the flattening filter; a finding that has been experimentally confirmed in an *in vitro* study by Berbeco *et al* [43]. These findings are also consistent with the known increase in the contribution of low energy photons in a FFF delivery. The advantage of the inherently softer FFF primary beam is lessened at increasing treatment depths for small field sizes. Modulation of the external clinical beam with the multileaf collimator tends to decrease the proportion of low energy photons, therefore providing less enhancement than the corresponding open field for both STD and FFF delivery techniques.

We also demonstrated that a 6 MV photon beam generated using a clinical linear accelerator with a carbon target will provide a substantial increase in low energy photons compared to conventional

beams with a Cu/W target. These additional low energy photons will translate into a multifold increase in endothelial dose enhancement when incident upon AGuIX nanoparticles in close proximity. A full study of 3D treatment planning with a 6 MV carbon target beam will be the subject of a future study.

Due to the complexity of biological systems, the unknown influence of the tumor microenvironment as well as the response of the rest of the tumor system to local vascular damage, the values given in the results may not translate to clinical outcomes in a linear fashion. However, the relative damage enhancements expected due to differing depth, field size, and delivery mode should translate readily to the human system. In a future clinical application, nanoparticle could be administered prior to radiation therapy to enhance tumor damage. The amount, concentration, frequency, and timing of injection are all factors that have not yet been determined. Numerous safety studies are necessary before clinical implementation of this technology. Given the known biocompatibility of AGuIX and the precision with which modern radiation therapy can be delivered, we expect less toxicity than for comparable chemoradiotherapeutics.

The results of this work predict a dose enhancement to tumor blood vessel endothelial cells using conventional therapeutic (MV) X-rays and quantify the relative change in enhancement with treatment depth and field size. The radiation dose delivered to tumor endothelial cells during AGuIX-aided radiation therapy will depend on the location in the body, treatment beam parameters as well as the local concentration of nanoparticle. The concept of customizing photon spectra via a fastswitching target is a novel concept which could offer a further personalized solution for each unique clinical scenario.

It is noteworthy that the work describe a dose enhancement induced by the presence of nanoparticle in the endothelial cells. The same conclusions can be made with a tumor targeted nanoparticle.

2.5 PUBLICATIONS

The effect of flattening filter free delivery on endothelial dose enhancement with gold nanoparticles

Alexandre Detappe

Dana-Farber Cancer Institute, Brigham and Women's Hospital and Harvard Medical School, Boston, Massachusetts 02115 and Medical Physics Department, Joseph Fourier University, Grenoble 38000, France

Panagiotis Tsiamas

Dana-Farber Cancer Institute, Brigham and Women's Hospital and Harvard Medical School, Boston, Massachusetts 02115 and Medical Physics Department, Medical School, University of Thessaly, Larisa 41100, Greece

Wilfred Ngwa, Piotr Zygmanski, Mike Makrigrigorgos, and Ross Berbeco^{a)}

Dana-Farber Cancer Institute, Brigham and Women's Hospital and Harvard Medical School, Boston, Massachusetts 02115

(Received 15 October 2012; revised 29 January 2013; accepted for publication 29 January 2013; published 12 February 2013)

Purpose: The aim of this study is to quantify and to compare the dose enhancement factor from gold nanoparticles (AuNP) to tumor endothelial cells for different concentrations of AuNP, and clinical MV beam configurations.

Methods: Tumor endothelial cells are modeled as slabs measuring $10 \times 10 \times 2 \mu\text{m}$. A spherical AuNP is simulated on the surface of the endothelial cell, within the blood vessel. 6 MV photon beams with and without the flattening filter are investigated for different field sizes, depths in material and beam modulation. The incident photon energy spectra for each configuration is generated using EGSnrc. The dose enhancement in the tumor endothelial cell is found using an analytical calculation. The endothelial dose enhancement factor is defined to be the ratio of the dose deposited with and without AuNPs.

Results: It is found that clinical beam parameters may be chosen to maximize the effect of gold nanoparticles during radiotherapy. This effect is further amplified $\sim 20\%$ by the removal of the flattening filter. Modulation of the clinical beam with the multileaf collimator tends to decrease the proportion of low energy photons, therefore providing less enhancement than the corresponding open field.

Conclusions: The results of this work predict a dose enhancement to tumor blood vessel endothelial cells using conventional therapeutic (MV) x-rays and quantify the relative change in enhancement with treatment depth and field size. © 2013 American Association of Physicists in Medicine. [<http://dx.doi.org/10.1118/1.4791671>]

Key words: gold nanoparticle, vascular-disrupting agent, flattening filter free, dose enhancement, Monte-Carlo

I. INTRODUCTION

There has been an increasing interest in nanoparticles for cancer treatment.¹⁻⁴ Recent work has showed their potential to improve drug delivery,⁵ imaging contrast,⁶ and radiation therapy.^{2,7} The use of gold nanoparticles (AuNP) as a radio-enhancer is especially compelling because of their biocompatibility,⁸ ease of surface functionalization, and high atomic number ($Z = 79$). This last property is important in the generation of short range photoelectrons or Auger electrons when irradiated with low energy photons which can enhance the dose locally. Theoretical results have been buttressed by preclinical studies showing the potential for significant therapeutic gain when AuNP are administered prior to radiation therapy.²

Previous Monte Carlo studies have prematurely dismissed high energy photons as a clinically enhancing source.⁹⁻¹¹ This is mainly due to the common assumption of a homogeneous distribution of AuNP within the tumor. While most

of these studies calculate dose to the whole tumor, some authors have acknowledged that a substantial local enhancement is possible.^{11,12} Coupled with experimental studies of AuNP accumulation in tumor vasculature,^{13,14} these results suggest the potential use of gold nanoparticles as vascular disrupting agents (VDA) during clinical (MV) radiotherapy.

Analytical calculations of brachytherapy¹⁵ and external beam radiotherapy¹² have shown the potential benefit of targeted gold nanoparticles as VDA. The goal of VDA therapies is to collapse a solid tumor with a vascular structure by depriving it of nutrients and oxygen.¹⁶ We have hypothesized that AuNPs can be used in combination with standard radiation therapy for this same purpose. In our concept, the therapy target can be covered by conventional radiation doses, while the local dose enhancement is delivered in close proximity to the AuNPs.

In this work, we extend the previous analytic calculations by including photon energy spectra generated with Monte Carlo under various clinical conditions. The underlying

hypothesis is that increasing proportions of low energy photons will lead to larger endothelial dose enhancement factors (EDEF). The goal of this paper is to determine the EDEF under these various clinical beam configurations simulated for a 6 MV linac. The results will provide a basis for further translational research.

II. MATERIALS AND METHODS

II.A. Photon energy spectra

The photon energy spectra used in this study are generated using the EGSnrc Monte Carlo code for a clinical linac-generated 6 MV photon beam. Standard (STD) delivery and delivery without the flattening filter (FFF) are investigated for different field sizes, depths in material and beam modulation. The investigated beam conditions are shown in Table I.

All beams represent a specific configuration of the linear accelerator which has been experimentally validated in our clinic.¹⁷ In this study, all calculations are performed at the central axis. Intensity-modulated radiation therapy (IMRT) is simulated by a 1 cm sweeping gap (SW). The fluence in $\text{MeV}^{-1} \cdot \text{cm}^{-2}$ is obtained from these simulations for each 65 keV energy bin between 0 and 6.5 MeV. The dose is calculated with the DOSXYZnrc code. The phantom size simulated is $100 \times 100 \times 40$ cm and placed at 100 cm from the source (SSD 100 cm). The calculation is based on a uniform voxel measuring $1.0 \times 1.0 \times 0.5$ cm. Thus, the fluence is divided by the dose calculated in mGy, for each depth in water (2, 10, and 20 cm). The fluence in $\text{MeV}^{-1} \cdot \text{cm}^{-2} \cdot \text{mGy}^{-1}$ is used for the rest of the study. Examples of the photon energy spectrum are shown in Fig. 1 for STD and FFF deliveries, at 10 cm depth for a 10×10 cm² field.

II.B. The analytical calculation

The analytical calculation we used is presented in a previous paper.¹² Each AuNP is simulated as a sphere on the exterior surface of an endothelial cell (Fig. 2). This is a conservative location for the AuNP as endocytosis is likely to occur. The size of the AuNP is arbitrary in this calculation as it will cancel out when the enhancement relative to AuNP concentration is calculated. Self-absorption of photoelectrons within the AuNP is not considered, as it is negligible for MV beams.¹⁸ The endothelial cell is simulated as a thin slab measuring $2 \mu\text{m}$ (thickness) $\times 10 \mu\text{m}$ (length) $\times 10 \mu\text{m}$ (width).

TABLE I. Clinical configurations simulated for STD and FFF at the central axis.

Field size (cm ²)	Depth in water		
	2 cm	10 cm	20 cm
3×3	+	+	+
5×5	+	+	+
10×10	+	+	+
10×10 (SW)	+	+	+
14×28	+	+	+

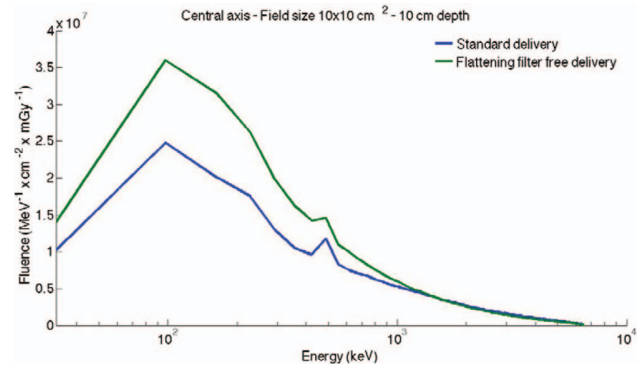


FIG. 1. Representation of the fluence in $\text{MeV}^{-1} \cdot \text{cm}^{-2} \cdot \text{mGy}^{-1}$ at the central axis for a 10×10 cm² field size with a semilog scale.

The positioning of the nanoparticles along the exterior of the endothelial cell is not an important consideration because lateral equilibrium is assumed.

III. RESULTS

The energy bin with the largest contribution has a mean value of 97.5 keV. For this energy bin, the probability to create a photoelectron is equal to 6.9×10^{-4} per photon incident upon a gold nanoparticle with a 100 nm diameter. The size is arbitrarily chosen for ease of comparison with the earlier work. As in that study, the nanoparticle size ends up canceling out when the overall local concentration is investigated. The additional dose deposited inside the adjacent endothelial cell by one AuNP-photon interaction at this energy is 3.7×10^{-3} Gy.

With a local concentration of AuNPs equal to 30 mg/ml, a STD delivery method, at 2 cm depth, for a field size 10×10 cm², the EDEF is equal to 1.64 for the 97.5 keV energy bin. This result is similar to our previous study using a different source for the photon energy spectra.¹² Summing all of the energy bins for this set-up, the total EDEF is 2.1. The results for EDEF as a function of depth are shown in Fig. 3 for a concentration of AuNPs equal to 30 mg/ml of tissue.

In general, EDEF increases with field size, going from 1.2 (3×3 cm², STD, 20 cm depth) to 3.9 (14×28 cm², STD, 20 cm depth). The total range in EDEF calculated is from 1.2

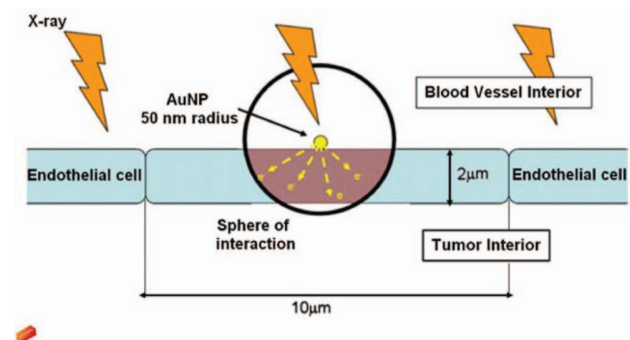


FIG. 2. The sphere of interaction represents the range of photoelectrons generated by AuNPs [Berbeco *et al.* (Ref. 22)].

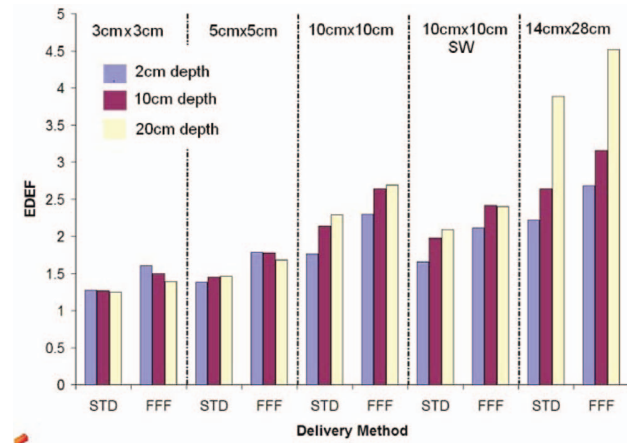


FIG. 3. The total EDEF with 30 mg/ml of gold nanoparticles for 3 different depths: 2, 10, and 20 cm for 5 field sizes: 3×3 , 5×5 , 10×10 , 10×10 (SW), and 14×28 cm².

(3×3 cm², STD, 20 cm depth) to 4.5 (14×28 cm², FFF, 20 cm depth). The differences in EDEF for each configuration can be explained by the effects of field size, depth, and delivery mode, on the spectral content of the photon beam at the point of interaction.

For field sizes greater than 5×5 cm², EDEF increases with increasing depth for both STD and FFF deliveries. For 5×5 cm² and below, EDEF is roughly constant with depth for STD delivery and decreases slightly with depth for FFF delivery.

EDEF increases linearly as a function of the local AuNP concentration, regardless of depth and delivery type. This is due to the linear component of concentration in the calculation. For each field size and depth, the EDEF is highest for FFF, then FFF SW, then STD, and the least for STD SW.

The EDEF for FFF deliveries are always higher than for the corresponding STD delivery, due to the inclusion of more low energy photons in the primary beam. The percentage difference between FFF and STD is greatest for the smallest field sizes and shallowest depths (Fig. 3). For the same method of delivery, a higher value of the EDEF is obtained for the open beams than the respective modulated one.

IV. DISCUSSION

Hainfeld *et al.*² demonstrated experimentally that it is possible to enhance the effects of radiation therapy by prior administration of AuNPs in a murine tumor model. This study and the theoretical ones that followed have focused mainly on irradiation with kV x-rays, due to the clear advantage, in terms of photoelectric interaction efficiency as well as Auger electron production. However, the use of kV x-rays in humans is severely limited due to either gross under-coverage of the tumor, very poor skin-sparing in the patient or necessitating the implantation of radioisotopes, an invasive procedure which is only appropriate for a small subset of patients. By focusing our attention on MV photon beams produced by clinical lin-

ear accelerators, we prepare for a broader clinical application and potentially clearer path to clinical trials.

In this study, we have calculated the dose enhancement due to photoelectric interactions only, excluding the contributions of Auger electrons as well as Compton interactions. Auger production was not included because it has been shown that the impact of Auger electrons is most substantial below 20 keV incident photons.¹⁹ In addition, the very short range of Auger electrons necessitates close proximity of the source with the target DNA, something which is not included in our conservative model. The cross-section for Compton interactions has little dependence on the atomic number (Z) of the material and, therefore, is not expected to contribute substantially to the EDEF. It should be noted, however, that if our assumptions are incorrect and Auger and Compton interactions were left out in error, this would only lead to larger dose enhancement than is reported in this study. Therefore, our results can be taken as a conservative estimate on these grounds.

Published experimental results in cell culture indicate similar findings albeit with less energy dependence than expected. Using fitted LQ parameters, Chithrani *et al.*²⁰ showed dose enhancement factors of 1.66 (105 kVp), 1.43 (220 kVp), 1.18 (¹³⁷Cs), and 1.17 (6 MVp). Jain *et al.*²¹ found factors of 1.41 (160 kVp), 1.29 (6 MV), and 1.16 (15 MV) for MDA-MB-231 cells and no significant effect for L132 or DU145 cells. Similar effects were seen by Liu *et al.*,⁷ but the published results are not easily comparable. While some of these differences may be due to nanoparticle formulation, cell line, experimental setup, dose calculation, and other experimental procedures, it is still possible that some other factor is limiting the efficacy of the kV beams. Speculation on this is beyond the scope of the current work, but it is something that should be investigated.

In this paper, we have calculated the dose enhancement to tumor endothelial cells, anticipating that targeted gold nanoparticles may be used as vascular disrupting agents, when irradiated with clinical photon beams. The results of this study indicate that clinical beam parameters may be chosen to maximize the proportion of low energy photons incident on the nanoparticles, and thereby maximizing the therapeutic effect. When more scattering material (e.g., larger field sizes, depths in tissue) precedes the AuNP, the beam will be relatively “softer” than the primary, alone. An exception occurs for very small field sizes (3×3 cm²). In this case, the enhancement decreases slightly as a function of depth, as the primary beam is the dominant contributor.

The enhancement effect for every field size and depth investigated is amplified by the removal of the flattening filter; a finding that has been experimentally confirmed in an *in vitro* study by Berbeco *et al.*²² These findings are also consistent with the known increase in the contribution of low energy photons in a FFF delivery. The advantage of the inherently softer FFF primary beam is lessened at increasing treatment depths for small field sizes. Modulation of the external clinical beam with the multileaf collimator tends to decrease the proportion of low energy photons, therefore providing less enhancement than the corresponding open field for both STD and FFF delivery techniques.

Due to the complexity of biological systems, the unknown influence of the tumor microenvironment as well as the response of the rest of the tumor system to local vascular damage, the values given in the results may not translate to clinical outcomes in a linear fashion. However, the relative damage enhancements expected due to differing depth, field size, and delivery mode should translate readily to the human system.

In a future clinical application, AuNP could be administered prior to radiation therapy to enhance tumor damage. The amount, concentration, frequency, and timing of injection are all factors that have not yet been determined. Numerous safety studies are necessary before clinical implementation of this technology. Given the known biocompatibility of gold and the precision with which modern radiation therapy can be delivered, we expect less toxicity less than for comparable chemoradiotherapeutics.

V. CONCLUSIONS

The results of this work predict a dose enhancement to tumor blood vessel endothelial cells using conventional therapeutic (MV) x-rays and quantify the relative change in enhancement with treatment depth and field size. The radiation dose delivered to tumor endothelial cells during AuNP-aided radiation therapy will depend on the location in the body, treatment beam parameters as well as the local concentration of AuNP. Experiments at the preclinical level are planned to further corroborate these results.

ACKNOWLEDGMENTS

The project described was supported, in part, by a Brigham and Women's Hospital Biomedical Research Institute Seed Grant and by Award No. R03CA164645 from the National Cancer Institute. The content is solely the responsibility of the authors and does not necessarily represent the official views of the National Cancer Institute or the National Institutes of Health.

³⁾Electronic mail: rberbeco@lroc.harvard.edu

¹J. F. Hainfeld, F. A. Dilmanian, D. N. Slatkin, and H. M. Smilowitz, "Radiotherapy enhancement with gold nanoparticles," *J. Pharm. Pharmacol.* **60**(8), 977–985 (2008).

²J. F. Hainfeld, D. N. Slatkin, and H. M. Smilowitz, "The use of gold nanoparticles to enhance radiotherapy in mice," *Phys. Med. Biol.* **49**(18), N309–N315 (2004).

³S. Jain, D. G. Hirst, and J. M. O'Sullivan, "Gold nanoparticles as novel agents for cancer therapy," *Br. J. Radiol.* **85**(1010), 101–113 (2012).

⁴S. M. Moghimi, A. C. Hunter, and J. C. Murray, "Long-circulating and target-specific nanoparticles: Theory to practice," *Pharmacol. Rev.* **53**(2), 283–318 (2001).

⁵D. W. Siemann, D. J. Chaplin, and M. R. Horsman, "Vascular-targeting therapies for treatment of malignant disease," *Cancer* **100**(12), 2491–2499 (2004).

⁶R. Popovtzer *et al.*, "Targeted gold nanoparticles enable molecular CT imaging of cancer," *Nano Lett.* **8**(12), 4593–4596 (2008).

⁷C. J. Liu *et al.*, "Enhancement of cell radiation sensitivity by pegylated gold nanoparticles," *Phys. Med. Biol.* **55**(4), 931–945 (2010).

⁸E. E. Connor, J. Mwamuka, A. Gole, C. J. Murphy, and M. D. Wyatt, "Gold nanoparticles are taken up by human cells but do not cause acute cytotoxicity," *Small* **1**(3), 325–327 (2005).

⁹S. H. Cho, "Estimation of tumour dose enhancement due to gold nanoparticles during typical radiation treatments: A preliminary Monte Carlo study," *Phys. Med. Biol.* **50**(15), N163–N173 (2005).

¹⁰S. H. Cho, B. L. Jones, and S. Krishnan, "The dosimetric feasibility of gold nanoparticle-aided radiation therapy (GNRT) via brachytherapy using low-energy gamma-/x-ray sources," *Phys. Med. Biol.* **54**(16), 4889–4905 (2009).

¹¹B. L. Jones, S. Krishnan, and S. H. Cho, "Estimation of microscopic dose enhancement factor around gold nanoparticles by Monte Carlo calculations," *Med. Phys.* **37**(7), 3809–3816 (2010).

¹²R. I. Berbeco, W. Ngwa, and G. M. Makrigiorgos, "Localized dose enhancement to tumor blood vessel endothelial cells via megavoltage x-rays and targeted gold nanoparticles: New potential for external beam radiotherapy," *Int. J. Radiat. Oncol., Biol., Phys.* **81**(1), 270–276 (2011).

¹³E. A. Murphy *et al.*, "Nanoparticle-mediated drug delivery to tumor vasculature suppresses metastasis," *Proc. Natl. Acad. Sci. U.S.A.* **105**(27), 9343–9348 (2008).

¹⁴S. D. Perrault, C. Walkey, T. Jennings, H. C. Fischer, and W. C. W. Chan, "Mediating tumor targeting efficiency of nanoparticles through design," *Nano Lett.* **9**(5), 1909–1915 (2009).

¹⁵W. Ngwa, G. M. Makrigiorgos, and R. I. Berbeco, "Applying gold nanoparticles as tumor-vascular disrupting agents during brachytherapy: Estimation of endothelial dose enhancement," *Phys. Med. Biol.* **55**(21), 6533–6548 (2010).

¹⁶J. W. Lippert, "Vascular disrupting agents," *Bioorg. Med. Chem.* **15**(2), 605–615 (2007).

¹⁷P. Tsiamas *et al.*, "A modification of flattening filter free linac for IMRT," *Med. Phys.* **38**(5), 2342–2352 (2011).

¹⁸M. K. K. Leung, J. C. L. Chow, D. B. Chithrani, M. J. G. Lee, B. Oms, and D. A. Jaffray, "Irradiation of gold nanoparticles by x-rays: Monte Carlo simulation of dose enhancements and the spatial properties of the secondary electrons production," *Med. Phys.* **38**(2), 624–631 (2011).

¹⁹F. Van den Heuvel, J. P. Locquet, and S. Nuyts, "Beam energy considerations for gold nano-particle enhanced radiation treatment," *Phys. Med. Biol.* **55**(16), 4509–4520 (2010).

²⁰D. B. Chithrani *et al.*, "Gold nanoparticles as radiation sensitizers in cancer therapy," *Radiat. Res.* **173**(6), 719–728 (2010).

²¹S. Jain *et al.*, "Cell-specific radiosensitization by gold nanoparticles at megavoltage radiation energies," *Int. J. Radiat. Oncol., Biol., Phys.* **79**(2), 531–539 (2011).

²²R. I. Berbeco *et al.*, "DNA damage enhancement from gold nanoparticles for clinical MV photon beams," *Radiat. Res.* **178**(6), 604–608 (2012).

Low Z target switching to increase tumor endothelial cell dose enhancement during gold nanoparticle-aided radiation therapy

Ross I. Berbeco^{a)} and Alexandre Detappe

Department of Radiation Oncology, Brigham and Women's Hospital, Dana-Farber Cancer Institute and Harvard Medical School, Boston, Massachusetts 02115

Panagiotis Tsiamas

Department of Radiation Oncology, St. Jude Children's Hospital, Memphis, Tennessee 38105

David Parsons, Mammo Yewondwossen, and James Robar

Department of Radiation Oncology and Department of Physics and Atmospheric Science, Dalhousie University, Halifax, Nova Scotia B3H 1V7, Canada

(Received 1 July 2015; revised 13 October 2015; accepted for publication 28 November 2015; published 31 December 2015)

Purpose: Previous studies have introduced gold nanoparticles as vascular-disrupting agents during radiation therapy. Crucial to this concept is the low energy photon content of the therapy radiation beam. The authors introduce a new mode of delivery including a linear accelerator target that can toggle between low Z and high Z targets during beam delivery. In this study, the authors examine the potential increase in tumor blood vessel endothelial cell radiation dose enhancement with the low Z target.

Methods: The authors use Monte Carlo methods to simulate delivery of three different clinical photon beams: (1) a 6 MV standard (Cu/W) beam, (2) a 6 MV flattening filter free (Cu/W), and (3) a 6 MV (carbon) beam. The photon energy spectra for each scenario are generated for depths in tissue-equivalent material: 2, 10, and 20 cm. The endothelial dose enhancement for each target and depth is calculated using a previously published analytic method.

Results: It is found that the carbon target increases the proportion of low energy (<150 keV) photons at 10 cm depth to 28% from 8% for the 6 MV standard (Cu/W) beam. This nearly quadrupling of the low energy photon content incident on a gold nanoparticle results in 7.7 times the endothelial dose enhancement as a 6 MV standard (Cu/W) beam at this depth. Increased surface dose from the low Z target can be mitigated by well-spaced beam arrangements.

Conclusions: By using the fast-switching target, one can modulate the photon beam during delivery, producing a customized photon energy spectrum for each specific situation. © 2016 American Association of Physicists in Medicine. [<http://dx.doi.org/10.1118/1.4938410>]

Key words: radiation therapy, nanoparticle, dose enhancement, vascular disruption

1. INTRODUCTION

While nanoparticle-based cancer therapy has been an active area of research for several years, current approaches are beset by significant challenges including inadequate diffusion of nanoparticles into the tumor and the poor tissue penetration of the activating agent (optical, IR, UV, kV x-rays, etc.).^{1,2} The treatment concept described in this paper overcomes these challenges and offers a simple clinical workflow for improving cancer therapy in combination with high energy external beam radiation therapy.

We propose to target tumor blood vessels with gold nanoparticles (GNPs) prior to radiation therapy with a clinical linear accelerator. There is a growing body of evidence that vascular targets could be more important for anticancer therapy than clonogenic cell death alone.^{3–11} Garcia-Barros *et al.* proposed that damage to tumor vasculature during radiation therapy (specifically, apoptosis in the endothelial cells) may be a more important mechanism for tumor eradication than clonogenic cell death.³ A recent review by Park *et al.* enumerated the

experimental evidence that radiation-induced tumor vascular damage is contributing to the success of stereotactic radiation therapy procedures.⁴ Murphy *et al.* have shown that nanoparticle-mediated drug delivery to tumor vasculature can even have an antimetastatic effect.¹² Accordingly, for radiation therapy combined with GNP, a higher concentration of GNP near the vasculature provides a biological advantage over a homogeneous distribution throughout the tumor.¹³ Serendipitously, accumulation in the vasculature is expected for nanoparticles of a certain size.¹⁴ Nanoparticle concentration and duration in the tumor vasculature can be further optimized by molecular targeting.^{12,14}

The photoelectric interaction of low energy (<150 keV) photons with gold atoms leads to the emission of short-range electrons. Auger interactions occur at very low energies and emitted Auger electrons are quickly absorbed before contributing to the dose enhancement.^{15–17} Using Monte Carlo techniques, it has been found that the nanoscopic photoelectric dose enhancement for a clinical 6 MV photon beam can be many orders of magnitude, close to the GNP.^{18,19} Similarly,

endothelial cells in close proximity to GNP are expected to receive a highly selective boost, exceeding the predictions for homogeneously distributed GNP.²⁰

Chemical vascular-disrupting agents (VDAs) have been developed and tested clinically and preclinically. It has been shown that chemical VDA improves the effects of radiation therapy in preclinical models.^{21–23} However, recent human clinical trials of chemical VDA have resulted in unacceptable toxicities, limiting translation.^{4,5,11,24,25} By using biocompatible GNP, coupled with precise image-guided radiation therapy, we anticipate a reduction in associated normal tissue toxicities.

The concept of GNP as vascular-disrupting agents when combined with external beam radiation therapy was first introduced in a theoretical study by Berbeco *et al.*¹³ An analytical calculation was performed based on a conservative geometry of a GNP localized adjacent to endothelial cells. The results of that study demonstrated the feasibility of providing substantial radiation dose enhancement to tumor endothelial cells during clinical radiation therapy procedures. Experimental evidence has also shown that gold nanoparticle aided radiation therapy can lead to increased cell death, *in vitro*,^{26–28} and increased tumor vascular damage, *in vivo*.^{29,30} A recent study by Kunjachan *et al.* demonstrated tumor vascular disruption after radiation combined with vascular-targeted gold nanoparticles in a multitude of experimental assays.³¹

Clinical radiation beams produced by a linear accelerator have substantial skin sparing and deep tissue penetration properties. However, an existing obstacle to gold nanoparticle-enhanced radiation therapy is the low proportion of low energy (<150 keV) photons in a clinical beam that will interact most strongly with the GNP. In a nominal 6 MV beam, only 8% of the photon spectrum is comprised of photons with energies less than 150 keV at 10 cm depth in tissue.

To overcome this obstacle, we propose a modification of the linear accelerator target to deliver more low energy photons—i.e., a “softer” beam. The goal is to design a target that balances increased GNP interactions with maintenance of normal tissue dose constraints. We will show that a 6 MV beam produced using a carbon target will almost quadruple the proportion of low energy (<150 keV) photons at 10 cm depth, which corresponds to 7.7 times the endothelial dose enhancement of a standard clinical beam. We will also show

that the corresponding 52% relative increase in surface dose is entirely mitigated by the use of multiple beam angles, a common practice in clinical radiation therapy.

A prototype switching target has been built and demonstrated on a clinical linear accelerator (Fig. 1). The device is compact, occupying, for testing purposes, a single port of the carousel of the linear accelerator (21iX, Varian Medical Systems, Inc.). The two targets included in the prototype are composed of copper/tungsten (Cu/W) and carbon (C), respectively. The switching mechanism operates at ~250 ms and is controlled externally. A complete description of the device will be presented in a separate publication. One application of the switching target is intermittent high contrast beam’s-eye-view (BEV) imaging during radiation therapy.^{32,33} However, a similar device can be used in the future to customize the photon energy spectrum for each treatment field, depending on the patient anatomy, target location, and geometry of normal tissues. In principle, both therapy and BEV imaging functions of the low Z switching target can be used simultaneously, a concept that is beyond the current scope of work. In the following study, we examine the dosimetric advantage of including a low Z linear accelerator target in gold nanoparticle aided radiation therapy.

2. METHODS AND MATERIALS

2.A. Monte Carlo photon spectrum generation

A Varian 2100EX Clinac was simulated using BEAMnrc. The model was modified from previous work,³² to account for changes present in the most recent High Energy Accelerator Monte Carlo Data Package provided by Varian Medical Systems under a nondisclosure agreement. These modifications largely consisted of the inclusion of the metal plating on the dielectric windows of the monitor chamber. To simulate the low Z target, the Cu/W target and flattening filter were removed and the carbon target placed 9 mm from the beryllium exit window. Directional bremsstrahlung splitting was used with a splitting radius of 10 cm for a jaw defined 10×10 cm,² at a source-to-surface distance (SSD) of 100 cm, with a bremsstrahlung splitting number of 2000. AE = ECU and AP = PCUT values of 0.521 and 0.010 MeV, respectively, were used. Phase-spaces were scored at the water surface and at depths of 2, 10, and 20 cm. Dose was similarly calculated

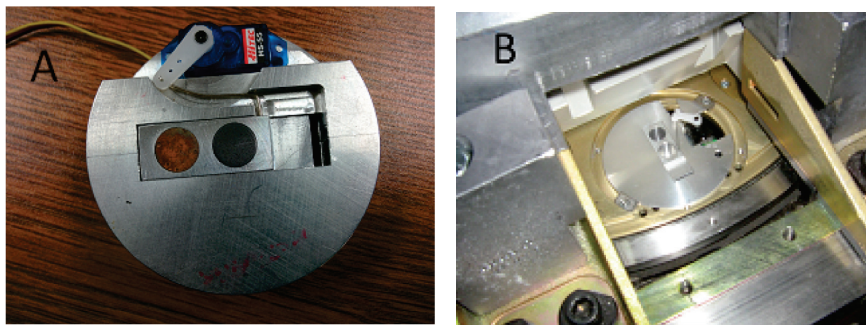


Fig. 1. (A) The switching target (Cu/W and C) with electric motor and external control, (B) the switching target in the carousel of a Varian linear accelerator at Dalhousie University.

TABLE I. Thermal conductivity of target materials.

Target material	Thermal conductivity ($\text{W m}^{-1} \text{K}^{-1}$)
Diamond	900–2300
Graphite	119–165
Copper	401
Tungsten	173

at mentioned depths using DOSXYZnrc. BEAMdp was used to determine spectral distributions of the phase space files.

Previous theoretical and experimental investigations of beryllium ($Z = 4$) and aluminum ($Z = 13$) targets demonstrated the production of large amounts of low energy photons.³⁴ However, these target materials are not practical for clinical applications. For example, beryllium has a low neutron activation energy and is toxic/carcinogenic when machined. Aluminum is inexpensive and convenient to machine, but has a low melting point (660°C). In addition, it has been shown that reducing the atomic number of the target to values lower than carbon (e.g., beryllium) has the effect of increasing the relative photon content at very low energies leading to increases in surface dose without substantial low energy photons at clinically relevant depths.³²

For these reasons, we chose to investigate carbon in the current work. Carbon has a low atomic number ($Z = 6$) and no melting point (sublimes at $\sim 3600^\circ\text{C}$). Table I shows the thermal conductivity of potential target materials. Although the efficiency of bremsstrahlung is approximately Z^2 overall, within the bounds of the primary collimator (e.g., $\pm 14^\circ$), the dependence on Z is weak.^{35,36}

We generated Monte Carlo photon spectra for the following cases: (1) “standard” flat 6 MV beam with a Cu/W target, (2) flattening filter free (FFF) beam with a Cu/W target, and (3) FFF beam with a C target. This last beam is referred to as “6 MV (Carbon)” in this study. We used a 10×10 cm aperture at isocenter and 100 cm SSD for all beams. As the beams penetrate deeper in tissue, beam hardening (due to selective absorption of low energy primary photons) or softening (due to patient/phantom scatter) can decrease or increase the proportion of low energy photons. To study this effect, we generated spectra at 2, 10, and 20 cm depth in tissue. In addition to studying the relative endothelial dose enhancement, we also investigated the effect of the carbon target beam on entrance dose.

The Monte Carlo methods of photon beam generation with low Z targets used in this study have been previously validated experimentally.³² In those studies, photon depth dose measurements were acquired for both carbon and aluminum targets and excellent agreement with the Monte Carlo predictions was demonstrated.

2.B. An analytical calculation method for endothelial dose enhancement

We used a previously published method for estimating endothelial dose enhancement.^{13,37} Briefly, the tumor vascular endothelial cells are modeled as flat rectangular slabs.

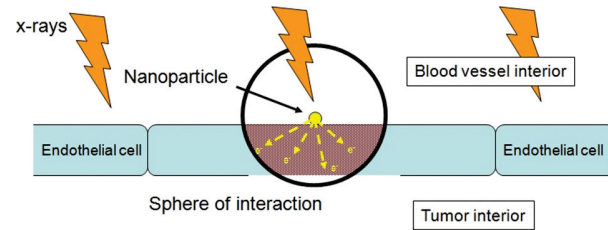


FIG. 2. Simplified model of endothelial cell layer between intravascular cavity and tumor cells. The gold nanoparticles are attached to the vascular side of the endothelium. The range of photoelectrons generated within the GNPs is shown as a “sphere of interaction” with the nanoparticle at the center. The extra dose deposited in the nearest endothelial cell by GNP photoelectron emissions (shaded region) is used to calculate the dose enhancement. Reprinted with permission from Berbeco, Ngwa, and Makrigrigorgos, *Int. J. Radiat. Oncol., Biol., Phys.* **81**(1), 270–276 (2011).

For the calculation, gold nanoparticles are placed just outside the endothelial cell (Fig. 2). This is a conservative model, as endothelial cell uptake of gold nanoparticles, previously demonstrated *in vitro* and *in vivo*, will increase the expected dose enhancement. Only photoelectric interactions are included as Auger effects will be extremely short range (\sim several nanometer) and substantial self-shielding is expected. The photoelectric interaction cross section is provided in tables by NIST.³⁸ The range and dose deposition of emitted photoelectrons is calculated using the method of Cole.³⁹ The generation of photoelectrons will depend greatly on the energy of the incident photon. Photons above roughly 250 keV contribute very little to the dose enhancement. Only dose deposited within the “sphere of interaction” is included in the calculation.

Beam “softening” with a low Z target is expected to increase GNP therapeutic effectiveness.^{13,18,37,40–42} Our previous theoretical calculations combining Monte Carlo with the analytical microdosimetry calculation described above^{13,37} predict a roughly 50%–150% increase in dose to the tumor endothelial cells, for a 6 MV standard (Cu/W) beam. Factors that affect the therapeutic efficacy include depth in tissue,¹³ removal of the FFF, and the energy of the electron beam incident on the target.

The Monte Carlo generated spectra for the targets listed above are used to evaluate relative increase in endothelial dose enhancement. Like other reported calculations of gold nanoparticles in radiation therapy, this analytical calculation has not been validated *in vivo*. However, the concept of increasing DNA damage for larger proportions of low energy photons in a therapy beam has been validated *in vitro*.²⁷ Due to the lack of any clear absolute metric of the consequences of endothelial dose enhancement, we report our results as relative endothelial dose enhancement, where the standard Cu/W target is the reference. In this way, we are able to show the relative advantage of the lower atomic number linear accelerator target. The relative enhancement of each target is calculated at each depth, providing the increase in endothelial dose enhancement factor (EDEF) for the low Z target under the same treatment conditions as the conventional target. The explicit expression for the calculation

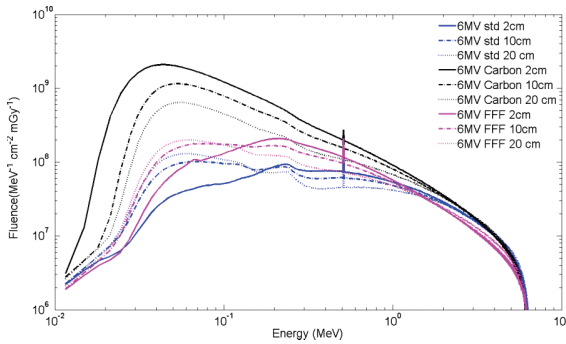


Fig. 3. Photon energy spectra at depth = 2, 10, and 20 cm for 6 MV delivery with a standard flat beam (Cu/W target), a FFF (Cu/W target) beam, and a carbon target beam. Note the substantial increase in low energy photons at all depths for the carbon target relative to the Cu/W target.

of the relative improvement in EDEF is $EDEF_{\text{new target}} / EDEF_{\text{standard flat(Cu/W)}}$.

3. RESULTS

The photon energy spectra calculated with the Monte Carlo for 6 MV standard (Cu/W), 6 MV FFF (Cu/W), and 6 MV (carbon) are shown in Fig. 3. These spectra are generated for depths of 2, 10, and 20 cm in tissue. Figure 4 shows the percentage of low energy photons (25–150 keV) for each target and depth combination. Relative to the 6 MV standard (Cu/W) beam, the 6 MV FFF beam shows a substantial increase in low energy photons for all depths. At 10 cm depth, the 6 MV standard beam is composed of 8% low energy photons compared to 11% for the FFF beam. The 6 MV carbon target beam has a much larger proportion of low energy photons at all depths than either of the Cu/W beams (standard or FFF). At 10 cm depth, the 6 MV carbon target beam is composed of 28% low energy photons. This is nearly four times the low energy photon content of the standard 6 MV beam and more than two and a half times that of the 6 MV FFF beam. Of note, the 6 MV carbon target beam becomes harder at greater depths whereas both 6 MV standard and FFF beams become softer at greater depths in tissue.

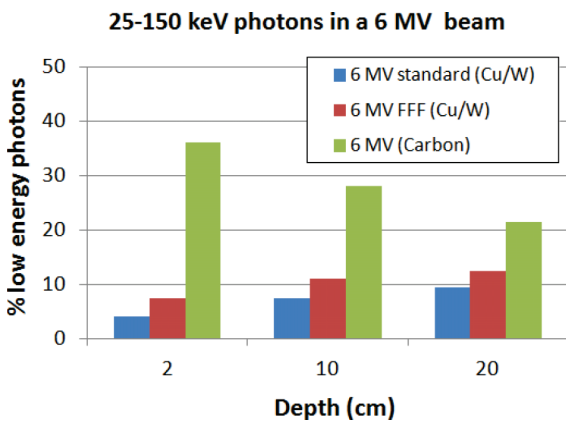


Fig. 4. The percentage of low energy photons (25–150 keV) for a standard (Cu/W target) beam, a FFF (Cu/W target) beam, and a carbon target beam.

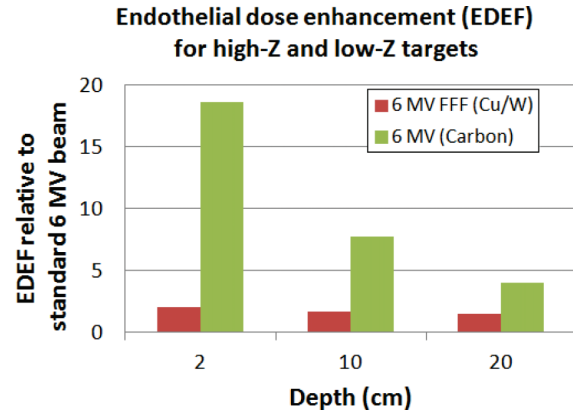


Fig. 5. The expected increase in the EDEF for 6 MV FFF (Cu/W) and 6 MV (carbon), respectively. Results are shown relative to a 6 MV standard (Cu/W) beam. At 10 cm depth, the carbon target provides 7.7 times the EDEF.

As expected from the Monte Carlo photon energy spectrum results, the relative improvement in EDEF for the carbon target beam is substantial at all depths. The calculation of relative increase in EDEF is made independently for each depth condition, using the entire photon energy spectrum. Figure 5 shows the relative EDEF for the carbon target beam compared to the 6 MV FFF beam. At 2 cm depth, the carbon target beam provides 18.6 times the endothelial dose enhancement as a 6 MV standard beam. This reduces to 7.7 times at 10 cm depth and 4.0 times at 20 cm depth as the relative difference in the proportion of low energy photons decreases at the deepest depths. The 6 MV FFF beam would supply more than twice as much endothelial dose at 2 cm, decreasing to 1.5 times at 20 cm depth.

Due to the relative nature of the calculation in this paper, the size and concentration of the nanoparticles do not influence the results. In addition, no assumptions have been made about coating (e.g., PEG) or targeting (e.g., RGD).

The Monte Carlo data were also used to investigate the increase in surface dose and loss of penetration depth for standard and proposed beams. The percent depth dose (PDD) curves for the 6 MV standard (Cu/W), 6 MV FFF (Cu/W), 6 MV (carbon) normalized to deliver 100% dose at 10 cm

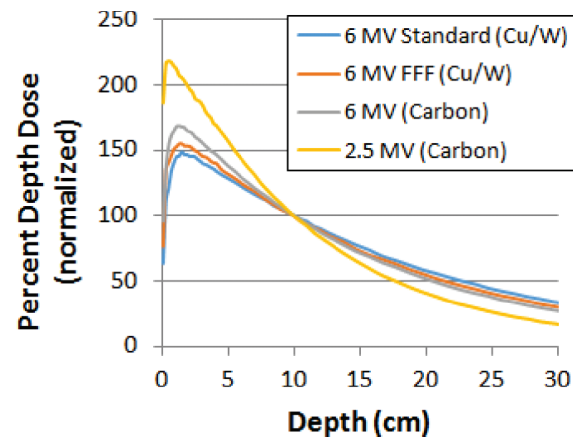


Fig. 6. PDD for 6 MV standard (Cu/W), 6 MV FFF (Cu/W target), 6 MV (carbon), 2.5 MV (C), normalized to 100% at 10 cm depth.

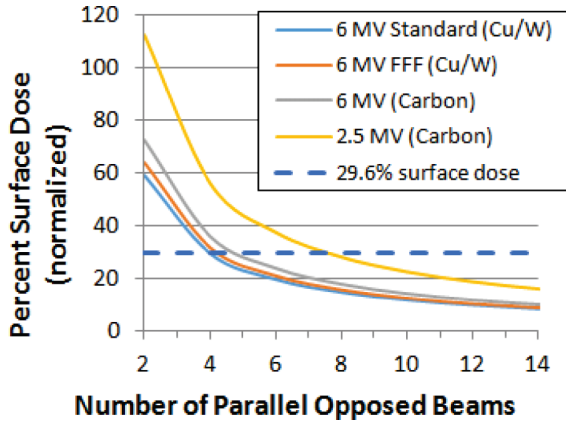


FIG. 7. Normalized percent skin dose as a function of number of parallel opposed treatment beams from different gantry angles. A 2.5 MV (carbon) beam requires eight beam angles to limit the surface dose to the same level as four beam angles of a 6 MV standard (Cu/W) beam (29.6%) while still delivering 100% dose to the tumor.

depth are shown in Fig. 6. We define the surface dose as the central axis dose at 1 mm as a percentage of d_{max} .

The loss of penetration depth and reduced skin sparing effects of beams with more low energy photons contribute to higher entrance dose. Beams of 6 MV FFF (Cu/W) and 6 MV (carbon) contribute 21% and 52% more surface dose than a standard flat 6 MV beam, respectively. However, Fig. 7 shows the reduction in surface dose by the use of treatment plans consisting of multiple angles, as are most commonly used clinically. We simulated parallel opposed beams to include both entrance and exit doses, representing a worst-case scenario. Cylindrical symmetry is assumed with a separation of 20 cm. The normalization is 100% to a point on the central axis at 10 cm depth. To achieve the same or less surface dose (29.6%) as a 4-field standard flat 6 MV delivery, a 6 MV (carbon) beam requires five beams to reach the same level of skin sparing as a 4-field 6 MV standard

(Cu/W) delivery, while still delivering 100% dose to the tumor at 10 cm depth. In these figures, we also show the results for a 2.5 MV (carbon) beam. Currently, used for imaging only, this beam could have therapeutic use in the future.

4. DISCUSSION

In this study, it has been demonstrated that a 6 MV photon beam generated using a clinical linear accelerator with a carbon target will provide a substantial increase in low energy photons compared to conventional beams with a Cu/W target. These additional low energy photons will translate into a multifold increase in endothelial dose enhancement when incident upon gold nanoparticles in close proximity. A full study of 3D treatment planning with a 6 MV carbon target beam will be the subject of a future study.

One potential application of this work is the use of a fast-switching target (FST) to generate custom photon energy spectra. Different clinical scenarios of gold nanoparticle-aided radiation therapy will call for different mixes of low/high energy photon spectra. This will depend on beam angle, field size, patient thickness, and proximity of normal tissues, dose fractionation, and other clinical parameters. Toggling between different targets during beam delivery will generate a customized photon energy spectrum (Fig. 8). The optimal spectrum can be determined prior to treatment delivery similar to the modulation of multileaf collimators in intensity-modulated radiation therapy.

This study is focused on photon beams with a peak energy of 6 MV. Lower energy beams with alternative targets could offer similar advantages in increased proportion of low energy photons. Some currently available linear accelerators are able to deliver imaging beams of 2.5 MV using a low Z target. Previously published studies have shown that 40%–50% of the primary photons from a 2.5 MV (carbon) beam are in the diagnostic range.³³ However, these beam lines are not approved for human radiation therapy and will also likely

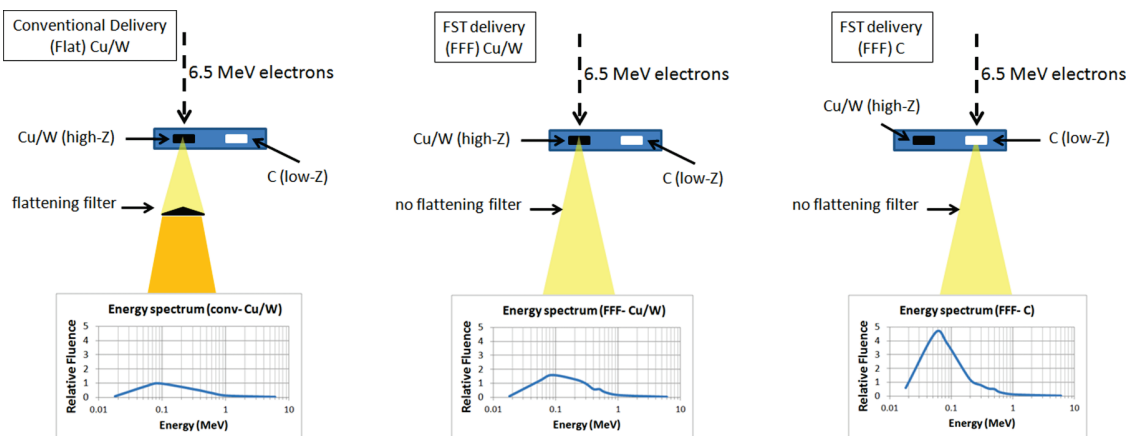


FIG. 8. Conventional delivery (left) is contrasted with FST delivery (middle and right). These drawings depict incoming 6.5 MeV electrons colliding with the linear accelerator target, generating photons for radiation therapy. The resultant photon energy spectra for 10 cm depth in tissue are shown for each delivery mode, respectively. These spectra are shown in greater detail in Fig. 3. (Left) Conventional (conv-Cu/W) delivery is shown with the standard Cu/W target and a flattening filter. (Middle) FST delivery with only the high Z (FFF-Cu/W) target, the flattening filter is removed. (Right) FST delivery with only the low Z (FFF-C) target, the flattening filter is removed.

suffer from a low dose-rate. An additional challenge will be the balance of tumor coverage and skin sparing for deep-seated tumors. Simulated PDD and surface dose calculations are shown in Figs. 6 and 7 for comparison with the 6 MV beams.

Collateral advantages of the fast-switching target research include novel clinical imaging concepts. We anticipate that both volumetric and planar imaging with the therapy beam will be greatly improved by the target modifications presented here, resulting in improved patient setup and beam's-eye-view in-treatment imaging.^{34,43–45} For example, fast and periodic imaging of a lung tumor with a low Z target could be used to update predictive models of respiratory motion, without interruption of the treatment delivery. Previously published imaging work with low Z targets demonstrated a marked improvement in image contrast using a 2.35 MV beam with a carbon target.³³

5. CONCLUSION

Our results indicate that replacing the Cu/W target with a carbon target in a clinical linear accelerator should result in a multifold increase in the radiation dose enhancement to tumor blood vessel endothelial cells when GNP is in close proximity. The resulting disruption of tumor vasculature can provide a new therapeutic tool for clinical situations where the deliverable radiation dose is limited by adjacent normal tissue. The concept of customizing photon spectra via a fast-switching target is a novel concept which could offer a further personalized solution for each unique clinical scenario.

ACKNOWLEDGMENTS

This project was supported, in part, by a grant from Varian Medical Systems, Inc. (J.R.) and the National Cancer Institute of the National Institutes of Health under Award Nos. R03CA164645 and R21CA188833 (R.I.B.). The content is solely the responsibility of the authors and does not necessarily represent the official views of the National Cancer Institute or the National Institutes of Health.

^{a)}Author to whom correspondence should be addressed. Electronic mail: rberbeco@partners.org

¹D. K. Chatterjee, T. Wolfe, J. Lee, A. P. Brown, P. K. Singh, S. R. Bhattarai, P. Diagaradjane, and S. Krishnan, "Convergence of nanotechnology with radiation therapy—insights and implications for clinical translation," *Transl. Cancer Res.* **2**(4), 256–268 (2013).

²W. Ngwa, H. Korideck, A. I. Kassis, R. Kumar, S. Sridhar, G. M. Makrigrigios, and R. A. Cormack, "In vitro radiosensitization by gold nanoparticles during continuous low-dose-rate gamma irradiation with I-125 brachytherapy seeds," *Nanomed.: Nanotechnol., Biol. Med.* **9**(1), 25–27 (2013).

³M. Garcia-Barros, F. Paris, C. Cordon-Cardo, D. Lyden, S. Rafii, A. Haimovitz-Friedman, Z. Fuks, and R. Kolesnick, "Tumor response to radiotherapy regulated by endothelial cell apoptosis," *Science* **300**(5622), 1155–1159 (2003).

⁴H. J. Park, R. J. Griffin, S. Hui, S. H. Levitt, and C. W. Song, "Radiation-induced vascular damage in tumors: Implications of vascular damage in ablative hypofractionated radiotherapy (SBRT and SRS)," *Radiat. Res.* **177**(3), 311–327 (2012).

⁵D. W. Siemann, "The unique characteristics of tumor vasculature and preclinical evidence for its selective disruption by tumor-vascular disrupting agents," *Cancer Treat. Rev.* **37**(1), 63–74 (2011).

⁶P. Carmeliet and R. K. Jain, "Molecular mechanisms and clinical applications of angiogenesis," *Nature* **473**(7347), 298–307 (2011).

⁷J. N. Rich, "Cancer stem cells in radiation resistance," *Cancer Res.* **67**(19), 8980–8984 (2007).

⁸T. Reya, S. J. Morrison, M. F. Clarke, and I. L. Weissman, "Stem cells, cancer, and cancer stem cells," *Nature* **414**(6859), 105–111 (2001).

⁹L. E. Ailles and I. L. Weissman, "Cancer stem cells in solid tumors," *Curr. Opin. Biotechnol.* **18**(5), 460–466 (2007).

¹⁰H. J. Mauceri, N. N. Hanna, M. A. Beckett, D. H. Gorski, M. J. Staba, K. A. Stellato, K. Bigelow, R. Heimann, S. Gately, M. Dhanabal, G. A. Soff, V. P. Sukhatme, D. W. Kufe, and R. R. Weichselbaum, "Combined effects of angiostatin and ionizing radiation in antitumor therapy," *Nature* **394**(6690), 287–291 (1998).

¹¹D. W. Siemann, D. J. Chaplin, and M. R. Horsman, "Vascular-targeting therapies for treatment of malignant disease," *Cancer* **100**(12), 2491–2499 (2004).

¹²E. A. Murphy, B. K. Majeti, L. A. Barnes, M. Makale, S. M. Weis, K. Lutu-Fuga, W. Wrasidlo, and D. A. Cheresh, "Nanoparticle-mediated drug delivery to tumor vasculature suppresses metastasis," *Proc. Natl. Acad. Sci. U. S. A.* **105**(27), 9343–9348 (2008).

¹³R. I. Berbeco, W. Ngwa, and G. M. Makrigrigios, "Localized dose enhancement to tumor blood vessel endothelial cells via megavoltage x-rays and targeted gold nanoparticles: New potential for external beam radiotherapy," *Int. J. Radiat. Oncol., Biol., Phys.* **81**(1), 270–276 (2011).

¹⁴S. D. Perrault, C. Walkey, T. Jennings, H. C. Fischer, and W. C. W. Chan, "Mediating tumor targeting efficiency of nanoparticles through design," *Nano Lett.* **9**(5), 1909–1915 (2009).

¹⁵F. Van den Heuvel, J. P. Locquet, and S. Nuyts, "Beam energy considerations for gold nano-particle enhanced radiation treatment," *Phys. Med. Biol.* **55**(16), 4509–4520 (2010).

¹⁶S. J. McMahon, W. B. Hyland, M. F. Muir, J. A. Coulter, S. Jain, K. T. Butterworth, G. Schettino, G. R. Dickson, A. R. Hounsell, J. M. O'Sullivan, K. M. Prise, D. G. Hirst, and F. J. Currell, "Biological consequences of nanoscale energy deposition near irradiated heavy atom nanoparticles," *Sci. Rep.* **1**, 18 (2011).

¹⁷M. Douglass, E. Bezak, and S. Penfold, "Monte Carlo investigation of the increased radiation deposition due to gold nanoparticles using kilovoltage and megavoltage photons in a 3D randomized cell model," *Med. Phys.* **40**(7), 071710 (9pp.) (2013).

¹⁸P. Tsiamas, B. Liu, F. Cifter, W. F. Ngwa, R. I. Berbeco, C. Kappas, K. Theodorou, K. Marcus, M. G. Makrigrigios, E. Sajo, and P. Zygmanski, "Impact of beam quality on megavoltage radiotherapy treatment techniques utilizing gold nanoparticles for dose enhancement," *Phys. Med. Biol.* **58**(3), 451–464 (2013).

¹⁹B. L. Jones, S. Krishnan, and S. H. Cho, "Estimation of microscopic dose enhancement factor around gold nanoparticles by Monte Carlo calculations," *Med. Phys.* **37**(7), 3809–3816 (2010).

²⁰S. H. Cho, "Estimation of tumour dose enhancement due to gold nanoparticles during typical radiation treatments: A preliminary Monte Carlo study," *Phys. Med. Biol.* **50**(15), N163–N173 (2005).

²¹R. Murata, D. W. Siemann, J. Overgaard, and M. R. Horsman, "Improved tumor response by combining radiation and the vascular-damaging drug 5,6-dimethylxanthenone-4-acetic acid," *Radiat. Res.* **156**(5), 503–509 (2001).

²²D. W. Siemann and A. M. Rojiani, "The vascular disrupting agent ZD6126 shows increased antitumor efficacy and enhanced radiation response in large, advanced tumors," *Int. J. Radiat. Oncol., Biol., Phys.* **62**(3), 846–853 (2005).

²³W. R. Wilson, A. E. Li, D. S. M. Cowan, and B. G. Siim, "Enhancement of tumor radiation response by the antivascular agent 5,6-dimethylxanthenone-4-acetic acid," *Int. J. Radiat. Oncol., Biol., Phys.* **42**(4), 905–908 (1998).

²⁴D. W. Siemann and M. R. Horsman, "Vascular targeted therapies in oncology," *Cell Tissue Res.* **335**(1), 241–248 (2009).

²⁵D. W. Siemann, E. Mercer, S. Lepler, and A. M. Rojiani, "Vascular targeting agents enhance chemotherapeutic agent activities in solid tumor therapy," *Int. J. Cancer* **99**(1), 1–6 (2002).

²⁶D. B. Chithrani, S. Jelveh, F. Jalali, M. van Prooijen, C. Allen, R. G. Bristow, R. P. Hill, and D. A. Jaffray, "Gold nanoparticles as radiation sensitizers in cancer therapy," *Radiat. Res.* **173**(6), 719–728 (2010).

²⁷R. I. Berbeco, H. Korideck, W. Ngwa, R. Kumar, J. Patel, S. Sridhar, S. Johnson, B. Price, A. Kimmelman, and G. M. Makrigrigios, "DNA damage enhancement from gold nanoparticles for clinical MV photon beams," *Radiat. Res.* **178**(6), 604–608 (2012).

- ²⁸S. Jain, J. A. Coulter, A. R. Hounsell, K. T. Butterworth, S. J. McMahon, W. B. Hyland, M. F. Muir, G. R. Dickson, K. M. Prise, F. J. Currell, J. M. O'Sullivan, and D. G. Hirst, "Cell-specific radiosensitization by gold nanoparticles at megavoltage radiation energies," *Int. J. Radiat. Oncol., Biol., Phys.* **79**(2), 531–539 (2011).
- ²⁹J. F. Hainfeld, D. N. Slatkin, and H. M. Smilowitz, "The use of gold nanoparticles to enhance radiotherapy in mice," *Phys. Med. Biol.* **49**(18), N309–N315 (2004).
- ³⁰D. Y. Joh, L. Sun, M. Stangl, A. Al Zaki, S. Murty, P. P. Santoiemma, J. J. Davis, B. C. Baumann, M. Alonso-Basanta, D. Bhang, G. D. Kao, A. Tsourkas, and J. F. Dorsey, "Selective targeting of brain tumors with gold nanoparticle-induced radiosensitization," *PLoS One* **8**(4), e62425 (2013).
- ³¹S. Kunjachan, A. Detappe, R. Kumar, T. Ireland, L. Cameron, D. E. Biancur, V. Motto-Ros, L. Sancey, S. Sridhar, G. M. Makrigiorgos, and R. I. Berbeco, "Nanoparticle mediated tumor vascular disruption: A novel strategy in radiation therapy," *Nano Lett.* **15**(11), 7488–7496 (2015).
- ³²D. Parsons and J. L. Robar, "Beam generation and planar imaging at energies below 2.40 MeV with carbon and aluminum linear accelerator targets," *Med. Phys.* **39**(7), 4568–4578 (2012).
- ³³D. Parsons, J. L. Robar, and D. Sawkey, "A Monte Carlo investigation of low-Z target image quality generated in a linear accelerator using Varian's VirtualLinac," *Med. Phys.* **41**(2), 021719 (6pp.) (2014).
- ³⁴E. J. Orton and J. Robar, "Megavoltage image contrast with low atomic number target materials and amorphous silicon electronic portal imagers," *Phys. Med. Biol.* **54**, 1275–1289 (2009).
- ³⁵C. Karzmark, C. Nunan, and E. Tanabe, *Medical Electron Accelerators* (McGraw-Hill, Inc., Texas, 1992).
- ³⁶B. Nordell and A. Brahme, "Angular distribution and yield from bremsstrahlung targets (for radiation therapy)," *Phys. Med. Biol.* **29**(7), 797–810 (1984).
- ³⁷A. Detappe, P. Tsiamas, W. Ngwa, P. Zygmanski, M. Makrigiorgos, and R. Berbeco, "The effect of flattening filter free delivery on endothelial dose enhancement with gold nanoparticles," *Med. Phys.* **40**(3), 031706 (4pp.) (2013).
- ³⁸NIST Database, <http://www.nist.gov/srd/physics.html>.
- ³⁹A. Cole, "Absorption of 20-Ev to 50000-Ev electron beams in air and plastic," *Radiat. Res.* **38**(1), 7–33 (1969).
- ⁴⁰P. Tsiamas, P. Mishra, F. Cifter, R. I. Berbeco, K. Marcus, E. Sajo, and P. Zygmanski, "Low-Z linac targets for low-MV gold nanoparticle radiation therapy," *Med. Phys.* **41**(2), 021701 (10pp.) (2014).
- ⁴¹J. L. Robar, S. A. Riccio, and M. A. Martin, "Tumour dose enhancement using modified megavoltage photon beams and contrast media," *Phys. Med. Biol.* **47**(14), 2433–2449 (2002).
- ⁴²J. Robar, "Generation and modelling of megavoltage photon beams for contrast-enhanced radiation therapy," *Phys. Med. Biol.* **51**, 5487–5504 (2006).
- ⁴³J. Rottmann, P. Keall, and R. Berbeco, "Real-time soft tissue motion estimation for lung tumors during radiotherapy delivery," *Med. Phys.* **40**(9), 091713 (7pp.) (2013).
- ⁴⁴J. Rottmann, P. J. Keall, and R. I. Berbeco, "Markerless EPID image guided dynamic multileaf collimator tracking for lung tumors," *Phys. Med. Biol.* **58**(12), 4195–4204 (2013).
- ⁴⁵D. Leary and J. L. Robar, "CBCT with specification of imaging dose and CNR by anatomical volume of interest," *Med. Phys.* **41**, 011909 (7pp.) (2014).

3

AGuIX, an effective radiosensitizer : *in vitro* proof of concept

Contents

3.1	Motivations	49
3.2	Nanoparticle uptake by cells	50
3.2.1	MRI quantification	50
3.2.2	Inductively coupled plasma mass spectrometry validation	50
3.3	In vitro proof of concept	52
3.3.1	Proof of concept with preclinical radiation beam	52
3.3.2	Proof of concept with clinical radiation beam	54
3.4	Conclusion	56
3.5	Publication	56

3.1 MOTIVATIONS

Previous assessment of the polysiloxane-based gadolinium AGuIX nanoparticles (Si-GdNP) has mostly focused on their imaging properties [13, 44-47], their efficacy to be used as a theranostic agent for radiation therapy with microbeam radiation therapy/preclinical machines and for photodynamic therapy [48-50]. In radiation therapy, *in vitro* experiments have included different cell lines and preclinical irradiation beams (microbeam radiation therapy, hadron therapy, proton therapy, low energy X-ray, and high-energy X-ray). Researchers have shown early evidence of radiosensitization [51-55]. In addition, *in vivo* experiments with intravenous or intra-tumoral injection for subcutaneous and orthotopic lesions have been performed with preclinical radiation beams [13, 45]. The aim of this study is to characterize the uptake of the AGuIX in pancreatic cancer cells by magnetic resonance imaging (MRI), and investigate the radiation dose enhancement effect attributable to AGuIX when irradiating the cells with a clinical linear accelerator at 6 MV. This represents the first step towards demonstrating an *in vivo* effect for pancreatic cancer. The gadolinium-based platform is particularly relevant for pancreatic cancer due to the poor prognosis, proximity of organs at risk, and targeting difficulty for this disease in radiation therapy. The nanoparticle offers a solution that is highly compatible with

the current trend in radiation oncology towards MRI-based patient simulation and MRI-Linac treatment devices. There may be a strong potential for this nanoparticle in future MRI-guided radiation therapy for pancreatic cancer [8-56].

As described previously, nanoparticles made of high atomic number (Z) elements cause local amplification of radiation dose due to the emission of low energy photoelectrons and Auger electron interactions [13, 31]. The interaction cross-section is highly dependent on the energy of the incident photons, with lower energy photons having a much higher probability of interaction. In clinical radiation therapy, roughly 95% of patient treatments are performed with high-energy X-ray beams produced by clinical linear accelerators with peak energy of 6 MV. This is in contrast to preclinical X-ray irradiators with peak energies of 200-300 kV. For this reason, many investigators have dismissed the potential for clinical radiation therapy improvement with nanoparticles [57, 58]. The data presented in this study refute those previous conclusions. In addition to the physical dose enhancement induced by metallic nanoparticles, radiation-induced biochemical reactions may also contribute to the overall tumor damage, however, the essential mechanism is still under investigation [24]. This chapter has for focus to demonstrate the potential of AGuIX nanoparticle as an efficient radiosensitizer with a pancreatic cell line, and then to understand the influence of the clinical radiation setup with clinical radiation beams.

3.2 NANOPARTICLE UPTAKE BY CELLS

3.2.1 MRI QUANTIFICATION

The concentration of the nanoparticles inside the cells was analyzed with a Bruker Biospin 7T Magnetic Resonance Imaging (MRI) scanner. The longitudinal relaxivity of the nanoparticles is approx. 60 mM^{-1} per nanoparticle [59]. First, a calibration curve without cells was acquired for various concentrations of nanoparticles in the cell culture solution. The concentration of AGuIX used for the experiment is given in gadolinium equivalent species and chosen based on published literature. Cells were incubated with 0.5 mM (0.43 mg/L) of AGuIX at 37 C and 5 % CO_2 for 30 min, 1 h, 3 h, 6 h, 24 h and 48 h. After incubation, the cells were washed and trypsinized to remove any excess nanoparticles in the solution before scanning. All MRI scans featured a RARE-T1 map imaging-sequence with 2 mm slice thickness, repetition time of 10 ms, echo time of 21.4 ms, echo train length of 4, flip angle of 180, and matrix size 256x128 pixels. Each measurement was performed in triplicate (Fig. 3.1).

3.2.2 INDUCTIVELY COUPLED PLASMA MASS SPECTROMETRY VALIDATION

Inductively coupled plasma mass spectrometry (ICP-MS) was used to validate the MRI results. For this procedure, the cells were dissolved in a radio-immuno precipitation RIPA buffer and then suspended in water until analysis. ICP-MS is used to determine the exact quantity of Gadolinium. As with the MRI measurements, incubation times were 30 min, 1 h, 3 h, 6 h, 24 h and 48 h. Each time point was measured in triplicate (Fig. 3.2).

Results from both MRI and ICP-MS uptake analyses are shown in fig. 3.2. Both methods give consistent results and show that the nanoparticles uptake saturates at about 1.25 pg per cell after 30 min incubation time for 0.43 mg/L of AGuIX incubated. MRI and ICP-MS results both show a constant level of nanoparticles inside the cells after 30 min of incubation.

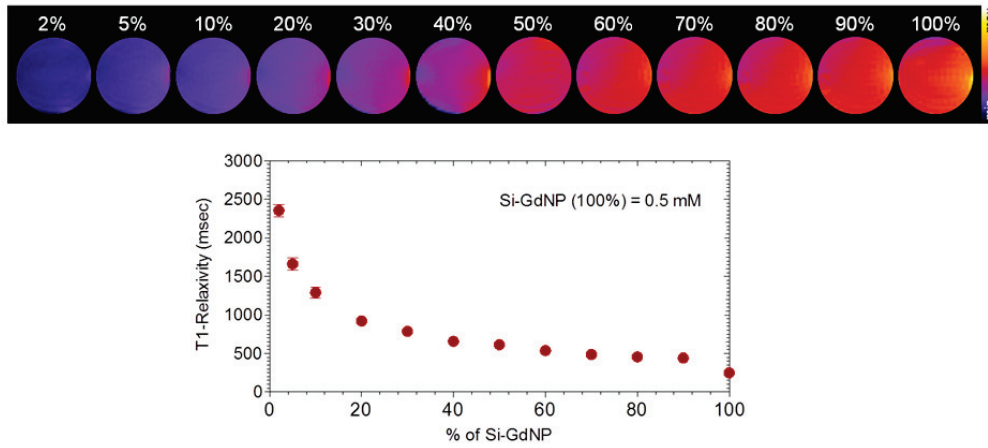


Figure 3.1: MRI phantom studies and cellular uptake studies. Color-coded T1 relaxation time pixel map of AGuIX demonstrates dose-dependent increase in MR signal intensity. Further quantification of the calibration data shows a dose-dependent correlation. Image courtesy of Detappe *et al.* [11]

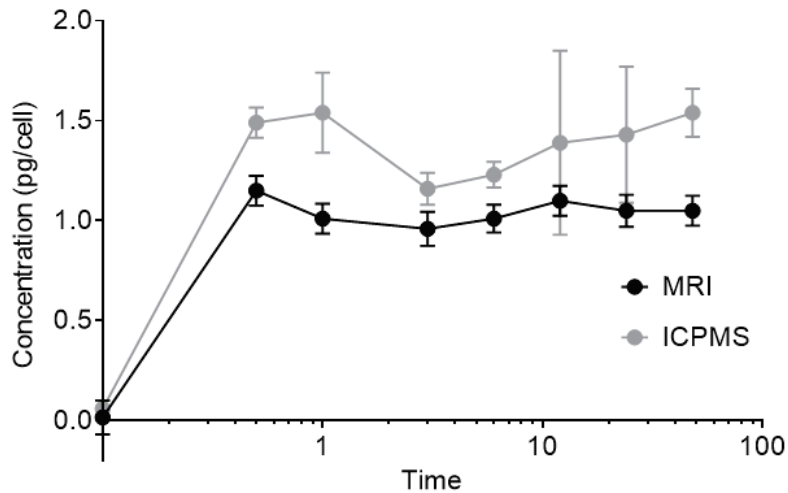


Figure 3.2: Pancreatic adenocarcinoma cell lines (Panc-1) were incubated for different time points with 0.43 mg/L of AGuIX. The concentration in pg/cell is measured by MRI and crosschecked by ICP-MS. The MRI measurement is determined with a calibration curve allowing the translation between the concentration of AGuIX and the relaxivity time. For both methods of measurement, the uptake plateaus after 30 min. Image courtesy of Detappe *et al.* [12]

3.3 IN VITRO PROOF OF CONCEPT

3.3.1 PROOF OF CONCEPT WITH PRECLINICAL RADIATION BEAM

BIOLOGICAL DAMAGES INDUCED BY NANOPARTICLES

Capan-1 cells were irradiated to 4 Gy and 10 Gy with 220 kVp beams, \pm AGuIX (0.43 mg/ml). Cells were fixed with 4% v/v formaldehyde for 15 min at room temperature (RT), and then washed twice with PBS. Cells were permeabilized with BSA 1%, FBS 10%, 0.3% triton-100 for 1 h, RT. The cells were incubated overnight at 4 C with 53BP1 antibody (H-300, Santacruz, USA), diluted 1 to 1000 in PBS containing 1% BSA, 0.1% triton x-100, then washed five times with PBS. Slides were mounted with Dapi Fluoromount-G (SouthernBiotech, USA). Fluorescence microscopy images were processed to visualize the foci. The DNA damages induced by the nanoparticles were determined by counting the number of cells with >10 foci.

The nanoparticles were endocytosed and prominently localized as clusters in the sub-cellular compartments. High degree of DNA damages was observed in the nanoparticle-treated cancer cells at the tested radiation doses of 4 and 10 Gy. The density of 53BP1-radiation induced foci formation is highest in the 10 Gy treated sample with $>90\%$ of the cells exhibiting specific DNA damage (Fig. 3.3a). Distinct quantitative and dose-dependent variations were found in the nanoparticle-treated vs. non-treated samples ($78.1 \pm 3.5\%$ vs. $60.5 \pm 4.1\%$ at 4 Gy and $95.4 \pm 2.3\%$ vs. $79.4 \pm 3.8\%$ at 10 Gy) (Fig. 3.3b).

APOPTOSIS ASSAY

Apoptosis was quantified by Allophycocyanin Annexin V/7-Aminoactinomycin D staining (Biolegends, USA) followed by flow cytometry analysis according to the manufacturer's instructions using BD FACSCanto II (BD Biosciences, USA). Measurements were performed with and without nanoparticles after incubation for 15 min at 0.43 mg/ml concentration. After irradiation, three different time points were analyzed: 15 min, 24 h, and 48 h.

FACS analysis was performed to quantitatively estimate the changes in early and late apoptosis for samples with/ without radiation (\pm IR) and with/ without AGuIX \pm (Si-GdNP). Although capan-1 pancreatic cells are known to exhibit a slightly elevated basal DNA damage threshold, the combined AGuIX and radiation experimental arm $+(Si-GdNP)/+IR$ demonstrated high early and late apoptosis (41.8% and 23% respectively) compared to the other controls (15.7% and 18.7%) (Fig. 3.3c). This trend remained consistent at 24 h and 48 h post-IR (Fig. 3.3d).

CLONOGENIC ASSAY

Capan-1 cells were incubated with 0.43 mg/ml of AGuIX for 15 min prior to irradiation with an open field 220 kVp beam. Radiation dose levels of 2, 4, 6, 8, and 10 Gy were employed. The cells were further incubated for another 4 h after irradiation and afterwards washed with PBS, trypsinized and counted. The cells were seeded in 10 cm dishes at 300 cells per plate and allowed to grow for 10 days, before staining with a 1% crystal violet in 10% ethanol dye solution. The plates were digitally scanned and automatically counted with an in-house developed software tool. Measurements were performed in triplicate. The effect of the AGuIX is quantified by the calculation of the dose enhancement factor (DEF) using Matlab (v. R2013b). The DEF is the ratio of the area under the survival curves with and without nanoparticles.

The clonogenic cell survival assay confirmed significant ($P < 0.01$) decrease in cell survival when AGuIX and radiation were combined. The calculated radiation DEF for $+Si-GdNP/+IR$ samples was found to be 1.37 (Fig. 3.3e).

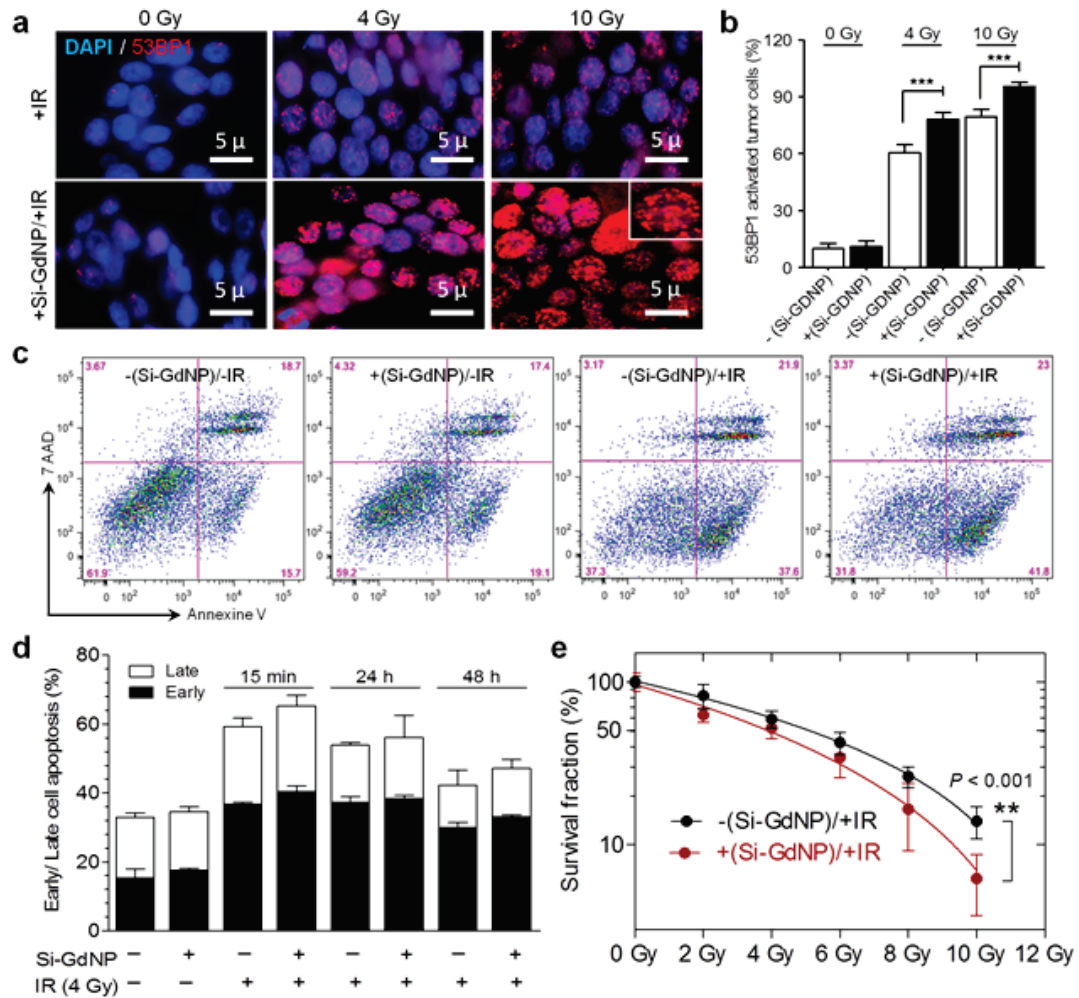


Figure 3.3: *In vitro* radiation studies. (a) Qualitative and quantitative evaluation of radiation damage in pancreatic cancer cells (capan-1) treated +/-Si-GdNP (0.43 mg/mL) at 0, 4 and 10 Gy (220 kVp). High 53BP1 radiation-induced foci expression is observed in the nanoparticle-treated and irradiated samples (+Si-GdNP/+IR) compared to the respective controls. Magnification: 63x. (b) Measurement of 53BP1- foci activated cells clearly shows significant dose-response differences (* $P < 0.01$). (c) Radiation-induced early and late apoptosis was assessed under different set experimental conditions (at 4 Gy) using Annexin V-APC/ 7-AAD based FACS analysis. For the +Si-GdNP/+IR samples, comparatively high early (black bar) and late (white bar) apoptosis (41.8% and 23%) was observed with respect to the controls (-Si-GdNP/-IR: 15.7% and 18.7%; +Si-GdNP/-IR: 19.1% and 17.4%; -Si-GdNP/+IR: 37.6% and 21.9%). (d) Temporal variations in early and late apoptosis were measured. The data clearly shows high early (solid black) and late (solid white) apoptosis for +Si-GdNP/+IR at all prescribed irradiation time points. (e) Clonogenic survival assay showing the effect of radiation \pm Si-GdNP. The dose enhancement factor was 1.37 (** $P < 0.01$). All data are represented as a mean \pm SD. P-values were calculated using two-tailed student t-test.

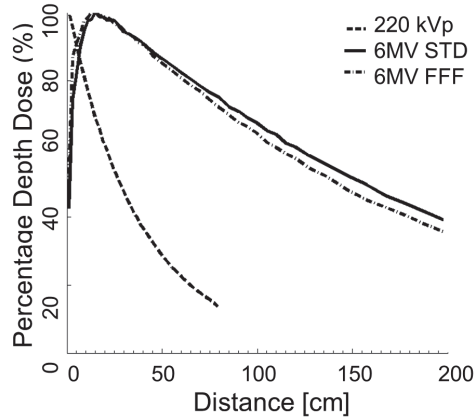


Figure 3.4: Percentage depth dose (PDD) for the 3 photon beams. The maximum dose for the 220 kVp occurs at the surface while it is at approximately 1.5 cm for both 6 MV beams.

For the highest probability of a photoelectric interaction with the K-shell of Gadolinium, the incident photon should have an energy just above 50 keV. With an energy peak around 220 kV and an average energy close to 50 keV, it is expected to obtain the highest dose enhancement with a preclinical radiation beam in comparison to clinical radiation beams with energy that peak around 6 MeV and exhibiting an average energy around 1.25 MeV. However, it is not clinically feasible to use low energy photons to treat the majority of patients (especially pancreatic cancer patients) due to the poor penetration depth and skin-sparing properties. Figure 3.4 shows a comparison of the percentage depth dose (PDD) of the radiation beams used in this study.

3.3.2 PROOF OF CONCEPT WITH CLINICAL RADIATION BEAM

To increase the probability of interaction between the clinical energy spectra and the nanoparticles, our proposed solution is to use the clinical setup to induce a beam softening. By increasing the scattering, the interaction probability in the patient is increased by Compton effect before to reach the nanoparticles in the tumor and create photoelectrons. The goal of this study is to demonstrate the influence of external parameters on the nanoparticles effectiveness to act as radiosensitizers with a clinical workflow. Thus, by modifying parameters such as tumor depth to simulate the tumor positioning in the patient; variation of the field size for a better conformality of the treatment; and radiation beam (i.e. flattening filter and flattening filter free), we showed the importance and the influence of the scattering to increase the nanoparticles activation.

The best trade-off between penetration depth and proportion of low energy photons is the use of a 6 MV flattening filter free beam (6 MV-FFF) [60]. The 6 MV-FFF radiation beam liberated a significant amount of low energy photons compared to its analogue 6 MV beam allowing a substantial local dose enhancement with the presence of nanoparticles, as expected from previous analytical modelisations.

We demonstrated that for a specific and realistic irradiation setup maximizing the generation of low energy photons, the use of a clinical 6 MV-FFF radiation beam reaches similar dose enhancement levels than published results using the same nanoparticle and concentration with a preclinical radiation beam (220 kV), as well as a significant dose enhancement increase compared to its analogue megavoltage beam (6 MV).

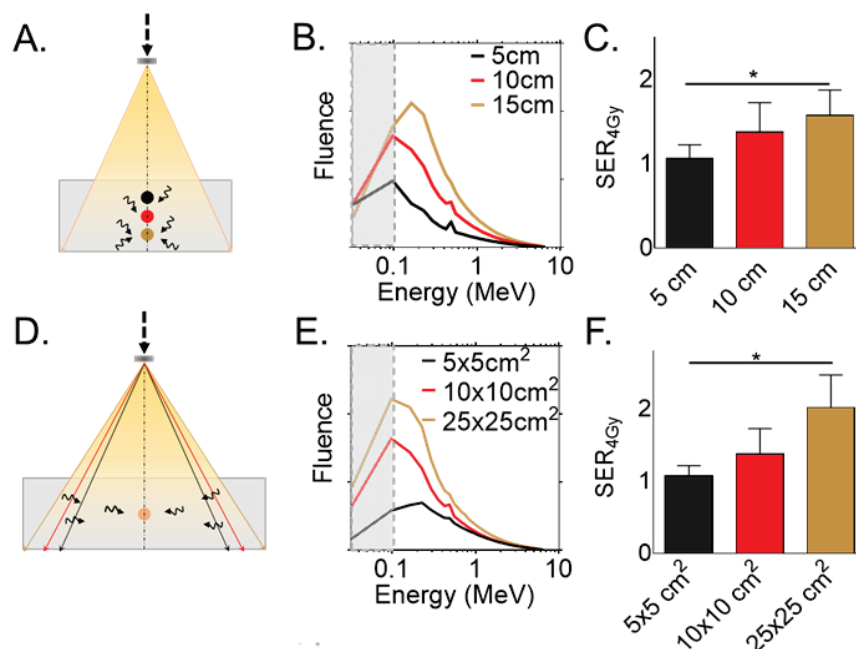


Figure 3.5: Energy dependence for radiosensitization with clinical radiation beam. (A) Schematic representation of the irradiation setup for the depth study. The dark arrows represent the expected low energy photons generated by the scattering. (B) Monte-Carlo simulation confirmed this increase. The grey color represents the amount of potential amount of low energy photons from 10 keV to 100 keV which will interact by photoelectric effect with the gadolinium nanoparticle used as radiosensitizer in this study. (C) Sensitivity enhancement ratio at 4 Gy (SER_{4Gy}) calculated as the ratio of cell survival IR alone and IR+AGuIX showed the increase of efficacy of the nanoparticles induced by the increase of scattering (D-F) Same experiment was performed by modifying the field size confirming the impact of the scattering to improve the dose enhancement.

INFLUENCE OF THE CLINICAL RADIATION SETUP

The influence of the clinical radiation setup was tested *in vitro* by using capan-1 pancreatic adenocarcinoma cells incubated with 0.5 mg/L of AGuIX and irradiated with a single fraction of 4 Gy with a clinical 6 MV-FFF radiation beam (Varian, TrueBeam). The sensitivity enhancement ratio at 4 Gy (SER_{4Gy}) defined as the ratio of survival fractions after irradiation with and without nanoparticles was used to compare the results. The modification of the depth (from 5 cm to 15 cm) served to evaluate the impact of the beam softening (Fig. 3.5A). A correlation is observed between the increase of low energy photon modeled by Monte-Carlo (Fig. 3.5B) and the *in vitro* results observed. A significant increase of the radiosensitization properties of the nanoparticles between 5 cm and 15 cm depth ranging from a $SER_{4Gy} = 1.06$ at 5 cm to 1.58 at 15 cm depth ($p < 0.05$) (Fig. 3.5C) is observed. This trend remained consistent with the field size variation ($SER_{4Gy} = 1.07$ with $5 \times 5 \text{ cm}^2$ to 2.02 with a $25 \times 25 \text{ cm}^2$ field size, $p < 0.05$) (Fig. 3.5D-F). These results confirmed that by degrading the quality of the beam (beam softening) by increasing the depth and field size, nanoparticles could be more effective under clinical radiations.

FLATTENING FILTER FREE RADIATION: AN ADVANTAGEOUS SOLUTION

The 6 MV-FFF beam is mainly used in clinic for stereotactic body radiation therapy/stereotactic radiosurgery (SBRT/SRS). The flattening filter radiation beam corresponded to the common clinical 6 MV radiation beam. The increase dose rate in the 6 MV-FFF beam accelerates the treatment while delivering while delivering a higher dose to the patient. For this reason, the flattening filter is removed from the clinical machine, generating more scattering than clinical beam for the same irradiation dose (Fig. 3.6A). The clinical machine used for the experiment was modeled by Monte-Carlo to quantify

this discrepancy (2.6-fold more low energy photon generated with the 6 MV-FFF compared to the 6 MV beam) (Fig. 3.6B).

The increase in nanoparticles activation with the 6 MV-FFF leads to an increase un observed ROS (Fig. 3.6C). The increase is linear with the radiation dose ($R^2 = 0.97$) and the difference between 6 MV and 6 MV-FFF beams increase with a dose ranging from a 1.12-fold increase with 0.5 mg/L of nanoparticles incubated ($P < 0.05$) to 1.36-fold with 1 mg/L of nanoparticles ($p < 0.001$). The ROS generation increase induced by the presence of nanoparticles under irradiation with 6 MV-FFF beam compared to irradiation with 6 MV beam led to a significant improvement of clonogenic cell death ($P = 0.029$) (Fig. 3.6D).

The DEF obtained with the 6 MV-FFF beam ($DEF = 1.36$) is similar to the one observed with the preclinical radiation beam (220 kV) ($DEF = 1.37$) and is substantially higher than with the 6 MV radiation beam ($DEF = 1.22$). The generation of oxidative stress and physical effects due to the presence of the nanoparticles resulted in an increase of DNA double strand breaks as observed by the 53BP1-radiation induced foci formation (Fig. 3.6E). Over 70% of the cells exhibited specific DNA damage for the +Si-GdNP/6 MV-FFF group compared to 58% for the +Si-GdNP/6 MV ($P = 0.0041$) (Fig. 3.6F). The high density of 53BP1 foci observed in the control groups are due to the elevated basal DNA-damage of the capan-1 cells (approx. 7%).

3.4 CONCLUSION

To summarize, we demonstrated that a significant dose escalation can be obtained by coupling a clinical radiation beam with polysiloxane-based nanoparticles chelated with high-Z atoms. One of the possible mechanisms to explain the effects observed *in vitro* would be mainly attribute to biological effects. Thus, the nanoparticles reached the cytoplasm under the form of clusters as demonstrated by the TEM images. The cluster form increased the cross-section of radiation within the cell resulting in the generation of a large amount of secondary electrons that in turn led to the creation of ROS. The increase in biological effects, such as the generation of hydrogen peroxide, has a longer range of action (a few mm) than the physical effects (a few μm) allowing to reach and damage the DNA. The amount of low energy photons (i.e., beam softening) generated by the clinical beam and its setup is directly correlated to the probability of interaction between the photons and the nanoparticles, and thus, directly correlated to the efficacy of the treatment. For this reason, it was expected to obtain a better radiosensitizing effect induced by the 6 MV-FFF beam radiation than by a regular 6 MV beam radiation. From a translational point of view, these result suggest to be attentive to the radiation path as the kidney, liver, and spleen may have to be irradiated to reach the tumor, suggesting a significant amount of secondary effects.

As demonstrated analytically, our results confirmed that increasing the amount of low energy photons increases the radiation dose enhancement induced by AGuIX. A solution proposed to increase the radiosensitizing efficacy of the nanoparticles is to replace the Cu/W target used to create the photons with a carbon target. Hence, an increase of approximately 30% of low energy photons would be generated at a 10 cm depth. This new generation of clinical machines would offer a unique clinical scenario for personalized treatment without modifying the nanoparticles chemistry.

3.5 PUBLICATION

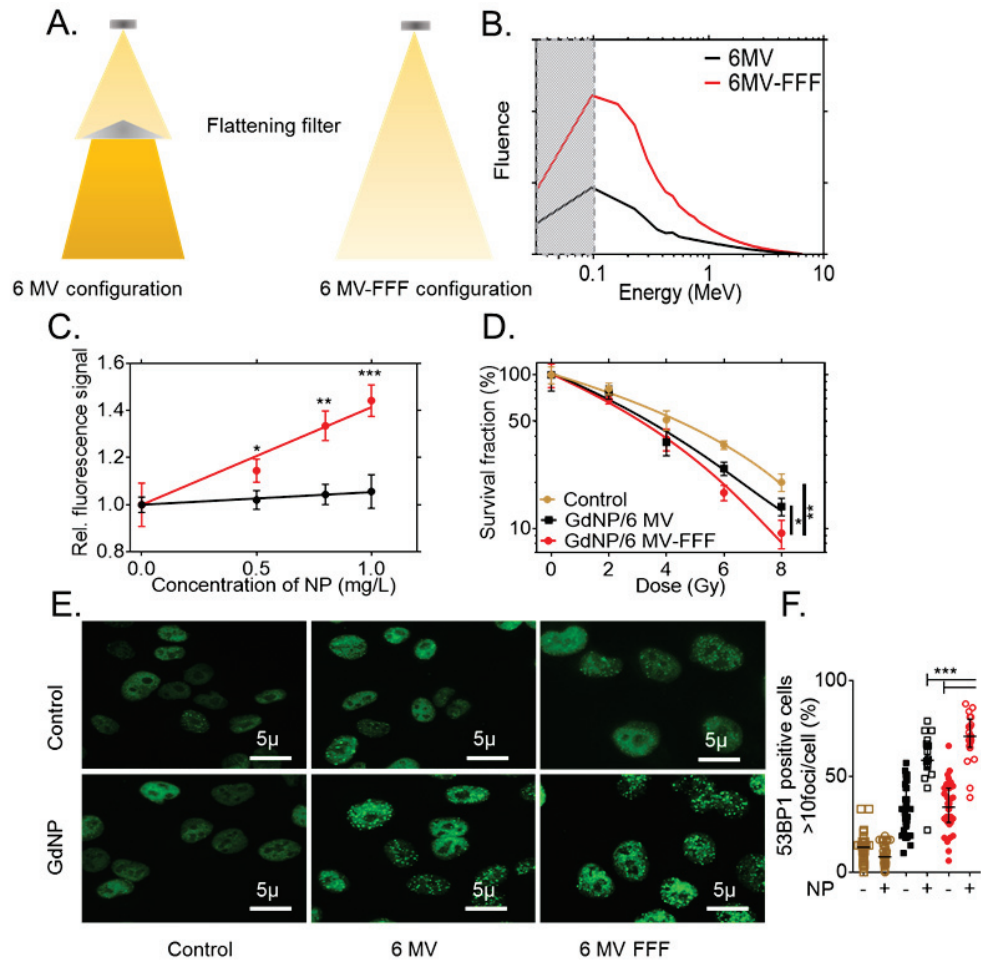


Figure 3.6: *In vitro* radiation comparison between 6 MV and 6 MV-FFF clinical beams. (A) Schematic representation of the 6 MV and 6 MV-FFF configuration. The use of the flattening filter created a beam hardening by absorbing the low energy photons. (B) By consequences, the amount of low energy photons is higher for the 6 MV-FFF compared to the 6 MV as determined by Monte-Carlo. (C) Clonogenic assay performed with-out nanoparticles (6 MV-FFF alone as control), with gadolinium nanoparticle (NP)/6 MV and with NP/6 MV-FFF. (D) Reactive oxygen species measurement quantified as the ratio of fluorescences readed with and without nanoparticles after 10 Gy radiation. (E-F) Qualitative and quantitative representation of the DNA damage after 53BP1-staining. Magnification 63x. All data are represented as a mean \pm SD. Statistical tests were performed using Kruskal Wallis test, *P < 0.05, **P < 0.001, ***P < 0.0001.

RESEARCH

Open Access



AGuIX nanoparticles as a promising platform for image-guided radiation therapy

Alexandre Detappe^{1,2*}, Sijumon Kunjachan¹, Joerg Rottmann¹, James Robar³, Panagiotis Tsiamas¹, Houari Korideck¹, Olivier Tillement² and Ross Berbeco^{1*}

*Correspondence:
Alex_Detappe@DFCI.harvard.edu; RBerbeco@LROC.harvard.edu
¹ Radiation Oncology Department, Dana-Farber Cancer Institute, Brigham and Women's Hospital, Harvard Medical School, Boston, MA 02215, USA
Full list of author information is available at the end of the article

Abstract

AGuIX are gadolinium-based nanoparticles developed mainly for imaging due to their MR contrast properties. They also have a potential role in radiation therapy as a radiosensitizer. We used MRI to quantify the uptake of AGuIX in pancreatic cancer cells, and TEM for intracellular localization. We measured the radiosensitization of a pancreatic cancer cell line in a low-energy (220 kVp) beam, a standard 6 MV beam (STD) and a flattening filter free 6 MV beam (FFF). We demonstrated that the presence of nanoparticles significantly decreases cell survival when combined with an X-ray beam with a large proportion of low-energy photons (close to the k-edge of the nanoparticles). The concentration of nanoparticles in the cell achieves its highest level after 15 min and then reaches a plateau. The accumulated nanoparticles are mainly localized in the cytoplasm, inside vesicles. We found that the 6 MV FFF beams offer the best trade-off between penetration depth and proportion of low-energy photons. At 10 cm depth, we measured a $DEF_{20\%}$ of 1.30 ± 0.47 for the 6 MV FFF beam, compared to 1.23 ± 0.26 for the 6 MV STD beam. Additional measurements with un-incubated nanoparticles provide evidence that chemical processes might also be contributing to the dose enhancement effect.

Keywords: Nanomedicine, MRI, Gadolinium, Dose enhancement, Flattening filter free

Background

Nanoparticles made from high-Z materials are promising agents to increase radiosensitivity of cancer cells during the application of radiation therapy. Hainfeld et al. (2004, 2008) demonstrated therapeutic enhancement with gold nanoparticles (GNP) in a 250 kVp X-ray beam. The dose-enhancing effect was attributed to the photoelectric effect and the increased generation of Auger electrons (Pradhan et al. 2009; Jelveh and Chithrani 2011; Dorsey et al. 2013; Kumar et al. 2013). Further studies have confirmed the dose-enhancing effect of GNP in 6 MV X-ray beams, an energy range that is typically used for clinical radiation therapy (Detappe et al. 2013; Berbeco et al. 2011; Cho 2005; Jones et al. 2010; Lin et al. 2014; Robar et al. 2002; McMahon et al. 2008; Ngwa et al. 2014).

However, even though gold nanoparticles may be efficient radiosensitizers, it remains difficult to measure their exact concentration within the tumor with current clinically available imaging methods. To address this issue, multimodal nanoparticles have been

proposed that combine both therapeutic and diagnostic functionality. Mignot et al. 2013 developed a gadolinium-based nanoparticle, AGuIX, which is a non-toxic magnetic resonance contrast agent and sufficiently small (sub-5 nm diameter) to allow for renal clearance (Le Duc et al. 2014). With an atomic number of $Z = 64$, gadolinium is a high- Z material and therefore also contributes substantial radiation dose enhancement. (Sancey et al. 2014).

Previous assessment of AGuIX nanoparticles has mostly focused on their imaging properties (Di Corato et al. 2013; Le Duc et al. 2011; Bianchi et al. 2014a, b; Paul et al. 2014). *In vitro* experiments have included different cell lines and preclinical irradiation beams (microbeam radiation therapy, low-energy X-ray). Researchers have shown early evidence of radiosensitization (Bianchi et al. 2013; Aspod et al. 2013; Mowat et al. 2011; Porcel et al. 2014; Stefančíková et al. 2014; Luchette et al. 2014). In addition, *in vivo* experiments with intravenous or intra-tumoral injection for subcutaneous and orthotopic lesions have been performed in preclinical radiation beams (Le Duc et al. 2011; Bianchi et al. 2014a).

The aim of the current study is to characterize the uptake of the AGuIX nanoparticles in pancreatic cancer cells by magnetic resonance imaging (MRI), and investigate the radiation dose enhancement effect attributable to AGuIX when irradiating the cells with a clinical linear accelerator at 6 MV. This represents the first step towards demonstrating an *in vivo* effect for pancreatic cancer. The AGuIX platform is particularly relevant for pancreatic cancer due to the poor prognosis, proximity of organs at risk, and targeting difficulty for this disease in radiation therapy. AGuIX offers a solution that is highly compatible with the current trend in radiation oncology towards MRI-based patient simulation and MRI-Linac treatment devices (Raaymakers et al. 2011; Keall et al. 2014). There may be a strong future for AGuIX in future MRI-guided radiation therapy for pancreatic cancer.

Methods

Cell culture

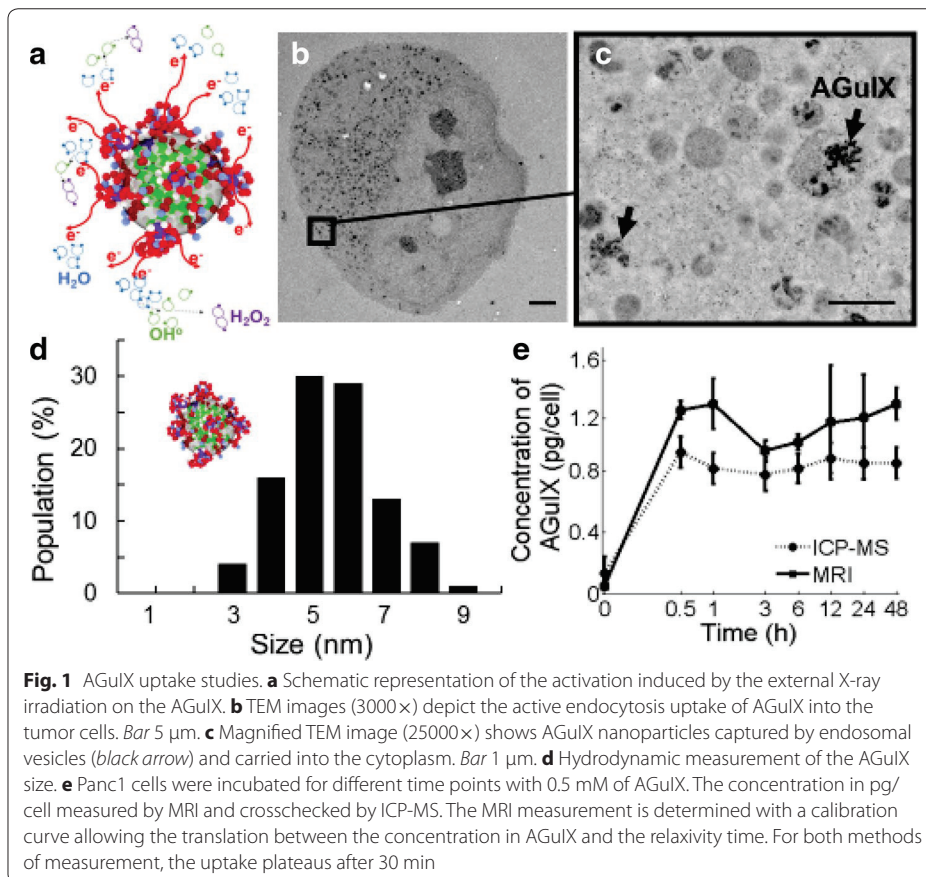
Panc1 cells were cultured in Dulbecco's Modified Eagle Medium (DMEM), supplemented with 10 % fetal bovine serum (FBS) (Sigma, USA), 1 % Penicillin Streptomycin Glutamine (Invitrogen, USA) and were stored in a humidified incubator at 37 °C and 5 % CO₂.

AGuIX nanoparticles (Nano-H Inc., France)

The nanoparticles are composed of a polysiloxane shell surrounded by DOTA (1,4,7,10-tetra-azacyclododecane-1-glutaric anhydride-4,7,10-triacetic acid) covalently bound to the inorganic matrix and Gadolinium (Fig. 1a). The size of each nanoparticle was measured by dynamic light scattering (DLS) and is 5 ± 0.1 nm (Fig. 1d) with a mass of 10 ± 1 kDa. More detailed information on the production process of the nanoparticles may be found in the references (Detappe et al. 2013).

AGuIX uptake analysis with MRI and ICP-MS

The concentration of the nanoparticles inside the cells was analyzed with a Bruker Bio-spin 7T Magnetic Resonance Imaging (MRI) scanner. First, a calibration curve without



cells was acquired for various concentrations of nanoparticles in the cell culture solution. The concentration of AGuIX particles used for the experiment is given in gadolinium equivalent species and chosen based on published literature (Rima et al. 2013). Cells were incubated with 0.5 mM (0.5 mg/L) of AGuIX at 37 °C and 5 % CO₂ for 30 min, 1 h, 3 h, 6 h, 24 h and 48 h. After incubation, the cells were washed and trypsinized to remove any excess nanoparticles in the solution before scanning. All MRI scans featured a RARE-T1 map imaging-sequence with 2 mm slice thickness, repetition time of 10 ms, echo time of 21.4 ms, echo train length of 4, flip angle of 180°, and matrix size 256 × 128 pixels. Each measurement was performed in triplicate.

Inductively coupled plasma mass spectrometry (ICP-MS) was used to validate the MRI results. For this procedure, the cells were dissolved in a radio-immuno precipitation RIPA buffer and then suspended in water until analysis. ICP-MS is used to determine the exact quantity of Gadolinium. As with the MRI measurements, incubation times were 30 min, 1 h, 3 h, 6 h, 24 h and 48 h. Each time point was measured in triplicate.

Localization of AGuIX within Panc1 cells

Transmission electronic microscopy (TEM) was performed to investigate the local nanoparticle distribution within the cells. A concentration of 0.5 mM of AGuIX was

incubated for 1 h with Panc1 cells, followed by washing out residual nanoparticles and staining with 4 % formaldehyde and 1 % glutaraldehyde in 0.1 M Pb for imaging.

Irradiation and setup

We investigated cell response to low-energy and high-energy photon irradiation for a dose range of 2–10 Gy. For low-energy experiments, we used a Small Animal Radiation Research Platform (SARRP) operated at 220 kVp (0.15 mm Cu filter) and a source to cell distance of 35 cm. For high-energy irradiations, we used a clinical linear accelerator (TrueBeam, Varian Inc, USA) operated at 6 MV with and without a flattening filter in the beam line. Using a flattening filter is the current standard (STD) in radiation therapy while the use of flattening filter free beams (FFF) is still relatively novel to clinical application. Cells were placed on 5 cm of water equivalent material and another 10 cm on top to allow for full scattering and back scattering conditions. The source to cell distance was 100 cm, field size $10 \times 10 \text{ cm}^2$ and dose rate 400 cGy/min for both STD and FFF deliveries.

Clonogenic assay

Panc1 cells were incubated in DMEM with 0.5 mM of AGuIX following the specifications below, and then irradiated. After irradiations, the cells were incubated for another 4 h; afterwards they were washed with PBS, trypsinized and counted. The cells were replated in 10 cm dishes at 300 cells per plate and allowed to grow for 10 days, before staining with a 1 % crystal violet and 10 % ethanol dye solution. The plating efficiency was $67 \pm 7 \%$. The plates were digitally scanned and automatically counted with software developed in our group. Measurements were performed in triplicate.

For the 6 MV irradiations, the cells were incubated 1 h and the medium unwashed. For the low-energy photon experiments, 4 different configurations were investigated:

- A. Irradiation without any nanoparticles.
- B. Cells were not incubated with nanoparticles. Nanoparticles were placed in the media just prior the irradiation. We called this configuration +IR/–incubation.
- C. Cells were incubated with the nanoparticles and the media was changed just prior the irradiation. We called this +IR/+washing.
- D. Cells were incubated with the nanoparticles and were irradiated. We called this +IR/–washing.

The (B) experiment (+IR/–incubation) is a test of the hypothesis that a dose enhancement effect can be caused by nanoparticles located outside the cell. A positive result supports the presence of some long-range effects beyond just photoelectric and Auger processes.

Data analysis

We quantified the effect of the nanoparticles utilizing three methods commonly found in the literature (Sancey et al. 2014; Jain et al. 2011; Chithrani et al. 2010; Roeske et al. 2007). The Dose Enhancement Factor (DEF) is the ratio of the area between the survival curves with and without nanoparticles. The $\text{DEF}_{20\%}$ is the ratio of doses at 20 % survival

for irradiation without nanoparticles versus with nanoparticles. The sensitivity enhancement ratio at 4 Gy (SER_{4Gy}) is the ratio of survival fractions at 4 Gy for irradiation without and with nanoparticles.

To characterize the radiation response of the Panc1 cells with and without AGuIX, we employed the classical linear quadratic model (LQM):

$$S(D) = \exp(-\alpha D - \beta D^2)$$

Here, S is the cell survival fraction, D the irradiation dose and α and β are parameters representing direct lethal and sub-lethal damage, respectively. Statistical significance of cell survival changes with the application of nanoparticles is calculated using a Kruskal–Wallis test.

Results and discussion

Uptake measurement

Results from both MRI and ICP-MS uptake analyses are shown in Fig. 1. Both methods give consistent results and show that AGuIX uptake saturates at about 1.25 pg per cell after 30 min incubation time for 0.5 mM of AGuIX incubated.

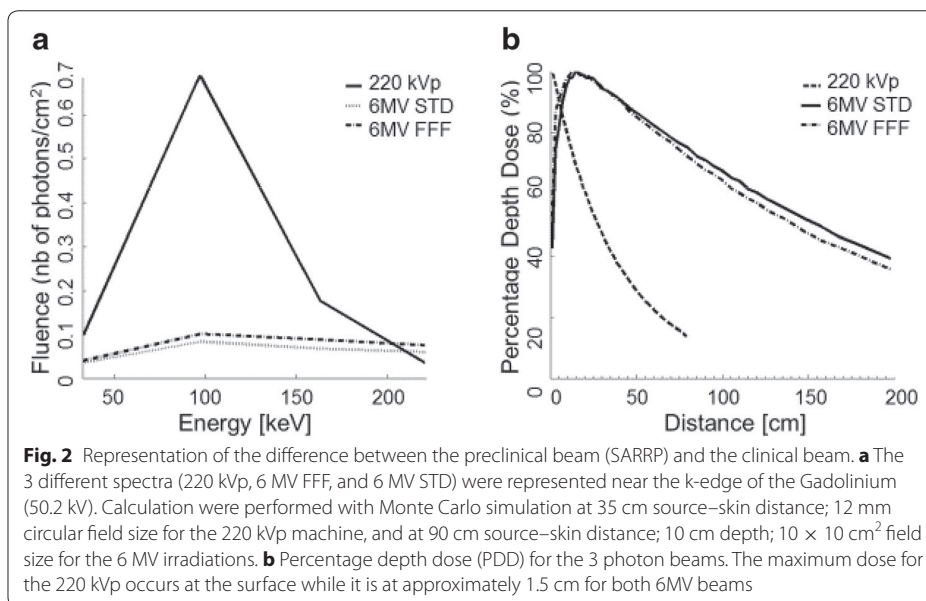
TEM imaging (Fig. 1b, c) reveals that after 1 h of incubation, the nanoparticles are predominantly localized in vacuoles in the cytoplasm. This result is in agreement with the previously published studies that applied AGuIX to other cell lines (Stefančíková et al. 2014; Rima et al. 2013).

MRI and ICP-MS results both show a constant level of nanoparticles inside the cells after 30 min of incubation. The MRI measurement is systematically larger than the ICP-MS measurement. This is because the T1 signal is sensitive to the size of nanoparticles, which decrease during hydrolysis (which occurs due to the low AGuIX concentration) (Le Duc et al. 2014).

Activation of the nanoparticles

For the highest probability of a photoelectric interaction with the K-shell of Gadolinium, the incident photon should have an energy just above 50 keV. Figure 2a shows a comparison of the low-energy photon spectra for the beams used in this study. Spectra are generated using EGSnrc Monte Carlo code (Tsiamas et al. 2011, 2014).

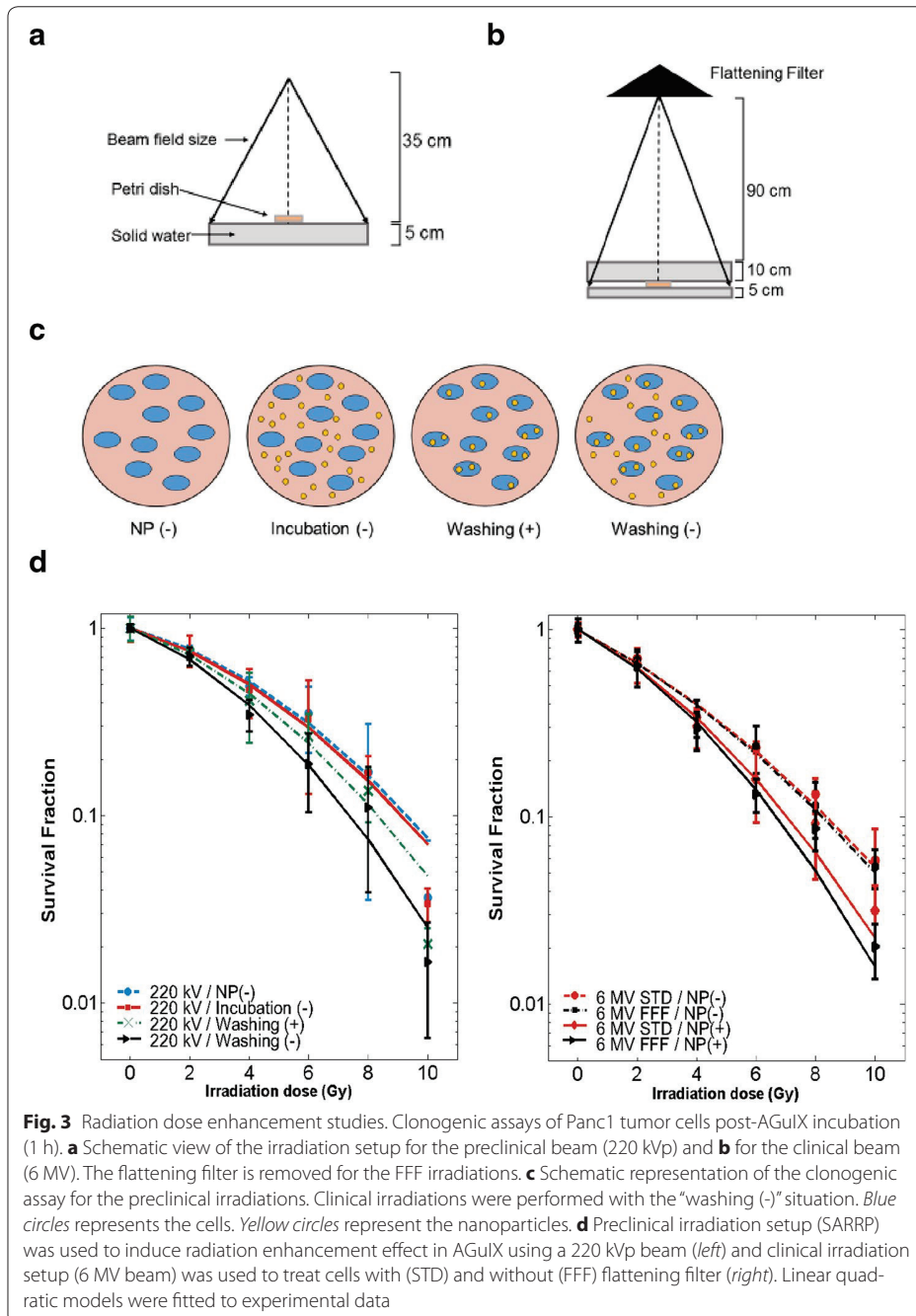
From these distributions, it is clear that 220 kVp is expected to have the highest dose enhancement. However, it is not clinically feasible to use low-energy photons to treat the majority of patients (especially pancreatic cancer patient) due to the poor penetration depth and skin-sparing properties. Figure 2b shows a comparison of the percentage depth dose (PDD) for the radiation beams used in this study. The best trade-off between penetration depth and proportion of low-energy photons exists for the 6 MV FFF beam. Further modifications of the 6 MV beam, including the use of a low-Z target, (Parsons et al. 2014) may also improve the dose enhancement while preserving the deep penetration properties.



Dose enhancement effects

A significant radiosensitization effect was observed for all the clonogenic assays performed (Fig. 3). Results of the dose enhancement studies are summarized in Table 1. The dose enhancement effect appears to increase with the proportion of low-energy photons in the spectrum as expected (Detappe et al. 2013; Berbeco et al. 2011). For the high-energy (clinical) photon beams, cell killing is significantly increased by the removal of the flattening filter in the FFF beam, compared to the STD beam ($p = 0.014$, Wilcoxon). The SER_{4Gy} is 1.20 ± 0.04 for the FFF irradiation and 1.12 ± 0.04 for the STD. The $DEF_{20\%}$ is 1.30 ± 0.05 for the FFF and 1.23 ± 0.03 for the STD.

While the physical property of the incident radiation beams clearly provides a therapeutic advantage, there may be other factors contributing as well. Figure 1b, c shows the nanoparticles clustered inside the cytoplasm, away from the DNA. Radiosensitization was observed for this scenario as well as for non-incubated nanoparticles (located outside the cell) (Fig. 3d). McMahon et al. (2011) demonstrated the role of Auger electrons to create a local effect and the impact of nanoparticle clustering. This local effect increases the formation of reaction oxygen species (ROS), such as OH^\bullet , H_2O_2 , or $HOCl$. Some of these ROS have high chemical stabilities and a long-range action (few mm) that may increase the cell death even if the nanoparticles are not localized in the cells. The results shown in Fig. 3d are similar to those obtained by Porcel et al. (2014) for hadrontherapy. Thus, in addition to the physical properties, a biological or chemical effect should be explored to explain the measured radiosensitization.



Conclusion

AGuIX nanoparticles create significant dose enhancement in Panc1 cell lines for low- and high-energy photon irradiation. Using a 6 MV flattening filter free (FFF) beam improves dose enhancement compared to a standard 6 MV beam. Because of their contrast in MRI images, AGuIX have excellent potential as theranostic agents (Lux et al. 2011; Kunjachan et al. 2012).

Table 1 Dose enhancement effect in terms of DEF, DEF_{20 %} and SER_{4Gy} for Panc1 cells incubated with 0.5 mM AGuIX

Preparation	Irradiation				
	220 kVp			6 MV FFF	6 MV STD
	AGuIX no incubation	AGuIX 1h incubation washing	AGuIX 1h incubation unwashing	AGuIX 1h incubation unwashing	
DEF	1.09	1.17	1.46	1.23	1.19
DEF 20 %	1.01	1.1	1.31	1.3	1.23
Sensitivity (SER _{4Gy})	1.05	1.19	1.41	1.2	1.12
<i>p</i> value	0.131	0.038	***	0.009	0.011

p values were calculated using a Kruskal Wallis to test the effect of the nanoparticles with the control

*** *p* < 0.001

Authors' contributions

AD, JR and HK performed the irradiations studies. AD and SK performed the biological part of the study. JR and PT generated the simulation data. AD, SK and RB conceived the study, and participated in its design and coordination. OT provided the nanoparticles. All authors helped to draft the manuscript. All authors read and approved the final manuscript.

Competing interests

The authors declare that they have no competing interests.

Author details

¹ Radiation Oncology Department, Dana-Farber Cancer Institute, Brigham and Women's Hospital, Harvard Medical School, Boston, MA 02215, USA. ² Institut Lumière-Matière, Université Claude Bernard, 69000 Lyon, France. ³ Department of Medical Physics, Nova Scotia Cancer Centre, Dalhousie University, Halifax, NS B3H 1V7, Canada.

Received: 26 March 2015 Accepted: 25 August 2015

Published online: 02 September 2015

References

Aspord C, Laurin D, Janier MF, Mandon CA, Thivolet C, Villiers C, Mowat P, Madec AM, Tillement O, Perriat P, et al. Paramagnetic nanoparticles to track and quantify in vivo immune human therapeutic cells. *Nanoscale*. 2013;5(23):11409–15.

Berbeco R, Ngwa W, Makrigiorgos M. Localized dose enhancement to tumor blood vessel endothelial cells via megavoltage X-rays and targeted gold nanoparticles: new potential for external beam radiotherapy. *Int J Radiat Oncol Biol Phys*. 2011;81(1):270–6.

Bianchi A, Dufort S, Lux F, Courtois A, Tillement O, Coll JL, Crémillieux Y. Quantitative biodistribution and pharmacokinetics of multimodal gadolinium-based nanoparticles for lungs using ultrashort TE MRI. *MAGMA*. 2014b;27(4):303–16.

Bianchi A, Dufort S, Lux F, Fortin PY, Tassali N, Tillement O, Coll JL, Crémillieux Y. Targeting and in vivo imaging of non-small-cell lung cancer using nebulized multimodal contrast agents. *Proc Natl Acad Sci USA*. 2014a;111(25):9247–52.

Bianchi A, Lux F, Tillement O, Crémillieux Y. Contrast enhanced lung MRI in mice using ultra-short echo time radial imaging and intratracheally administrated Gd-DOTA-based nanoparticles. *Magn Reson Med*. 2013;70(5):1419–26.

Chithrani DB, Jelveh S, Jalali F, van Prooijen M, Allen C, Bristow RG, Hill RP, Jaffray DA. Gold nanoparticles as radiation sensitizers in cancer therapy. *Radiat Res*. 2010;173(6):719–28.

Cho SH. Estimation of tumour dose enhancement due to gold nanoparticles during typical radiation treatments: a preliminary Monte Carlo study. *Phys Med Biol*. 2005;50(15):N163–73.

Di Corato R, Gazeau F, Le Visage C, Fayol D, Levitz P, Lux F, Letourneur D, Luciani N, Tillement O, Wilhelm C. High-resolution cellular MRI: gadolinium and iron oxide nanoparticles for in-depth dual-cell imaging of engineered tissue constructs. *ACS Nano*. 2013;7(9):7500–12.

Detappe A, Tsiamas P, Ngwa W, Zygmanski P, Makrigiorgos M, Berbeco R. The effect of flattening filter free delivery on endothelial dose enhancement with gold nanoparticles. *Med Phys*. 2013;40(3):031706.

Dorsey JF, Sun L, Joh DY, Witztum A, Kao GD, Alonso-Basanta M, Avery S, Hahn SM, Al Zaki A, Tsourkas A. Gold nanoparticles in radiation research: potential applications for imaging and radiosensitization. *Transl Cancer Res*. 2013;2(4):280–91.

Le Duc G, Miladi I, Alric C, Mowat P, Bräuer-Krisch E, Bouchet A, Khalil E, Billotey C, Janier M, Lux F, et al. Toward an image-guided microbeam radiation therapy using gadolinium-based nanoparticles. *ACS Nano*. 2011;5(12):9566–74.

Le Duc G, Roux S, Paruta-Tuarez A, Dufort S, Brauer E, Marais A, Truillet C, Sancey L, Perriat P, Lux F, et al. Advantages of gadolinium based ultrasmall nanoparticles vs molecular gadolinium chelates for radiotherapy guided by MRI for glioma treatment. *Cancer Nanotechnol*. 2014;5:4.

Hainfeld JF, Dilmanian FA, Slatkin DN, Smilowitz HM. Radiotherapy enhancement with gold nanoparticles. *J Pharm Pharmacol*. 2008;60(8):977–85.

- Hainfeld JF, Slatkin DN, Smilowitz H. The use of gold nanoparticles to enhance radiotherapy in mice. *Phys Med Biol*. 2004;49(18):N309–15.
- Jain S, Coulter JA, Hounsell AR, Butterworth KT, McMahon SJ, Hyland WB, Muir MF, Dickson GR, Prise KM, Currell FJ, O'Sullivan JM, Hirst DG. Cell-specific radiosensitization by gold nanoparticles at megavoltage radiation energies. *Int J Radiat Oncol Biol Phys*. 2011;79:531–9.
- Jelveh S, Chithrani DB. Gold nanostructures as a platform for combinational therapy in future cancer therapeutics. *Cancers (Basel)*. 2011;3(1):1081–110.
- Jones BL, Krishnan S, Cho SH. Estimation of microscopic dose enhancement factor around gold nanoparticles by Monte Carlo calculations. *Med Phys*. 2010;37(7):3809–16.
- Keall PJ, Barton M, Crozier S. The Australian magnetic resonance imaging-linac program. *Semin Radiat Oncol*. 2014;24(3):203–6.
- Kumar R, Korideck H, Ngwa W, Berbeco RI, Makrigiorgos GM, Sridhar S. Third generation gold nanoplatform optimized for radiation therapy. *Transl Cancer Res*. 2013;2(4). doi:10.3978/j.issn.2218-676X.2013.07.02.
- Kunjachan S, Jayapaul J, Mertens ME, Storm G, Kiessling F, Lammers T. Theranostic systems and strategies for monitoring nanomedicine-mediated drug targeting. *Curr Pharm Biotechnol*. 2012;13(4):609–22.
- Lin Y, McMahon SJ, Scarpelli M, Paganetti H, Schuemann J. Comparing gold nano-particle enhanced radiotherapy with protons, megavoltage photons and kilovoltage photons: a Monte Carlo simulation. *Phys Med Biol*. 2014;59(24):7675–89.
- Luchette M, Korideck H, Makrigiorgos M, Tillement O, Berbeco R. Radiation dose enhancement of gadolinium-based AGuIX nanoparticles on HeLa cells. *Nanomedicine*. 2014;10(8):1751–5.
- Lux F, Mignot A, Mowat P, Louis C, Dufort S, Bernhard C, Denat F, Boschetti F, Brunet C, Antoine R, et al. Ultrasmall rigid particles as multimodal probes for medical applications. *Angew Chem Int Ed Engl*. 2011;50(51):12299–303.
- McMahon SJ, Hyland WB, Muir MF, Coulter JA, Jain S, Butterworth KT, Schettino G, Dickson GR, Hounsell AR, O'Sullivan JM, et al. Biological consequences of nanoscale energy deposition near irradiated heavy atom nanoparticles. *Sci Rep*. 2011;1:18.
- McMahon SJ, Mendenhall MH, Jain S, Currell F. Radiotherapy in the presence of contrast agents: a general figure of merit and its application to gold nanoparticles. *Phys Med Biol*. 2008;53:5635–51.
- Mignot A, Truillet C, Lux F, Sancey L, Louis C, Denat F, Boschetti F, Bocher L, Gloter A, Stéphan O, et al. A top-down synthesis route to ultrasmall multifunctional Gd-based silica nanoparticles for theranostic applications. *Chemistry*. 2013;19(19):6122–36.
- Mowat P, Mignot A, Rima W, Lux F, Tillement O, Roulin C, Dutreix M, Bechet D, Huger S, Humbert L, et al. In vitro radiosensitizing effects of ultrasmall gadolinium based particles on tumour cells. *J Nanosci Nanotechnol*. 2011;11(9):7833–9.
- Ngwa W, Kumar R, Sridhar S, Korideck H, Zygmanski P, Cormack RA, Berbeco R, Makrigiorgos M. Targeted radiotherapy with gold nanoparticles: current status and future perspectives. *Nanomed (Lond)*. 2014;9(7):1063–82.
- Parsons D, Robar JL, Sawkey D. A Monte Carlo investigation of low-Z target image quality generated in a linear accelerator using Varian's VirtualLinac. *Med Phys*. 2014;41(2):021719.
- Paul G, Prado Y, Dia N, Rivière E, Laurent S, Roch M, Elst LV, Muller RN, Sancey L, Perriat P, et al. MnII-containing coordination nanoparticles as highly efficient T1 contrast agents for magnetic resonance imaging. *Chem Commun (Camb)*. 2014;50(51):6740–3.
- Porcel E, Tillement O, Lux F, Mowat P, Usami N, Kobayashi K, Furusawa Y, Le Sech C, Li S, Lacombe S. Gadolinium-based nanoparticles to improve the hadrontherapy performances. *Nanomedicine*. 2014;10(8):1601–8.
- Pradhan AK, Nahar SN, Montenegro M, Yu Y, Zhang HL, Sur C, Mrozik M, Pitzer RM. Resonant X-ray enhancement of the Auger effect in high-Z atoms, molecules, and nanoparticles: potential biomedical applications. *J Phys Chem A*. 2009;113(45):12356–63.
- Raaymakers BW, de Boer JC, Knox C, Crijns SP, Smit K, Stam MK, van den Bosch MR, Kok JG, Lagendijk JJ. Integrated megavoltage portal imaging with a 1.5 T MRI linac. *Phys Med Biol*. 2011;56(19):207–14.
- Rima W, Sancey L, Aloy MT, Armandy E, Alcantara GB, Epicier T, Malchère A, Joly-Pottuz L, Mowat P, Lux F, et al. Internalization pathways into cancer cells of gadolinium-based radiosensitizing nanoparticles. *Biomaterials*. 2013;34(1):181–95.
- Robar JL, Riccio SA, Martin MA. Tumour dose enhancement using modified megavoltage photon beams and contrast media. *Phys Med Biol*. 2002;47:2433–49.
- Roeske JC, Nunez L, Hoggarth M, Labay E, Weichselbaum RR. Characterization of the theoretical radiation dose enhancement from nanoparticles. *Technol Cancer Res Treat*. 2007;6(5):395–401.
- Sancey L, Lux F, Kotb S, Roux S, Dufort S, Bianchi A, Crémillieux Y, Fries P, Coll JL, Rodriguez-Lafrasse C, et al. The use of theranostic gadolinium-based nanoprobe to improve radiotherapy efficacy. *Br J Radiol*. 2014;87(1041):20140134.
- Stefančíková L, Porcel E, Eustache P, Li S, Salado D, Marco S, Guerquin-Kern JL, Réfrégiers M, Tillement O, Lux F, et al. Cell localisation of gadolinium-based nanoparticles and related radiosensitising efficacy in glioblastoma cells. *Cancer Nanotechnol*. 2014;5(1):6.
- Tsiamas P, Sajo E, Cifter F, Theodorou K, Kappas C, Makrigiorgos M, Marcus K, Zygmanski P. Beam quality and dose perturbation of 6 MV flattening-filter-free linac. *Phys Med*. 2014;30(1):47–56.
- Tsiamas P, Seco J, Han Z, Bhagwat M, Maddox J, Kappas C, Theodorou K, Makrigiorgos M, Marcus K, Zygmanski P. A modification of flattening filter free linac for IMRT. *Med Phys*. 2011;38(5):2342–5239.

4

Theranostic nanoparticles for image-guided radiation therapy

Contents

4.1	Motivations	67
4.2	Animal model	68
4.3	Pharmacokinetics and biodistribution studies	68
4.3.1	Biodistribution in mice	68
4.3.2	Laser Induced Breakdown Spectroscopy (LIBS) imaging	69
4.4	Non-human primates: biodistribution and pharmacokinetics study	70
4.4.1	Biodistribution study in non-human primates	70
4.4.2	Pharmacokinetics study in non-human primates	70
4.5	In vivo radiation studies	72
4.5.1	Preclinical radiations	72
4.5.2	Clinical radiations	75
4.5.3	Enhanced in vivo clinical outcomes with nanoparticles and flattening filter free beams	78
4.6	Conclusion	78
4.7	Publications	80

4.1 MOTIVATIONS

Radiation therapy is part of the clinical standard-of-care for more than 50% of cancer patients [61]. Although radiation is highly effective in killing cancer cells, it is often not possible to deliver a curative radiation dose without inducing collateral damage in adjacent healthy tissues. Radiation dose escalation can significantly improve local tumor control and thereby improve patient survival [62]. Intensity-modulated radiation therapy (IMRT), volumetric modulated arc therapy (VMAT) and image-guided radiation therapy (IGRT) are recent techniques that have substantially improved

tumor-specific radiation dose delivery [63-65]. However, even with these technical advancements, effective radiation treatment is elusive for many intransigent tumors because of the dose-limiting irradiation of healthy tissues.

MRI-guided radiation therapy is an emerging clinical reality which has been identified as an important technology for clinical innovation [66-68]. In view of this, we formulated the previously described AGuIX nanoparticles (Si-GdNP). Because of the intrinsic properties of gadolinium, the AGuIX can be used for imaging (tumor delineation and quantification) and therapy (radiation amplification) applications. This formulation provides three main benefits compared to its molecular analogue: i) the DOTA complex restricts direct exposure and systemic release of Gd^{3+} and its eventual distribution in biological compartments [14]. Once intravenous-administered, the AGuIX accumulates in the tumor via the EPR-effect, following which MR imaging and irradiation are performed [70]. ii) Due to the relatively small size of AGuIX, it is rapidly excreted by the renal clearance pathway, minimizing off-target toxicities [11]. iii) AGuIX has a longer biological $t_{1/2}$ compared to FDA-approved molecular gadolinium chelates [71]. In the study presented in this chapter, we confirm AGuIX as a safe and effective MRI and radiation amplification agent with strong translational potential.

4.2 ANIMAL MODEL

Immunocompromised CrTac: NCr-Fox1nu mice (Taconic biosciences, Inc.) were injected with 3×10^6 capan-1 cells subcutaneously in the flank. Tumors were allowed to reach a size of 6-7 mm³ before initiating *in vivo* experiments. The capan-1 tumor bearing mice were injected with \pm AGuIX (0.25 mg/g) and treated \pm irradiation (10 Gy). Mice were followed for 12 weeks after irradiation. A tumor >2.5 cm in any dimension was considered as terminal end-point and the animal was sacrificed using standard institutional protocols. The Institutional Animal Care and Use Committee (IACUC) of the Dana-Farber Cancer Institute approved the *in vivo* experiments for this study.

4.3 PHARMACOKINETICS AND BIODISTRIBUTION STUDIES

4.3.1 BIODISTRIBUTION IN MICE

The biodistribution study with capan-1 tumor bearing mice (n=3/group) was performed on a preclinical 7 Tesla BioSpec 70/20 MRI scanner (Bruker BioSpin, United States). For the *in vivo* studies, a dose equivalent of 0.25 mg/g of AGuIX was injected intravenously. A T1 RARE-VTR sequence using a repetition time of 9000 ms, echo time of 19.6 ms, and a flip angle of 180 was used. The acquisition matrix size and reconstructed matrix were 400 x 200 pixels, the field of view 200 x 200 μm^2 , and the slice thickness 3 mm. Animals were pre-scanned, and then imaged at 2, 15, 30, and 45 min, and 1, 3 and 6 h post-AGuIX injection. A region of interest was drawn across tumor and other vital organs and the T1-contrast was measured and correlated to its respective calibrations (ParaVision (v. 5.1)). For the phantom T1 relaxivity measurements, different dilutions of AGuIX (0.01 mM to 0.5 mM) were prepared in de-ionized water and imaged using the same set-up as above. Signal amplitudes were average and T1 relaxivity measurements calculated for absolute quantification of the nanoparticles.

Whole body MR imaging (VTR-T1 sequence, 7 T, Bruker BioSpin, United States) was performed using capan-1 tumor bearing mice (6-8 mm²) and the longitudinal AGuIX accumulation was non-invasively visualized in tumor and healthy organs. As early as 1 min post-intravenous injection of AGuIX (0.25 mg/g), delineated tumor margins were visible due to gadolinium based MR contrast. EPR-mediated progressive accumulation of AGuIX in the tumor peaked at 15 min post-intravenous injections ($2.27 \pm 0.44\%$ ID). The MR signal from the kidneys and bladder were also prominent at 15 min (R. kidney: $13.85 \pm 0.98\%$ ID; L. kidney: $11.92 \pm 1.58\%$ ID; bladder: $14.85 \pm 1.49\%$ ID) and gradually declined thereafter, implying early clearance of AGuIX. Furthermore, comparably less accumulation ($5.84 \pm 1.04\%$ ID) was observed in the liver, which steeply declined after 15 min (2.26

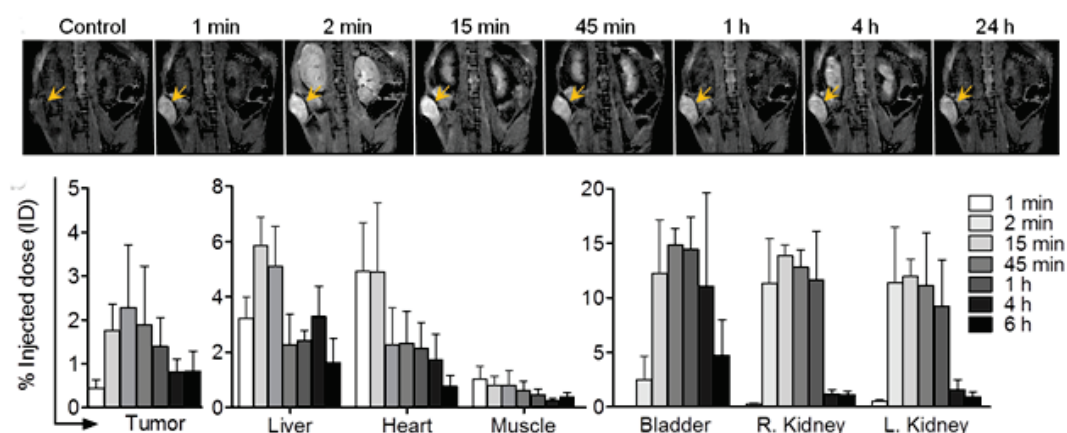


Figure 4.1: Whole body MR imaging in mice. T1-weighted MR imaging (7T, Bruker BioSpec, US) of AGuIX (0.25 mg/g) injected in mice bearing capan-1 pancreatic tumors (n=3/group) shows early tumor delineation (at 1 min-post-intravenous injections). Progressively high tumor accumulation in the tumor was observed due to the EPR- (enhanced permeability and retention) effect. Further quantification showed maximum tumor accumulation of AGuIX at 15 min post-intravenous administration and substantially high renal clearance. Some accumulation in the liver (6% ID) was also observed.

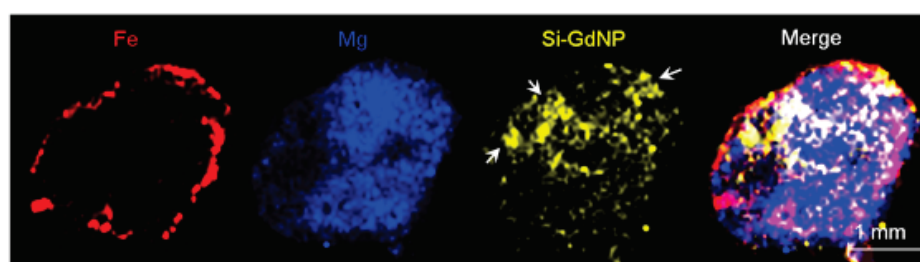


Figure 4.2: Intratumoral AGuIX (Si-GdNP) localization in capan-1 tumors at 15 min post-injection was imaged using laser-induced breakdown spectroscopy. The localization of the nanoparticle was performed by imaging the silica atoms of AGuIX.

± 1.09 %ID at 45 min post-intravenous injections). Nominal late accumulation was observed in other secondary organs such as muscle and heart (Fig. 4.1).

4.3.2 LASER INDUCED BREAKDOWN SPECTROSCOPY (LIBS) IMAGING

Paraffin-embedded tumor samples harvested 15 min after injection of the AGuIX were prepared for LIBS imaging [72]. To precisely measure the microscopic distribution of AGuIX within the tumor, laser induced breakdown spectroscopy (LIBS) imaging was performed. To this end, capan-1 tumors were excised at 15 min post-intravenous administration of AGuIX (0.25 mg/g). Silicon (Si) served as surrogate markers for AGuIX localization in the tumor due to the chemically-coupled polysiloxane construct (-Si-O-Si-) in the nanoparticle design (Fig. 1.2). Heterogeneous distribution of ultra-small nanoparticles in the tumor was clearly evident from the -Si- LIBS signal (the analysis on the Gd was not possible due to their insufficient concentration). Higher vascularity was demonstrated in the periphery of the tumor compared to the core (as inferred from the Fe signal) and AGuIX accumulation was slightly more prominent in the periphery (Fig. 4.2).

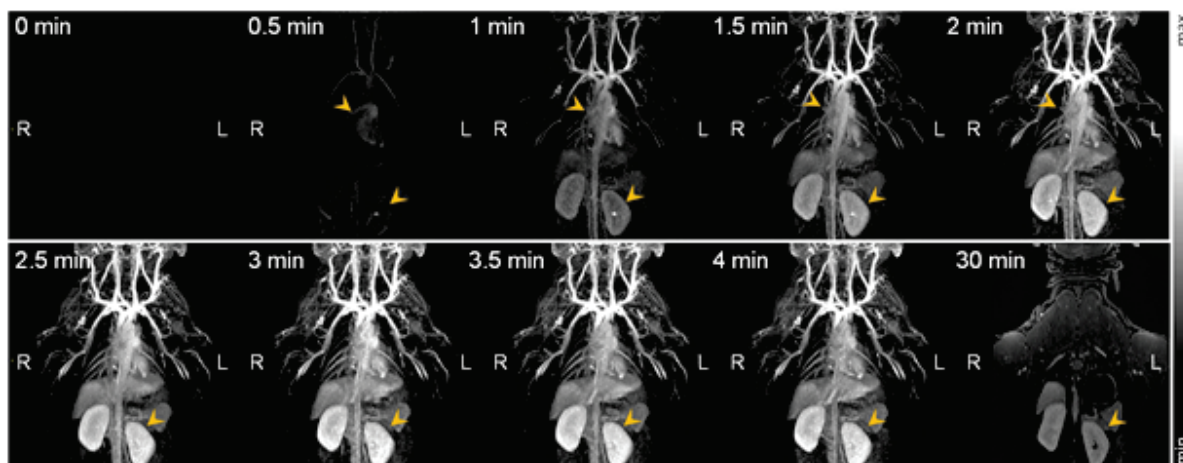


Figure 4.3: Biodistribution studies were carried out in cynomolgus monkeys ($n = 3/$ group) after administration of a single bolus infusion of 100 mg/kg AGuIX via external saphenous vein and was performed by the Wil Research group. Whole body MR imaging (T1 sequence) was carried out at different time points to visualize the early circulation and longitudinal renal clearance.

4.4 NON-HUMAN PRIMATES: BIODISTRIBUTION AND PHARMACOKINETICS STUDY

There are specific requirements that need to be met in order to proceed to a phase I clinical trial. In order to verify that we meet these requirements, we studied the biodistribution of the AGuIX nanoparticles and their toxicity in a larger animal model. The experiments were conducted by Wil Research company. They applied the good laboratory practice to obtain a dataset eligible for the phase 1 clinical trial.

4.4.1 BIODISTRIBUTION STUDY IN NON-HUMAN PRIMATES

Biodistribution studies were carried out in cynomolgus monkeys (*macaca fascicularis*) ($n = 3$) after administration of a single intravenous bolus infusion of 200 mg/kg of AGuIX (via external saphenous vein) using a 3T Prisma MRI scanner (Siemens, Germany). Animals were anesthetized with ketamine-xylazine (100 - 200 mg/kg). We used a T1 sequence with a repetition time of 3 ms, echo time of 1.12 ms, and a flip angle of 25 degree. The slice thickness was 1 mm. The acquisition matrix size and reconstructed matrix were 352 x 286 pixels, and the field of view was 280 x 227.5 mm². Animals were scanned during the first 4 min and 30 min- post-intravenous injections.

The early systemic circulation and longitudinal renal clearance of AGuIX were clearly visualized by whole body MR imaging. At 30 seconds post-intravenous injection, the nanoparticle-related MR signal (T1) was observed in peripheral vessels near the heart (Fig. 4.3). The MR images illustrate the early circulation of AGuIX over the next 2 to 4 min. At 30 min post-intravenous administration, a substantial decline in the AGuIX signal was observed with an overall reduction in the T1-contrast in the kidneys (Fig. 4.4). In agreement with the mice biodistribution profile, the monkey data confirmed the rapid renal clearance of AGuIX. A magnified MR image of the posterior kidney section shows late-retention (30 min) of AGuIX in the collecting ducts of the renal capillaries, indicating renal excretion (Fig. 4.4).

4.4.2 PHARMACOKINETICS STUDY IN NON-HUMAN PRIMATES

A total of 24 cynomolgus monkeys (*macaca fascicularis*) ($n=6$ /group; 3 males/group and 3 females/group) were assigned to 4 groups: control-, low-, moderate-, and high- AGuIX cohorts in

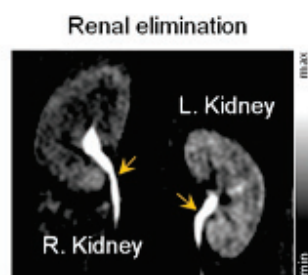


Figure 4.4: Blood samples were collected after administration of a single bolus injection of 150, 300 and 450 mg/kg of AGuIX (2.5 mL/kg equiv.) to cynomolgus monkeys (n=24/group; 12 males and 12 females) and pharmacokinetic parameters were analyzed. All data are represented as a mean \pm SD.

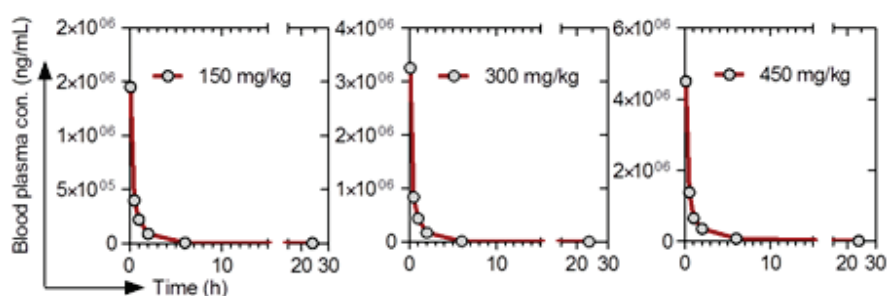


Figure 4.5: Blood samples were collected after administration of a single bolus injection of 150, 300 and 450 mg/kg of AGuIX (Si-GdNP) (2.5 mL/kg equiv.) to cynomolgus monkeys (n=24/group; 12 male and 12 females) and pharmacokinetic parameters were analyzed. All data are represented as a mean \pm SD.

order to perform a pharmacokinetic study of the nanoparticles. The corresponding doses of 0, 150, 300, and 450 mg/kg/administration were administered once per week for 2 weeks (day 0 and day 7). Blood samples were collected following each administration at 5 and 30 min, 1, 2, 6 and 24 h. The blood plasma distribution kinetics was analyzed based on a non-compartment model (Kinetica 4.4.1, Thermo Fisher). All the animals were observed for mortality, clinical signs, ophthalmology, body weight, food consumption, hematology, biochemistry, pathology, toxicokinetics and urinary parameters. Euthanasia was performed two weeks after the final injection.

AGuIX nanoparticles were injected at three different doses: low, moderate and high (150, 300 and 450 mg/kg, respectively), to evaluate the dose-dependent blood plasma distribution kinetics. For all tested doses, after an initial peak in concentration, the AGuIX signal rapidly declined from 0.5 to 6 h (Fig. 4.5).

By 9 h post-administration, the total AGuIX concentration in the blood had fallen to negligibly low amounts indicating that long-term toxicity events are unlikely in large animals; a factor that strongly supports clinical translation.

AGuIX toxicity was determined with excised organs from cynomolgus monkeys. H&E staining was performed on the tissue specimens of vital organs treated (\pm) AGuIX. Even at the highest tested dose (450 mg/kg), no apparent histological differences or toxicities were observed in the heart, lung, kidney and liver. Pharmacokinetic evaluations were carried out based on a non-compartmental model (KineticaTM 4.4.1, Thermo Fisher) using 3 different doses: 150, 300, and 450 mg/kg, injected intravenous twice in a one-week time interval (Fig. 4.6).

Based on the absence of any antemortem or postmortem findings, the no-observed-effect level (NOEL) in the present study was determined to be 450 mg/kg/administration in both female and

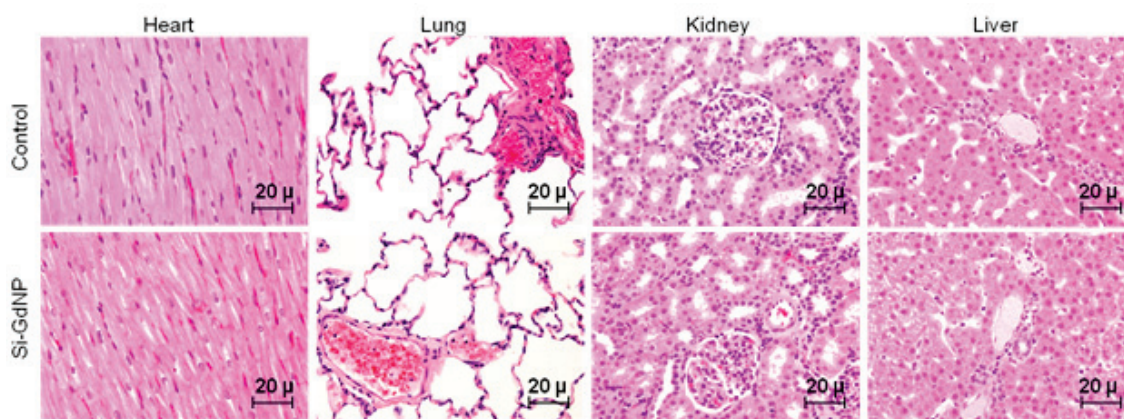


Figure 4.6: Histological H&E staining was performed on the organs excised from monkeys after administration of the highest dose of AGuIX (Si-GdNP) (450 mg/kg) via external saphenous vein in both male and female monkeys. No unscheduled deaths or clinical symptoms were observed in any of the treated animals.

male tested monkeys. At a dose of 150 mg/kg/administration, systemic exposure (area under the curve) of AGuIX on day 8 was calculated to be 3419 ng.h/mL in males and 2842 ng.h/mL in females. The nanoparticles exhibit a biological $t_{1/2}$ of 2.2 h and a clearance rate of 187 mL/h/kg and 171 mL/h/kg in both males and females respectively, indicating an effective elimination process (Fig. 4.5). All pharmacokinetic parameters were independent of gender variation as evident from the M/F ratio (Fig. 4.7). By the end of day 1, there was negligible presence of AGuIX in the systemic circulation indicating that long-term toxicity issues are unlikely.

4.5 IN VIVO RADIATION STUDIES

To test the therapeutic radiosensitization efficacy of nanoparticles in reducing aggressive tumor growth and improving overall animal survival in combination with preclinical and clinical radiation beams, we injected 0.25 mg/g of nanoparticles into capan-1 tumor xenografts ($n = 8$) and performed image-guided radiation therapy at 10 Gy using both preclinical and clinical beams. The measured tumor volumes demonstrated significant differences in the tumor burden in the treated vs non-treated groups.

Tumor growth was tracked with volumetric cone beam computed tomography (CBCT) images acquired with a Small Animal Radiation Research Platform (SARRP) (Xtrahl, Inc.). The volumes were measured using 3D Slicer software (v.4.3.1). The tumor was manually segmented to track its volume.

4.5.1 PRECLINICAL RADIATIONS

A targeted image-guided radiation therapy procedure was implemented preclinically based on a common clinical workflow wherein the tumor was delineated based on an MR image for 3D treatment planning and the 3D radiation dose calculations were performed (Fig. 4.8a-d).

Mice were imaged and irradiated using the SARRP. They were anesthetized with 1-3% isoflurane for the duration of each procedure (imaging or irradiation). Similar to the clinical workflow, a CBCT was performed on each mouse to calculate the dosimetry and to determine the radiation beam arrangement (65 kVp, 1.5 mA). Treatment was performed using a 12 mm circular collimator (220 kVp, 13 mA). The radiation dose was delivered in one fraction of 10 Gy by two beams at 0 and 90 angles (Fig. 4.8b). The treatment planning system Muriplan (v.1.3.0) was used to calculate the dose distribution in the tumor and healthy organs prior to the irradiation. The calculated isodose

Dose (mg/kg/adm)	Sex		C _{max} (mg/mL)	T _{max} (h)	AUC _{last} (mg.h/mL)	AUC _{infinity} (mg.h/mL)	T _{1/2} (h)	Cl (L/h)/kg	MRT (h)	V _{ss} (L/kg)
150	M	Mean	1429	0.0830-0.0830	812	812	2.13	0.187	1.05	0.195
		STD	109	NA	109	109	0.0342	0.0269	0.0669	0.0148
		CV(%)	8	NA	13.4	13.4	1.61	14.4	6.37	7.6
		n	3	3	3	3	3	3	3	3
	F	Mean	1422	0.0830-0.0830	884	885	2.21	0.171	1.33	0.225
		STD	263	NA	111	112	0.122	0.0233	0.401	0.0543
		CV(%)	19	NA	12.6	12.6	5.52	13.6	30.2	24.2
		n	3	3	3	3	3	3	3	3
	M/F ratio	1	NA	0.918	0.918	NA	NA	NA	NA	
	300	M	Mean	3305	0.0830-0.0830	1866	1866	2.17	0.162	1.09
STD			353	NA	163	163	0.0802	0.0134	0.0403	0.0208
CV(%)			11	NA	8.72	8.71	3.69	8.31	3.7	11.8
n			3	3	3	3	3	3	3	3
F		Mean	3216	0.083-0.0830	1695	1696	2.09	0.178	1.04	0.184
		STD	127	NA	127	128	0.0324	0.0129	0.0604	0.0135
		CV(%)	4	NA	7.52	7.52	1.55	7.29	5.82	7.32
		n	3	3	3	3	3	3	3	3
M/F ratio		1	NA	1.1	1.1	NA	NA	NA	NA	
450		M	Mean	4792	0.0830-0.0830	4051	4079	3.57	0.111	2.81
	STD		287	NA	350	324	1.12	0.00923	0.559	0.0884
	CV(%)		6	NA	8.63	7.95	31.4	8.33	19.9	28.1
	n		3	3	3	3	3	3	3	3
	F	Mean	4541	0.0830-0.0830	2890	3045	2.34	0.15	1.26	0.185
		STD	311	NA	482	NA	NA	NA	NA	NA
		CV(%)	9	NA	16.7	26.5	2.69	26.5	33.3	7.02
		n	3	3	3	2	2	2	2	2
	M/F ratio	1	NA	1.4	1.34	NA	NA	NA	NA	

Figure 4.7: Pharmacokinetic evaluation was carried out using non-compartmental model (KineticATM 4.4.1, Thermo Fisher) at three different doses to determine parameters such as C_{max} (maximum peak concentration), T_{max} (time for C_{max}), AUC (area under the curve), T_{1/2} (half-life), CL (clearance), MRT (mean residence time), V_{ss} (volume of steady state distribution).

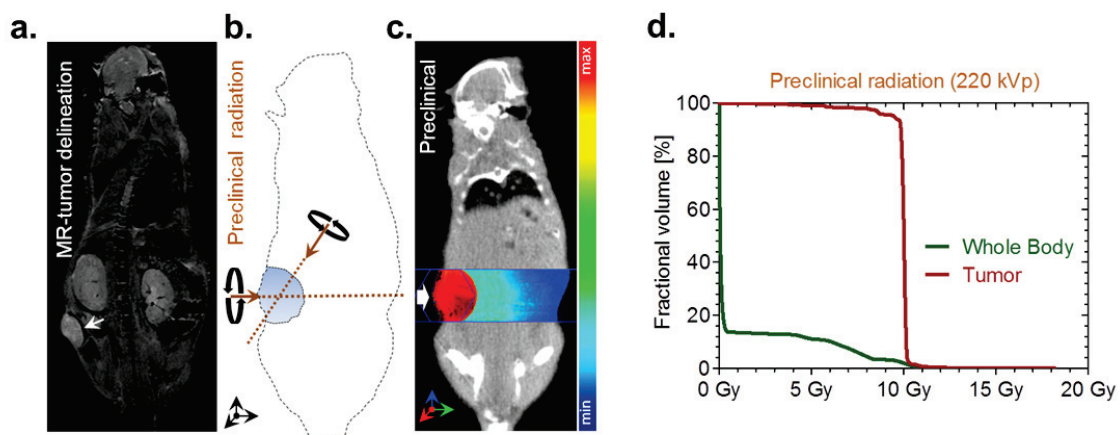


Figure 4.8: MR-guided radiation therapy dosimetry. (a) MR-guided tumor delineation (T1-VTR acquisition) was performed after injection of 0.25 mg/g AGuIX in capan-1-tumor xenografts. (b-c) Schematic depiction of the radiation setup in which tumor xenografts were irradiated with preclinical (10 Gy, orthogonal, 220 kV) radiation beams (brown dotted lines). The radiation dose distribution in the tumor and surrounding tissues were calculated on a cone-beam CT image. (d-e) Schematic depiction of the radiation setup in which tumor xenografts were irradiated with clinical (10 Gy, unilateral, 6 MV) radiation beams (orange dotted line). For each case, care was taken to deliver homogenous radiation to the tumor while sparing the healthy tissues (as performed in the clinic). The qualitative 3D isodose distributions show maximum radiation dose in the tumor. (f-g) The dose-volume histogram shows that more than 95% of the tumor received 95% of the prescription dose under preclinical conditions and 90% of the tumor received 90% of the dose under clinical conditions.

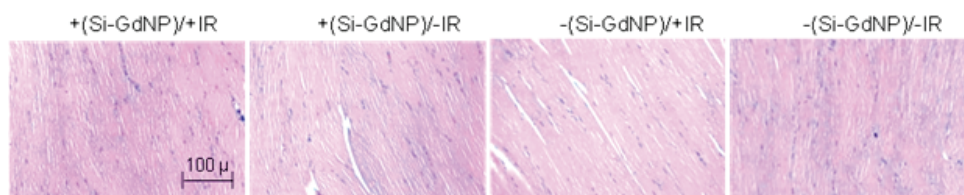


Figure 4.9: Radiation effect in mice muscle tissue. H&E staining of muscle tissue excised from irradiated mouse bearing capan-1 pancreatic tumor 15 min post-intravenous injection and its respective controls. No qualitative damage to the muscle tissue was observed in the irradiated and non-irradiated samples. Blue: nucleus; Pink: cytoplasm.

levels show maximum radiation dose in the tumor while substantially sparing the surrounding healthy tissues (Fig. 4.8c-d).

In addition, no histological damage was observed in the muscle tissue excised from the proximity of the irradiated tumor (Fig. 4.9) confirming the precise radiation therapy delivered to the animals..

SURVIVAL STUDY

The preclinical beam (220 kVp) produced a 6-fold difference ($P < 0.002$) in the tumor size for +(Si-GdNP)/+IR compared to the non-treated controls: +(Si-GdNP)/-IR (1.42 ± 0.12 vs. 6.51 ± 1.35 cm³) by day 20 (Fig. 4.10a). The survival of non-treated cohorts -(Si-GdNP)/-IR and +(Si-GdNP)/-IR was 30 days (Fig. 4.10b), compared to 45 days with radiation alone and 85 days ($P < 0.0001$, Mantel-Cox test) for nanoparticle combined radiation +(Si-GdNP)/+IR.

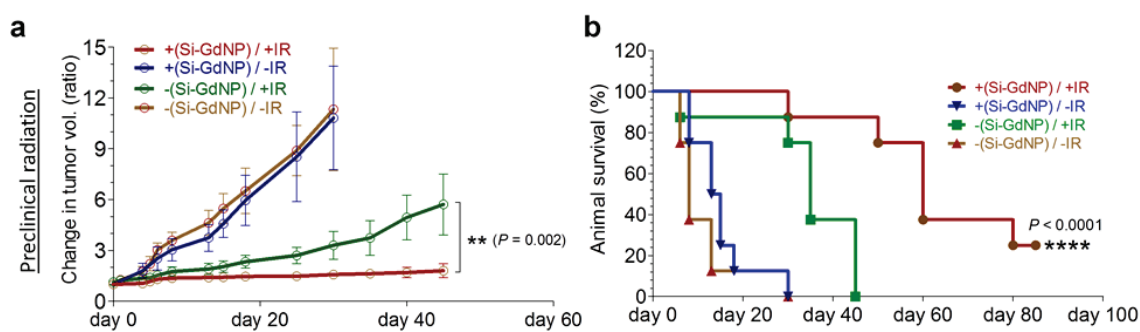


Figure 4.10: Tumor survival studies and radiation damage assessment. (a) Tumor volume measurements were performed on capan-1 tumor-bearing mice ($n = 8/\text{cohort}$) treated with and without AGuIX and preclinical (220 kV) irradiation. (b) The Kaplan-Meier survival curves demonstrate significant survival benefit when AGuIX is included with preclinical radiation ($n = 8/\text{cohort}$). Statistical significance was calculated using the log-rank (Mantel-Cox) test. A tumor size of 2.2 cm^3 was considered as the terminal end-point.

RADIATION-INDUCED DNA DAMAGE

Animals were irradiated 15 min after injection of the AGuIX following the same procedure as the survival study above. The tumor was harvested 30 min after irradiation and fixed in 2% formalin followed by paraffin embedding. Thin tumor sections of $5 \mu\text{m}$ were cut and the tissue sections were counterstained for H&E staining and γH2AX staining. A similar procedure was performed to quantify the toxicity in the healthy organs using primary antibody, Abcam ab26350 and secondary antibody, ser139 (Cell signaling Technologies, USA). Images were analyzed using a Zeiss Axio microscope at 63x magnification.

DNA double-strand breaks in tumor cells is a principal indicator of specific biological radiation response. In our initial qualitative analysis (by γH2AX staining), the *in vivo* treated tumors confirmed massive DNA damage for the $+(\text{Si-GdNP})/+\text{IR}$ cohort compared to the $-(\text{Si-GdNP})/+\text{IR}$ (Fig. 4.11a). No significant DNA damage was observed in healthy organs such as kidney, lung, heart and liver. Interestingly, both liver and kidney -the organs that were proximal to the irradiation site- were largely unaffected by the tumor-targeted irradiation and local dose enhancement. Further analysis of the tumor tissue demonstrated more than 80% DNA damage in the nanoparticle plus radiation treated cohort $+(\text{Si-GdNP})/+\text{IR}$. The magnitude of damage was 60% for the radiation only group $-(\text{Si-GdNP})/+\text{IR}$ and $<10\%$ for other controls $-(\text{Si-GdNP})/-\text{IR}$ and $+(\text{Si-GdNP})/-\text{IR}$ (Fig. 4.11b). These results clearly validate and confirm the dual-targeting concept wherein both targeted-radiation therapy and EPR-driven tumor accumulation of high atomic number nanoparticles combine to amplify the radiation response specifically in cancer cells while largely sparing surrounding healthy tissues.

4.5.2 CLINICAL RADIATIONS

To perform clinical irradiations, mice were anesthetized and placed in a cage after intraperitoneally injecting $0.1 \text{ mL}/20 \text{ g}$ mouse of ketamine/xylazine mixture. A pack of solid water equivalent to 2 cm was wrapped across the back of mice (Fig. 4.12). The treatment planning system ECLIPSE (Aria V.11) which is routinely used for patients treated in the clinic, was used to calculate the dose distribution in tumor and healthy organs. The AAA calculation algorithm for a $5.5 \times 10 \text{ cm}^2$ field size, gantry at 180 degrees, and surface-skin distance of 90 cm was used. Simulation was performed for the 6 MV irradiation beam (TrueBeam-Varian, CA) (Fig. 4.12). The capan-1 tumor-bearing mice were then injected with 0.25 mg/g of AGuIX intravenous. Fifteen minutes post-injection, radiation treatment was performed with 10 Gy. Four groups ($-\text{Si-GdNP}/-\text{IR}$; $+\text{Si-GdNP}/-\text{IR}$; $-\text{Si-GdNP}/+\text{IR}$; $+\text{Si-GdNP}/+\text{IR}$) of 5 mice each were used to characterize the effect of the Si-GdNP as a radiosensitizer.

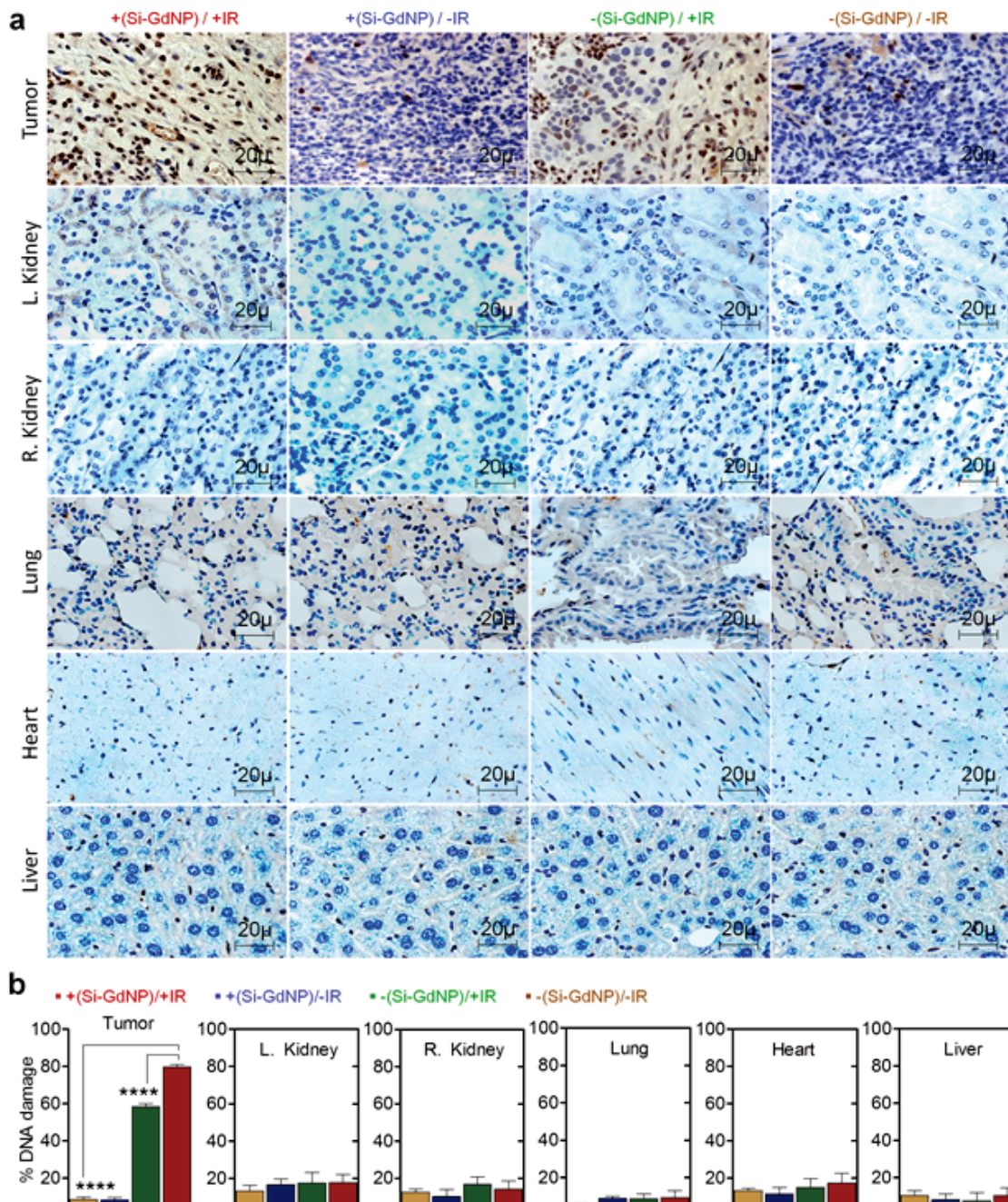


Figure 4.11: Tumor survival studies and radiation damage assessment. (a) Tumor volume measurements were performed on capan-1 tumor-bearing mice ($n = 8/\text{cohort}$) treated with and without AGuIX (Si-GdNP) and pre-clinical (220 kV) irradiation. (b) The Kaplan-Meier survival curves demonstrate significant survival benefit when AGuIX is included with preclinical radiation ($n = 8/\text{cohort}$). Statistical significance was calculated using the log-rank (Mantel-Cox) test. A tumor size of 2.2 cm^2 was considered as the terminal end-point.

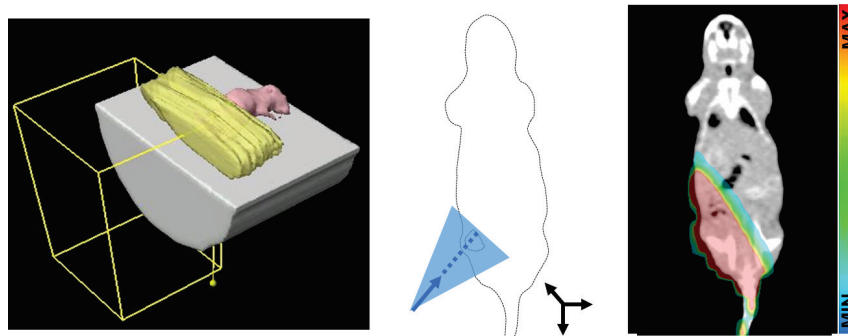


Figure 4.12: Dosimetry study performed with clinical settings. (left) 3D representation of the radiation setup. Animal was placed on top of 10 cm of solid water to create a beam softening and mimic the position of a pancreas in a patient. In addition, the mouse was wrapped into 2 cm of bolus for scattering. (middle) Schematic representation of the 2D tumor segmentation. (right) Dosimetry results performed with Eclipse V12., software used in clinic for patients.

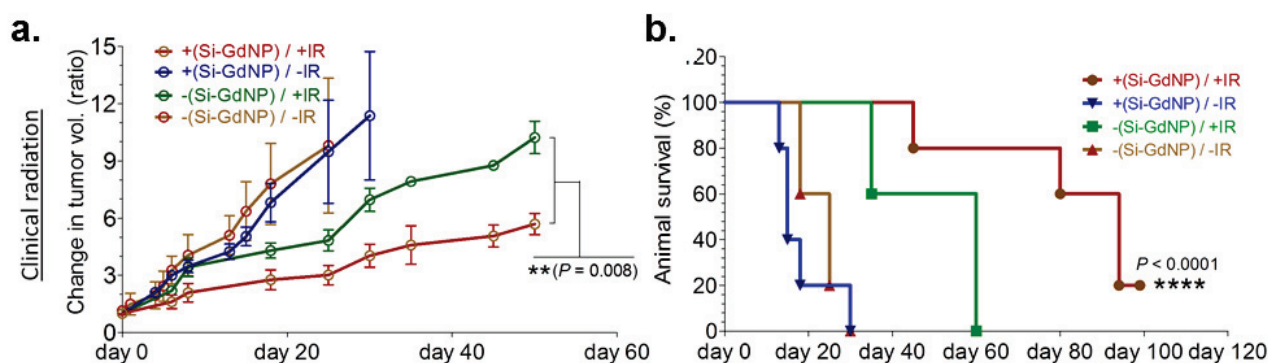


Figure 4.13: Tumor survival studies and radiation damage assessment. (a) Tumor volume measurements were performed on capan-1 tumor-bearing mice (n = 5/cohort) treated with and without AGuIX (Si-GdNP) and clinical (6 MV) radiation. (b) The Kaplan-Meier survival curves demonstrate significant survival benefit when AGuIX is included with clinical radiation (n = 5/ cohort). Statistical significance was calculated using the log-rank (Mantel-Cox) test.

SURVIVAL STUDIES

With clinical irradiation (6 MV), a statistically significant reduction in tumor size was measured for the +(Si-GdNP)/+IR group compared to the -(Si-GdNP)/+IR group (2.69 ± 0.16 vs. 5.32 ± 0.19 cm³) by day 50 ($P < 0.0001$, Mantel-Cox test) (Fig. 4.13a). Survival was extended by more than 30 days (70%) compared to the -(Si-GdNP)/+IR treated group (Fig. 4.13b). This is the first published demonstration of the therapeutic efficacy of Si-GdNP under clinical radiation therapy conditions.

RADIATION-INDUCED DNA DAMAGE

Animals were irradiated 15 minutes after injection of the AGuIX following the same procedure as the survival study above. The tumor was harvested 30 min after irradiation and fixed in 2% formalin followed by paraffin embedding. Tumor slices of approximately 5 μ m were cut. Sections were counterstained for γ H2AX staining (antibody Abcam ab11174). Images were analyzed using a Zeiss Axio microscope at 63X magnification.

The histopathological evaluation by γ H2AX staining revealed a significant increase in DNA damage for treatment groups that included radiation and AGuIX, consistent with the tumor growth and

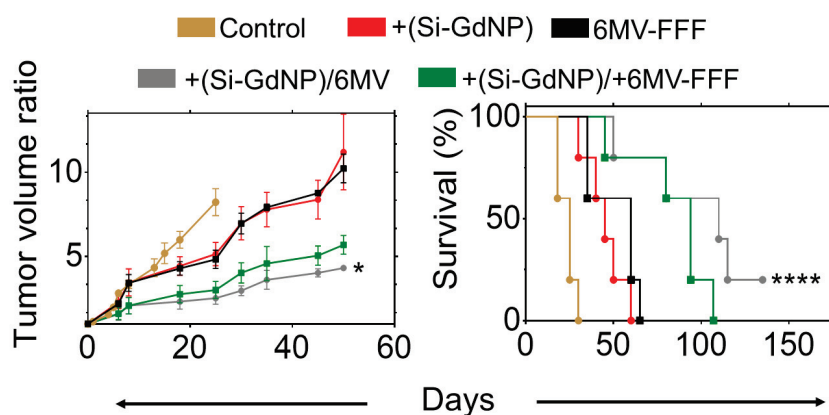


Figure 4.14: Tumor growth and survival studies comparison between 6 MV and 6 MV-FFF radiation beam with nanoparticles and radiation damage assessment. (a) Tumor volume measurements were performed on capan-1 tumor-bearing mice ($n = 5/\text{cohort}$) treated with and without AGuIX (Si-GdNP) and clinical (6 MV) radiation. (b) The Kaplan-Meier survival curves demonstrate significant survival benefit when AGuIX is included with clinical radiation ($n = 5/\text{cohort}$). Statistical significance was calculated using the log-rank (Mantel-Cox) test.

survival results. The rate of DNA damage for 6 MV-FFF/(Si-GdNP), 6 MV-STD/(Si-GdNP) and 6 MV-STD was $78 \pm 4\%$, $36 \pm 6\%$ and $13 \pm 3\%$, respectively (Fig. 4.15). For the irradiated kidney, a significant enhancement of the DNA damage is observed ($P=0.0019$) compared to the non-irradiated groups, indicating a need to ensure kidney sparing is prioritized during the treatment planning process. No other toxicities were observed in any of the other healthy organs.

4.5.3 ENHANCED IN VIVO CLINICAL OUTCOMES WITH NANOPARTICLES AND FLATTENING FILTER FREE BEAMS

While we demonstrated the feasibility and the *in vitro* efficacy of the flattening filter free radiation beam compared to its analogue flat beam, it remained important to validate the data *in vivo*. Thus, 6 MV-STD and 6 MV-FFF clinical radiation beams were delivered to capan-1 tumor-bearing mice using the same dosimetry as described previously (Fig. 4.12). The time lapse between the nanoparticles injection and irradiation (15 min) was determined from the biodistribution studies (Fig. 4.1). The tumor growth and survival studies demonstrated a statistically significant benefit for either 6 MV-STD or 6 MV-FFF with AGuIX with a 1.5-fold difference in the tumor burden size by day 50 between +Si-GdNP/6 MV-FFF and +Si-GdNP/6 MV groups ($P=0.0411$) and a median lifetime expended by 16 days ($P<0.0001$). The tumor burden difference with the radiation control group (-SiGdNP/+IR) is equal to 2.6-fold with an improving median lifetime of 65 days. Statistically significant benefit was also seen for 6 MV-FFF with AGuIX compared to 6 MV-STD with AGuIX (Fig. 4.14).

4.6 CONCLUSION

The 6 MV-FFF radiation beam was originally developed to create a higher dose rates for treatments to provide a better organ motion management, improve the dose delivery accuracy for gated treatment, and improve the patient comfort during treatment.

By exploiting the flattening filter removal potential to increase the speed of treatment, the combination of nanoparticles and low energy photon generation increase led to a significant therapeutic tumor suppression compared to the 6 MV radiation beam with the same level of dose enhancement achieved than with a preclinical radiation beam. The efficacy of the 6 MV-FFF radiation beam compared to its analogue flattened radiation beam with the presence of nanoparticles in the tumor cells

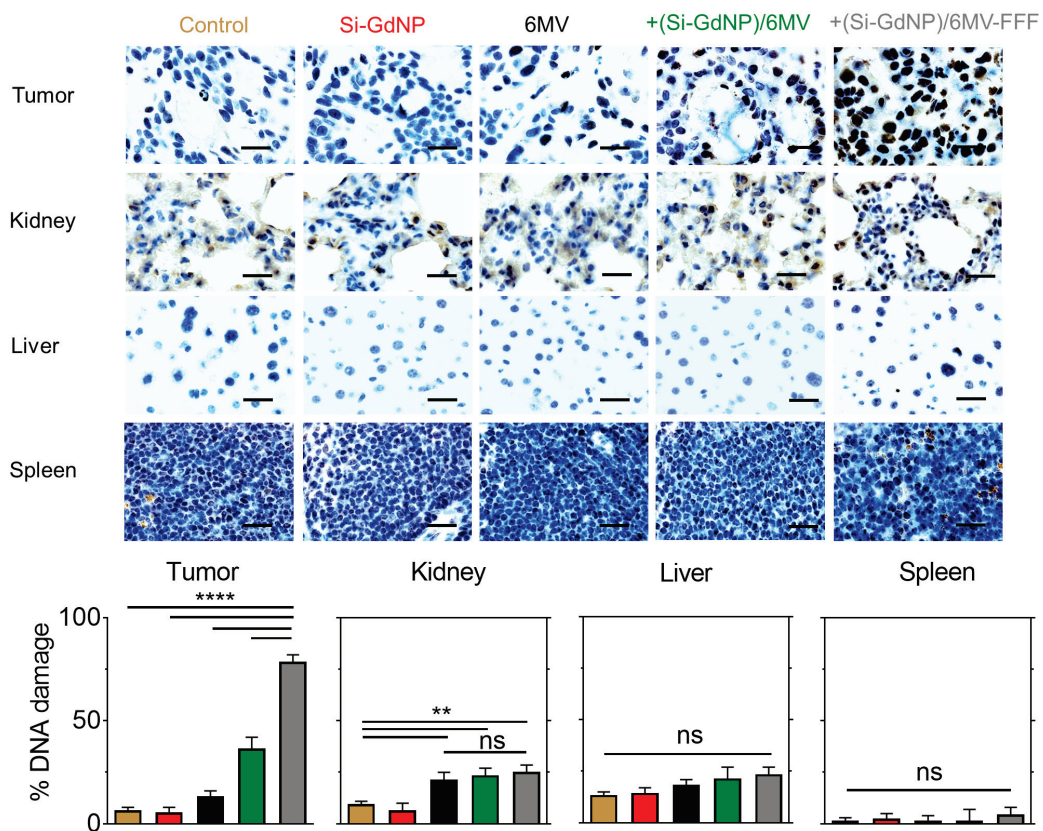


Figure 4.15: 6 MV vs. 6 MV-FFF clinical radiation damage assessment. Qualitative representation of DNA double strand breaks in the tumor and surrounding tissues shown by γ H2AX staining. Scale bar = 20 μ m. Quantification of positive nuclei (brown nuclei) counted over 30 images. All data are represented as a mean \pm SD. Statistical tests were performed using a Kruskal-Wallis test for the tumor growth study and the DNA damage quantification whereas a Log-Rank test was performed for the survival study. **P < 0.01, ****P < 0.0001.

presents a highly translational therapeutic new proof of concept for this field of research. We demonstrated that the use of an unflattened radiation therapy beams combined to nanoparticles promoted tumor targeting *in vivo* for enhanced efficacy against capan-1 xenograft tumor model compared to clinical radiation beam and nanoparticles or radiation alone.

With clinical radiation therapy practices incorporating more and more MR imaging, the clinical rationale for AGuIX is only increasing. This is the first study demonstrating the safe and therapeutically beneficial administration of AGuIX for image-guided radiation therapy using clinical 6 MV radiation beams. This is a major advancement in this field and provides a strong rationale for clinical translation. To this end, we have been careful to design and demonstrate a procedure that is highly compatible with current and emerging clinical workflows.

The combination of imaging contrast and radiosensitization without increased toxicity to healthy organs makes AGuIX formulation an excellent candidate for future clinical translation in radiation therapy [72]. One of the remaining questions is the underlying mechanism of gadolinium-based radiosensitization. While physical interactions between photons and high atomic materials can partly explain the biological effects, theoretical accounts have struggled to model this effect accurately. It may be that a series of physiological mechanisms such as the induction of free radicals, e.g. generation of OH° and H_2O_2 , can lead to an increase in indirect tumor cell killing. The detailed mechanism of high atomic number radiosensitization still remains to be investigated.

Regulatory toxicity studies in non-human primates showed that the rapid renal clearance of AGuIX perfectly fits with the physiological glomerular filtration rate in non-human primates [73]. At the highest dose tested in these species (450 mg/kg), toxicity studies demonstrated adequate tolerance of intravenous administration of AGuIX, predicting a human equivalent dose (HED) of 145 mg/kg [74]. The experimental data in mice and non-human primates clearly substantiates and justifies the clinical translational potential of AGuIX. Intravenous administration of nanoparticles fits current clinical workflows for radiation therapy based on pre-treatment MR imaging as well as the emerging practice of real-time MR guidance on combined MR-linac devices. In either scenario, AGuIX will be a valuable clinical tool for safe and effective imaging and therapy of cancer.

There is still a room to improve the efficacy of the nanoparticles by modifying the radiation machine [75]. Thus, other technologies such as the modification of the target as suggested by our group could lead to a subsequent enhancement of this therapeutic approach. By replacing the Cu/W target used to create the photons in the 6 MV and 6 MV-FFF beam by a carbon target, an increase of approximately 30% of low energy photons would be generated at a 10 cm depth. As demonstrated analytically previously [36-60] and confirmed by our *in vitro* and *in vivo* results, we correlated in this study the increase of low energy photons amount to the radiation dose enhancement to the tumor.

4.7 PUBLICATIONS



Advanced multimodal nanoparticles delay tumor progression with clinical radiation therapy



Alexandre Detappe^{a,b,1}, Sijumon Kunjachan^{a,*,1}, Lucie Sancey^b, Vincent Motto-Ros^b, Douglas Biancur^a, Pascal Drane^a, Romain Guieze^c, G. Mike Makrigrigios^a, Olivier Tillement^b, Robert Langer^d, Ross Berbeco^{a,*}

^a Department of Radiation Oncology, Dana-Farber Cancer Institute, Brigham and Women's Hospital, Harvard Medical School, Boston, MA 02215, USA

^b Lyon-1 University, Institut Lumière Matière, CNRS UMR5306, Lyon, France

^c Division of Medical Oncology, Dana-Farber Cancer Institute, Brigham and Women's Hospital, Harvard Medical School, Boston, MA 02215, USA

^d Department of Chemical Engineering, David H. Koch Institute for Integrative Cancer Research, Massachusetts Institute of Technology, Cambridge, MA 02139, USA

ARTICLE INFO

Article history:

Received 28 April 2016

Received in revised form 29 June 2016

Accepted 12 July 2016

Available online 14 July 2016

Keywords:

Image-guided radiation therapy

Radiosensitizer

Theranostics

Nanoparticles

ABSTRACT

Radiation therapy is a major treatment regimen for more than 50% of cancer patients. The collateral damage induced on healthy tissues during radiation and the minimal therapeutic effect on the organ-of-interest (target) is a major clinical concern. Ultra-small, renal clearable, silica based gadolinium chelated nanoparticles (SiGdNP) provide simultaneous MR contrast and radiation dose enhancement. The high atomic number of gadolinium provides a large photoelectric cross-section for increased photon interaction, even for high-energy clinical radiation beams. Imaging and therapy functionality of SiGdNP were tested in *cynomolgus* monkeys and pancreatic tumor-bearing mice models, respectively. A significant improvement in tumor cell damage (double strand DNA breaks), growth suppression, and overall survival under clinical radiation therapy conditions were observed in a human pancreatic xenograft model. For the first time, safe systemic administration and systematic renal clearance was demonstrated in both tested species. These findings strongly support the translational potential of SiGdNP for MR-guided radiation therapy in cancer treatment.

© 2016 Elsevier B.V. All rights reserved.

1. Introduction

Radiation therapy is part of the clinical standard-of-care for more than 50% of cancer patients [1]. Although radiation is highly effective in killing cancer cells, it is often not possible to deliver a curative radiation dose without inducing collateral damage in adjacent healthy tissues. Radiation dose escalation can significantly improve local tumor control and thereby improve patient survival [2]. Intensity-modulated radiation therapy (IMRT), volumetric modulated arc therapy (VMAT) and image-guided radiation therapy (IGRT) are recent techniques that have substantially improved tumor-specific radiation dose delivery [3–5]. However, even with these progressing technical advancements, effective radiation treatment is elusive for many intransigent tumors because of the dose-limiting toxicity in healthy tissues.

Nanotechnology has great potential in cancer radiation therapy. Radiosensitizing and radiation dose enhancing agents (nanoparticles) can increase the effects of radiation within the disease site while maintaining the current clinical constraints on dose to healthy

organs [6–8]. Nanoparticles made of high atomic number (*Z*) elements cause local amplification of radiation dose due to the emission of low energy photoelectrons and Auger electron interactions [9,10]. The interaction cross-section is highly dependent on the energy of the incident photons, with lower energy photons having a much higher probability of interaction. In clinical radiation therapy, ~95% of patient treatments are performed with high-energy X-ray beams produced by clinical linear accelerators with peak energy of 6 MV. This is in contrast to the preclinical X-ray irradiators with peak energies in the range of 200–300 kV. For this reason, many investigators have dismissed the potential for using clinical radiation therapy improvement with nanoparticles [11,12]. However, our data strongly refutes previous conclusions and shows that even with high-energy clinical beams, substantial DNA damage and tumor suppression can be invoked.

In addition to the physical dose enhancement induced by high-*Z* metallic nanoparticles, radiation-induced biochemical reactions may also contribute to the overall tumor damage. However, the essential mechanism is premature and still under investigation [13]. The radiosensitizing potential of gold (*Au*), gadolinium (*Gd*), hafnium (*Hf*), and bismuth (*Bi*) have been investigated preclinically [10,14–17]. Among these, *Gd*-based nanoparticles have the unique translational advantage of acting both as a radiation dose enhancement agent and MR imaging contrast agent, simultaneously.

* Corresponding authors at: Department of Radiation Oncology, Dana-Farber Cancer Institute, Brigham and Women's Hospital, Harvard Medical School, 450 Brookline Avenue, Boston, MA 02215, USA.

¹ These authors contributed equally to this work.

MRI-guided radiation therapy is an emerging clinical reality [5,18–21]. In view of this, we formulated an *ultrasmall* (~1–5 nm) silica-based nanoparticle (SiGdNP) in which Gd³⁺ is chemically chelated to a rigid polysiloxane matrix with DOTA (1,4,7,10-tetra-azacyclododecane-1-glutaric anhydride-4,7,10-triacetic acid). Because of the intrinsic properties of Gd, the SiGdNP can be used for imaging (tumor delineation/quantification) and therapy (radiation amplification) applications. This formulation of Gd that is directly entrapped in the DOTA complex is a clinically viable formulation and provides three major benefits: i) the DOTA complex restricts direct exposure and systemic release of Gd³⁺ and its eventual distribution in biological compartments [22,23]. Once *i.v.*-administered, the SiGdNP accumulate in the tumor *via* the *enhanced permeability and retention* (EPR) effect, following which MR imaging and irradiation is performed [24,25]. ii) Due to the relatively small size of SiGdNP, it is rapidly excreted by the renal clearance pathway, minimizing off-target toxicities [26]. iii) SiGdNP has a longer (biological) $t_{1/2}$ compared to its molecular gadolinium chelates [27]. In this study, we confirm SiGdNP as a safe and effective MRI and radiation amplification agent with strong translational potential.

2. Material and methods

2.1. Gadolinium-based nanoparticles

The gadolinium-based nanoparticles (SiGdNP) were synthesized and purified in compliance with GMP standards at Nano-H (Lyon, France). Structurally, SiGdNP is composed of an inorganic matrix of polysiloxane surrounded by covalently bound DOTAGA (Gd) ((1,4,7,10-tetra-azacyclododecane-1-glutaric anhydride-4,7,10-triacetic acid)-Gd³⁺).

2.2. Characterization of the nanoparticles

Lyophilized nanoparticles were dispersed in PBS (7.4) for one hour at room temperature (Gd³⁺: 100 mM). Hydrodynamic size and zeta potential measurements were carried out with a Zetasizer NanoS DLS (Malvern Instrument) at further diluted concentrations (Gd³⁺ = 10 mM). Average (diameter) size of 3.5 ± 1 nm and a zeta potential of 9 ± 5.5 mV was obtained for the SiGdNP formulation.

2.3. Cell culture

Capan-1 (human pancreatic adenocarcinoma) cells were cultured in Iscove's Modified Eagle Medium (IMEM), supplemented with 20% fetal bovine serum (FBS) (Sigma, USA) and 1% Penicillin-Streptomycin Glutamine (Invitrogen, USA). Optimal conditions of 37 °C and 5% CO₂ was observed in a humidified incubator.

2.4. Clonogenic assay

Capan-1 cells were incubated with 0.43 mg/ml of SiGdNP for 15 min prior to irradiation with an open field 220 kVp beam. Radiation dose levels of 2, 4, 6, 8, and 10 Gy were employed. The cells were further incubated for another 4 h after irradiation and afterwards washed with PBS, trypsinized and counted. The cells were seeded in 10 cm dishes at 300 cells per plate and allowed to grow for 10 days, before staining with a 1% crystal violet in 10% ethanol dye solution. The plates were digitally scanned and automatically counted with an in-house developed software tool. Measurements were performed in triplicate. The effect of the SiGdNP is quantified by the calculation of the dose enhancement factor (DEF) using Matlab (v. R2013b). The DEF is the ratio of the area under the survival curves with and without nanoparticles.

2.5. Apoptosis assay

Apoptosis was quantified by Allophycocyanin Annexin V/7-Aminoactinomycin D staining (Biolegends, USA) followed by flow cytometry analysis according to the manufacturer's instructions using BD FACSCanto II (BD Biosciences, USA). Measurements were performed with and without nanoparticles after incubating for 15 min at 0.43 mg/ml concentration. After irradiation, three different time points were analyzed: 15 min, 24 h, and 48 h.

2.6. In vitro experiments

Capan-1 cells were irradiated to 4 Gy and 10 Gy with 220 kVp beams, +/- SiGdNP (0.43 mg/ml). Cells were fixed with 4% v/v formaldehyde for 15 min at room temperature (RT), and then washed twice with PBS. Cells were permeabilized with BSA 1%, FBS 10%, 0.3% triton-100 for 1 h, RT. The cells were incubated overnight at 4 °C with 53BP1 antibody (H-300, Santacruz, USA), diluted 1 to 1000 in PBS containing 1% BSA, 0.1% triton x-100, then washed five times with PBS. Slides were mounted with Dapi Fluoromount-G (SouthernBiotech, USA). Fluorescence microscopy images were processed to visualize the foci. The DNA damage induced by the nanoparticles was determined by counting the number of cells with >10 foci.

3. Mice studies

All animal studies were approved and carried out according to the US and European animal ethical committee, after approval by local and governmental agencies.

3.1. Survival study

Immunocompromised CrTac: NCr-Fox1tm mice (Taconic biosciences, Inc.) were injected with 3 × 10⁶ capan-1 cells subcutaneously in the flank. A total of 8 mice per group were used for the preclinical irradiation (220 kV) and 5 mice per group for the clinical irradiation studies (6 MV). Tumors were allowed to reach a size of ~6 × 7 mm² before initiating *in vivo* experiments. The capan-1-tumor bearing mice were intravenously injected with +/- SiGdNP (0.25 mg/g) and treated +/- irradiation (10 Gy). Mice were followed for 12 weeks after irradiation. A tumor >2.5 cm in any dimension was considered as terminal endpoint and sacrificed using standard institutional protocols. The Institutional Animal Care and Use Committee (IACUC) of the Dana-Farber Cancer Institute approved the *in vivo* experiments for this study.

3.2. Magnetic resonance imaging

The biodistribution study with capan-1 tumor bearing mice ($n = 3$ /group) was performed on a preclinical 7 Tesla BioSpec 70/20 MRI scanner (Bruker BioSpin, United States). For the *in vivo* studies, a dose equivalent of 0.25 mg/g of SiGdNP was injected intravenously. A T1 RARE-VTR sequence using a repetition time of 9000 ms, echo time of 19.6 ms, and a flip angle of 180° was used. The acquisition matrix size and reconstructed matrix were 400 × 200 pixels, and the field of view was 200 × 200 μm², and slice thickness was 3 mm. Animals were pre-scanned, and then imaged at 2, 15, 30, and 45 min, and 1, 3 and 6 h post-SiGdNP injection. A region of interest was drawn across tumor and other vital organs and the T1-contrast was measured and correlated to its respective calibrations (ParaVision (v. 5.1)). For the phantom T₁ relaxivity measurements, different dilutions of SiGdNP (0.01 mM to 0.5 mM) was prepared in de-ionized water and imaged using the exact set-up as above. Signal amplitudes were average and T₁ relaxivity measurements calculated for absolute quantification of the nanoparticles.

4. Monkey studies

All animal studies were approved and carried out according to the European animal ethical committee guidelines.

4.1. Magnetic resonance imaging

Biodistribution study was carried out in cynomolgus monkeys (*macaca fascicularis*) ($n = 3/\text{group}$) using a 3 T Prisma MRI scanner (Siemens, Germany) at 200 mg/kg of SiGdNP. Animals were anaesthetized with ketamine-xylazine (100–200 mg/kg). A T1 sequence using a repetition time of 3 ms, echo time of 1.12 ms, and a flip angle of 25° was used. The slice thickness was ~ 1 mm. The acquisition matrix size and reconstructed matrix were 352×286 pixels, and the field of view was 280×227.5 mm². Animals were scanned during the first 4 min and 30 min-*p.i.*

4.2. Pharmacokinetics and toxicity study

A total of 24 cynomolgus monkeys (*macaca fascicularis*) ($n = 6/\text{group}$; 3 males and 3 females/group), were assigned to 4 groups: *control*-, *low*-, *moderate*-, and *high*- SiGdNP cohorts. The corresponding doses of 0, 150, 300, and 450 mg/kg/administration were administered once per week for 2 weeks (day 0 and day 7). Blood samples were collected following each administration at 5 and 30 min, 1, 2, 6 and 24 h. The blood plasma distribution kinetics was analyzed based on a non-compartment model (Kinetica 4.4.1, Thermo Fisher). All the animals were observed for mortality, clinical signs, ophthalmology, body weight, food consumption, hematology, biochemistry, pathology, toxicokinetics and urinary parameters. Euthanasia was performed two weeks after the final injection.

4.3. Laser induced breakdown spectroscopy (LIBS) imaging

Paraffin-embedded tumor samples harvested 15 min after injection of the SiGdNP were prepared for LIBS imaging. Briefly, the instrumental setup was based on an optical microscope that combined a LIBS laser injection line, a standard optical imaging apparatus, and a 3D motorized platform for sample positioning. The LIBS experiment used Nd: YAG

laser pulses of 1064 nm and 5 mJ energy, which were vertically focused onto the sample by a high-power $15\times$ magnification objective to produce the laser-induced plasma. The pulse duration was 5 ns and the repetition rate was 10 Hz. During the experiments, the paraffin embedded sample was translated along two axes to image, pixel by pixel, the region of interest. During the sample scan, trigonometric surface positioning was used to compensate for any flatness anomalies and the laser energy was stabilized throughout the experiment by using a servo control loop. The optical signal was collected using a Czerny-Turner spectrometer equipped with a 1200-l/mm grating and an intensified charge-coupled device (ICCD) camera (Shamrock 303 and iStar, Andor Technology). In this configuration, a spectral range of 30 nm was accessible with a spectral resolution of about 0.15 nm. The spectral range covered in this case, from 282 to 317 nm, allowed lines originating from Mg (285 nm), Si (288 nm) and Iron (302 nm) to be detected.

4.4. Radiation therapy

Mice were imaged and irradiated using the Small Animal Radiation Research Platform (SARRP) (Xtrahl, Inc.). Animals were anaesthetized with 1–3% isoflurane for the duration of each procedure (imaging or irradiation). Similar to the clinical workflow, a cone beam computed tomography (CBCT) was performed on each mouse to calculate the dosimetry and to determine the radiation beam arrangement (65 kVp, 1.5 mA). Treatment was performed using a 12 mm circular collimator (220 kVp, 13 mA). The radiation dose was delivered in one fraction of 10 Gy by two beams at 0° and 90° angles. The treatment planning system Muriplan (v.1.3.0) was used to calculate the dose distribution in the tumor and healthy organs prior to the irradiation. Four groups (–SiGdNP/–IR; +SiGdNP/–IR; –SiGdNP/+IR; +SiGdNP/+IR) of 8 mice each were used to characterize the effect of the SiGdNP as a radiosensitizer.

To perform clinical irradiation, animals were anesthetized and placed in a cage after intra-peritoneally injecting 0.1 mL/20 g mouse wt. of ketamine/xylazine mixture. 10 cm solid water (CIRS, Inc) was placed between the mouse and the radiation source and an additional 2 cm of tissue equivalent clinical bolus material used for backscatter. The treatment planning system ECLIPSE (Aria V.11) which is routinely used for patients treated in the clinic, was used to calculate

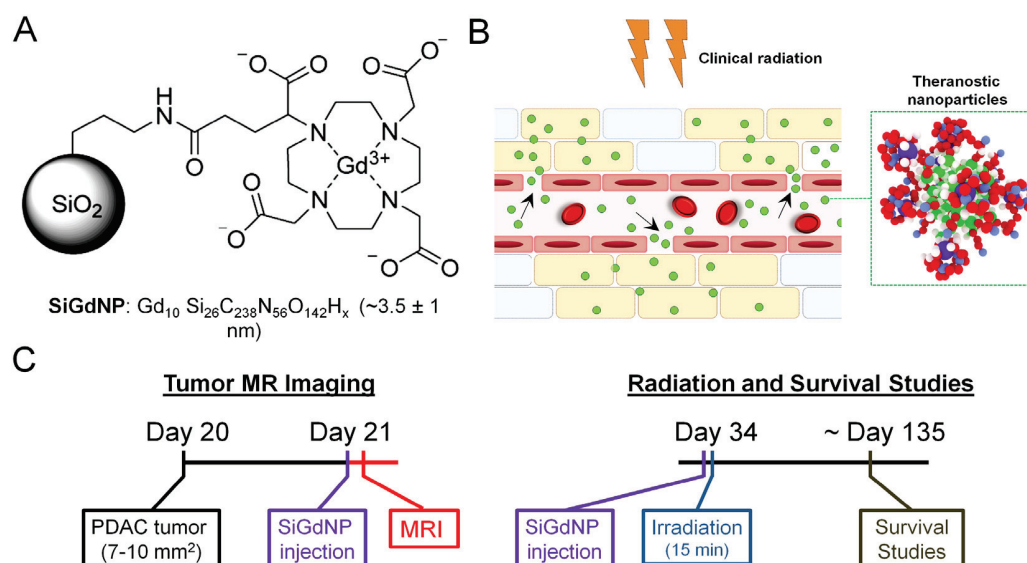


Fig. 1. Experimental design and concept. (A) Illustrative representation of ultra-small (~ 3 nm) SiGdNP. The nanoparticle is comprised of a polysiloxane (–Si–O–Si–) backbone where gadolinium atoms are chemically embedded in the DOTA chelating agent outside the core. This spatial arrangement reduces toxicity and simultaneously sustains and improves therapeutic efficacy. (B) An illustration of tumor accumulation of SiGdNP due to the enhanced permeability and retention (EPR) effect. (C) The experimental timeline was designed for compatibility with current clinical workflows. The current study design includes tumor inoculation (day 0), growth (\sim day 20), SiGdNP injection (\sim day 21), followed by MR imaging, tumor delineation, treatment planning and radiation delivery.

the dose distribution in tumor and healthy organs. The AAA calculation algorithm for a $5.5 \times 10 \text{ cm}^2$ field size, gantry at 180° , and surface-skin distance of 90 cm was used. Simulation was performed for the standard and flattening filter free 6 MV irradiation beams (TrueBeam-Varian, CA). The capan-1 tumor-bearing mice was then injected with 0.25 mg/g of SiGdNP *i.v.*. Fifteen minutes post-injection, radiation treatment was performed with 10 Gy. Four groups (-SiGdNP/-IR; +SiGdNP/-IR; -SiGdNP/+IR; +SiGdNP/+IR) of 5 mice each were used to characterize the effect of the SiGdNP as a radiosensitizer.

4.5. Tumor volume tracking

Tumor growth was tracked with volumetric CBCT images acquired with the SARRP. The volumes were measured using the 3D Slicer software (v. 4.3.1). The tumor was manually segmented to track its volume.

In parallel, a caliper measurement was performed on a daily basis to confirm the results of the image-based volume study.

5. Histological studies

5.1. Mice studies

Animals were irradiated 15 min after injection of the SiGdNP following the same procedure as the survival study above. The tumor was harvested 30 min after irradiation and fixed in 2% formalin followed by paraffin embedding. Thin tumor sections of $\sim 5 \mu\text{m}$ were cut and the tissue sections were counterstained for H&E staining and γH2AX staining. A similar procedure was performed to quantify the toxicity in the healthy organs using primary antibody, Abcam ab26350 and secondary antibody, ser139 (Cell signaling Technologies, USA). Images were analyzed using a Zeiss Axio microscope at $63\times$ magnification.

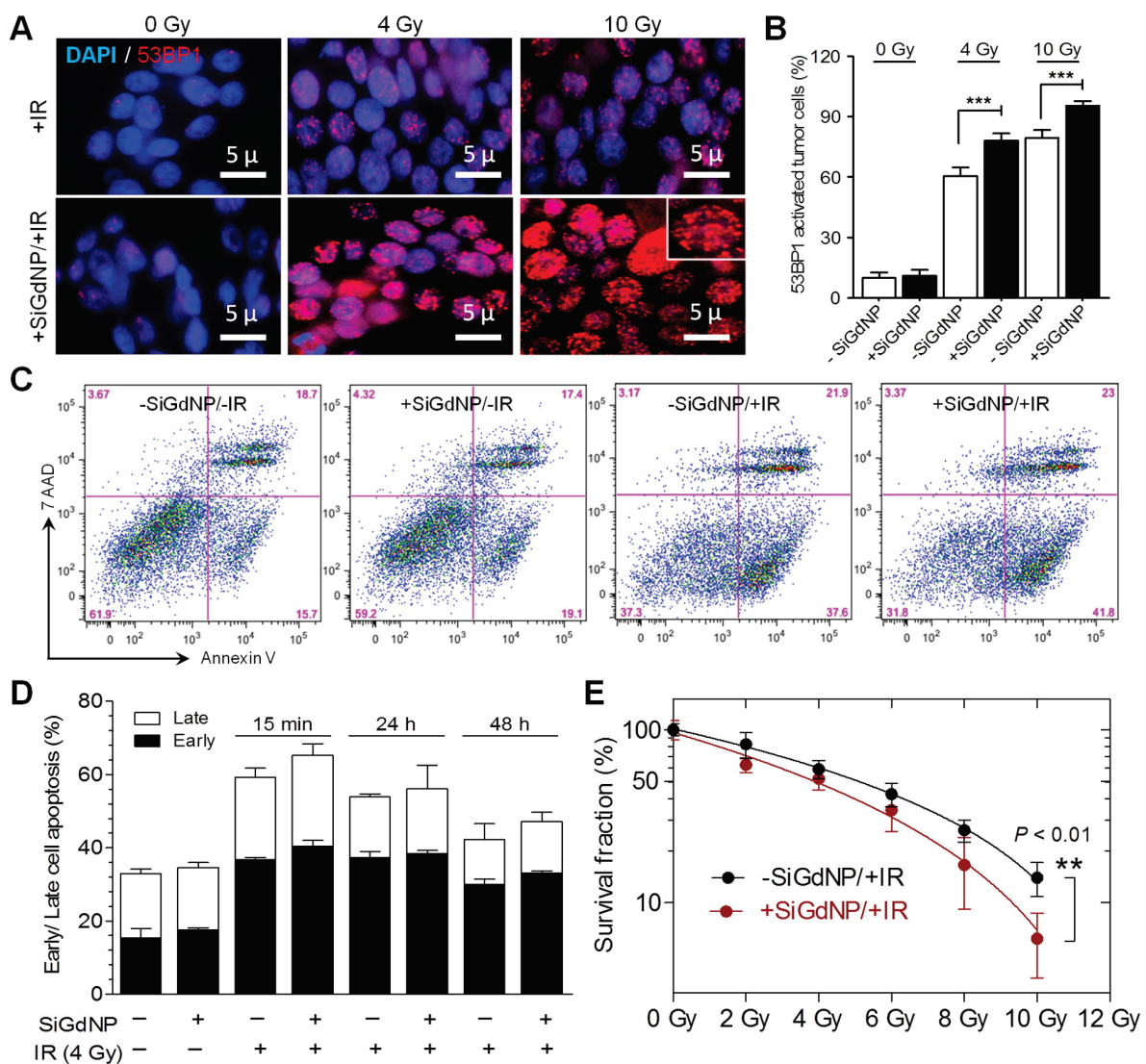


Fig. 2. *In vitro* radiation studies. (A) Qualitative and quantitative evaluation of radiation damage in pancreatic cancer cells (capan-1) treated +/- SiGdNP (0.43 mg/mL) at 0, 4 and 10 Gy (220 kVp). High 53BP1 radiation-induced foci expression is observed in the nanoparticle-treated and irradiated samples +SiGdNP/+IR compared to the respective controls. Magnification: $63\times$. (B) Measurement of 53BP1-foci activated cells clearly shows significant dose-response differences ($***P < 0.001$). (C) Radiation-induced early and late apoptosis was assessed under different set experimental conditions (at 4 Gy) using Annexin V-APC/7-AAD based FACS analysis. For the +SiGdNP/+IR samples, high early (black bar) and late (white bar) apoptosis (41.8% and 23%) was observed with respect to the controls (-SiGdNP/-IR: 15.7% and 18.7%; +SiGdNP/-IR: 19.1% and 17.4%; -SiGdNP/+IR: 37.6% and 21.9%). (D) Temporal variations in early/late apoptosis were measured. The data clearly shows high early (solid black) and late (solid white) apoptosis for +SiGdNP/+IR at all prescribed irradiation time points. (E) Clonogenic survival assay showing the effect of radiation +/- SiGdNP. The dose enhancement factor was 1.37 ($**P < 0.01$). All data represents mean \pm SD. *P*-values were calculated using two-tailed student's *t*-test.

5.2. Monkey studies

H&E staining was performed on tissue sections excised from the heart, lung, kidneys and liver to visualize the toxicity induced by the nanoparticles.

5.3. Statistical analysis

Statistics was performed with GraphPad (GraphPad Prism 5.0). The differences between the groups were evaluated by two-tailed unpaired *t*-test. Statistical tests for the *in vivo* survival studies were performed with a mantel-cox log-rank test (Kaplan-Meier).

6. Results and discussion

6.1. Gadolinium-based theranostic nanoparticles

SiGdNP was synthesized using earlier reported methods [22,28], wherein gadolinium atoms were chemically chelated with DOTA and covalently entrapped within a polysiloxane (-Si-O-Si-) network (Fig. 1a, Fig. S1a). With a hydrodynamic size of 3.5 ± 1 nm, a surface charge of 9 ± 5.5 mV and other optimal physicochemical properties (Fig. S1b–d), SiGdNP demonstrated substantial MR imaging capabilities *in vitro* (Fig. S2a–b). When administered *in vivo*, these nanoparticles permeate the (fenestrated) tumor blood vessels and are taken up by the

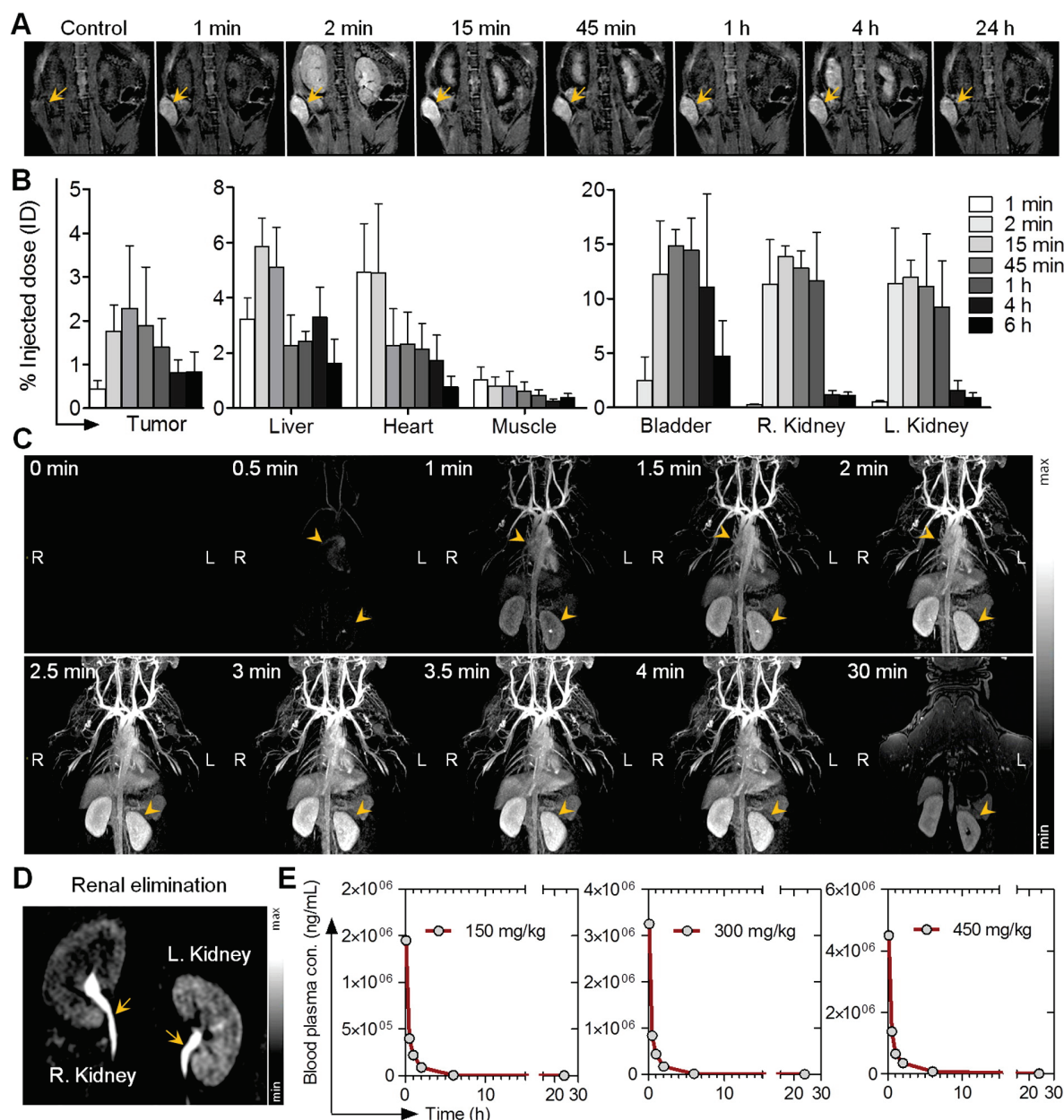


Fig. 3. Whole body MR imaging and blood plasma kinetics in mice and monkeys. (A–B) T1-weighted MR imaging (7T, Bruker BioSpec, US) of SiGdNP (0.25 mg/g) injected in mice bearing capan-1-pancreatic tumors ($n = 3$ /group) shows early tumor discrimination (at 1 min-*post-iv.*) followed by increasing accumulation. Maximum tumor accumulation of SiGdNP occurs at 15 min *post-iv.* Some accumulation in the liver (~ 6 %ID) was also observed. (C–D) Biodistribution studies were carried out in cynomolgus monkeys ($n = 3$ /group) after administration of a single bolus infusion of 100 mg/kg SiGdNP via external saphenous vein. Whole body MR imaging (T1 sequence) was carried out at different time points to visualize the early circulation and longitudinal renal clearance. The elimination of SiGdNP via the kidneys (collecting ducts) was clearly visible. (E) Blood samples were collected after administration of a single bolus injection of 150, 300 and 450 mg/kg of SiGdNP (2.5 mL/kg equiv.) to cynomolgus monkeys ($n = 24$; 12 male and 12 female) and pharmacokinetic parameters were analyzed. All data are represented as a mean \pm SD.

malignant tumor cells due to EPR effect [29,30]. Retention of nanoparticles within the tumor facilitated longitudinal (noninvasive) MR imaging and target-specific radiosensitization (Fig. 1b–c).

7. Radiosensitization potential of SiGdNP *in vitro*

The radiosensitization potential of SiGdNP (0.43 mg/mL) was tested in capan-1 pancreatic adenocarcinoma cells. The nanoparticles were endocytosed and prominently localized as clusters in the sub-cellular compartments (Fig. S2c) [9,31]. High degree of DNA damage was observed in the nanoparticle-treated cancer cells at the tested radiation doses of 4 and 10 Gy. The density of 53BP1-radiation induced foci formation is highest in the 10 Gy treated sample with >90% of the cells exhibiting specific DNA damage (Fig. 2a). Distinct quantitative and dose-dependent variations were found in the nanoparticle-treated vs. non-treated samples ($78.1 \pm 3.5\%$ vs. $60.5 \pm 4.1\%$ at 4 Gy and $95.4 \pm 2.3\%$ vs. $79.4 \pm 3.8\%$ at 10 Gy) (Fig. 2b). FACS analysis was performed to quantitatively estimate the changes in early and late apoptosis for samples with/without radiation (+/-IR) and with/without nanoparticles +/-SiGdNP. Although capan-1 pancreatic cells are known to exhibit a slightly elevated basal DNA damage threshold [32], the combined SiGdNP and radiation experimental arm +SiGdNP/+IR demonstrated high early and late apoptosis (41.8% and 23% respectively) compared to the other controls (15.7% and 18.7%) (Fig. 2c). This trend remained consistent at 24 and 48 h post-IR (Fig. 2d). The clonogenic cell survival assay confirmed significant ($P < 0.01$) decrease in cell survival when SiGdNP and radiation were combined. The calculated

radiation dose enhancement factor (DEF) for +SiGdNP/+IR samples was found to be 1.37 (Fig. 2e).

8. Noninvasive MRI-based biodistribution studies in mice and monkeys

Whole body MR imaging (VTR-T₁ sequence, 7 T, Bruker BioSpin, United States) was performed using capan-1-tumor bearing mice ($\sim 6 \times 8 \text{ mm}^2$) and the longitudinal SiGdNP accumulation was noninvasively visualized in tumor and healthy organs. As early as 1 min post-*i.v.* injection of SiGdNP (0.25 mg/g), delineated tumor margins were visible due to gadolinium based MR contrast (Fig. 3a). EPR-mediated progressive accumulation of SiGdNP in the tumor peaked at 15 min *p.i.* ($2.27 \pm 0.44 \%$ ID). The MR signal from the kidneys and bladder were also prominent at 15 min (R. kidney: $13.85 \pm 0.98 \%$ ID; L. kidney: $11.92 \pm 1.58 \%$ ID; bladder: $14.85 \pm 1.49 \%$ ID) and gradually declined thereafter, implying early clearance of ultra-small SiGdNP (Fig. 3b). Furthermore, comparably less accumulation ($5.84 \pm 1.04 \%$ ID) was observed in the liver, which steeply declined after 15 min ($2.26 \pm 1.09 \%$ ID at 45 min *p.i.*) (Fig. 3b). The minimal accumulation in peripheral organs is primarily attributed to the rapid RES uptake of SiGdNP by the circulating macrophages. However, the fate of SiGdNP after liver deposition has not been determined. Nominal late accumulation was observed in other secondary organs such as muscle and heart [26].

Biodistribution studies were carried out in cynomolgus monkeys (*macaca fascicularis*) ($n = 3$) after administration of a single *i.v.* bolus infusion of 200 mg/kg of SiGdNP (via external saphenous vein). The early systemic circulation and longitudinal renal clearance of SiGdNP was

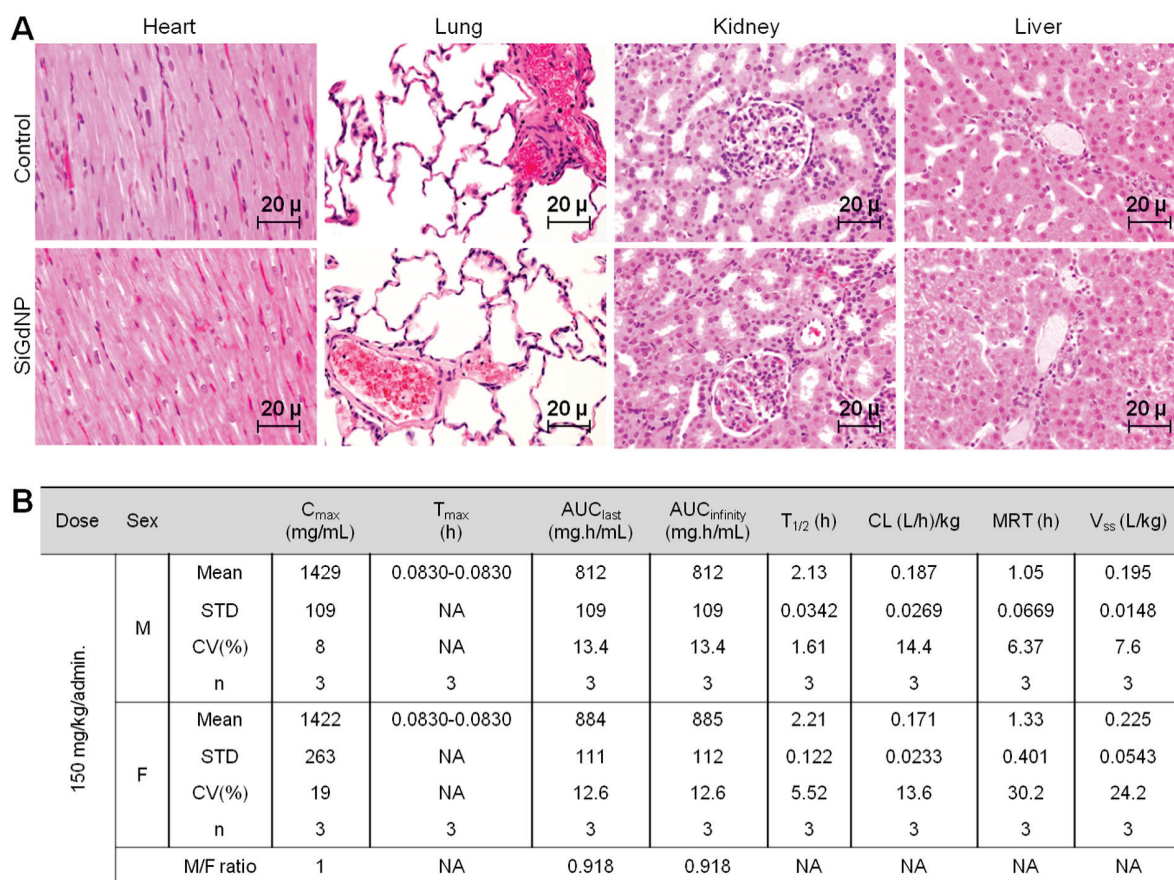


Fig. 4. Toxicity studies and pharmacokinetic profiling in monkeys. (A) H&E staining was performed on the organs excised from monkeys after administration of the highest dose of SiGdNP ($\sim 450 \text{ mg/kg}$) via external saphenous vein in both male and female monkeys. No unscheduled deaths or clinical symptoms were observed in any of the treated animals. (B) Blood plasma samples were used for pharmacokinetic and pharmacodynamic evaluations based on non-compartmental analysis (KineticTM 4.4.1, Thermo Fisher) to determine parameters such as C_{\max} (maximum peak concentration), T_{\max} (time for C_{\max}), AUC (area under the curve), $T_{1/2}$ (half-life), CL (clearance), MRT (mean residence time), V_{ss} (volume of steady state distribution).

clearly visualized by whole body MR imaging. At 30 s post-*i.v.* injection, the nanoparticle-related MR signal (T_1) was observed in peripheral vessels near the heart (Fig. 3c). The MR images illustrate the early circulation of SiGdNP over the next 2 to 4 min (Movie 1). At 30 min post-*i.v.* administration, a substantial decline in the SiGdNP signal was observed with an overall reduction in the T_1 -contrast in the kidneys (Fig. 3c). In agreement with the mice biodistribution profile, the monkey data confirmed the rapid renal clearance of SiGdNP. A magnified MR image of the posterior kidney section shows late-retention (30 min) of SiGdNP in the collecting ducts of the renal capillaries, indicating renal excretion (Fig. 3d).

In another set of experiments in cynomolgus monkeys ($n = 24$), SiGdNP was injected at three different doses: *low*, *moderate* and *high* (150, 300 and 450 mg/kg, respectively), to evaluate the dose-dependent blood plasma distribution kinetics. For all tested doses, after an initial peak in concentration, the SiGdNP signal rapidly declined from 0.5 to 6 h (Fig. 3e). By ~9 h post-administration, the total SiGdNP

concentration in the blood had fallen to negligibly low amounts indicating that long-term toxicity events are unlikely in large animals; a factor that strongly supports its clinical translation.

9. Toxicity and pharmacokinetic profiling in monkeys

SiGdNP toxicity was determined with excised organs from cynomolgus monkeys. H&E staining was performed on the tissue specimens of vital organs treated (+/–) SiGdNP. Even at the highest tested dose (450 mg/kg), no apparent histological differences or toxicities were observed in the heart, lung, kidney and liver (Fig. 4a). Pharmacokinetic evaluations were carried out based on a non-compartmental model (Kinetica™ 4.4.1, Thermo Fisher) using 3 different doses: 150, 300, and 450 mg/kg, injected *i.v.* twice in a one-week time interval (Fig. 4b, Fig. S3). Based on the absence of any *antemortem* or *postmortem* findings, the no-observed-effect level (NOEL) in the present study was determined to be 450 mg/kg/administration in both female and male

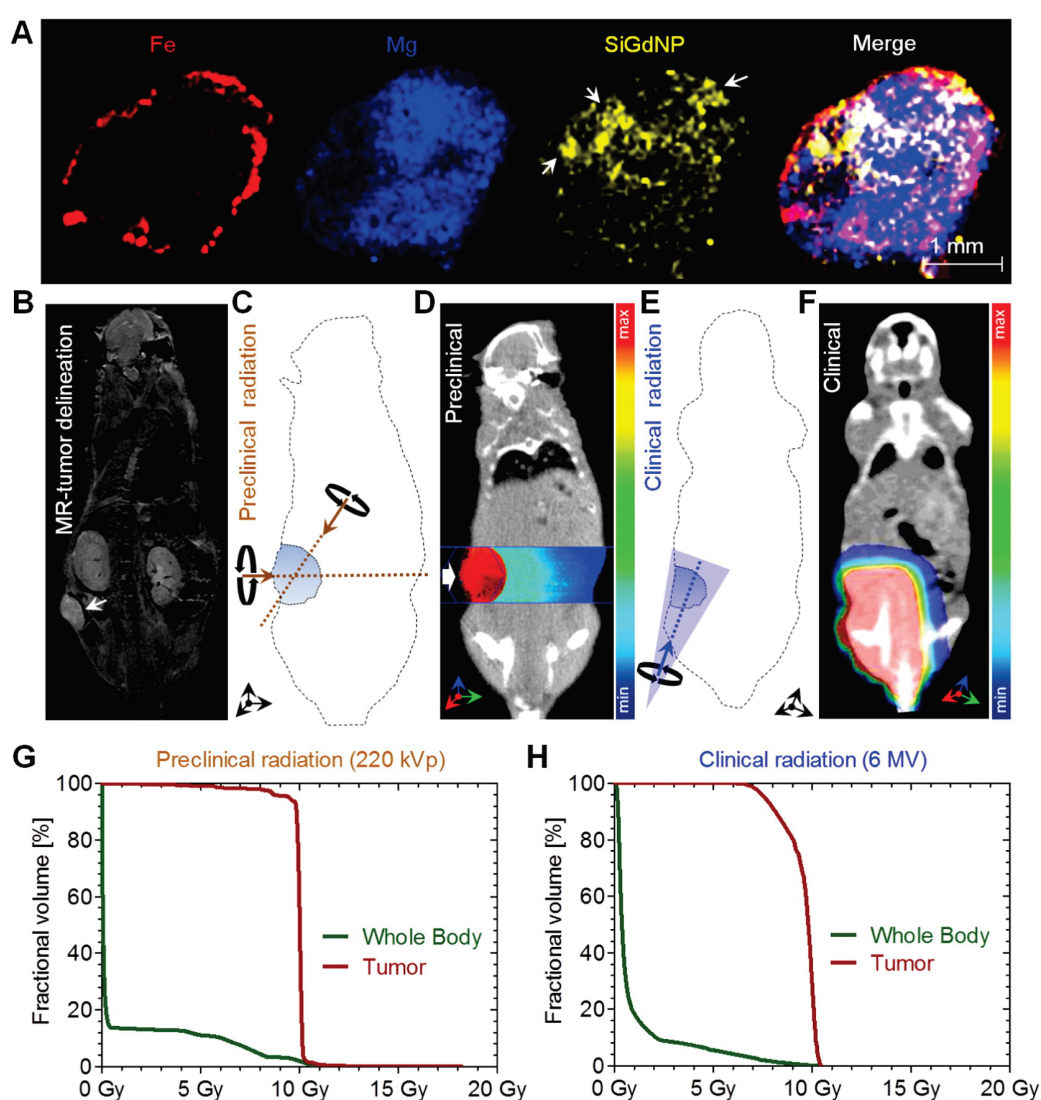


Fig. 5. Tumor localization and image-guided radiation therapy. (A) Intratumoral SiGdNP localization in capan-1 tumors at 15 min post-injection was imaged using laser-induced breakdown spectroscopy. (B) MR-guided tumor delineation (T1-VTR acquisition) was performed after injection of 0.25 mg/g SiGdNP in capan-1-tumor xenografts. (C–D) Schematic depiction of the radiation setup in which tumor xenografts were irradiated with preclinical (10 Gy, orthogonal, 220 kV) radiation beams (brown dotted lines). The radiation dose distribution in the tumor and surrounding tissues were calculated on a cone-beam CT image. (E–F) Schematic depiction of the radiation setup in which tumor xenografts were irradiated with clinical (10 Gy, unilateral, 6 MV) radiation beams (blue dotted line). For each case, care was taken to deliver homogenous radiation to the tumor while sparing the healthy tissues (as performed in the clinics). The qualitative isodose distributions show maximum radiation dose in the tumor. (G–H) The dose-volume histograms shows that more than 95% of the tumor received 95% of the prescription dose in under preclinical conditions and 90% of the tumor received 90% of the dose under clinical conditions. (For interpretation of the references to color in this figure legend, the reader is referred to the web version of this article.)

tested monkeys. At a dose of 150 mg/kg/administration, systemic exposure (*area under the curve*) of SiGdNP on day 8 was calculated to be 3419 ng·h/mL in males and 2842 ng·h/mL in females. The nanoparticles exhibit a (biological) $t_{1/2}$ of ~2.2 h and a clearance rate of 187 mL/h/kg and 171 mL/h/kg in both males and females, respectively, indicating an effective elimination process (Fig. 4b). All pharmacokinetic parameters were independent of gender variations as evident from the M/F ratio (Fig. 4b, Fig. S3). By the end of day 1, there was negligible presence of SiGdNP in the systemic circulation.

10. Tumor localization and image-guided radiation therapy

To precisely measure the microscopic distribution of SiGdNP within the tumor, laser induced breakdown spectroscopy (LIBS) imaging was performed. To this end, capan-1 tumors were excised at 15 min post-*i.v.* administration of SiGdNP (0.25 mg/g). Silicon (Si) served as surrogate markers for SiGdNP localization in the tumor due to the chemically-coupled polysiloxane construct (-Si-O-Si-) in the nanoparticle design (Fig. S1a). Heterogeneous distribution of ultra-small nanoparticles in the tumor was clearly evident from the 'Si' LIBS signal (Fig. 5a). Higher vascularity was demonstrated in the periphery of the tumor compared to the core (as inferred from the Fe signal) and SiGdNP accumulation was slightly more prominent in the periphery (Fig. 5a).

A targeted image-guided radiation therapy procedure was implemented pre-clinically based on a common clinical workflow wherein the tumor was delineated based on an MR image for treatment planning and the 3D radiation dose calculations were performed (Fig. 5b). For preclinical irradiation (220 kV), the treatment plan consisted of a pair of orthogonal beams with the isocenter at the center of the tumor (Fig. 5c). The calculated isodose levels show maximum radiation dose in the tumor while substantially sparing the surrounding healthy tissues (Fig. 5d). To perform the clinical irradiations (6 MV), the tumor was positioned in the treatment beam with the body of the mouse protected by the collimator of the clinical linear accelerator. In order to simulate clinical photon scattering conditions, 10 cm of solid water (CIRS, Inc.) was placed between the source and the mouse and the tumor was wrapped in 1 cm of tissue-equivalent bolus material, providing some backscatter.

A 3D dose calculation was performed with the clinical treatment planning system (Aria V. 11, Varian Medical Systems, Inc). The calculated isodose levels show maximum radiation dose (10 Gy) in the tumor (Fig. 5e–f). No histological damage was observed in the muscle tissue excised from the proximity of the irradiated tumor (Fig. S4). The dose-volume histograms (DVH) for each setup confirmed that more than 95% of the tumor received >95% of the prescribed dose for preclinical irradiation and >90% for the clinical irradiation (Fig. 5g–h).

11. Survival studies and radiation-induced DNA damage

To test the therapeutic radiosensitization efficacy of nanoparticles in reducing aggressive tumor growth and improving overall animal survival in combination with preclinical and clinical radiation beams, we injected intravenously ~0.25 mg/g of nanoparticles to capan-1 tumor xenograft models ($n = 8$) and performed image-guided radiation therapy at 10 Gy using both preclinical and clinical beams. The measured tumor volumes (using 3D slicer) demonstrated significant differences in the tumor burden in the treated vs. non-treated groups. The preclinical beam (220 kVp) produced a ~3-fold difference ($P < 0.002$) in the tumor size for nanoparticle with radiation compared to radiation alone (+SiGdNP/+IR compared to -SiGdNP/+IR) (Fig. 6a). The survival of non-treated cohorts +SiGdNP/-IR and -SiGdNP/-IR was ~30 days (Fig. 6b), compared to ~45 days with radiation alone and ~85 days ($P < 0.0001$, Mantel-Cox test) for nanoparticle combined radiation (+SiGdNP/+IR). With clinical irradiation (6 MV), a statistically significant reduction in tumor size was measured for nanoparticles with radiation versus radiation alone, i.e. the +SiGdNP/+IR group compared to the -SiGdNP/+IR group (2.69 ± 0.16 vs. 5.32 ± 0.19 cm³) by day 50 ($P < 0.0001$, Mantel-Cox test) (Fig. 6c). Survival was extended by more than 60 days when compared to -SiGdNP/-IR and +SiGdNP/-IR, and almost 40 days compared to the -SiGdNP/+IR (Fig. 6d). This is the first study that demonstrates the therapeutic efficacy of silica-based gadolinium nanoparticles under clinical radiation therapy conditions.

DNA double-strand breaks in tumor cells is a principal indicator of specific biological radiation response. In our initial qualitative analysis

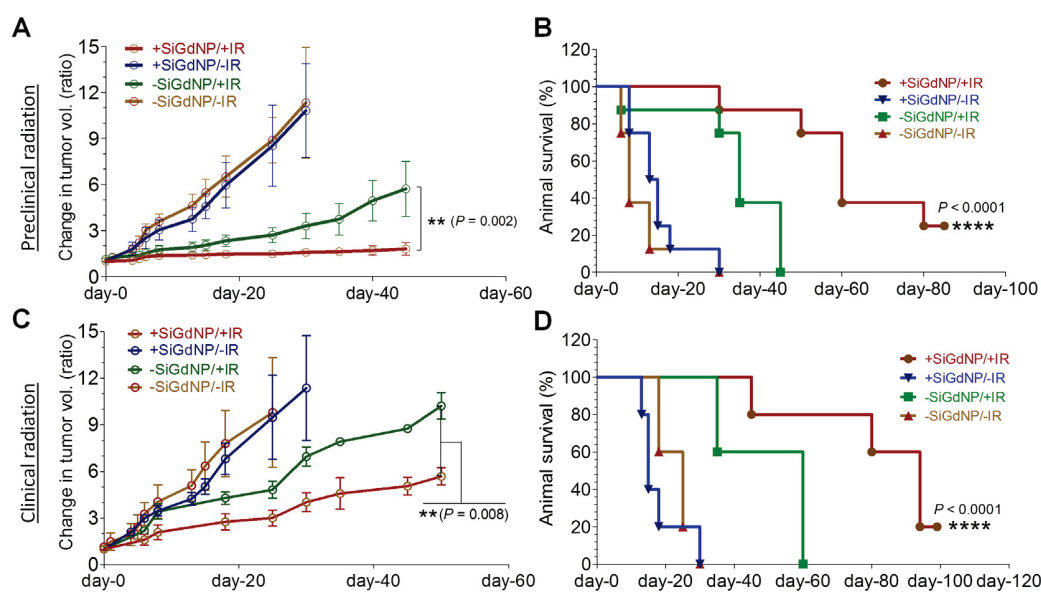


Fig. 6. Tumor survival studies and radiation damage assessment. (A) Tumor volume measurements were performed on capan-1-tumor-bearing mice ($n = 8$ /cohort) treated with and without SiGdNP and preclinical (220 kV) irradiation. (B) The Kaplan-Meier survival curves demonstrate significant survival benefit when SiGdNP is included with preclinical radiation ($n = 8$ /cohort). Statistical significance was calculated using the log-rank (Mantel-Cox) test. A tumor size of ~2.2 cm³ was considered as the terminal end-point. (C) Tumor volume measurements were performed on capan-1-tumor-bearing mice ($n = 5$ /cohort) treated with and without SiGdNP and clinical (6 MV) radiation. (D) The Kaplan-Meier survival curves demonstrate significant survival benefit when SiGdNP is included with clinical radiation ($n = 5$ /cohort). Statistical significance was calculated using the log-rank (Mantel-Cox) test.

(by γ H2AX staining), the *in vivo* treated tumors confirmed massive DNA damage for the +SiGdNP/+IR cohort compared to the -SiGdNP/+IR (Fig. 7a). No significant DNA damage was observed in healthy organs such as kidney, lung, heart and liver. Interestingly, both liver and kidney- the organs that were proximal to the irradiation site, were largely unaffected by the tumor-targeted irradiation and local dose enhancement. Further analysis of the tumor tissue demonstrated more than 80% DNA damage in the nanoparticle plus radiation

treated cohort +SiGdNP/+IR. The magnitude of damage was ~60% for the radiation only group -SiGdNP/+IR and <10% for other controls -SiGdNP/-IR and +SiGdNP/-IR (Fig. 7b). These results clearly validate and confirm the dual-targeting concept wherein both targeted-radiation therapy and EPR-driven tumor accumulation of high atomic number nanoparticles combine to amplify the radiation response specifically in cancer cells while largely sparing surrounding healthy tissues.

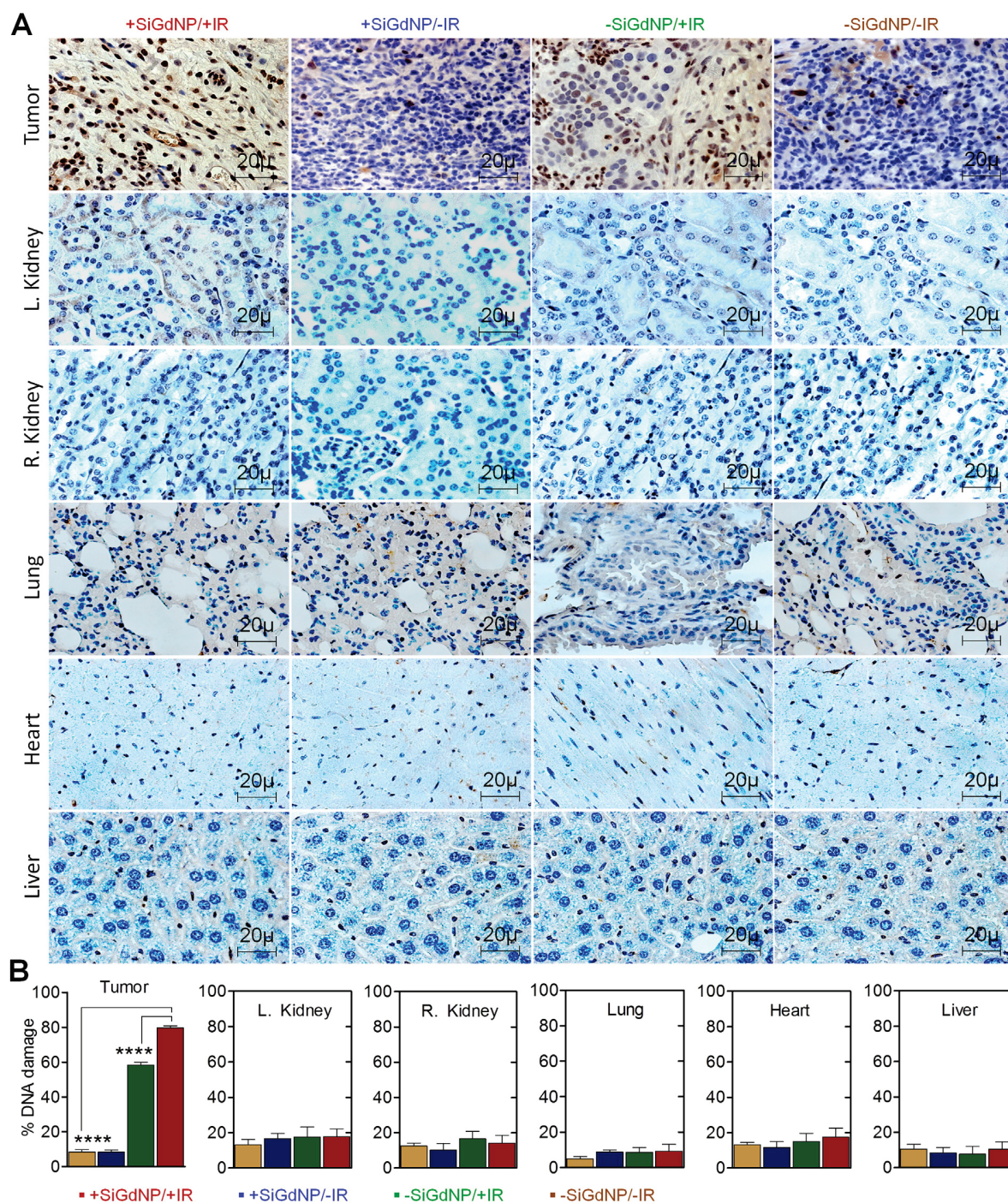


Fig. 7. Preclinical radiation-induced DNA damage studies. (a) Radiation-induced DNA double strand breaks in the tumor and other vital organs are shown with γ H2AX staining. The damaged tumor cell nuclei are stained in 'brown' (γ H2AX+) and the viable cells in 'blue' (γ H2AX-). Magnification: 100 \times . (b) γ H2AX+ nuclei were counted across multiple image planes ($n = 50$) and further quantified. The values represent average \pm SD. (For interpretation of the references to color in this figure legend, the reader is referred to the web version of this article.)

Nanotechnology has great potential in cancer drug delivery, imaging and radiation therapy [33,34]. The ability to design and modulate multifunctional nanoparticles has paved the way for hybrid strategies to image and treat cancer [35–37]. In this regard, high atomic number ferromagnetic and paramagnetic nanoparticles can facilitate noninvasive imaging and concurrent radiation dose amplification for more accurate and effective treatment of cancer. With clinical radiation therapy practices incorporating more and more MR imaging, the clinical rationale for SiGdNP is only increasing.

While gadolinium-based nanoparticles have been used for image-guided drug delivery applications in previously reported *in vivo* studies [9,38,39], the current study focuses on using them as both radiation dose amplification and imaging agents. This is the first study demonstrating the safe and therapeutically beneficial administration of SiGdNP for image-guided radiation therapy using clinical 6 MV radiation beams. This is a major advancement in this field and provides a strong rationale for clinical translation. To this end, we have been careful to design and demonstrate a procedure that is highly compatible with current and emerging clinical workflows.

The combination of imaging contrast and radiosensitization without increased toxicity in healthy organs makes SiGdNP formulation an excellent candidate for future clinical translation in radiation therapy [6]. Long-term elimination from the tissues, degradation kinetics, and toxicity of SiGdNP has been previously tested using PET and MR imaging [40–42]. Regulatory toxicity studies in non-human primates showed that the rapid renal clearance of SiGdNP perfectly fits with the physiological glomerular filtration rate in nonhuman primates [43]. At the highest dose tested in these species (450 mg/kg), toxicity studies demonstrated adequate tolerance of intravenous administration of SiGdNP, predicting a human equivalent dose (HED) of ~145 mg/kg [44]. One of the remaining questions is the underlying mechanism of gadolinium-based radiosensitization. While physical interactions between photons and high atomic materials can partly explain the biological effects, theoretical accounts have struggled to model this effect accurately. It may be that a series of physiological mechanisms such as the induction of free radicals, e.g. generation of OH^\cdot , H_2O_2 , and O_2^\cdot , can lead to an increase in indirect tumor cell killing. The detailed mechanism of high atomic number radiosensitization still remains to be investigated.

12. Conclusion

The experimental data in mice and nonhuman primates shown in this study clearly substantiates and justifies the clinical translational potential of SiGdNP. Intravenous administration of nanoparticles fits current clinical workflows for radiation therapy based on pre-treatment MR imaging as well as the emerging practice of real-time MR guidance on combined MR-linac devices. In either scenario, SiGdNP will serve as a valuable clinical nanomedicine for safe and effective imaging and therapy of cancer.

Supplementary data to this article can be found online at <http://dx.doi.org/10.1016/j.jconrel.2016.07.021>.

Competing financial interests

O. T. has one patent (WO2011135101) protecting the gadolinium nanoparticle (AGuIX®) design. The authors have no other relevant affiliations or financial interests with any organization or entity with a financial interest in or financial conflict with the subject matter or materials discussed in the manuscript apart from those disclosed.

Acknowledgments

We acknowledge the efforts by F. Rossetti and F. Lux for the synthesis of gadolinium-based nanoparticles and S. Peled and E. Canet-Soulas for their help with MR acquisitions. This project was supported, in part, by the JCRT Foundation and the Nano-H, France.

References

- [1] R.L. Siegel, K.D. Miller, A. Jemal, Cancer statistics, *CA Cancer J. Clin.* 65 (2015) 5–29.
- [2] J. Schuemann, R. Berbeco, D.B. Chithrani, S.H. Cho, R. Kumar, S.J. McMahon, S. Sridhar, S. Krishnan, Roadmap to Clinical Use of Gold Nanoparticles for Radiation Sensitization, *Int. J. Radiat. Oncol. Biol. Phys.* 94 (2016) 189–205.
- [3] A.S. Reese, W. Lu, W.F. Regine, Utilization of intensity-modulated radiation therapy and image-guided radiation therapy in pancreatic cancer: is it beneficial? *Semin. Radiat. Oncol.* 24 (2014) 132–139.
- [4] N. Trakul, A.C. Koong, P.G. Maxim, D.T. Chang, Modern radiation therapy techniques for pancreatic cancer, *Gastroenterol. Clin. North Am.* 41 (2012) 223–235.
- [5] L.A. Dawson, D.A. Jaffray, Advances in image-guided radiation therapy, *J. Clin. Oncol.* 25 (2007) 938–946.
- [6] E.J. Moding, M.B. Kastan, D.G. Kirsch, Strategies for optimizing the response of cancer and normal tissues to radiation, *Nat. Rev. Drug. Discov.* 12 (2013) 526–542.
- [7] P. Retif, S. Pinel, M. Toussaint, C. Frochet, R. Chouikrat, T. Bastogne, M. Barberi-Heyob, Nanoparticles for radiation therapy enhancement: the key parameters, *Theranostics* 5 (2015) 1030–1044.
- [8] A.B. Satterlee, H. Yuan, L. Huang, A radio-theranostic nanoparticle with high specific drug loading for cancer therapy and imaging, *J. Control Release* 217 (2015) 170–182.
- [9] A. Detappe, S. Kunjachan, J. Rottmann, J. Robar, P. Tsiamas, H. Korideck, O. Tillement, R. Berbeco, AGuIX nanoparticles as a promising platform for image-guided radiation therapy, *Cancer Nanotechnol* 6 (2015) 4.
- [10] M. Luchette, H. Korideck, M. Makrigiorgos, O. Tillement, R. Berbeco, Radiation dose enhancement of gadolinium-based AGuIX nanoparticles on HeLa cells, *Nanomedicine* 10 (2014) 1751–1755.
- [11] E. Lechtman, N. Chattopadhyay, Z. Cai, S. Mashouf, R. Reilly, J.P. Pignol, Implications on clinical scenario of gold nanoparticle radiosensitization in regards to photon energy, nanoparticle size, concentration and location, *Phys. Med. Biol.* 56 (2011) 4631–4647.
- [12] S.H. Cho, Estimation of tumour dose enhancement due to gold nanoparticles during typical radiation treatments: a preliminary Monte Carlo study, *Phys. Med. Biol.* 50 (2005) N163–N173.
- [13] M.W. Dewhirst, Y. Cao, B. Moeller, Cycling hypoxia and free radicals regulate angiogenesis and radiotherapy response, *Nat. Rev. Cancer* 8 (2008) 425–437.
- [14] S. Kunjachan, A. Detappe, R. Kumar, T. Ireland, L. Cameron, D.E. Biancur, V. Motto-Ros, L. Sancey, S. Sridhar, G.M. Makrigiorgos, R.I. Berbeco, Nanoparticle mediated tumor vascular disruption: a novel strategy in radiation therapy, *Nano. Lett.* 15 (2015) 7488–7496.
- [15] J. Marill, N.M. Anesary, P. Zhang, S. Vivet, E. Borghi, L. Levy, A. Pottier, Hafnium oxide nanoparticles: toward an *in vitro* predictive biological effect? *Radiat. Oncol.* 9 (2014) 150.
- [16] S.H. Kurtzman, A. Russo, J.B. Mitchell, W. DeGraff, W.F. Sindelar, M.W. Brechbiel, O.A. Gansow, A.M. Friedman, J.J. Hines, J. Gamson, et al., 212Bismuth linked to an antipancratic carcinoma antibody: model for alpha-particle-emitter radioimmunotherapy, *J. Natl. Cancer Inst.* 80 (1988) 449–452.
- [17] M. Ma, Y. Huang, H. Chen, X. Jia, S. Wang, Z. Wang, J. Shi, Bi2S3-embedded mesoporous silica nanoparticles for efficient drug delivery and interstitial radiotherapy sensitization, *Biomaterials* 37 (2015) 447–455.
- [18] I.J. Chetty, M.K. Martel, D.A. Jaffray, S.H. Benedict, S.M. Hahn, R. Berbeco, J. Deye, R. Jeraj, B. Kavanagh, S. Krishnan, N. Lee, D.A. Low, D. Mankoff, L.B. Marks, D. Ollendorf, H. Paganetti, B. Ross, R.A. Siochi, R.D. Timmerman, J.W. Wong, Technology for Innovation in Radiation Oncology, *Int. J. Radiat. Oncol. Biol. Phys.* 93 (2015) 485–492.
- [19] S. Kunjachan, J. Ehling, G. Storm, F. Kiessling, T. Lammers, Noninvasive imaging of nanomedicines and nanotheranostics: principles, progress, and prospects, *Chem. Rev.* (2015).
- [20] M. Riboldi, R. Orecchia, G. Baroni, Real-time tumour tracking in particle therapy: technological developments and future perspectives, *Lancet. Oncol.* 13 (2012) e383–e391.
- [21] E.K. Chow, D. Ho, Cancer nanomedicine: from drug delivery to imaging, *Sci. Transl. Med.* 5 (2013) (216rv214).
- [22] A. Mignot, C. Truillet, F. Lux, L. Sancey, C. Louis, F. Denat, F. Boschetti, L. Bocher, A. Gloter, O. Stephan, R. Antoine, P. Dugourd, D. Luneau, G. Novitchi, L.C. Figueiredo, P.C. de Moraes, L. Bonneviot, B. Albel, F. Ribot, L. Van Lokeren, I. Dechamps-Olivier, F. Chuburu, G. Lemerrier, C. Villiers, P.N. Marche, G. Le Duc, S. Roux, O. Tillement, P. Perriat, A top-down synthesis route to ultrasmall multifunctional Gd-based silica nanoparticles for theranostic applications, *Chemistry* 19 (2013) 6122–6136.
- [23] C.U. Herborn, E. Honold, M. Wolf, J. Kemper, S. Kinner, G. Adam, J. Barkhausen, Clinical safety and diagnostic value of the gadolinium chelate gadoterate meglumine (Gd-DOTA), *Invest. Radiol.* 42 (2007) 58–62.
- [24] Y. Matsumura, H. Maeda, A new concept for macromolecular therapeutics in cancer chemotherapy: mechanism of tumorotropic accumulation of proteins and the anti-tumor agent smancs, *Cancer Res.* 46 (1986) 6387–6392.
- [25] U. Prabhakar, H. Maeda, R.K. Jain, E.M. Sevick-Muraca, W. Zamboni, O.C. Farokhzad, S.T. Barry, A. Gabizon, P. Grodzinski, D.C. Blakey, Challenges and key considerations of the enhanced permeability and retention effect for nanomedicine drug delivery in oncology, *Cancer Res.* 73 (2013) 2412–2417.
- [26] L. Sancey, S. Kotb, C. Truillet, F. Appaix, A. Marais, E. Thomas, B. van der Sanden, J.P. Klein, B. Laurent, M. Cottier, R. Antoine, P. Dugourd, G. Panczer, F. Lux, P. Perriat, V. Motto-Ros, O. Tillement, Long-term *in vivo* clearance of gadolinium-based AGuIX nanoparticles and their biocompatibility after systemic injection, *ACS Nano* 9 (2015) 2477–2488.
- [27] G. Le Duc, S. Roux, A. Paruta-Tuarez, S. Dufort, E. Brauer, A. Marais, C. Truillet, L. Sancey, P. Perriat, F. Lux, O. Tillement, Advantages of gadolinium based ultrasmall

- nanoparticles vs molecular gadolinium chelates for radiotherapy guided by MRI for glioma treatment, *Cancer Nanotechnol.* 5 (2014) 4.
- [28] F. Lux, A. Mignot, P. Mowat, C. Louis, S. Dufort, C. Bernhard, F. Denat, F. Boschetti, C. Brunet, R. Antoine, P. Dugourd, S. Laurent, L. Vander Elst, R. Muller, L. Sancey, V. Josserand, J.L. Coll, V. Stupar, E. Barbier, C. Remy, A. Broisat, C. Ghezzi, G. Le Duc, S. Roux, P. Perriat, O. Tillement, Ultrasmall rigid particles as multimodal probes for medical applications, *Angew. Chem. Int. Ed. Engl.* 50 (2011) 12299–12303.
- [29] H. Maeda, Y. Matsumura, EPR effect based drug design and clinical outlook for enhanced cancer chemotherapy, *Adv. Drug Deliv. Rev.* 63 (2011) 129–130.
- [30] S. Kunjachan, R. Pola, F. Gremse, B. Theek, J. Ehling, D. Moeckel, B. Hermanns-Sachweh, M. Pechar, K. Ulbrich, W.E. Hennink, G. Storm, W. Lederle, F. Kiessling, T. Lammers, Passive versus active tumor targeting using RGD- and NGR-modified polymeric nanomedicines, *Nano Lett.* 14 (2014) 972–981.
- [31] W. Rima, L. Sancey, M.T. Aloy, E. Armandy, G.B. Alcantara, T. Epicier, A. Malchere, L. Joly-Pottuz, P. Mowat, F. Lux, O. Tillement, B. Burdin, A. Rivoire, C. Boule, I. Anselme-Bertrand, J. Pourchez, M. Cottier, S. Roux, C. Rodriguez-Lafresse, P. Perriat, Internalization pathways into cancer cells of gadolinium-based radiosensitizing nanoparticles, *Biomaterials* 34 (2013) 181–195.
- [32] Y.H. Li, X. Wang, Y. Pan, D.H. Lee, D. Chowdhury, A.C. Kimmelman, Inhibition of non-homologous end joining repair impairs pancreatic cancer growth and enhances radiation response, *PLoS One* 7 (2012), e39588.
- [33] R. Langer, Where a pill won't reach, *Sci. Am.* 288 (2003) 50–57.
- [34] M.J. Mitchell, C.S. Chen, V. Ponmudi, A.D. Hughes, M.R. King, E-selectin liposomal and nanotube-targeted delivery of doxorubicin to circulating tumor cells, *J. Control. Release* 160 (2012) 609–617.
- [35] A.S. Thakor, S.S. Gambhir, Nanoncology: the future of cancer diagnosis and therapy, *CA Cancer J. Clin.* 63 (2013) 395–418.
- [36] R. Langer, R. Weissleder, Nanotechnology, *JAMA* 313 (2015) 135–136.
- [37] Y. Zhao, D.Y. Alakhova, J.O. Kim, T.K. Bronich, A.V. Kabanov, A simple way to enhance Doxil(R) therapy: drug release from liposomes at the tumor site by amphiphilic block copolymer, *J. Control. Release* 168 (2013) 61–69.
- [38] F. Lux, L. Sancey, A. Bianchi, Y. Cremillieux, S. Roux, O. Tillement, Gadolinium-based nanoparticles for theranostic MRI-radiosensitization, *Nanomedicine (Lond.)* 10 (2015) 1801–1815.
- [39] C. Alric, J. Taleb, G. Le Duc, C. Mandon, C. Billotey, A. Le Meur-Herland, T. Brochard, F. Vocanson, M. Janier, P. Perriat, S. Roux, O. Tillement, Gadolinium chelate coated gold nanoparticles as contrast agents for both X-ray computed tomography and magnetic resonance imaging, *J. Am. Chem. Soc.* 130 (2008) 5908–5915.
- [40] C. Truillet, P. Bouziotis, C. Tsoukalas, J. Brugiere, M. Martini, L. Sancey, T. Brichart, F. Denat, F. Boschetti, U. Darbost, I. Bonnamour, D. Stellas, C.D. Anagnostopoulos, V. Koutoulidis, L.A. Mouloupoulos, P. Perriat, F. Lux, O. Tillement, Ultrasmall particles for Gd-MRI and (68) Ga-PET dual imaging, *Contrast Media Mol. Imaging* 10 (2015) 309–319.
- [41] L. Sancey, S. Kotb, C. Truillet, F. Appaix, A. Marais, E. Thomas, B. van der Sanden, J.P. Klein, B. Laurent, M. Cottier, R. Antoine, P. Dugourd, G. Panczer, F. Lux, P. Perriat, V. Motto-Ros, O. Tillement, Long-term in vivo clearance of gadolinium-based AGuX nanoparticles and their biocompatibility after systemic injection, *ACS Nano* 9 (2015) 2477–2488.
- [42] C. Truillet, F. Lux, O. Tillement, P. Dugourd, R. Antoine, Coupling of HPLC with electrospray ionization mass spectrometry for studying the aging of ultrasmall multifunctional gadolinium-based silica nanoparticles, *Anal. Chem.* 85 (2013) 10440–10447.
- [43] R. Iwama, T. Sato, K. Sakurai, K. Takasuna, T. Ichijo, K. Furuhashi, H. Satoh, Estimation of glomerular filtration rate in cynomolgus monkeys (*Macaca fascicularis*), *J. Vet. Med. Sci.* 76 (2014) 1423–1426.
- [44] S. Reagan-Shaw, M. Nihal, N. Ahmad, Dose translation from animal to human studies revisited, *FASEB J.* 22 (2008) 659–661.

SCIENTIFIC REPORTS

OPEN

Key clinical beam parameters for nanoparticle-mediated radiation dose amplification

Received: 06 June 2016
Accepted: 07 September 2016
Published: xx xx xxxx

Alexandre Detappe^{1,2}, Sijumon Kunjachan¹, Pascal Drané¹, Shady Kotb^{1,2}, Marios Myronakis¹, Douglas E. Biancur¹, Thomas Ireland³, Matthew Wagar¹, Francois Lux², Olivier Tillement² & Ross Berbeco¹

As nanoparticle solutions move towards human clinical trials in radiation therapy, the influence of key clinical parameters on therapeutic efficacy must be considered. In this study, we have investigated the clinical radiation therapy delivery variables that may significantly affect nanoparticle-mediated radiation dose amplification. We found a benefit for situations which increased the proportion of low energy photons in the incident beam. Most notably, “unflattened” photon beams from a clinical linear accelerator results in improved outcomes relative to conventional “flat” beams. This is measured by significant DNA damage, tumor growth suppression, and overall improvement in survival in a pancreatic tumor model. These results, obtained in a clinical setting, clearly demonstrate the influence and importance of radiation therapy parameters that will impact clinical radiation dose amplification with nanoparticles.

Nanoparticles composed of high atomic number materials can amplify the effects of radiation therapy while maintaining current clinical radiation dose constraints on healthy organs^{1,2}. Radiation dose amplification from metallic nanoparticles occurs when incident photon beams produce short range secondary electrons via the photoelectric effect^{3–5}. The cross-section for photoelectric interactions is proportional to Z^4-Z^5 , where Z is the atomic number of the metallic atom. Subsequent generation of Auger electrons and reactive oxygen species (ROS) can also enhance the radiation effects^{6–9}. The concept of nanoparticle-mediated radiation dose amplification has been demonstrated in preclinical models for several nanoparticle formulations^{10–13} mainly in low energy (keV) pre-clinical photon beams^{10,11,14–18}. However, the translational significance of these studies are limited as low energy photons have poor tissue penetration and are seldom used clinically¹⁹. The current study is focused on the evaluation of clinical radiation beam parameters for dose amplification. We evaluated the impact of treatment field size, distance from the central beam axis, tumor depth in tissue, and “flattening filter free” (FFF) delivery on nanoparticle-mediated radiation dose amplification.

Most often, high energy photon beams (≥ 6 MV) generated by a medical linear accelerator are used to treat cancer due to the increased skin sparing properties. However, these high energy beams are actually composed of a spectrum of photon energies, including a substantial component of low energy photons (< 150 kV)^{20,21}. In addition, scatter within the medium/tissue contributes to an increasing proportion of low energy photons as a function of depth. Preliminary investigations of nanoparticle radiation dose amplification in clinical photon beams have been performed^{22–26}. We present the first investigation of key clinical parameters that must be considered prior to clinical translation.

In modern radiation therapy, medical linear accelerators generate high energy electron beams which are directed to a Cu/W target to produce photons for therapy. This photon beam is shaped by several different methods depending on the clinical application. Collimator jaws and/or smaller multi-leaf collimators (MLC) give the radiation beam a size and shape conforming to the shape of the therapy target (e.g. tumor). A flattening filter is often used to create a homogeneous radiation dose across the treatment field within the patient. This filter also removes many low energy photons and effectively reduces the overall dose-rate^{27,28}. The medical linear accelerators are mounted on a rotating gantry and patients are placed on robotic treatment “couches” enabling

¹Department of Radiation Oncology, Dana-Farber Cancer Institute, Brigham and Women’s Hospital, Harvard Medical School, Boston, US. ²Lyon-1 University, Institut Lumière Matière, CNRS UMR5306, Lyon, France. ³LA-ICP-MS and ICP-ES Laboratories, Boston University, Boston, MA 02215, US. Correspondence and requests for materials should be addressed to R.B. (email: RBerbeco@LROC.Harvard.edu)

radiation delivery from multiple angles to avoid healthy organs-at-risk. Depending on the angle of radiation delivery, some amount of healthy tissue must be traversed by the photon beam before reaching the radiotherapy target. Three-dimensional radiation dose calculations are performed using analytic algorithms or Monte Carlo methods for clinical treatment planning purposes. During the planning process, several treatment parameters can be optimized in order to maximize the dose to the tumor while minimizing dose to healthy tissue. For this experimental study, we have used a pancreatic adenocarcinoma model. Pancreatic cancers have a low survival rate²⁰ and are difficult to treat effectively with radiation due to their anatomical location, as well as inter-fractional and intra-fractional position uncertainties. Recent clinical evidence also suggests that pancreatic tumors may respond to radiation dose escalation²¹. The need for increased efficacy of radiation therapy combined with more precise tumor localization suggests the implementation of a novel agent which can facilitate both radiation dose amplification and increased image contrast, simultaneously. The nanoparticle tested in this study exhibits high MRI contrast²⁹, low toxicity³⁰, and high radiation dose amplification^{15,17,31}. AGuIX (Active Guidance for Irradiation by X-rays) are ultrasmall (<5 nm) polysiloxane based nanoparticles with chelates of gadolinium entrapped in a DOTA structure^{15,17,29–32}. AGuIX is currently approved for a Phase I clinical trial for magnetic resonance-guided radiation therapy^{15,19,30,31,33,34}.

Results

Clinical radiation delivery parameters affect *in vitro* radiation dose amplification. The influence of clinical radiation delivery parameters was tested *in vitro* with capan-1 pancreatic adenocarcinoma cells incubated with 0.43 mg/L of silica-based gadolinium nanoparticles (GdNP) before irradiation with a clinical 6 MV photon beam (TrueBeam, Varian Medical Systems, Inc.) (Supplementary Fig. 1). Measurements were made at three depths (5 cm, 10 cm and 15 cm) in solid water (CIRS, Inc) (Fig. 1A). The Monte Carlo-based photon energy spectra (Fig. 1B) shows the increase in the proportion of low energy photons as a function of depth in tissue. We observed a significant increase in sensitivity enhancement ratio at 4 Gy (SER_{4Gy}) ranging from 1.01 at 5 cm to 1.48 at 15 cm depth ($p < 0.05$) (Fig. 1C). Similarly, enlarging the field size also increases the proportion of low energy photons due to increased scatter within the solid water, leading to greater SER ($SER_{4Gy} = 1.01$ with $5 \times 5 \text{ cm}^2$ to 1.82 with a $25 \times 25 \text{ cm}^2$ field size, $p < 0.05$) (Fig. 1D–F). Moving the point of measurement laterally from the central axis (CAX) to the edge of the treatment field decreases the proportion of low energy photons leading to lower effect farther from the CAX. We found $SER_{4Gy} = 1.82$ at the CAX and 1.32 at 10 cm lateral distance from the axis ($p < 0.05$) (Fig. 1G–I). These results support our hypothesis that clinical conditions that create softer radiation beams (more low energy photons) will improve the dose amplification properties of high Z nanoparticles.

***In vitro* evaluation of flattening filter free radiation delivery.** Removal of the flattening filter results in higher dose-rate radiation beams with a larger intensity closer to the central axis and more low energy photons overall (Fig. 2A). In Monte Carlo simulations, the 6 MV-FFF beam has 2.6 times as many low energy photons (<100 keV) as the 6 MV beam. (Fig. 2B). Without nanoparticles present, the clonogenic cell survival was not significantly different for the 6 MV-FFF beam compared to the 6 MV beam (Supplementary Fig. S2). After incubation with GdNP, clonogenic cell survival was significantly decreased with the 6 MV-FFF beam compared to the 6 MV beam ($P = 0.029$) (Fig. 2C). The dose enhancement factor (DEF) obtained with the 6 MV-FFF beam ($DEF = 1.36$) is similar to the one measured with a preclinical radiation beam (220 kV) ($DEF = 1.37$)¹⁹ and is substantially higher than with the 6 MV radiation beam ($DEF = 1.22$). When combined with GdNP (0.43 mg/L), the 6 MV-FFF beam led to greater ROS generation than 6 MV ($P < 0.05$). The ROS signal is linear with the radiation dose ($R^2 = 0.97$) and the difference between the 6 MV and 6 MV-FFF beams is more significant at higher nanoparticle doses (Fig. 2D). An increase in DNA double strand breaks is observed as suggested by the increase of 53BP1 foci formation induced post-irradiation (Fig. 2E). More than 70% of the cells exhibited 53BP1 foci for the +GdNP/6 MV-FFF group compared to 58% for +GdNP/6 MV ($P = 0.0041$) (Fig. 2F). Note that the observed density of 53BP1 foci in the control groups are due to the basal DNA-damage of capan-1 cells (approx. 7%)³⁵.

Gadolinium-based nanoparticles biodistribution. *In vivo* experiments were carried out using capan-1 tumor-bearing mice. The time point for highest tumor uptake was determined by whole body-MR imaging (T1 map, 7T, Bruker BioSpin, United States) and inductively coupled plasma mass spectrometry (ICP-MS) after systemic injection of 0.25 mg/g of GdNP (Fig. 3A). The nanoparticles were quickly cleared by the kidneys and bladder with a maximum peak in each organ 15 min post injection (15%ID and 18%ID, respectively). After 24 hrs, the GdNP accumulation in the kidneys and bladder were 4%ID and 6%ID, respectively. Due to the lack of lymphatic drainage and the leakiness of the tumor model, a peak in nanoparticle uptake is observed in the MRI data 15 minutes post-injection (~2.3%ID). The ICP-MS measurement confirmed this measurement (2.6%ID) (Fig. 3B).

***In vivo* therapy studies.** 6 MV and 6 MV-FFF clinical radiation beams were delivered to capan-1 subcutaneous tumor-bearing mice (Fig. 4A). The tumor growth and survival studies demonstrated a statistically significant benefit for both 6 MV and 6 MV-FFF with GdNP. An approximately 1.5-fold difference in the tumor size by day 50 between +GdNP/6 MV-FFF and +GdNP/6 MV groups ($P = 0.0411$) was observed and the median lifetime extended by 16 days (+18%) ($P < 0.0001$) (Fig. 4B). Histopathological evaluation by γ H2AX staining revealed a significant increase in DNA damage for treatment groups that included radiation and GdNP, consistent with the tumor growth and survival results. The rate of DNA damage for 6 MV-FFF/GdNP, 6 MV/GdNP and 6 MV (no GdNP) was $78 \pm 4\%$, $36 \pm 6\%$ and $13 \pm 3\%$, respectively (Fig. 4C,D). For the ipsilateral kidney, a significant increase in DNA damage is observed ($P = 0.0019$) compared to the non-irradiated groups, indicating a need to ensure kidney sparing is prioritized during the treatment planning process. However, the kidney damage was not significantly greater with nanoparticles present. No other toxicities were observed in any of the other healthy organs studied.

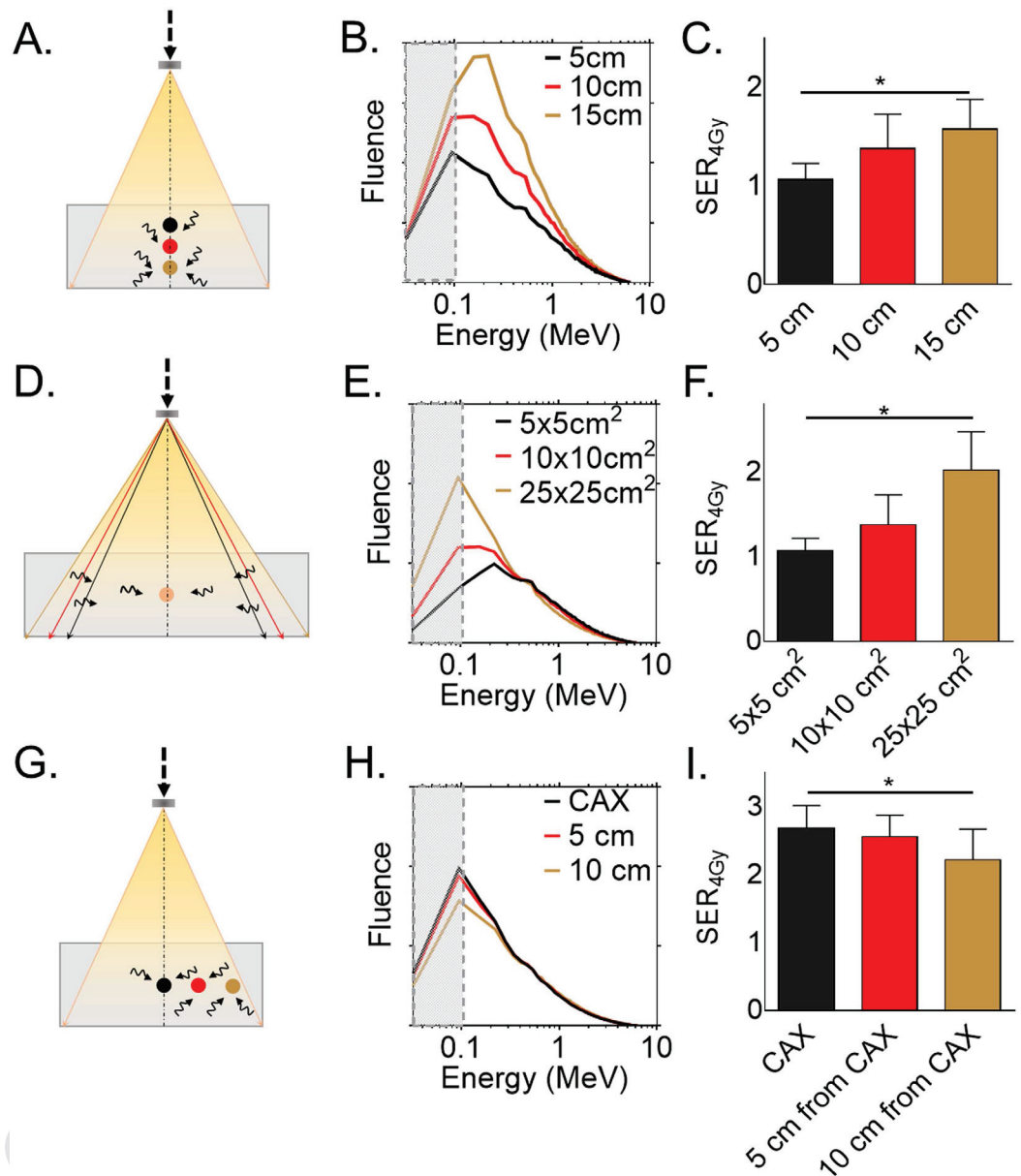


Figure 1. Key clinical beam parameters for nanoparticle-mediated radiation dose amplification. (A) Schematic representation of the irradiation (IR) setup for the depth dependence study. The dark arrows represent the expected low energy photons generated by scatter. (B) Monte-Carlo simulation of the depth conditions indicate an increasing proportion of low energy photons for greater depths. The grey shaded area shows the range from 10 keV to 100 keV which will interact most strongly with the gadolinium nanoparticles. (C) Sensitivity enhancement ratio at 4 Gy (SER_{4Gy}) calculated as the ratio of cell survival with IR alone and IR + GdNP. Increased efficacy is shown as a function of depth. Similar experiments were performed by (D–F) modifying the field size or (G–I) the distance from the central axis (CAX) of the radiation beam. Data are represented as a mean \pm SD. Statistical tests were performed using Kruskal Wallis test, * $P < 0.05$.

Discussion

A complete theory of the mechanism responsible for the observed biological effect of nanoparticle-mediated radiation dose amplification is not yet known. The results of this study demonstrate a dependence on low energy photons that supports the hypothesis that the photoelectric effect plays an important role. However, previous studies have suggested that other processes may also contribute to the observed results^{3,9,10,36}. We found that situations with increased photoelectric interaction probability (more low energy photons) tend to increase ROS generation as well. Tertiary products, such as hydrogen peroxide, have a longer range of action (a few mm) than photoelectrons (a few μ m), increasing the potential to damage the DNA and cause cell death. Recently, Taggart *et al.* demonstrated that protein disulphide isomerase and mitochondrial oxidation could be novel targets for

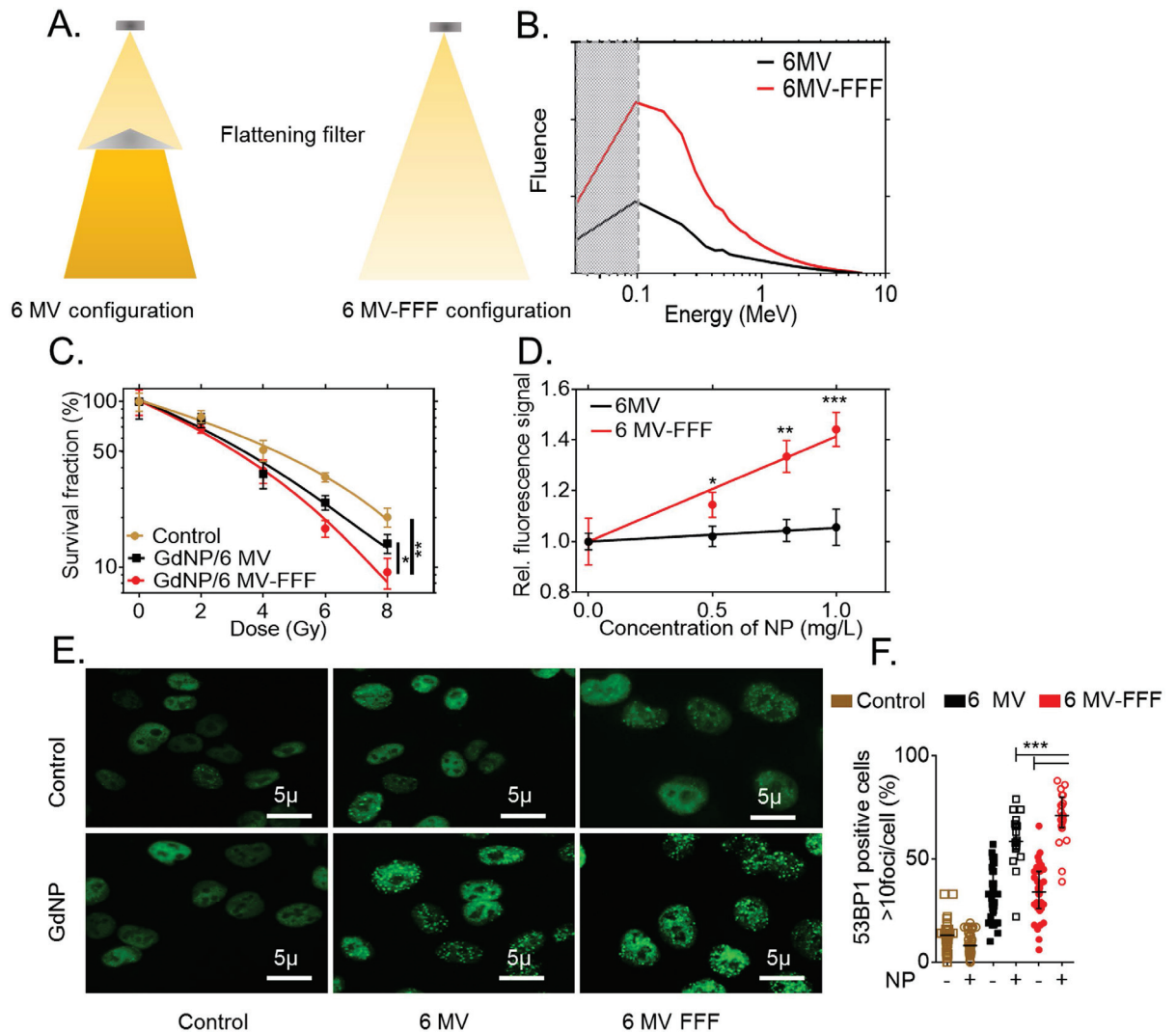


Figure 2. *In vitro* radiation dose amplification studies in clinical 6 MV and 6 MV-FFF radiation beams.

(A) Schematic representation of the 6 MV and 6 MV-FFF treatment configuration. The flattening filter creates a beam hardening effect. (B) The amount of low energy photons is higher for 6 MV-FFF compared to 6 MV, as determined by Monte Carlo simulations. (C) Clonogenic survival assay performed with radiation alone shows the increased efficacy of GdNP and 6 MV and 6 MV-FFF. (D) Reactive oxygen species measurement quantified as the ratio of fluorescence with and without different doses of GdNP after 4 Gy irradiation. The 6 MV-FFF beam provides greater relative signal at all nanoparticle doses. (E) Qualitative and (F) quantitative representation of the DNA repair (53BP1) after administration of GdNP and irradiation with 6 MV or 6 MV-FFF after 4 Gy irradiation. Magnification 63x. All data are represented as a mean \pm SD. Statistical tests were performed using Kruskal Wallis test, * $P < 0.05$, ** $P < 0.01$, *** $P < 0.001$.

radiosensitization⁹. A full understanding of all of the relevant biophysical factors will be important for designing a nanoparticle strategy that maximizes the therapeutic benefit.

We have shown that key clinical beam parameters can be exploited to increase the efficacy of nanoparticles in external beam radiation therapy. In general, delivering more low energy photons (a softer beam) will result in greater biological effect. The flattening filter free (FFF) delivery mode is a recent clinical innovation mainly used to increase the dose rate and thus decrease the radiation delivery time. This is particularly important in the context of stereotactic treatments in which large amounts of radiation are delivered in a single treatment. That the FFF mode includes a larger proportion of low energy photons is a collateral advantage for nanoparticle-mediated radiation dose amplification. In the presence of GdNP, FFF beams lead to greater DNA damage and improved survival compared to standard 6 MV beams. Similarly, other technologies such as the modification of the linear accelerator target, as suggested by Berbeco *et al.* could also provide a greater benefit⁴. In that study, it was shown that, by replacing the Cu/W target with a carbon target, the proportion of low energy photons would almost triple at 10 cm depth. In the current study, we show that even a ~40% increase in the low energy photon content has a statistically significant effect on tumor growth and survival.

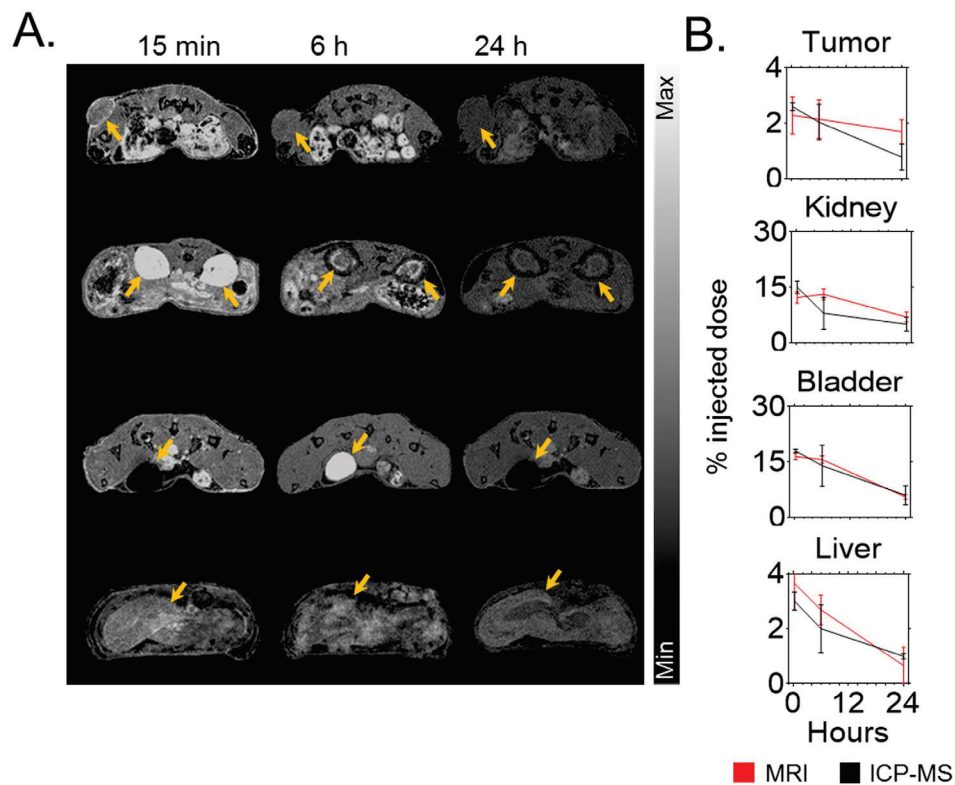


Figure 3. Biodistribution study. (A) Axial magnetic resonance images post-i.v. injection of GdNP. Yellow arrows show the tumor, kidney, bladder, and liver uptake of nanoparticles, respectively, between 15 min and 24 h post-injection. (B) Biodistribution comparison between non-invasive MRI quantification ($n = 3$) and ICP-MS ($n = 3$ /time point) after intravenous injection of 0.25 mg/g GdNP.

Beyond the radiation beam characteristics, there are other clinical factors which will affect nanoparticle-mediated radiation dose amplification. Tumor vascularity, permeability, and other biological factors will have consequences for nanoparticle uptake, distribution and therapeutic efficacy. Tumor location, visibility on imaging and motion due to respiration or other physiological processes are common clinical challenges which can be alleviated by contrast agents such as the one presented in this study. This is particularly relevant for MR-guided radiation therapy either in the pre-treatment or in-treatment setting. Both are current and emerging modalities in clinical radiation therapy, indicating a growing need for agents that can serve as both MRI contrast agents and radiation dose amplification agents. In this context, the AGuIX nanoparticle is uniquely suited to simultaneously provide both greater accuracy and efficacy in clinical radiation therapy.

Conclusion

We have shown that clinical radiation delivery parameters will have a significant effect on the radiation dose amplification provided by high-Z nanoparticles. Most notable is the benefit of the flattening filter free delivery mode, a common modality for modern radiation therapy procedures. Further advances, both in nanoparticle synthesis and radiation therapy delivery, should provide additional therapeutic advantages.

Material and Methods

Monte Carlo simulation. The clinical radiation therapy beams, both 6 MV and 6 MV-FFF were simulated using the Geant4 Monte Carlo code. All beams simulated represent a specific configuration of the linear accelerator which has been experimentally validated in our clinic³⁷. A photon fluence is obtained from these simulations for each energy bin between 0 MeV and 6.33 MeV. The simulation model replicated the geometry of our experimental setup: A 6-well plate was placed between two solid water phantoms with lateral dimensions of 30×30 cm² and thicknesses of 15 cm (top) and 5 cm (bottom).

Cell culture. Capan-1 human pancreatic adenocarcinoma cells were acquired from American Type Culture Collection (ATCC, Manassas, VA) and cultured in Iscove's Modified Eagle Medium, with 20% fetal bovine serum, and 2% Penicillin Streptomycin Glutamine. The cells were stored in a humidified incubator at 37 °C and 5% CO₂.

Silica-based gadolinium nanoparticle. Nanoparticles (GdNP) were purchased from CheMatech in their lyophilized form (CheMatech, Dijon, France). For use, the GdNP were resuspended in ultrapure distilled water (Invitrogen, NY) at a concentration of 100 mg/mL before dilution at the appropriate concentration for experiments. The complete physical characterization of these nanoparticles was performed by Lux *et al.*³⁸.

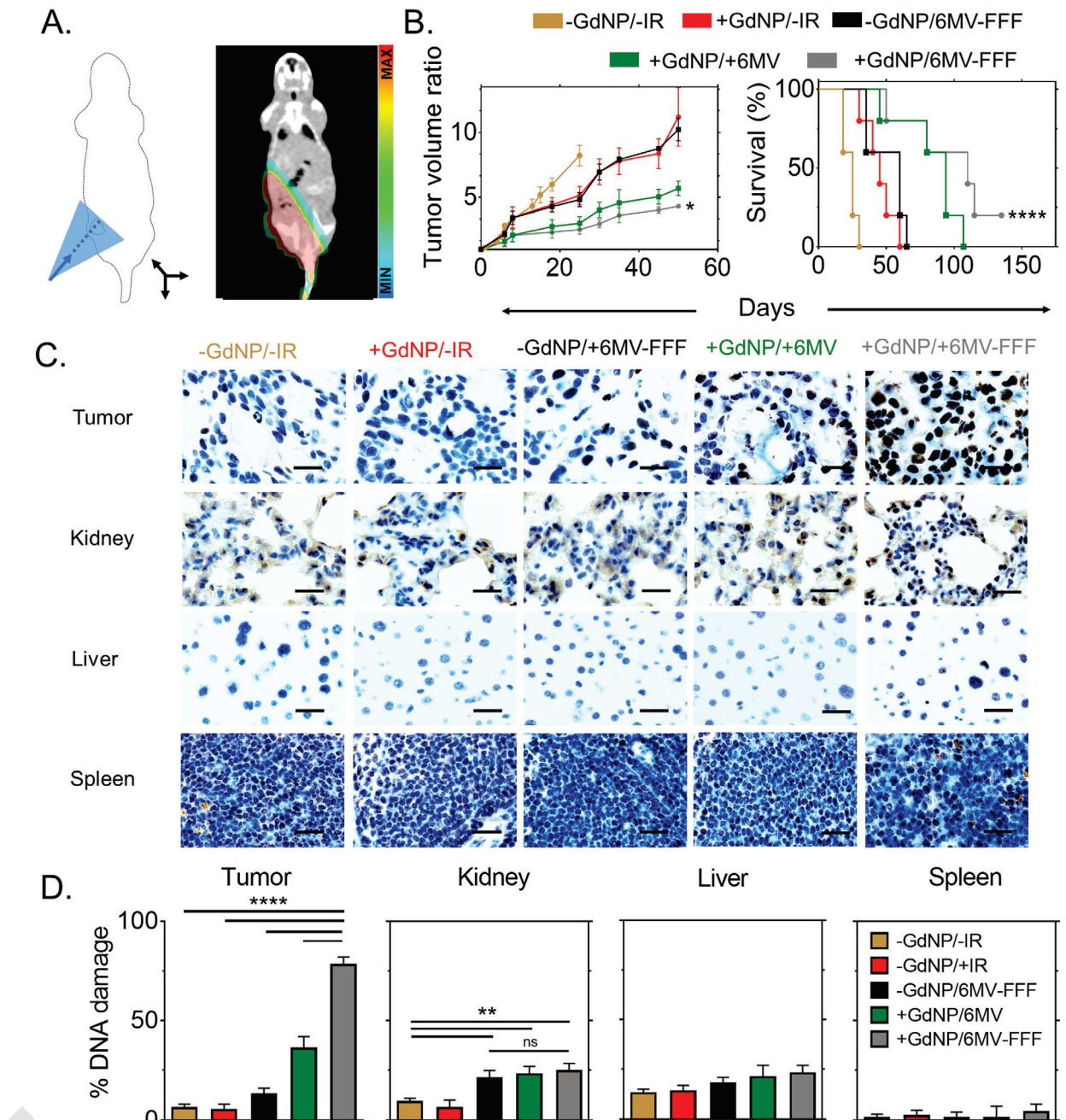


Figure 4. In vivo therapy outcomes and toxicity assessment. (A) (left) Experimental setup for irradiation with a clinical photon beam and (right) 3D radiation dose calculation using a CT scan and the clinical treatment planning system (B) Tumor growth study ($n = 5/\text{group}$) shows a 1.5-fold difference in the tumor size by day 50 between +GdNP/6 MV-FFF and +GdNP/6 MV groups ($P = 0.0411$) while an extended median lifetime by 16 days ($P < 0.0001$) was observed in the survival study. (C) DNA double strand breaks in the tumor and surrounding tissues shown by γH2AX staining. Scale bar = $20\mu\text{m}$. (D) Quantification of γH2AX positive nuclei ('brown') counted over 30 images. All data are represented as a mean \pm SD. Statistical tests were performed using a Kruskal-Wallis test for the tumor growth study and the DNA damage quantification whereas a Log-Rank test was performed for the survival study. * $P < 0.05$, ** $P < 0.01$, *** $P < 0.001$.

Clonogenic Assay. Capan-1 cells were incubated for 15 minutes with 0.43 mg/mL of GdNP prior to irradiation. Irradiations were performed with either a 6 MV or 6 MV-FFF beam, 90 cm source-to-surface distance (SSD), 10 cm depth in solid water, $15 \times 1\text{ cm}^2$ field size. Radiation doses of 0, 2, 4, 6, and 8 Gy were used. After irradiation, the cells were allowed to grow for 10 days, before staining with a 1% crystal violet and 10% ethanol dye solution. Measurements were performed in triplicate. The effect of the GdNP is quantified by the calculation of the dose

enhancement factor (DEF) using Matlab (V. R2013b). The DEF is the ratio of the area under the survival curves with and without nanoparticles.

Sensitivity measurements. Capan-1 cells were incubated for 15 minutes with 0.43 mg/mL of GdNP prior to irradiation. Comparison between different irradiation setups were performed to investigate the impact of the change in each clinical parameter. The depths studied were 5 cm, 10 cm and 20 cm and the field sizes were $5 \times 5 \text{ cm}^2$, $10 \times 10 \text{ cm}^2$, and $25 \times 25 \text{ cm}^2$, with a constant source-to-cells distance of 100 cm and a single irradiation to 4 Gy with the 6 MV clinical beam. Sensitivity enhancement ratio at 4 Gy ($\text{SER}_{4\text{Gy}}$) is defined as the ratio of cell survival with and without nanoparticles at 4 Gy, while the dose enhancement factor (DEF) is defined as the ratio of cell survival with and without nanoparticles from 0 to 8 Gy.

Reactive oxygen species measurement. Capan-1 cells (10,000 cells/well) were seeded in 96-well plates and grown for 24 h. The cells were then incubated with different concentrations of nanoparticles for 30 min, and washed with PBS to remove nanoparticles that were not internalized by the cells. Afterwards, cells were incubated with $10 \mu\text{M}$ dihydrorhodamine 123 (DHR123) for 3 h. Prior to irradiation, cells were washed with PBS to remove excess DHR. Irradiations were performed with a single fraction of 4 Gy irradiation (10 cm depth, $15 \times 15 \text{ cm}^2$ field size) with 6 MV or 6 MV-FFF radiation beams. The fluorescence signal was measured 3 h post-irradiation using a plate reader (POLARstar omega, BMG LABTECH) with an excitation wavelength of 480 nm and an emission wavelength of 520 nm.

DNA damage quantification. Capan-1 cells were irradiated with clinical 6 MV and 6 MV-FFF beams, with and without GdNP (0.43 mg/ml). Immunofluorescence was performed as previously described³⁹. Cells were fixed, permeabilized, and incubated with 53BP1 primary antibody (H-300, Santacruz, USA) and secondary antibody (Alexa Fluor IgG 488 goat anti-rabbit) prior to mounting with Dapi Fluoromount-G (SouthernBiotech, USA). Fluorescence microscopy images were analyzed using a Zeiss Axio microscope at 63X magnification. DNA damage induced by the GdNP was determined by counting the number of cells with more than 10 foci.

In vivo experiments. All animal studies were approved and carried out according to the Animal Care and Use Committee of the Dana-Farber Cancer Institute. Immuno-compromised CrTac: NCr-*Fox1nu* mice were injected with 5×10^6 Capan-1 cells subcutaneously in the flank. Tumors were allowed to reach 5 mm in the long-axis before experiment, and a maximum size of 2 cm in the longest axis before euthanasia.

Biodistribution study. MRI and inductively coupled plasma mass spectrometry (ICP-MS) were used to determine the biodistribution of the nanoparticles in the capan-1 tumor-bearing mice ($n = 3$). The *in vivo* biodistribution measurements were performed with a dose equivalent of 0.25 mg/g of GdNP injected intravenously. MRI quantification was performed at different time points post injection from 1 min to 24 h by using a T1 RARE-VTR sequence with a repetition time of 9000 ms, echo time of 19.6 ms, and a flip angle of 180° . The acquisition matrix size and reconstructed matrix were 400 pixels x 200 pixels, with a field of view of $200 \times 200 \mu\text{m}^2$, and a 3 mm slice thickness. The T_1 map acquisition was then correlated to the calibration curve to calculate the absolute quantification of nanoparticles. For ICP-MS, animals were sacrificed at 15 min, 6 h, and 24 h post-injection. The organs were dissolved in HCl, HNO_3 , and H_2O_2 . Gadolinium concentrations were analyzed on a VG Plasma Quad Excell ICP-MS with the isotope Gd^{155} .

Radiation therapy irradiation protocol. A CT scan was performed in order to delineate the tumor and calculate the 3D radiation dose distribution. Animals were anesthetized with a mix of ketamine/xelazine (2:1) and wrapped with 2 cm of flexible tissue-equivalent material. The clinical treatment planning system Eclipse (Aria, V.11) was used to calculate the dose distribution in the tumor and healthy organs using the analytical anisotropic algorithm (AAA) for a $5.5 \times 10 \text{ cm}^2$ field size, gantry at 180 degree, and SSD of 90 cm. Blocking of healthy organs and tissue was performed with the primary collimator. A 10 cm depth for the tumor was created with solid water (CIRS, Inc). Dose calculation was performed for the standard and flattening filter free 6 MV irradiation beams. Irradiations were performed 15 mins after intravenous injection of 0.25 mg/g GdNP.

Survival study. Five groups (-GdNP/-IR; +GdNP/-IR; -GdNP/+6 MV-FFF; +GdNP/+6 MV; +GdNP/+6 MV-FFF) of five mice each were used to measure the therapeutic efficacy. Irradiations were performed 15 minutes after intravenous administration. The tumor response was measured by volume studies using cone-beam CT (CBCT) imaging (65 kV and 0.5 mA). Two CBCT per week were performed after treatment, and the tumor volumes were normalized to the first CBCT acquired before the treatment. Volume was measured using the 3D Slicer software (V. 4.3.1). Animals were euthanized when the tumor size reached 2 cm in the longest axis. Body weight was measured and behavior observed throughout the experiment to assess systemic toxicity.

DNA damage assessment. Animals were irradiated 15 minutes after intravenous injection of the GdNP following the same procedure as the survival study above. The tumor was harvested 30 min after irradiation and fixed in 2% formalin followed by paraffin embedding. Tumor slices of approximately $5 \mu\text{m}$ were cut. Immunohistochemistry was performed with γH2AX staining (antibody Abcam ab11174) as a marker for DNA damage. Images were analyzed using a Zeiss Axio microscope at 63X magnification.

References

- Retif, P. *et al.* Nanoparticles for Radiation Therapy Enhancement: the Key Parameters. *Theranostics* **5**, 1030–1044, doi: 10.7150/thno.11642 (2015).
- Thakor, A. S. & Gambhir, S. S. Nanoncology: the future of cancer diagnosis and therapy. *CA: a cancer journal for clinicians* **63**, 395–418, doi: 10.3322/caac.21199 (2013).

3. McMahon, S. J., Paganetti, H. & Prise, K. M. Optimising element choice for nanoparticle radiosensitisers. *Nanoscale* **8**, 581–589, doi: 10.1039/c5nr07089a (2015).
4. Berbeco, R. I. *et al.* Low Z target switching to increase tumor endothelial cell dose enhancement during gold nanoparticle-aided radiation therapy. *Medical physics* **43**, 436, doi: 10.1118/1.4938410 (2016).
5. Lechtman, E. *et al.* Implications on clinical scenario of gold nanoparticle radiosensitization in regards to photon energy, nanoparticle size, concentration and location. *Physics in medicine and biology* **56**, 4631–4647, doi: 10.1088/0031-9155/56/15/001 (2011).
6. McMahon, S. J. *et al.* Biological consequences of nanoscale energy deposition near irradiated heavy atom nanoparticles. *Scientific reports* **1**, 18, doi: 10.1038/srep00018 (2011).
7. Seo, S. J. *et al.* Enhanced production of reactive oxygen species by gadolinium oxide nanoparticles under core-inner-shell excitation by proton or monochromatic X-ray irradiation: implication of the contribution from the interatomic de-excitation-mediated nanoradiator effect to dose enhancement. *Radiation and environmental biophysics* **54**, 423–431, doi: 10.1007/s00411-015-0612-7 (2015).
8. Ghaemi, B. *et al.* Harnessing the Cancer Radiation Therapy by Lanthanide-Doped Zinc Oxide Based Theranostic Nanoparticles. *ACS applied materials & interfaces* **8**, 3123–3134, doi: 10.1021/acsami.5b10056 (2016).
9. Taggart, L. E. *et al.* Protein disulphide isomerase as a target for nanoparticle-mediated sensitisation of cancer cells to radiation. *Nanotechnology* **27**, 215101, doi: 10.1088/0957-4484/27/21/215101 (2016).
10. Kunjachan, S. *et al.* Nanoparticle Mediated Tumor Vascular Disruption: A Novel Strategy in Radiation Therapy. *Nano letters* **15**, 7488–7496, doi: 10.1021/acs.nanolett.5b03073 (2015).
11. Maggiorella, L. *et al.* Nanoscale radiotherapy with hafnium oxide nanoparticles. *Future oncology* **8**, 1167–1181, doi: 10.2217/fon.12.96 (2012).
12. Liu, P. *et al.* Silver nanoparticles: a novel radiation sensitizer for glioma? *Nanoscale* **5**, 11829–11836, doi: 10.1039/c3nr01351k (2013).
13. Bianchi, A. *et al.* Targeting and *in vivo* imaging of non-small-cell lung cancer using nebulized multimodal contrast agents. *Proceedings of the National Academy of Sciences of the United States of America* **111**, 9247–9252, doi: 10.1073/pnas.1402196111 (2014).
14. Hainfeld, J. F., Slatkin, D. N. & Smilowitz, H. M. The use of gold nanoparticles to enhance radiotherapy in mice. *Physics in medicine and biology* **49**, N309–N315 (2004).
15. Kotb, S. *et al.* Gadolinium-Based Nanoparticles and Radiation Therapy for Multiple Brain Melanoma Metastases: Proof of Concept before Phase I Trial. *Theranostics* **6**, 418–427, doi: 10.7150/thno.14018 (2016).
16. Bobyk, L. *et al.* Photoactivation of gold nanoparticles for glioma treatment. *Nanomedicine : nanotechnology, biology, and medicine* **9**, 1089–1097, doi: 10.1016/j.nano.2013.04.007 (2013).
17. Le Duc, G. *et al.* Toward an Image-Guided Microbeam Radiation Therapy Using Gadolinium-Based Nanoparticles. *ACS Nano* **5**, 9566–9574, doi: 10.1021/nn202797h (2011).
18. Chang, M. Y. *et al.* Increased apoptotic potential and dose-enhancing effect of gold nanoparticles in combination with single-dose clinical electron beams on tumor-bearing mice. *Cancer science* **99**, 1479–1484, doi: 10.1111/j.1349-7006.2008.00827.x (2008).
19. Detappe, A. *et al.* AGuX nanoparticles as a promising platform for image-guided radiation therapy. *Cancer nanotechnology* **6**, 4, doi: 10.1186/s12645-015-0012-3 (2015).
20. Miller, K. D. *et al.* Cancer treatment and survivorship statistics, 2016. *CA: a cancer journal for clinicians*, doi: 10.3322/caac.21349 (2016).
21. Krishnan, S. *et al.* Focal Radiation Therapy Dose Escalation Improves Overall Survival in Locally Advanced Pancreatic Cancer Patients Receiving Induction Chemotherapy and Consolidative Chemoradiation. *International journal of radiation oncology, biology, physics* **94**, 755–765, doi: 10.1016/j.ijrobp.2015.12.003 (2016).
22. Liu, C. J. *et al.* Enhancement of cell radiation sensitivity by pegylated gold nanoparticles. *Physics in medicine and biology* **55**, 931–945, doi: 10.1088/0031-9155/55/4/002 (2010).
23. Liu, J., Liang, Y., Liu, T., Li, D. & Yang, X. Anti-EGFR-Conjugated Hollow Gold Nanospheres Enhance Radiocytotoxic Targeting of Cervical Cancer at Megavoltage Radiation Energies. *Nanoscale research letters* **10**, 218, doi: 10.1186/s11671-015-0923-2 (2015).
24. Burger, N. *et al.* A method for the efficient cellular uptake and retention of small modified gold nanoparticles for the radiosensitization of cells. *Nanomedicine : nanotechnology, biology, and medicine* **10**, 1365–1373, doi: 10.1016/j.nano.2014.03.011 (2014).
25. Berbeco, R. I. *et al.* DNA damage enhancement from gold nanoparticles for clinical MV photon beams. *Radiation research* **178**, 604–608, doi: 10.1667/RR3001.1 (2012).
26. Wolfe, T. *et al.* Targeted gold nanoparticles enhance sensitization of prostate tumors to megavoltage radiation therapy *in vivo*. *Nanomedicine : nanotechnology, biology, and medicine* **11**, 1277–1283, doi: 10.1016/j.nano.2014.12.016 (2015).
27. Yan, Y. *et al.* Dosimetric differences in flattened and flattening filter-free beam treatment plans. *Journal of medical physics / Association of Medical Physicists of India* **41**, 92–99, doi: 10.4103/0971-6203.181636 (2016).
28. De Puyseleer, A., Lechner, W., De Neve, W., Georg, D. & De Wagter, C. Absorbed dose measurements in the build-up region of flattened versus unflattened megavoltage photon beams. *Zeitschrift fur medizinische Physik* **26**, 177–183, doi: 10.1016/j.zemedi.2016.02.005 (2016).
29. Fries, P. *et al.* Evaluation of a Gadolinium-Based Nanoparticle (AGuX) for Contrast-Enhanced MRI of the Liver in a Rat Model of Hepatic Colorectal Cancer Metastases at 9.4 Tesla. *RoFo : Fortschritte auf dem Gebiete der Rontgenstrahlen und der Nuklearmedizin* **187**, 1108–1115, doi: 10.1055/s-0035-1553500 (2015).
30. Sancey, L. *et al.* Long-term *in vivo* clearance of gadolinium-based AGuX nanoparticles and their biocompatibility after systemic injection. *ACS nano* **9**, 2477–2488, doi: 10.1021/acs.nano.5b00552 (2015).
31. Sancey, L. *et al.* The use of theranostic gadolinium-based nanoprobe to improve radiotherapy efficacy. *The British journal of radiology* **87**, 20140134, doi: 10.1259/bjr.20140134 (2014).
32. Mignot, A. *et al.* A top-down synthesis route to ultrasmall multifunctional Gd-based silica nanoparticles for theranostic applications. *Chemistry* **19**, 6122–6136, doi: 10.1002/chem.201203003 (2013).
33. Luchette, M., Kordeck, H., Makrigrigios, M., Tillement, O. & Berbeco, R. Radiation dose enhancement of gadolinium-based AGuX nanoparticles on HeLa cells. *Nanomedicine : nanotechnology, biology, and medicine* **10**, 1751–1755, doi: 10.1016/j.nano.2014.06.004 (2014).
34. Lux, F. *et al.* Gadolinium-based nanoparticles for theranostic MRI-radiosensitization. *Nanomedicine (Lond)* **10**, 1801–1815, doi: 10.2217/nmm.15.30 (2015).
35. Li, Y. H. *et al.* Inhibition of non-homologous end joining repair impairs pancreatic cancer growth and enhances radiation response. *PLoS one* **7**, e39588, doi: 10.1371/journal.pone.0039588 (2012).
36. Her, S., Jaffray, D. A. & Allen, C. Gold nanoparticles for applications in cancer radiotherapy: Mechanisms and recent advancements. *Advanced drug delivery reviews*, doi: 10.1016/j.addr.2015.12.012 (2015).
37. Tsiamas, P. *et al.* A modification of flattening filter free linac for IMRT. *Medical physics* **38**, 2342–2352, doi: 10.1118/1.3571419 (2011).
38. Lux, F. *et al.* Ultrasmall rigid particles as multimodal probes for medical applications. *Angewandte Chemie* **50**, 12299–12303, doi: 10.1002/anie.201104104 (2011).
39. Lee, D. H. *et al.* A PP4 phosphatase complex dephosphorylates RPA2 to facilitate DNA repair via homologous recombination. *Nature structural & molecular biology* **17**, 365–372, doi: 10.1038/nsmb.1769 (2010).

Acknowledgements

This project was supported, in part, by award number R21 CA188833 from the National Cancer Institute (NCI). The content of this manuscript is solely the responsibility of the authors and does not necessarily represent the official views of the NCI or NIH. S.K. received financial support through the program “Investissement d’Avenir” (ANR-11-IDEX-0063) from the LABEX PRIMES of Lyon 1 University.

Author Contributions

A.D. and R.B. designed and conceived the experiments. A.D., S.K., P.D., S. K., M.M., D.E.B., T.I. and M.W. performed the experiments. The data was collected and analyzed by A.D. and R.B. The manuscript was written by A.D. and R.B. Nanoparticles were provided by F.L. and O.T. Technical support and conceptual advice was given by F.L. and O.T. All authors contributed to the final manuscript.

Additional Information

Supplementary information accompanies this paper at <http://www.nature.com/srep>

Competing financial interests: F.L. and O.T. have one patent to disclose: WO2011135101. This patent protects the nanoparticles used in this publication. The authors have no other relevant affiliations or financial involvement with any organization or entity with a financial interest in or financial conflict with the subject matter or materials discussed in the manuscript apart from those disclosed.

How to cite this article: Detappe, A. *et al.* Key clinical beam parameters for nanoparticle-mediated radiation dose amplification. *Sci. Rep.* **6**, 34040; doi: 10.1038/srep34040 (2016).



This work is licensed under a Creative Commons Attribution 4.0 International License. The images or other third party material in this article are included in the article’s Creative Commons license, unless indicated otherwise in the credit line; if the material is not included under the Creative Commons license, users will need to obtain permission from the license holder to reproduce the material. To view a copy of this license, visit <http://creativecommons.org/licenses/by/4.0/>

© The Author(s) 2016

5

Conclusion

AGuIX nanoparticles are efficient theranostic agents for the treatment of radioresistant tumors or tumors with close surrounding organ at risks. Due to their MR properties, AGuIX nanoparticles are more efficient preclinical contrast agents than current FDA-approved MR contrast agents to detect the tumor non-invasively. They also act as an effective radiosensitizer when irradiated by the radiation beam due to the gadolinium atoms [77].

To properly understand the distribution of the nanoparticles AGuIX in the tumor and healthy organs, a complete study of its pharmacokinetics and target site accumulation was performed on a tumor-bearing mouse pancreatic model, and on cynomolgus monkeys to test the good laboratory process batch to set path to a clinical trial which should start before the end of 2016.

Computed tomography (CT) is commonly used in clinic to detect the tumor and perform the dosimetry study using Hounsfield units. However, a lack of sensitivity is observed for soft tissues such as brain, prostate, or pancreatic cancers. For this reason, MRI is usually merged to CT to improve the diagnostic. More and more, radiation oncology departments use MRI for their enhanced sensitivity, specificity, and dose free imaging over CT scans. In addition, cone-beam computed tomography (CBCT) are used to monitor the positioning of the patient on the treatment couch and to perform gated treatment (image-guided radiation therapy). The increasing use of MRI in radiation therapy departments led to the development of a new generation of linear accelerator, replacing the CBCT by an MRI machine (MR-linac) allowing an enhanced imaging system and treatment accuracy (Fig. 5.1) [7, 8]. In our studies, we used MRI scans to determine the radiation therapy plan based on the amount of nanoparticles in the tumor, and the best irradiation timing to obtain the largest dose enhancement.

We studied the pancreatic cancer model. Treatment options are limited (5-yr overall survival below 7%) creating a need for innovative therapeutical approaches [61]. The location of the pancreas makes it challenging to deliver therapeutic radiation doses, while the dense fibrotic microenvironment and the inherent tumor pathophysiology which regulates the poor diffusion of nanoparticles (beyond tumor vasculature and its periphery) is a serious limitation to the clinical translationality of AGuIX-mediated radiation therapy. We demonstrated in this manuscript that an improvement of radiation therapy outcomes is observed with both preclinical and clinical radiation beam on the pancreatic tumor model. We tracked the nanoparticles, quantified their uptake by the tumor through a translational non-invasive imaging technique (MRI) and tested their non-toxicity after intravenous injection.



Figure 5.1: Current and future linear accelerators. A. A linear accelerator from Varian Inc. currently used in the clinic with the cone-beam CT attached. B. A MR-Linac prototyped by Viewray. Images courtesy of Varian and Viewray [78, 79].

Beyond the radiation beam parameters, there are other clinical factors which will affect nanoparticle-mediated radiation dose amplification. Tumor vascularity, permeability, and other biological factors will have consequences for nanoparticle uptake, distribution and therapeutic efficacy. Tumor location, visibility on imaging and motion due to respiration or other physiological processes are common clinical challenges which can be alleviated by contrast agents such as AGuIX. This is particularly relevant for MR-guided radiation therapy either in the pre-treatment or in-treatment setting. Both are current and emerging modalities in clinical radiation therapy, indicating a growing need for agents that can serve as both MRI contrast agents and radiation dose amplification agents. In this context, AGuIX nanoparticles are uniquely suited to simultaneously provide both greater accuracy and efficacy in clinical radiation therapy.

However, the choice of the pancreatic model is probably not the most adequate model to evaluate the nanoparticles for a first clinical trial due to the previously mentioned reasons. Thus, a clinical trial will be conducted on an other well-vascularized in-need disease: the brain tumors, including glioblastoma multiforme (GBM) and brain metastases, for which AGuIX already shown their efficacy at the preclinical level [77, 80]. Previous preclinical experiments demonstrated the efficacy of the nanoparticles as radiation enhancers for these tumor sites and their absence of side effect when combined to chemotherapy agents such as Temozolomide [81].

WHAT'S NEXT ?

The first clinical trial will be performed on brain cancers to evaluate the toxicity of AGuIX nanoparticles. Temozolomide is the agent of choice used in adjuvant treatment of GBM. However, the peak brain serum levels are only 17-20 % in the blood [82, 83]. Furthermore, chemotherapy drug concentrations rapidly decrease from the center of the tumor resulting in up to 40 fold lower concentrations in the peritumoral brain zone (PBZ) [84, 85]. Temozolomide's dose limiting toxicity of leukopenia and thrombocytopenia precludes the use of higher doses which could theoretically result in higher intratumoral concentrations. By combining the radiation therapy and AGuIX, a dual phenomena is expected to occur. The nanoparticles will help to disrupt the blood brain barrier (BBB) and will amplify the radiation therapy. The disruption of the BBB will lead to an increase of chemotherapy in the tumor and improve the treatment in a second time.

Being able to focus drug delivery to specific cancer locations through transient and localized disruption of the BBB shows great promise for improving cancer therapy outcomes [86]. Translation and standardization of these technologies into the clinic will potentially change the current landscape of neuro-oncological treatment paradigms.

Most current investigations assess the methods that modulate targeted regions around brain tumors to either limit the neo-angiogenesis or to increase vessel permeability around tumor site. In otherwise healthy regions of the brain, high doses of radiation have been shown to induce BBB permeability elevation, tight junction morphology changes, reductions in cell density and the formation of actin stress fibers in cerebral endothelial cells. Both techniques function with the idea of increasing chemotherapeutic agent delivery to radiosensitive tumors. Radiation effects on the brain vasculature are of crucial importance in the progression of radiation-induced central nervous system toxicity but it can also be used to modulate permeability. A study examining large single doses of irradiation on the cerebral microvasculature showed that ionizing radiation increases the BBB permeability with the permeability due to an increase in cell adhesion [87]. Additionally, apoptosis of endothelial, neural and glial cells, oxidative stress and neuroinflammation mediate radiation-induced secondary cell damage that leads to further endothelial dysfunction, disruption of BBB, inhibition of cell regeneration, demyelination and tissue necrosis [88].

The potential to combine the intravenous injection of AGuIX with radiation to sensitize both the vasculature and the tumor is an interesting new concept. The nanoparticles have recently received much attention as a potential tool in cancer treatment and diagnosis due to their low toxicity and ability to increase tissue sensitivity to radiation [89]. One can argue that with low dose irradiation in conjunction with circulating AGuIX can increase the endothelial local dose-response, and therefore locally induce BBB permeability with limited toxicity. Furthermore, with increased precision in both imaging (for stereotactic planning) and radiation treatments, we could in theory disrupt the BBB in strategic places of the brain (or tumor site) before the first chemotherapeutic drug injection to increase its distribution and efficacy.

To conclude, new strides in non-invasive stereotactic techniques effectively target diseased areas all over the central nervous system with extreme precision in order to eradicate tumors and improve therapeutic drug delivery. Radiation therapy exerts its effect via an integral disruption in the BBB, thereby altering its permeability and enabling the ability of locally applied or systemically infused therapeutically active agents to reach and penetrate targeted diseased area.

5.1 PUBLICATION

Stereotactic modulation of blood-brain barrier permeability to enhance drug delivery

Geoff Appelboom, Alexandre Detappe, Melissa LoPresti, Sijumon Kunjachan, Stefan Mitrasinovic, Serge Goldman, Steve D. Chang, and Olivier Tillement

Department of Neurosurgery, Stanford Medical Center, Stanford, California (G.A., S.D.C.); Department of Radiation Oncology, Dana-Farber Cancer Institute, Brigham and Women's Hospital, Harvard Medical School, Boston, Massachusetts (A.D., S.K.); Institut Lumière Matière, Université Claude Bernard Lyon 1, Villeurbanne, France (A.D., O.T.); Department of Neurosurgery, Baylor College of Medicine, Houston, Texas (M.L.); Department of Neurological Surgery, Columbia University Medical Center, New York, New York (S.M.); Department of Nuclear Medicine, Hôpital Erasme, Université Libre de Bruxelles, Brussels, Belgium (S.G.)

Corresponding Author: Geoff Appelboom, MD, PhD, Department of Neurosurgery, Stanford Medical Center, Stanford, California (ga@neuro-digital.com).

Drug delivery in the CNS is limited by endothelial tight junctions forming the impermeable blood-brain barrier. The development of new treatment paradigms has previously been hampered by the restrictiveness of the blood-brain barrier to systemically administered therapeutics. With recent advances in stereotactic localization and noninvasive imaging, we have honed the ability to modulate, ablate, and rewire millimetric brain structures to precisely permeate the impregnable barrier. The wide range of focused radiations offers endless possibilities to disrupt endothelial permeability with different patterns and intensity following 3-dimensional coordinates offering a new world of possibilities to access the CNS, as well as to target therapies. We propose a review of the current state of knowledge in targeted drug delivery using noninvasive image-guided approaches. To this end, we focus on strategies currently used in clinics or in clinical trials such as targeted radiotherapy and magnetic resonance guided focused ultrasound, but also on more experimental approaches such as magnetically heated nanoparticles, electric fields, and lasers, techniques which demonstrated remarkable results both *in vitro* and *in vivo*. We envision that biodistribution and efficacy of systemically administered drugs will be enhanced with further developments of these promising strategies. Besides therapeutic applications, stereotactic platforms can be highly valuable in clinical applications for interventional strategies that can improve the targetability and efficacy of drugs and macromolecules. It is our hope that by showcasing and reviewing the current state of this field, we can lay the groundwork to guide future research in this realm.

Keywords: electroporation, focused ultrasound, microbubbles, photodynamic therapy, vascular permeability.

Advanced stereotactic systems, particularly focused ultrasound and proton therapy, have received tremendous attention recently. Current developments in noninvasive stereotactic techniques can now effectively target diseased areas all over the CNS with extreme precision in order to eradicate tumors, ablate diseased circuits in the brain, and, with recent progress in neuroimaging, potentially improve drug delivery.^{1,2} The key to understanding these new breakthroughs in stereotactic radiosurgery is understanding the influence these modalities have on the blood-brain barrier (BBB) and their ability to disrupt its permeability.

The BBB is a consistent barrier system that protects the healthy brain from harmful substances. Endothelial cells lining the blood vessels constitute the main component of the BBB. They are surrounded by extracellular matrix, astrocytes, pericytes, vascular smooth muscle cells, and microglial cells

(Fig. 1). The close association of endothelial cells with astrocyte foot processes and the basement membrane of capillaries is important for the development and maintenance of the BBB properties. Furthermore, the proximity of tight junctions between brain endothelial cells limits intercellular translaminar flow to small hydrophilic molecules permitted through tight control of blood-brain exchange. In fact, compared with capillaries in other vital organs, the BBB is extremely influential at regulating molecular flow across its borders. It prevents up to 98% of all small-molecule therapeutics and essentially 100% of all unmodified large-molecule therapeutics from entering the brain due to the closely sealed tight junctions.³ Since peptide and protein therapeutics are generally excluded from the blood-brain transport, owing to the negligible permeability of the brain–capillary endothelial wall to these drugs, endothelial cells represent the major obstacle to the use of many potential

Received 26 February 2016; accepted 23 May 2016

© The Author(s) 2016. Published by Oxford University Press on behalf of the Society for Neuro-Oncology. All rights reserved. For permissions, please e-mail: journals.permissions@oup.com.

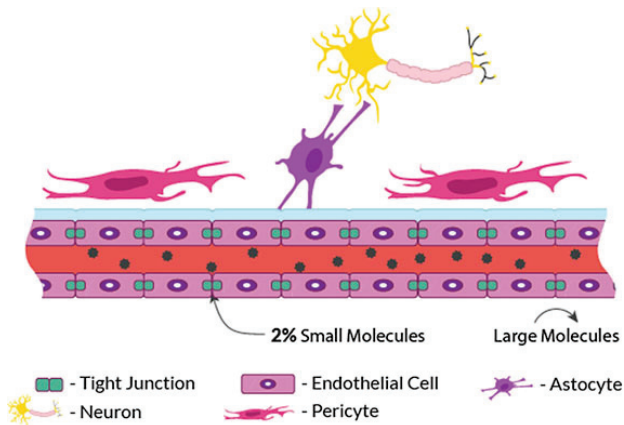


Fig. 1. Schematic illustration of BBB permeability.

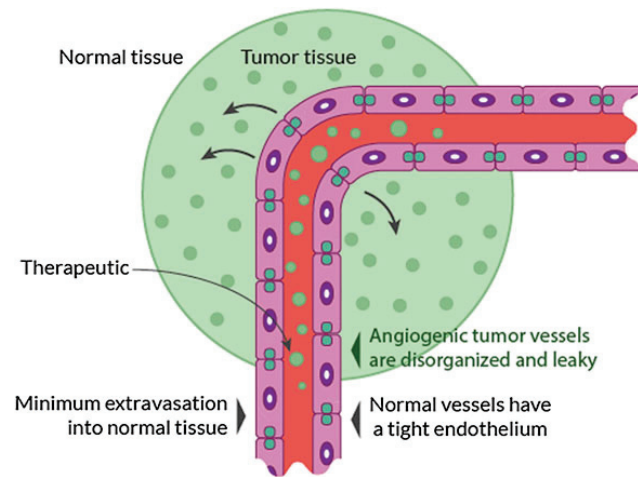


Fig. 2. Schematic illustration of the enhanced permeability and retention effect in and around the tumor site.

therapeutics against the majority of CNS disorders.¹ While the BBB essentially prevents the nonselective accumulation of potentially harmful neurotoxins, it also hinders the transport and efficacy of chemotherapeutics against tumor proliferation and invasion.

To a certain extent, brain tumors innately disrupt the BBB via local invasion of soluble secretion factors that actively degrade tight junctions, as well as the formation of abnormal blood vessels through the defective expression of tight junction proteins, namely occludin and claudin (Fig. 2). In the example of gliomas, the vasculature is immature, variably permeable, and inhomogeneously distributed⁴; these properties help brain tumors infiltrate intact brain parenchyma, leading to invasion and growth.

The enhanced permeability and retention (EPR) effect is attributed to the abnormal anatomy and physiology of tumors (ie, leaky vasculature, endothelial fenestrations, and poor lymphatic drainage).^{5–9} Many factors affect the EPR effect, including the pH, polarity, and size of the delivered substance. The tumor environment is variable and certain characteristics may hinder the EPR effect, such as hypovascularity, fibrosis, and necrosis.¹⁰ Furthermore, infiltrating cancer cells and

small metastatic seeds may be protected by the BBB in surrounding intact tissue.⁴ Even with the breakdown of the BBB in neuro-oncological disease, the fact remains that the tissue accumulation of chemotherapeutics for CNS metastases is 85% less intracranially compared with penetration and biodistribution for extracranial neoplasms.⁹

The limited efficacy of chemotherapeutic drugs has been attributed to an inability to achieve effective therapeutic concentrations of these drugs in the tumor due to the presence of the BBB. With limited penetrative treatments efficacious at targeting CNS tumors and the gravity of neuro-oncological disease, it is imperative to continue exploring promising advancements in treatment options. To improve their targeting and concentration in the CNS, chemotherapeutic drugs have to respect a list of specific criteria. These include favorable properties for passive diffusion through the BBB: small molecular weight, uncharged (or only partially ionized) at physiological pH, and lipid soluble without increasing plasma protein binding to avoid uptake by the liver or reticuloendothelial system.¹⁰

Attempts to identify newer, more penetrative chemotherapeutics that can effectively infiltrate the BBB affected by the tumor are still ongoing.¹¹ However, rather than designing therapeutic agents sufficiently small enough to penetrate the BBB, another approach is to transiently disrupt the BBB. The most recent of these great strides in neuro-oncological therapy is the modulation of both drug delivery and integrity of the BBB through functional and stereotactic mechanisms representing a promising strategy for enhancing treatment.¹¹ Since partial permeability is insufficient to allow the accumulation of therapeutic levels of drugs,⁹ solutions combining stereotactic methods and systemic treatments have been shown to enhance delivery and bioavailability of therapeutics.

This field within functional neuromodulation and stereotactic radiosurgery has the potential to enhance treatment paradigms in neuroscience. Here, we discuss the different stereotactic options to enhance BBB permeability with a focus on techniques that hold the potential to be translated clinically.

Clinical Implications for Neuro-Oncology

Clinicians have long been aware of the need for systemically administered agents with excellent penetration into the CNS for the optimal treatment of brain infections, brain tumors, and other serious neurological illnesses. Brain tumors have a low incidence but high lethality compared with other cancers. Despite advanced treatment protocols, the prognosis remains poor, with an overall median survival for glioblastoma multiforme (GBM) of ~14–15 months even after complete macroscopic surgical resection and adjuvant radiochemotherapy.¹²

Temozolomide is the agent of choice used in adjuvant treatment of GBM. However, the brain serum levels peak only at 17%–20% of that in the blood.^{13,14} Furthermore, chemotherapy drug concentrations rapidly decrease from the center of the tumor, resulting in up to 40-fold lower concentrations in the peritumoral brain zone.^{15,16} Up to 90% of recurrent tumors develop within the peritumoral brain zone, which is defined as the 2–3 cm margin from the primary site of surgery. This region is composed of normal BBB, decreasing the delivery of drugs to this area, leading to potential failure of water-soluble chemotherapy.¹⁷

Previous attempts to improve drug delivery to the CNS are well documented and have been pursued for over 3 decades; most of these strategies are invasive or not well localized. Intra-arterial drug administration, hyperosmolar solutions, biomolecules, high-dose chemotherapy, and direct intratumoral injection were among other solutions proposed.¹⁸ These techniques often require general anesthesia, intra-arterial catheterization, or a craniotomy, leading to many possible complications such as seizures, cerebrovascular events, and other significant toxicities.^{19,20} There have been innumerable efforts to attempt to minimize these risks and maximize benefits in treatment. Recent efforts have shown promise in transient disruption of the BBB in the outpatient setting with the use of pharmacological agents (bradykinin analog, verapamil, lobradimil, selective G-protein coupled receptor A_{2A} , regadenoson).^{21,22} However, diffuse delivery of a high dose of chemotherapeutic agents can cause undesirable side effects in normal tissues. Direct postoperative delivery (either through slow release systems or direct infusion) into the tumor site is, in theory, an effective way to maximize the chemotherapeutic dose while limiting peripheral dose. Being able to focus drug delivery to specific cancer locations through transient and localized disruption of the BBB shows great promise for improving cancer therapy outcomes. Specifically in this review we present the salient methods of localized and noninvasive image-guided strategies to modulate the BBB. Translation and standardization of these technologies into clinical practice will potentially change the current landscape of neuro-oncological treatment paradigms.

Focused Ultrasound

A rapidly developing field of study within stereotactic modulation involves the use of high-intensity focused ultrasound, most notably magnetic resonance guided focused ultrasound (MRgFUS). This technology holds high therapeutic yields and can be modified to induce thermal ablation, sonothrombolysis, and BBB disruption, allowing targeted therapies.¹² This noninvasive non-ionizing technique consists of delivering beams of focused ultrasound energy with extreme precision to heat, stimulate, and/or destroy regions of the brain while simultaneously allowing real-time imaging of the targeted brain region. These individual ultrasound beams are sent via a transducer through different parts of the skull and will sum coherently at the targeted site to modify the local environment.

This technique is already used outside of the scope of CNS disease; MRgFUS is currently used for the treatment of uterine fibroids, painful osseous metastases, and breast cancer, among others.³ Yet, currently, high-intensity focused ultrasound is gaining traction to modulate central neuropathic pain, essential tremor, Parkinson's disease, and adjunctive therapy for brain tumors.^{19,20} The first human case of MRgFUS modulation of BBB has been reported earlier to enhance chemotherapy treatment.²³

The exact mechanism of BBB modulation as a result of ultrasonic modulation is still under investigation; however, studies suggest that there is a combination of mechanical and heat stress, leading to enhanced local transport across the barrier via endocytosis, transcytosis, and tight junction disruption.^{4,10,24-26} Focused ultrasound (FUS) alone has been

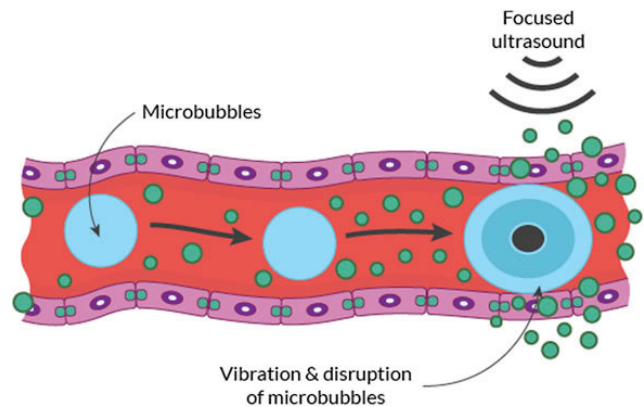


Fig. 3. Schematic illustration of FUS in the context of intravenous MB injection to transiently disrupt BBB permeability.

shown to thermally induce BBB disruption at the target site.²⁷ Mild to moderate increase in temperature has the potential to modify the local environment and increase transport across the BBB. Unfortunately, high temperatures (55° – 60°C) will inevitably induce cell death from thermal coagulation, even with short exposure times. It has been shown, in an MRI study assessing the effect of local hyperthermia, that the first tissue change consistently detected was disruption of the BBB, but in the setting of FUS-induced hyperthermia there is also a consistently associated damage to the healthy tissue surrounding the treatment site.¹⁴

MRgFUS holds additional therapeutic yield via the use of low power FUS in combination with microbubbles (MBs). The systemic injection of MBs can mechanically disrupt the BBB within the intravascular space through the effect of FUS.²⁸ The compressing nature of these gas bubbles will volumetrically expand and contract in response to ultrasound waves (stable cavitation), which may induce shock waves that disrupt the BBB transiently, opening it to therapeutic agents (Fig. 3). This phenomenon is also called sonoporation.²⁹ At high pressure amplitudes these bubbles can violently collapse (inertial cavitation), causing permanent tissue damage.³⁰ MBs increase the ultrasound signal locally disrupting the BBB and act more selectively in vascular regions, thereby allowing for tissue activation within microvessel walls.²⁴ Immuno-electron microscopy studies in normal brains have indicated that passage through the BBB after treatment with MB-enhanced ultrasound occurs via both paracellular and transcellular routes, inducing, at endothelial cell levels, an opening of tight junctions associated with a fenestration and channelization of the cells injuring the endothelium.^{30,31} Furthermore, enhanced active vesicular transport has been shown in and around cell surfaces with use of MBs.^{31,32}

MRgFUS is particularly interesting, since it allows for precise thermal feedback while the patient is in the MRI machine. Promising in vitro and in vivo results have shown passage of a large range of molecular sizes through the BBB as a result. Depending on the intensity of ultrasound energy applied and the number of procedures, the BBB disruptive effect has been found to be temporary and reversible without damaging neural cells or inducing intracerebral hemorrhage. This technique demonstrated capability to deliver compounds of varying sizes,

including antibodies, nanoparticles (NPs), liposomally encapsulated drugs,^{4,24,25,33} short interfering RNA, and viral vectors.^{26,34-37} In other words, MRgFUS can be used to induce reproducible BBB disruption without any neuronal damage at targeted locations, increasing the potential for safe drug delivery methods to previously inaccessible and eloquent locations.^{28,38,39}

While MRgFUS holds much promise, several unresolved issues evident from previous clinical trials have to be addressed. The lack of standardized protocols to determine where MRgFUS yields the most efficacious results is apparent. Many factors, such as individual ultrasound parameters, MB doses, attenuation factors (eg, skull thickness and density), technical factors (eg, accuracy of the phase correction), and physiological factors (eg, tissue perfusion), remain to be determined.³ The intensity required for BBB opening may differ among patients. Similarly, the location of MRgFUS will vary based on the disease, requiring further study into particular MRgFUS protocols and outcomes based on location. Additionally, there is a variability in timing and efficiency of BBB opening, ranging in studies from 30 min post-sonication up to 72 h depending on acoustic parameters (frequency, pulse repetition frequency, sonication duration, MB size, and pulse length).^{26,29,40-42} Translation of these results to human trials will require further studies to define the right parameters.⁴³

The transition of preclinical studies to the development of protocols for BBB opening in large non-primate animals has highlighted several challenges to clinical translation, one of which is to maximize targeting accuracy while minimizing the time and effort necessary for accurate targeting. While MRI targeting can provide a higher level of accuracy, the presence of the magnetic field limits the accessibility of this procedure to highly specialized clinical settings. There have been several recent studies investigating MRI-independent targeted BBB opening by monitoring the acoustic emissions from MBs through the use of a passive cavitation detector for real-time monitoring and treatment efficiency verification.^{44,45} The protocol uses a stereotactic targeting procedure, which has initially been shown to be accurate and reliable, with observed targeting error relatively small in rhesus monkeys (2.5 ± 1.2 mm laterally, 1.5 ± 1.3 mm along depth-axis, 3.1 ± 1.3 mm total).^{45,46}

Another challenge to translating this technology into clinical use is the real-time safety monitoring. Sonication with MBs will cause vascular damage when exposed to ultrasound levels that exceed MB thresholds, causing inertial cavitation. Specifically, the vascular damage may result in devastating and potentially fatal intracranial hemorrhage.⁴³ In human skulls, there are particular regions that may be at risk due to high MB concentrations found in large blood vessels and highly vascularized structures.^{45,46} Cavitation activity can be monitored by analyzing the differences between wave reflections with and without MBs. However, further studies will need to be conducted to quantify the threshold ranges for stable or inertial cavitation.⁴⁶ Unfortunately, much of the current data specifically focus on animal studies conducted in healthy brains, and there are several key differences between the BBB and environment within cancerous tissue, as well as key differences between animal tissue and human tissue, that must be accounted for.

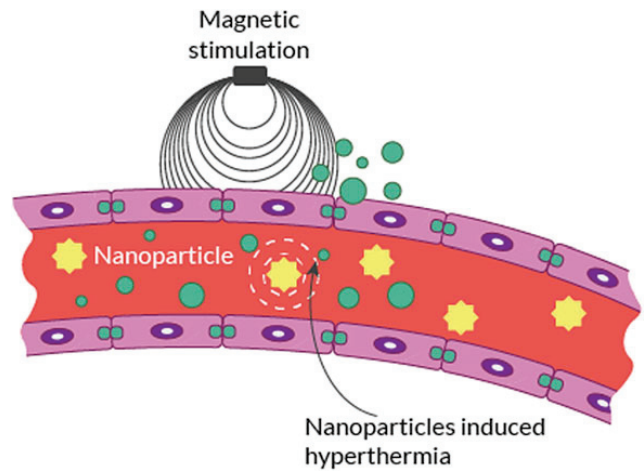


Fig. 4. Schematic illustration of NP activation using magnetic fields to induce targeted hyperthermia.

Magnetic Heating of Nanoparticles

It is well known that even mild focal hyperthermia (38° – 39°C) in and/or around the brain will lead to an increase in BBB permeability.^{6-8,27,47} Focal hyperthermia (42°C) has been shown to significantly increase flux of chemotherapy delivered to the brain in vitro and in vivo.⁴⁸ In a recent study centered on this principle, Tabatabaei et al⁸ proposed a novel method to deliver therapeutics across the BBB. They provided preliminary evidence that magnetic heating of magnetic nanoparticles (MNPs) with a low radiofrequency (RF) source can transiently increase BBB permeability (Fig. 4). The mechanism, “Néel relaxation,” is described as a low RF field magnetically exciting MNPs to release energy in the form of heat to their surroundings.^{49,50} Other research groups have also applied the Néel relaxation principle to superparamagnetic iron oxide NPs with alternating magnetic field to generate local hyperthermia for BBB modulation.⁵¹

Interestingly, no significant difference is observed when the temperature is increased, suggesting that the increased BBB permeability is not solely explained by the increase in temperature within these experiments, but could also be the result of MNP vibration or the difference of surface temperature against the surrounding temperature mechanically activating cell surface receptors.^{51,52} Since most of these experiments were conducted in vitro, we must remain cautious of the potential translation to in vivo studies. Furthermore, in case of imperfectly controlled environments, hyperthermia may generate a drastic increase in temperature, leading to cerebral damage.

Acoustic energy can be used to both vibrate intravenously administered MBs and magnetically heat MNPs, which allows both techniques to target brain regions and witness procedural outcomes in real time. Tabatabaei et al claim that MBs activated by MRgFUS have a shorter half-life in the vasculature and are quickly taken up by the reticuloendothelial system, in contrast to MNPs, which distribute and deposit within the surface of the target endothelium for a longer time.⁸ These modalities are not entirely benign. Mechanical stress associated with the MNPs can lead to high pressure shock waves that have the potential

to damage the cellular membrane near a rigid surface of the brain.⁸ In addition, the sound waves may propagate nonlinearly over a large region of biological structures before converging into a focal point, leading to undesirable side effects in those regions.⁸ The affinity of the MNPs for the surface of the targeted endothelium ensures that the thermal energy is exclusively dissipated to the BBB. Therefore, this cell-specific approach ultimately minimizes potential side effects and the overheating of surrounding structures such as astrocytes and neurons.

Stereotactic Radiation Therapy

Radiation therapy plays a critical role in cancer treatment paradigms, with diagnosed tumors in nearly 50% of patients receiving ionizing radiation during the course of treatment.⁵³ There are many types of radiation treatments, with selection based on the cancer type, disease location, and radiosensitivity. Ionizing radiation is defined as any radiant source with enough energy to generate a biologic response. Since Lars Leksell treated his first patient in 1906 with an X-ray tube attached to a stereotactic centered frame, many developments in precise stereotactic techniques have been performed. Recently, we have honed the ability to precisely focus radiation beams onto microscopic structures with a new generation of machines.^{54,55} Radiation therapy has the advantage to be very effective in killing cancer cells by depositing its energy in the tumor site and damaging its DNA. Ionizing radiation has the potential to not only alter tumor tissue, but also damage the glial, neuronal, and vasculature compartments of the brain. While the damage to normal brain tissue is often considered an adverse consequence of ionizing radiation, the targeted and controlled application of radiation to purposefully damage brain tissue may be key in the use of ionizing radiation to increase BBB permeability, as both endothelial cells and oligodendrocytes are radiation responsive.

There is a difference between enhancing the already permeable BBB around tumor sites and creating *de novo* openings of the BBB in otherwise healthy regions of the brain. Most current investigations assess the methods that modulate targeted regions around brain tumors to either limit the neo-angiogenesis or increase vessel permeability around the tumor site.⁹ In healthy regions of the brain, high doses of radiation have been shown to induce BBB permeability elevation, tight junction morphology changes, reductions in cell density, and the formation of actin stress fibers in cerebral endothelial cells.⁵⁶ Radiation effects on the brain vasculature are of crucial importance in the progression of radiation-induced CNS toxicity but can also be used to modulate permeability. A study examining large single doses of irradiation on the cerebral microvasculature showed that ionizing radiation increases the BBB permeability to fluorescein isothiocyanate-dextran molecules of various sizes.⁵⁷ Additionally, apoptosis of endothelial, neural, and glial cells, oxidative stress, and neuroinflammation mediate radiation-induced secondary cell damage that leads to further endothelial dysfunction, disruption of BBB, inhibition of cell regeneration, demyelination, and tissue necrosis.⁵⁸

What remains apparent is that the therapeutic window has yet to be determined, especially with radiation-induced injury of cerebrovascular vessels as a real collateral effect. Large

single doses of radiation disrupt the BBB and cause considerable edema, detectable with MRI for weeks to months post-irradiation.⁵⁹ The risk of disrupting the BBB appears to be low with small doses of radiation (<100 mGy), with only a few reports describing functional or morphological changes,²⁹ thereby establishing the accepted paradigm. Sándor et al showed recently that not only moderate and high doses of irradiation with 2 and 10 Gy, but also a single low dose of cranial irradiation with 0.1 Gy can induce BBB injury in adult mice.²⁹

It is evident that radiation can change BBB permeability; however, it is unclear what dose is best to achieve the desired results with the least negative outcomes, and at what time post-irradiation does the permeability reach a maximum and later reverse. It has been shown that a single high dose (20 Gy) leads to an increase in permeability as early as 24 hours but can be delayed up to 90 days post-irradiation.⁵⁸ Previous studies have concluded that the molecular response to single-dose irradiation is rapid, whereas the response to fractionated irradiation is slow.⁶⁰ While many studies aim to characterize the best timing of single-dose radiation to achieve the desired effects, a recent study examined the duration of these effects, observing acute and early delayed effects, with no BBB impairment at 6 months follow-up.²⁹

The potential to combine the use of radiation therapy to infiltrate the BBB with intravenous injection of NPs is an interesting new concept. NPs have recently received much attention as a potential tool in cancer treatment and diagnosis due to their low toxicity and ability to increase tissue sensitivity to radiation.⁶¹ NPs significantly increase the cellular DNA damage inflicted by ionizing radiation as well as markedly increasing DNA damage to blood-brain vessels. One can argue that low dose irradiation in conjunction with circulating NPs can increase the endothelial local dose response and therefore local BBB permeability with limited toxicity.⁶² Furthermore, with increased precision in both imaging and radiation treatments, we could in theory disrupt the BBB in strategic places in the brain or tumor bed before the administration of chemotherapeutics to increase their distribution and efficacy.

Electric Field Modulation

Physical modalities, other than ionizing radiation and thermal ablation, have not been systematically studied for radiomodulation of the BBB. One area of interest is the use of electric fields, which have been utilized in other fields of medicine but have remained relatively unexplored. Recently, frequency-tuned electric field therapy, also referred to as tumor-treating fields, have been studied and presented as a novel regional oncology therapy.⁶³ One example is the transient use of an electric current to open the BBB for chemotherapeutic drugs, also known as electrochemotherapy. This technique uses sublethal pulsed electric fields to disrupt the endothelial membrane and facilitate the uptake of a chemotherapeutic agent, such as bleomycin or cisplatin, and has been tried for treatment of cutaneous and subcutaneous tumors in addition to brain metastasis (Fig. 5).^{64,65} Irreversible electroporation is achieved via the use of electric pulses delivered through needle electrodes inducing a nonthermal focal ablation to the target by a series of electric pulses. It induces cell death by disrupting membrane integrity

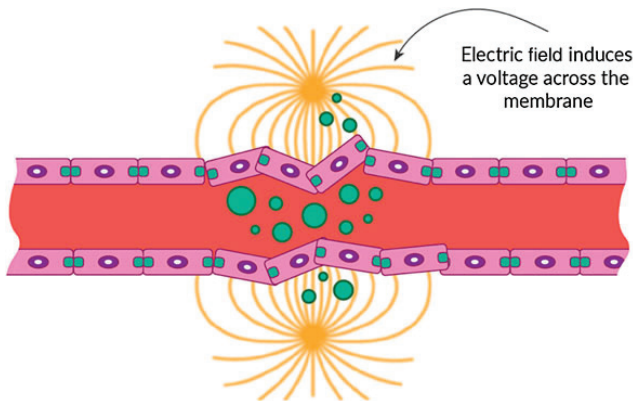


Fig. 5. Schematic illustration of electric fields across the BBB membrane, regionally disrupting its permeability.

and can also be used to produce nonthermal ablation of tumors.⁶⁶ The mechanism of action is through both an anti-microtubule effect and a thermal ablative property of the electric field that results as the frequency increases, causing dielectric losses and developing friction between rapidly oscillating molecules.⁴⁹ While there is potential for direct tumor treatment by the anti-mitotic properties of electric field therapy, what remains unclear is the potential of this modality in BBB disruption.

Laser Therapy

One additional neuromodulatory technology that has been shown to modulate BBB permeability within the CNS is laser therapy. For the past couple of years, MRI-guided laser interstitial thermal therapy (LITT) has emerged as an invasive ablation stereotactic technique.^{67,68} LITT is a minimally invasive therapy which involves inserting a thin laser probe, guided by MRI, to the core of a tumor mass, where it delivers hyperthermic ablation.⁶⁹ This technique has been successfully used for treatment of primary or secondary tumors and deep seizure foci in epilepsy. In a recent study, Leuthardt et al were able to demonstrate sustained, local disruption of the peritumoral BBB using MRI-guided LITT in 14 human patients.^{67,69} This demonstrates an unexplored method of BBB disruption and requires further investigation and generalization.

We expect other, more experimental, less invasive laser technology to be translated into the clinic. For example, laser-induced membranous defects in the capillary endothelium lead to transient disruption of the BBB and allow molecules to permeate into the brain parenchyma (Fig. 6). During the last decade, laser-induced hyperthermia has been used as a component of photodynamic therapy, which consists of treatment with a tumor-localizing photosensitizer and subsequent laser light activation.⁵⁰

On another note, near-infrared femtosecond pulsed lasers have been widely used for in vivo imaging because of their deep tissue penetration, reduced scattering, and localized non-linear absorption, which are ideal properties for CNS applications.⁵¹ Furthermore, it has been shown that femtosecond pulsed laser irradiation induces transient and reversible permeability of the targeted blood vessel wall, enabling extravasation

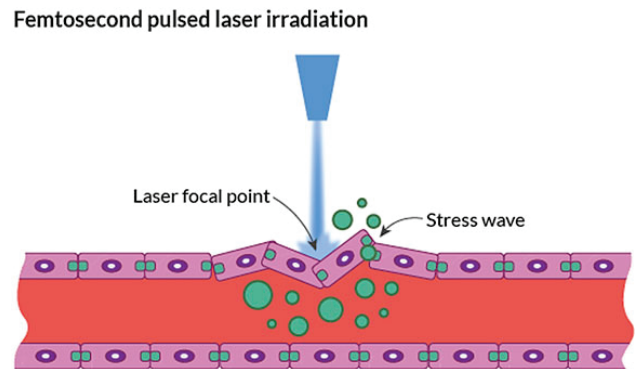


Fig. 6. Schematic illustration of laser disruption through focal lesions in the BBB.

of plasma along with bioactive macromolecules. This technology enables noninvasive tissue modulation via multiple effects, including the generation of intracellular calcium, dissection of intracellular organelles, transient plasma membrane permeability, induction of arterial contraction, and disruption of blood flow.⁴⁹ This ability to alter vascular and BBB permeability holds great promise for the role of laser therapy in BBB modulation for the administration of chemotherapeutics to treat neuro-oncological disease.

Conclusions

New strides in noninvasive stereotactic techniques effectively target diseased areas all over the CNS with extreme precision in order to eradicate tumors and improve therapeutic drug delivery. These modalities, including MRgFUS, ionizing radiation, electric field therapy, and laser therapy, exert their effects via a disruption in the BBB integrity, thereby altering its permeability and enabling the ability of locally applied or systemically infused therapeutically active agents to reach and penetrate targeted diseased areas. It is this key modulation of BBB permeability that holds the promise of these modalities in treating neuro-oncological diseases.

MRgFUS has become one of the most salient mechanisms of modulating BBB permeability in otherwise “healthy” areas of the brain, where the disruption needs to be transient to enhance drug delivery. When examining the literature, it is evident that MRgFUS holds many potential advantages, as it is characterized by a sharp thermal gradient, creating a more focal effect compared with the broader gradient of radiation dose. Theoretically, MRgFUS produces a sharply delineated lesion resulting from the homogeneous thermal dose, whereas radio-frequency heating dissipates with distance from a central ablation electrode. One imaging manifestation of this observation is that there is usually more vasogenic edema around RF lesions compared with MRgFUS.³

Compared with MRgFUS and RF ablation, stereotactic radiosurgery has the disadvantage of latent treatment effects and the possibility of more extensive tissue damage beyond the intended target.¹⁹ MRgFUS has the unique advantages of being able to track changes in BBB permeability in real time and to define the minimal dose necessary to provide drug delivery,

thereby efficiently controlling the therapeutic window. This was demonstrated by tracking changes in the MRI signal intensity with the extravasation via detection of hemorrhage during FUS-induced BBB opening.⁷⁰

In the population of patients with brain tumors, ionizing radiation holds many advantages as well. We have decades of clinical expertise manipulating radiation in the oncologic brain, and validated recommendations exist pertaining to the radiosensitivity of key brain structures. Moreover, radiosurgery is widely available around the world and radiation specialists could combine existing treatment protocols with BBB targeting, allowing for enhanced chemotherapeutic drug delivery. Depending on the underlying disease, a more permanent opening of the BBB may be more appropriate. We can therefore postulate that targeted low dose radiation around the tumor vasculature, before chemotherapy, could be an interesting option. Furthermore, recent research has been focusing on increasing endothelial cell sensitivity through the use of NPs. One recent study showed how combined gold NPs and radiotherapy resulted in markedly increased DNA damage to brain blood vessels, leading to a more targeted BBB disruption limiting peripheral toxicity and allowing for an intravascular radiosensitization.⁶⁰

Regardless of the modality of BBB permeabilization, what remains to be characterized is the optimal timeline for maximal BBB disruption and subsequent penetration. A short window can be positive but can also limit utility in a scenario where chemotherapeutic agents need to be administered to the patient for a longer period of time. Besides the importance of the timing for systemic treatments, length of infusions, and planning of chemotherapy regimens, it is important to know the time-to-recovery window to limit any possible brain injury via undesired penetration of nontherapeutic agents.⁵⁴ Therefore, while it is clear that noninvasive stereotactic neuromodulatory modalities increase BBB permeability, with various modalities having been studied to assorted degrees, much remains to be characterized to make the use of this technology a widely accepted tool for tumor treatment in the CNS.

Funding

No funding was received for this research.

Conflict of interest statement. This review is the sole work of its authors, and there are no conflicts of interest.

References

- Gabrieli JDE, Ghosh SS, Whitfield-Gabrieli S. Prediction as a humanitarian and pragmatic contribution from human cognitive neuroscience. *Neuron*. 2015;85(1):11–26.
- Fritz JV. Neuroimaging trends and future outlook. *Neurol Clin*. 2014;32(1):1–29.
- Ghanouni P, Pauly KB, Elias WJ, et al. Transcranial MRI-guided focused ultrasound: a review of the technologic and neurologic applications. *AJR Am J Roentgenol*. 2015;205(1):150–159.
- Treat LH, McDannold N, Zhang Y, et al. Improved anti-tumor effect of liposomal doxorubicin after targeted blood-brain barrier disruption by MRI-guided focused ultrasound in rat glioma. *Ultrasound Med Biol*. 2012;38(10):1716–1725.
- Lammers T, Koczera P, Fokong S, et al. Theranostic USPIO-loaded microbubbles for mediating and monitoring blood-brain barrier permeation. *Adv Funct Mater*. 2014;25(1):36–43.
- Kiyatkin EA, Sharma HS. Permeability of the blood-brain barrier depends on brain temperature. *Neuroscience*. 2009;161(3):926–939.
- Dokladny K, Moseley PL, Ma TY. Physiologically relevant increase in temperature causes an increase in intestinal epithelial tight junction permeability. *Am J Physiol Gastrointest Liver Physiol*. 2006;290(2):G204–G212.
- Tabatabaei SN, Girouard H, Carret A-S, et al. Remote control of the permeability of the blood–brain barrier by magnetic heating of nanoparticles: a proof of concept for brain drug delivery. *J Control Release*. 2015;206(C):49–57.
- Baetke SC, Lammers T, Kiessling F. Applications of nanoparticles for diagnosis and therapy of cancer. *BJR*. 2015;88(1054):20150207.
- Liu H-L, Hua M-Y, Yang H-W, et al. Magnetic resonance monitoring of focused ultrasound/magnetic nanoparticle targeting delivery of therapeutic agents to the brain. *Proc Natl Acad Sci U S A*. 2010;107(34):15205–15210.
- Baumann BC, Kao GD, Mahmud A, et al. Enhancing the efficacy of drug-loaded nanocarriers against brain tumors by targeted radiation therapy. *Oncotarget*. 2013;4(1):64–79.
- Stupp R, Hegi ME, Mason WP, et al. Effects of radiotherapy with concomitant and adjuvant temozolomide versus radiotherapy alone on survival in glioblastoma in a randomised phase III study: 5-year analysis of the EORTC-NCIC trial. *Lancet Oncol*. 2009;10(5):459–466.
- Portnow J, Badie B, Chen M, et al. The neuropharmacokinetics of temozolomide in patients with resectable brain tumors: potential implications for the current approach to chemoradiation. *Clin Cancer Res*. 2009;15(22):7092–7098.
- Ostermann S, Csajka C, Buclin T, et al. Plasma and cerebrospinal fluid population pharmacokinetics of temozolomide in malignant glioma patients. *Clin Cancer Res*. 2004;10(11):3728–3736.
- Deeken JF, Löscher W. The blood-brain barrier and cancer: transporters, treatment, and Trojan horses. *Clin Cancer Res*. 2007;13(6):1663–1674.
- Stewart DJ, Richard MT, Hugenholtz H, et al. Penetration of VP-16 (etoposide) into human intracerebral and extracerebral tumors. *J Neurooncol*. 1984;2(2):133–139.
- Hochberg FH, Pruitt A. Assumptions in the radiotherapy of glioblastoma. *Neurology*. 1980;30(9):907–911.
- Neuwelt EA, Maravilla KR, Frenkel EP, et al. Osmotic blood-brain barrier disruption. Computerized tomographic monitoring of chemotherapeutic agent delivery. *J Clin Invest*. 1979;64(2):684–688.
- Warren K, Jakacki R, Widemann B, et al. Phase II trial of intravenous lobradimil and carboplatin in childhood brain tumors: a report from the Children's Oncology Group. *Cancer Chemother Pharmacol*. 2006;58(3):343–347.
- Valtonen S, Timonen U, Toivanen P, et al. Interstitial chemotherapy with carmustine-loaded polymers for high-grade gliomas: a randomized double-blind study. *Neurosurgery*. 1997;41(1):44–49; discussion 48–49.

21. Jackson S, Anders NM, Mangraviti A, et al. The effect of regadenoson-induced transient disruption of the blood-brain barrier on temozolomide delivery to normal rat brain. *J Neurooncol.* 2015;126(3):433–439.
22. Fenart L, Buée-Scherrer V, Descamps L, et al. Inhibition of P-glycoprotein: rapid assessment of its implication in blood-brain barrier integrity and drug transport to the brain by an in vitro model of the blood-brain barrier. *Pharm Res.* 1998; 15(7):993–1000.
23. Mitrasinovic S, Appelboom G, Detappe A, et al. Focused ultrasound to transiently disrupt the blood brain barrier. *J Clin Neurosci.* 2016; 28:187–189.
24. Liu H-L, Hua M-Y, Chen P-Y, et al. Blood-brain barrier disruption with focused ultrasound enhances delivery of chemotherapeutic drugs for glioblastoma treatment 1. *Radiology.* 2010;255(2): 415–425.
25. Aryal M, Vykhodtseva N, Zhang Y-Z, et al. Multiple sessions of liposomal doxorubicin delivery via focused ultrasound mediated blood-brain barrier disruption: a safety study. *J Control Release.* 2015;204(C):60–69.
26. Burgess A, Huang Y, Querbes W, et al. Focused ultrasound for targeted delivery of siRNA and efficient knockdown of Htt expression. *J Control Release.* 2012;163(2):125–129.
27. McDannold N, Vykhodtseva N, Jolesz FA, et al. MRI investigation of the threshold for thermally induced blood-brain barrier disruption and brain tissue damage in the rabbit brain. *Magn Reson Med.* 2004;51(5):913–923.
28. Rodriguez A, Tatter S, Debinski W. Neurosurgical techniques for disruption of the blood-brain barrier for glioblastoma treatment. *Pharmaceutics.* 2015;7(3):175–187.
29. Sirsi SR, Borden MA. Advances in ultrasound mediated gene therapy using microbubble contrast agents. *Theranostics.* 2013; 2(12):1208–1222.
30. Behrens S, Daffertshofer M, Spiegel D, et al. Low-frequency, low-intensity ultrasound accelerates thrombolysis through the skull. *Ultrasound Med Biol.* 1999;25(2):269–273.
31. Sheikov N, McDannold N, Jolesz F, et al. Brain arterioles show more active vesicular transport of blood-borne tracer molecules than capillaries and venules after focused ultrasound-evoked opening of the blood-brain barrier. *Ultrasound Med Biol.* 2006;32(9): 1399–1409.
32. Sheikov N, McDannold N, Sharma S, et al. Effect of focused ultrasound applied with an ultrasound contrast agent on the tight junctional integrity of the brain microvascular endothelium. *Ultrasound Med Biol.* 2008;34(7):1093–1104.
33. Wei K-C, Chu P-C, Wang H-YJ, et al. Focused ultrasound-induced blood-brain barrier opening to enhance temozolomide delivery for glioblastoma treatment: a preclinical study. *PLoS One.* 2013; 8(3):e58995.
34. Wang S, Olumolade OO, Sun T, et al. Noninvasive, neuron-specific gene therapy can be facilitated by focused ultrasound and recombinant adeno-associated virus. *Gene Therapy.* 2014;22(1): 104–110.
35. Hsu P-H, Wei K-C, Huang C-Y, et al. Noninvasive and targeted gene delivery into the brain using microbubble-facilitated focused ultrasound. *PLoS One.* 2013;8(2):e57682.
36. Lin C-Y, Hsieh H-Y, Pitt WG, et al. Focused ultrasound-induced blood-brain barrier opening for non-viral, non-invasive, and targeted gene delivery. *J Control Release.* 2015;212(C):1–9.
37. Downs ME, Buch A, Sierra C, et al. Long-term safety of repeated blood-brain barrier opening via focused ultrasound with microbubbles in non-human primates performing a cognitive task. *PLoS One.* 2015;10(5):e0125911.
38. Ali IU, Chen X. Penetrating the blood-brain barrier: promise of novel nanoplatforms and delivery vehicles. *ACS Nano.* 2015; 9(10):9470–9474.
39. Watson KD, Lai C-Y, Qin S, et al. Ultrasound increases nanoparticle delivery by reducing intratumoral pressure and increasing transport in epithelial and epithelial-mesenchymal transition tumors. *Cancer Res.* 2012;72(6):1485–1493.
40. Samiotaki G, Konofagou EE. Dependence of the reversibility of focused- ultrasound-induced blood-brain barrier opening on pressure and pulse length in vivo. *IEEE Trans Ultrason Ferroelectr Freq Control.* 2013;60(11):2257–2265.
41. Choi JJ, Selert K, Vlachos F, et al. Noninvasive and localized neuronal delivery using short ultrasonic pulses and microbubbles. *Proc Natl Acad Sci U S A.* 2011;108(40): 16539–16544.
42. Choi JJ, Feshitan JA, Baseri B, et al. Microbubble-size dependence of focused ultrasound-induced blood-brain barrier opening in mice in vivo. *IEEE Trans Biomed Eng.* 2010;57(1):145–154.
43. Xu Z, Carlson C, Snell J, et al. Intracranial inertial cavitation threshold and thermal ablation lesion creation using MRI-guided 220-kHz focused ultrasound surgery: preclinical investigation. *J Neurosurg.* 2015;122(1):152–161.
44. Tung Y-S, Vlachos F, Choi JJ, et al. In vivo transcranial cavitation threshold detection during ultrasound-induced blood-brain barrier opening in mice. *Phys Med Biol.* 2010;55(20):6141–6155.
45. Marquet F, Teichert T, Wu S-Y, et al. Real-time, transcranial monitoring of safe blood-brain barrier opening in non-human primates. *PLoS One.* 2014;9(2):e84310.
46. McDannold N, Arvanitis CD, Vykhodtseva N, et al. Temporary disruption of the blood-brain barrier by use of ultrasound and microbubbles: safety and efficacy evaluation in rhesus macaques. *Cancer Res.* 2012;72(14):3652–3663.
47. Lai C-Y, Fite BZ, Ferrara KW. Ultrasonic enhancement of drug penetration in solid tumors. *Front Oncol.* 2013;3:204.
48. Gong W, Wang Z, Liu N, et al. Improving efficiency of adriamycin crossing blood brain barrier by combination of thermosensitive liposomes and hyperthermia. *Biol Pharm Bull.* 2011;34(7): 1058–1064.
49. Hergt R, Dutz S, Zeisberger M. Validity limits of the Néel relaxation model of magnetic nanoparticles for hyperthermia. *Nanotechnology.* 2010;21(1):015706.
50. Shah RR, Davis TP, Glover AL, et al. Impact of magnetic field parameters and iron oxide nanoparticle properties on heat generation for use in magnetic hyperthermia. *J Magn Magn Mater.* 2015;387:96–106.
51. Dan M, Bae Y, Pittman TA, et al. Alternating magnetic field-induced hyperthermia increases iron oxide nanoparticle cell association/uptake and flux in blood-brain barrier models. *Pharm Res.* 2015; 32(5):1615–1625.
52. Busquets M, Espargaró A, Sabaté R, et al. Magnetic nanoparticles cross the blood-brain barrier: when physics rises to a challenge. *Nanomaterials.* 2015;5(4):2231–2248.
53. Moding EJ, Kastan MB, Kirsch DG. Strategies for optimizing the response of cancer and normal tissues to radiation. *Nat Rev Drug Discov.* 2013;12(7):526–542.

54. De Salles AA, Gorgulho AA, Pereira JL, et al. Intracranial stereotactic radiosurgery. *Neurosurg Clin N Am*. 2013;24(4):491–498.
55. Adler JR. The future of robotics in radiosurgery. *Neurosurgery*. 2013;72(suppl 1):8–11.
56. Fauquette W, Amourette C, Dehouck M-P, et al. Radiation-induced blood-brain barrier damages: an in vitro study. *Brain Res*. 2012;1433:114–126.
57. Yuan H, Gaber MW, McColgan T, et al. Radiation-induced permeability and leukocyte adhesion in the rat blood-brain barrier: modulation with anti-ICAM-1 antibodies. *Brain Res*. 2003;969(1-2):59–69.
58. Sándor N, Walter FR, Bocsik A, et al. Low dose cranial irradiation-induced cerebrovascular damage is reversible in mice. *PLoS One*. 2014;9(11):e112397.
59. Yuan H, Gaber MW, Boyd K, et al. Effects of fractionated radiation on the brain vasculature in a murine model: blood-brain barrier permeability, astrocyte proliferation, and ultrastructural changes. *Int J Radiat Oncol Biol Phys*. 2006;66(3):860–866.
60. Gaber MW, Yuan H, Killmar JT, et al. An intravital microscopy study of radiation-induced changes in permeability and leukocyte-endothelial cell interactions in the microvessels of the rat pia mater and cremaster muscle. *Brain Res Brain Res Protoc*. 2004;13(1):1–10.
61. Kunjachan S, Detappe A, Kumar R, et al. Nanoparticle mediated tumor vascular disruption: a novel strategy in radiation therapy. *Nano Lett*. 2015;15(11):7488–7496.
62. Joh DY, Sun L, Stangl M, et al. Selective targeting of brain tumors with gold nanoparticle-induced radiosensitization. *PLoS One*. 2013;8(4):e62425.
63. Davies AM, Weinberg U, Palti Y. Tumor treating fields: a new frontier in cancer therapy. *Ann NY Acad Sci*. 2013;1291(1):86–95.
64. Miklavčič D, Mali B, Kos B, et al. Electrochemotherapy: from the drawing board into medical practice. *Biomed Eng Online*. 2014;13(1):29.
65. Linnert M, Iversen HK, Gehl J. Multiple brain metastases—current management and perspectives for treatment with electrochemotherapy. *Radiol Oncol*. 2012;46(4):271–278.
66. Neal RE, Rossmeisl JH, D'Alfonso V, et al. In vitro and numerical support for combinatorial irreversible electroporation and electrochemotherapy glioma treatment. *Ann Biomed Eng*. 2013;42(3):475–487.
67. Leuthardt EC, Duan C, Kim MJ, et al. Hyperthermic laser ablation of recurrent glioblastoma leads to temporary disruption of the peritumoral blood brain barrier. *PLoS One*. 2016;11(2):e0148613.
68. Hawasli AH, Bagade S, Shimony JS, et al. Magnetic resonance imaging-guided focused laser interstitial thermal therapy for intracranial lesions. *Neurosurgery*. 2013;73(6):1007–1017.
69. Hawasli AH, Ray WZ, Murphy RKJ, et al. Magnetic resonance imaging-guided focused laser interstitial thermal therapy for subinsular metastatic adenocarcinoma: technical case report. *Neurosurgery*. 2012;70:332–337; discussion 338.
70. Zhang F, Xu C-L, Liu C-M. Drug delivery strategies to enhance the permeability of the blood-brain barrier for treatment of glioma. *Drug Des Devel Ther*. 2015;9:2089–2100.

References

- [1] T. Budiharto, K. Haustermans, E. Van Cutsem, W. Van Steenbergen, B. Topal, R. Aerts, N. Ectors, D. Bielen, D. Vanbeckevoort, L. Goethals, and C. Verslype. A phase I radiation dose-escalation study to determine the maximal dose of radiotherapy in combination with weekly gemcitabine in patients with locally advanced pancreatic adenocarcinoma. *Radiat Oncol*, 3:30, 2008.
- [2] D. A. Jaffray. Image-guided radiotherapy: from current concept to future perspectives. *Nat Rev Clin Oncol*, 9(12):688–699, Dec 2012.
- [3] SciFinder, Pubmed. Keywords: Nanoparticle, Nanoparticle AND radiation
- [4] H. N. McQuaid, M. F. Muir, L. E. Taggart, S. J. McMahon, J. A. Coulter, W. B. Hyland, S. Jain, K. T. Butterworth, G. Schettino, K. M. Prise, D. G. Hirst, S. W. Botchway, and F. J. Currell. Imaging and radiation effects of gold nanoparticles in tumour cells. *Sci Rep*, 6:19442, 2016.
- [5] J. F. Hainfeld, D. N. Slatkin, and H. M. Smilowitz. The use of gold nanoparticles to enhance radiotherapy in mice. *Phys Med Biol*, 49(18):N309–315, Sep 2004.
- [6] Y. Min, J. M. Caster, M. J. Eblan, and A. Z. Wang. Clinical Translation of Nanomedicine. *Chem. Rev.*, 115(19):11147–11190, Oct 2015.
- [7] No authors listed. (P015) Radiation Biological Responses of MRI-Linac vs Linac in Human Head and Neck and Lung Cancer Cells. *Oncology (Williston Park, N.Y.)*, 29(4 Suppl 1), Apr 2015.
- [8] P. J. Keall, M. Barton, and S. Crozier. The Australian magnetic resonance imaging-linac program. *Semin Radiat Oncol*, 24(3):203–206, Jul 2014.
- [9] L. Sancey, F. Lux, S. Kotb, S. Roux, S. Dufort, A. Bianchi, Y. Cremillieux, P. Fries, J. L. Coll, C. Rodriguez-Lafrasse, M. Janier, M. Dutreix, M. Barberi-Heyob, F. Boschetti, F. Denat, C. Louis, E. Porcel, S. Lacombe, G. Le Duc, E. Deutsch, J. L. Perfettini, A. Detappe, C. Verry, R. Berbeco, K. T. Butterworth, S. J. McMahon, K. M. Prise, P. Perriat, and O. Tillement. The use of theranostic gadolinium-based nanoprobes to improve radiotherapy efficacy. *Br J Radiol*, 87(1041):20140134, Sep 2014.
- [10] F. Lux, L. Sancey, A. Bianchi, Y. Cremillieux, S. Roux, and O. Tillement. Gadolinium-based nanoparticles for theranostic MRI-radiosensitization. *Nanomedicine (Lond)*, 10(11):1801–1815, 2015.
- [11] L. Sancey, S. Kotb, C. Truillet, F. Appaix, A. Marais, E. Thomas, B. van der Sanden, J. P. Klein, B. Laurent, M. Cottier, R. Antoine, P. Dugourd, G. Panczer, F. Lux, P. Perriat, V. Motto-Ros, and O. Tillement. Long-term in vivo clearance of gadolinium-based AGuIX nanoparticles and their biocompatibility after systemic injection. *ACS Nano*, 9(3):2477–2488, Mar 2015.

- [12] A. Detappe, S. Kunjachan, J. Rottmann, J. Robar, P. Tsiamas, H. Korideck, O. Tillement, and R. Berbeco. AGuIX nanoparticles as a promising platform for image-guided radiation therapy. *Cancer Nanotechnol*, 6(1):4, 2015.
- [13] G. Le Duc, I. Miladi, C. Alric, P. Mowat, E. Brauer-Krisch, A. Bouchet, E. Khalil, C. Billotey, M. Janier, F. Lux, T. Epicier, P. Perriat, S. Roux, and O. Tillement. Toward an image-guided microbeam radiation therapy using gadolinium-based nanoparticles. *ACS Nano*, 5(12):9566–9574, Dec 2011.
- [14] A. Mignot, C. Truillet, F. Lux, L. Sancey, C. Louis, F. Denat, F. Boschetti, L. Bocher, A. Gloter, O. Stephan, R. Antoine, P. Dugourd, D. Luneau, G. Novitchi, L. C. Figueiredo, P. C. de Moraes, L. Bonneviot, B. Albela, F. Ribot, L. Van Lokeren, I. Dechamps-Olivier, F. Chuburu, G. Lemerrier, C. Villiers, P. N. Marche, G. Le Duc, S. Roux, O. Tillement, and P. Perriat. A top-down synthesis route to ultrasmall multifunctional Gd-based silica nanoparticles for theranostic applications. *Chemistry*, 19(19):6122–6136, May 2013.
- [15] C. Truillet, P. Bouziotis, C. Tsoukalas, J. Brugiére, M. Martini, L. Sancey, T. Brichart, F. Denat, F. Boschetti, U. Darbost, I. Bonnamour, D. Stellas, C. D. Anagnostopoulos, V. Koutoulidis, L. A. Moulopoulos, P. Perriat, F. Lux, and O. Tillement. Ultrasmall particles for Gd-MRI and (68) Ga-PET dual imaging. *Contrast Media Mol Imaging*, 10(4):309–319, 2015.
- [16] C. Truillet, P. Bouziotis, C. Tsoukalas, L. Sancey, F. Denat, F. Boschetti, D. Stellas, C. D. Anagnostopoulos, V. Koutoulidis, L. A. Moulopoulos, P. Perriat, F. Lux, and O. Tillement. Innovative multimodal DOTA/NODA nanoparticles for MRI and PET imaging for tumor detection. *EJNMMI Phys*, 1:A80, Jul 2014.
- [17] S. J. McMahon, H. Paganetti, and K. M. Prise. Optimising element choice for nanoparticle radiosensitisers. *Nanoscale*, 8(1):581–589, Jan 2016.
- [18] M. W. Dewhirst, Y. Cao, and B. Moeller. Cycling hypoxia and free radicals regulate angiogenesis and radiotherapy response. *Nat. Rev. Cancer*, 8(6):425–437, Jun 2008.
- [19] M. Luchette, H. Korideck, M. Makrigiorgos, O. Tillement, and R. Berbeco. Radiation dose enhancement of gadolinium-based AGuIX nanoparticles on HeLa cells. *Nanomedicine*, 10(8):1751–1755, Nov 2014.
- [20] M. Ma, Y. Huang, H. Chen, X. Jia, S. Wang, Z. Wang, and J. Shi. Bi2S3-embedded mesoporous silica nanoparticles for efficient drug delivery and interstitial radiotherapy sensitization. *Biomaterials*, 37:447–455, Jan 2015.
- [21] S. Kunjachan, A. Detappe, R. Kumar, T. Ireland, L. Cameron, D. E. Biancur, V. Motto-Ros, L. Sancey, S. Sridhar, G. M. Makrigiorgos, and R. I. Berbeco. Nanoparticle Mediated Tumor Vascular Disruption: A Novel Strategy in Radiation Therapy. *Nano Lett.*, 15(11):7488–7496, Nov 2015.
- [22] J. Marill, N. M. Anesary, P. Zhang, S. Vivet, E. Borghi, L. Levy, and A. Pottier. Hafnium oxide nanoparticles: toward an in vitro predictive biological effect? *Radiat Oncol*, 9:150, 2014.
- [23] S.H. Kurtzman, A. Russo, J.B. Mitchell, W DeGraff, W.F. Sindelar, M.W. Brechbiel, O.A. Gansow, A.M. Friedman, J.J. Hines, and J Gamson. 212Bismuth linked to an antipancreatic carcinoma antibody: model for alpha-particle-emitter radioimmunotherapy. *J Natl Cancer Inst*, 80(6):449–52, May 1988.
- [24] L. E. Taggart, S. J. McMahon, K. T. Butterworth, F. J. Currell, G. Schettino, and K. M. Prise. Protein disulphide isomerase as a target for nanoparticle-mediated sensitisation of cancer cells to radiation. *Nanotechnology*, 27(21):215101, May 2016.

- [25] Y. Matsumura and H. Maeda. A new concept for macromolecular therapeutics in cancer chemotherapy: mechanism of tumorotropic accumulation of proteins and the antitumor agent smancs. *Cancer Res.*, 46(12 Pt 1):6387–6392, Dec 1986.
- [26] D. Peer, J. M. Karp, S. Hong, O. C. Farokhzad, R. Margalit, R. Langer. Nanocarriers as an emerging platform for cancer therapy. *Nat Nanotechnol*, 2:12, 2007.
- [27] S. Kunjachan, R. Pola, F. Gremse, B. Theek, J. Ehling, D. Moeckel, B. Hermanns-Sachweh, M. Pechar, K. Ulbrich, W. E. Hennink, G. Storm, W. Lederle, F. Kiessling, and T. Lammers. Passive versus active tumor targeting using RGD and NGR modified polymeric nanomedicines. *Nano Lett*, 14:2, 2014.
- [28] D. K. Chatterjee, T. Wolfe, J. Lee, A. P. Brown, P. K. Singh, S. R. Bhattarai, P. Diagaradjane, and S. Krishnan. Convergence of nanotechnology with radiation therapy-insights and implications for clinical translation. *Transl Cancer Res*, 2(4):256–268, Aug 2013.
- [29] W. Ngwa, H. Korideck, A. I. Kassis, R. Kumar, S. Sridhar, G. M. Makrigiorgos, and R. A. Cormack. In vitro radiosensitization by gold nanoparticles during continuous low-dose-rate gamma irradiation with I-125 brachytherapy seeds. *Nanomedicine*, 9(1):25–27, Jan 2013.
- [30] F. Van den Heuvel, J. P. Locquet, and S. Nuyts. Beam energy considerations for gold nanoparticle enhanced radiation treatment. *Phys Med Biol*, 55(16):4509–4520, Aug 2010.
- [31] S. J. McMahon, W. B. Hyland, M. F. Muir, J. A. Coulter, S. Jain, K. T. Butterworth, G. Schettino, G. R. Dickson, A. R. Hounsell, J. M. O’Sullivan, K. M. Prise, D. G. Hirst, and F. J. Currell. Biological consequences of nanoscale energy deposition near irradiated heavy atom nanoparticles. *Theranostics*, 4:81-9, 2013.
- [32] M. Douglass, E. Bezak, and S. Penfold. Monte Carlo investigation of the increased radiation deposition due to gold nanoparticles using kilovoltage and megavoltage photons in a 3D randomized cell model. *Med Phys*, 40(7):071710, 2013.
- [33] P. Tsiamas, B. Liu, F. Cifter, W. F. Ngwa, R. I. Berbeco, C. Kappas, K. Theodorou, K. Marcus, M. G. Makrigiorgos, E. Sajo, and P. Zygmanski. Impact of beam quality on megavoltage radiotherapy treatment techniques utilizing gold nanoparticles for dose enhancement. *Phys Med Biol*, 58(3):451–464, Feb 2013.
- [34] B. L. Jones, S. Krishnan, and S. H. Cho. Estimation of microscopic dose enhancement factor around gold nanoparticles by Monte Carlo calculations. *Med Phys*, 37(7):3809–3816, Jul 2010.
- [35] P. Tsiamas, E. Sajo, F. Cifter, K. Theodorou, C. Kappas, M. Makrigiorgos, K. Marcus, and P. Zygmanski. Beam quality and dose perturbation of 6 MV flattening-filter-free linac. *Phys Med*, 30(1):47–56, Feb 2014.
- [36] R. I. Berbeco, W. Ngwa, and G. M. Makrigiorgos. Localized dose enhancement to tumor blood vessel endothelial cells via megavoltage X-rays and targeted gold nanoparticles: new potential for external beam radiotherapy. *Int. J. Radiat. Oncol. Biol. Phys.*, 81(1):270–276, Sep 2011.
- [37] G. M. Makrigiorgos, S. J. Adelstein, and A. I. Kassis. Limitations of conventional internal dosimetry at the cellular level. *J. Nucl. Med.*, 30(11):1856–1864, Nov 1989.
- [38] A. Cole. Absorption of 20-eV to 50,000-eV electron beams in air and plastic. *Radiat. Res.*, 38(1):7–33, Apr 1969.
- [39] S. D. Perrault, C. Walkey, T. Jennings, H. C. Fischer, and W. C. Chan. Mediating tumor targeting efficiency of nanoparticles through design. *Nano Lett.*, 9(5):1909–1915, May 2009.

- [40] B. D. Chithrani, A. A. Ghazani, and W. C. Chan. Determining the size and shape dependence of gold nanoparticle uptake into mammalian cells. *Nano Lett.*, 6(4):662–668, Apr 2006.
- [41] S. Jain, J. A. Coulter, A. R. Hounsell, K. T. Butterworth, S. J. McMahon, W. B. Hyland, M. F. Muir, G. R. Dickson, K. M. Prise, F. J. Currell, J. M. O’Sullivan, and D. G. Hirst. Cell-specific radiosensitization by gold nanoparticles at megavoltage radiation energies. *Int. J. Radiat. Oncol. Biol. Phys.*, 79(2):531–539, Feb 2011.
- [42] C. J. Liu, C. H. Wang, S. T. Chen, H. H. Chen, W. H. Leng, C. C. Chien, C. L. Wang, I. M. Kempson, Y. Hwu, T. C. Lai, M. Hsiao, C. S. Yang, Y. J. Chen, and G. Margaritondo. Enhancement of cell radiation sensitivity by pegylated gold nanoparticles. *Phys Med Biol*, 55(4):931–945, Feb 2010.
- [43] R. I. Berbeco, H. Korideck, W. Ngwa, R. Kumar, J. Patel, S. Sridhar, S. Johnson, B. D. Price, A. Kimmelman, and G. M. Makrigiorgos. DNA damage enhancement from gold nanoparticles for clinical MV photon beams. *Radiat. Res.*, 178(6):604–608, Dec 2012.
- [44] R. Di Corato, F. Gazeau, C. Le Visage, D. Fayol, P. Levitz, F. Lux, D. Letourneur, N. Luciani, O. Tillement, and C. Wilhelm. High-resolution cellular MRI: gadolinium and iron oxide nanoparticles for in-depth dual-cell imaging of engineered tissue constructs. *ACS Nano*, 7(9):7500–7512, Sep 2013.
- [45] A. Bianchi, S. Dufort, F. Lux, P. Y. Fortin, N. Tassali, O. Tillement, J. L. Coll, and Y. Cremillieux. Targeting and in vivo imaging of non-small-cell lung cancer using nebulized multimodal contrast agents. *Proc. Natl. Acad. Sci. U.S.A.*, 111(25):9247–9252, Jun 2014.
- [46] A. Bianchi, S. Dufort, F. Lux, A. Courtois, O. Tillement, J. L. Coll, and Y. Cremillieux. Quantitative biodistribution and pharmacokinetics of multimodal gadolinium-based nanoparticles for lungs using ultrashort TE MRI. *MAGMA*, 27(4):303–316, Aug 2014.
- [47] G. Paul, Y. Prado, N. Dia, E. Riviere, S. Laurent, M. Roch, L. V. Elst, R. N. Muller, L. Sancey, P. Perriat, O. Tillement, T. Mallah, and L. Catala. Mn(II)-containing coordination nanoparticles as highly efficient T(1) contrast agents for magnetic resonance imaging. *Chem. Commun. (Camb.)*, 50(51):6740–6743, Jun 2014.
- [48] H. Benachour, A. Seve, T. Bastogne, C. Frochot, R. Vanderesse, J. Jasniewski, I. Miladi, C. Billotey, O. Tillement, F. Lux, and M. Barbery-Heyob. Multifunctional peptide-conjugated hybrid silica nanoparticles for photodynamic therapy and MRI. *Theranostics*, 2(9):889–904, 2012.
- [49] P. Couleaud, D. Bechet, R. Vanderesse, M. Barbery-Heyoub, A. C. Faure, S. Roux, O. Tillement, S. Porhel, F. Guillemin, and C. Frochot. Functionalized silica-based nanoparticles for photodynamic nanoparticles. *Nanomedicine (Lond)*, 6(6):995–1009, 2011.
- [50] D. Bechet, F. Auger, P. Couleaud, E. Marty, L. Ravasi, N. Durieux, C. Bonnet, F. Plenat, C. Frochot, S. Mordon, O. Tillement, R. Vanderesse, F. Lux, P. Pierrat, F. Guillemin, and M. Barbery-Heyoub. Multifunctional ultrasmall nanoplatfoms for vascular-targeted interstitial photodynamic therapy of brain tumors guided by real-time MRI. *Nanomedicine*, 11(3):657–70, 2015.
- [51] A. Bianchi, F. Lux, O. Tillement, and Y. Cremillieux. Contrast enhanced lung MRI in mice using ultra-short echo time radial imaging and intratracheally administrated Gd-DOTA-based nanoparticles. *Magn Reson Med*, 70(5):1419–1426, Nov 2013.

- [52] C. Aspod, D. Laurin, M. F. Janier, C. A. Mandon, C. Thivolet, C. Villiers, P. Mowat, A. M. Madec, O. Tillement, P. Perriat, C. Louis, F. Berard, P. N. Marche, J. Plumaz, and C. Billotey. Paramagnetic nanoparticles to track and quantify in vivo immune human therapeutic cells. *Nanoscale*, 5(23):11409–11415, Dec 2013.
- [53] P. Mowat, A. Mignot, W. Rima, F. Lux, O. Tillement, C. Roulin, M. Dutreix, D. Bechet, S. Huger, L. Humbert, M. Barberi-Heyob, M. T. Aloy, E. Armandy, C. Rodriguez-Lafresse, G. Le Duc, S. Roux, and P. Perriat. In vitro radiosensitizing effects of ultrasmall gadolinium based particles on tumour cells. *J Nanosci Nanotechnol*, 11(9):7833–7839, Sep 2011.
- [54] E. Porcel, O. Tillement, F. Lux, P. Mowat, N. Usami, K. Kobayashi, Y. Furusawa, C. Le Sech, S. Li, and S. Lacombe. Gadolinium-based nanoparticles to improve the hadrontherapy performances. *Nanomedicine*, 10(8):1601–1608, Nov 2014.
- [55] L. Stefanaikova, E. Porcel, P. Eustache, S. Li, D. Salado, S. Marco, J. L. Guerquin-Kern, M. Refregiers, O. Tillement, F. Lux, and S. Lacombe. Cell localisation of gadolinium-based nanoparticles and related radiosensitising efficacy in glioblastoma cells. *Cancer Nanotechnol*, 5(1):6, 2014.
- [56] B. W. Raaymakers, J. C. de Boer, C. Knox, S. P. Crijns, K. Smit, M. K. Stam, M. R. van den Bosch, J. G. Kok, and J. J. Lagendijk. Integrated megavoltage portal imaging with a 1.5 T MRI linac. *Phys Med Biol*, 56(19):N207–214, Oct 2011.
- [57] E. Lechtman, N. Chattopadhyay, Z. Cai, S. Mashouf, R. Reilly, and J. P. Pignol. Implications on clinical scenario of gold nanoparticle radiosensitization in regards to photon energy, nanoparticle size, concentration and location. *Phys Med Biol*, 56(15):4631–4647, Aug 2011.
- [58] S. H. Cho. Estimation of tumour dose enhancement due to gold nanoparticles during typical radiation treatments: a preliminary Monte Carlo study. *Phys Med Biol*, 50(15):N163–173, Aug 2005.
- [59] A. Bianchi, D. Moncelet, F. Lux, M. Plissonneau, S. Rizzitelli, E. J. Ribot, N. Tassali, V. Bouchaud, O. Tillement, P. Voisin, Y. Cremilleux. Orotracheal administration of contrast agents: a new protocol for brain tumor targeting. *NMR Biomed*, 28(6):738–46, Jun 2015.
- [60] A. Detappe, P. Tsiamas, W. Ngwa, P. Zygmanski, M. Makrigrigios, and R. Berbeco. The effect of flattening filter free delivery on endothelial dose enhancement with gold nanoparticles. *Med Phys*, 40(3):031706, Mar 2013.
- [61] R.L. Siegel, K.D. Miller, and A. Jemal. Cancer statistics, 2015. *CA Cancer J Clin*, 65(1):5–29, Jan 2015.
- [62] J. Schuemann, R. Berbeco, D. B. Chithrani, S. H. Cho, R. Kumar, S. J. McMahon, S. Sridhar, and S. Krishnan. Roadmap to Clinical Use of Gold Nanoparticles for Radiation Sensitization. *Int. J. Radiat. Oncol. Biol. Phys.*, 94(1):189–205, Jan 2016.
- [63] A. S. Reese, W. Lu, and W. F. Regine. Utilization of intensity-modulated radiation therapy and image-guided radiation therapy in pancreatic cancer: is it beneficial? *Semin Radiat Oncol*, 24(2):132–139, Apr 2014.
- [64] N. Trakul, A. C. Koong, P. G. Maxim, and D. T. Chang. Modern radiation therapy techniques for pancreatic cancer. *Gastroenterol. Clin. North Am.*, 41(1):223–235, Mar 2012.
- [65] L. A. Dawson and D. A. Jaffray. Advances in image-guided radiation therapy. *J. Clin. Oncol.*, 25(8):938–946, Mar 2007.

- [66] I. J. Chetty, M. K. Martel, D. A. Jaffray, S. H. Benedict, S. M. Hahn, R. Berbeco, J. Deye, R. Jeraj, B. Kavanagh, S. Krishnan, N. Lee, D. A. Low, D. Mankoff, L. B. Marks, D. Ollendorf, H. Paganetti, B. Ross, R. A. Siochi, R. D. Timmerman, and J. W. Wong. Technology for Innovation in Radiation Oncology. *Int. J. Radiat. Oncol. Biol. Phys.*, 93(3):485–492, Nov 2015.
- [67] S. Kunjachan, J. Ehling, G. Storm, F. Kiessling, and T. Lammers. Noninvasive Imaging of Nanomedicines and Nanotheranostics: Principles, Progress, and Prospects. *Chem. Rev.*, 115(19):10907–10937, Oct 2015.
- [68] M. Riboldi, R. Orecchia, and G. Baroni. Real-time tumour tracking in particle therapy: technological developments and future perspectives. *Lancet Oncol.*, 13(9):e383–391, Sep 2012.
- [69] E.K. Chow and D. Ho. Cancer nanomedicine: from drug delivery to imaging. *Sci Transl Med*, 5(216):216rv4, Dec 2013.
- [70] U. Prabhakar, H. Maeda, R. K. Jain, E. M. Sevick-Muraca, W. Zamboni, O. C. Farokhzad, S. T. Barry, A. Gabizon, P. Grodzinski, and D. C. Blakey. Challenges and key considerations of the enhanced permeability and retention effect for nanomedicine drug delivery in oncology. *Cancer Res.*, 73(8):2412–2417, Apr 2013.
- [71] G. Le Duc, S. Roux, A. Paruta-Tuarez, S. Dufort, E. Brauer, A. Marais, C. Truillet, L. Sancey, P. Perriat, F. Lux, and O. Tillement. Advantages of gadolinium based ultrasmall nanoparticles vs molecular gadolinium chelates for radiotherapy guided by MRI for glioma treatment. *Cancer Nanotechnol*, 5(1):4, 2014.
- [72] L. Sancey, V. Motto-Ros, B. Busser, S. Kotb, J. M. Benoit, A. Pednoir, F. Lux, O. Tillement, G. Panczer, J. Yu. Laser Spectrometry for multi-elemental imaging of biological samples. *Sci Rep*, 4:6065, 2011.
- [73] E. J. Moding, M. B. Kastan, and D. G. Kirsch. Strategies for optimizing the response of cancer and normal tissues to radiation. *Nat Rev Drug Discov*, 12(7):526–542, Jul 2013.
- [74] R. Iwama, T. Sato, K. Sakurai, K. Takasuna, T. Ichijo, K. Furuhashi, and H. Satoh. Estimation of glomerular filtration rate in cynomolgus monkeys (*Macaca fascicularis*). *J. Vet. Med. Sci.*, 76(10):1423–1426, Oct 2014.
- [75] S. Reagan-Shaw, M. Nihal, and N. Ahmad. Dose translation from animal to human studies revisited. *FASEB J.*, 22(3):659–661, Mar 2008.
- [76] R. I. Berbeco, A. Detappe, P. Tsiamas, D. Parsons, M. Yewondwossen, and J. Robar. Low Z target switching to increase tumor endothelial cell dose enhancement during gold nanoparticle-aided radiation therapy. *Med Phys*, 43(1):436, Jan 2016.
- [77] G. LeDuc, S. Roux, A. Paruta-Tuarez, S. Dufort, E. Brauer, A. Marais, C. Truillet, S. Sancey, P. Pierrat, F. Lux, and O. Tillement. Advantages of gadolinium based ultrasmall nanoparticles vs molecular gadolinium chelates for radiotherapy guided by MRI for glioma treatment. *Cancer Nanotechnology*, 5:4, Jul 2014.
- [78] S. Kotb, A. Detappe, F. Lux, F. Appaix, E. L. Barbier, V. L. Tran, M. Plissonneau, H. Gehan, F. Lefranc, C. Rodriguez-Lafrasse, C. Verry, R. Berbeco, O. Tillement, and L. Sancey. Gadolinium-based nanoparticles and radiation therapy for multiple brain melanoma metastases: proof of concept before phase I trial. *Theranostics*, 6(3):418–27, Jan 2016.
- [79] Viewray Inc. [Http://www.viewray.com](http://www.viewray.com).
- [80] Varian Inc. [Http://www.varian.com](http://www.varian.com).

- [81] S. Mura and P. Couvreur. Nanotheranostics for personalized medicine. *Ed. World Scientific*
- [82] J. Portnow, B. Badie, M. Chen, A. Liu, S. Blanchard, and T. W. Synold. The neuropharmacokinetics of temozolomide in patients with resectable brain tumors: potential implications for the current approach to chemoradiation. *Clin. Cancer Res.*, 15(22):7092–7098, Nov 2009.
- [83] S. Ostermann, C. Csajka, T. Buclin, S. Leyvraz, F. Lejeune, L. A. Decosterd, and R. Stupp. Plasma and cerebrospinal fluid population pharmacokinetics of temozolomide in malignant glioma patients. *Clin. Cancer Res.*, 10(11):3728–3736, Jun 2004.
- [84] J. F. Deeken and W. Loscher. The blood-brain barrier and cancer: transporters, treatment, and Trojan horses. *Clin. Cancer Res.*, 13(6):1663–1674, Mar 2007.
- [85] D. J. Stewart, M. T. Richard, H. Hugenholtz, J. M. Dennerly, R. Belanger, J. Gerin-Lajoie, V. Montpetit, D. Nundy, J. Prior, and H. S. Hopkins. Penetration of VP-16 (etoposide) into human intracerebral and extracerebral tumors. *J. Neurooncol.*, 2(2):133–139, 1984.
- [86] S. Mitrasinovic, G. Appelboom, A. Detappe, and E. Sander Connolly. Focused ultrasound to transiently disrupt the blood brain barrier. *J Clin Neurosci*, 28:187–189, Jun 2016.
- [87] H. Yuan, M. W. Gaber, T. McColgan, M. D. Naimark, M. F. Kiani, and T. E. Merchant. Radiation-induced permeability and leukocyte adhesion in the rat blood-brain barrier: modulation with anti-ICAM-1 antibodies. *Brain Res.*, 969(1-2):59–69, Apr 2003.
- [88] N. Sandor, F. R. Walter, A. Bocsik, P. Santha, B. Schilling-Toth, V. Lener, Z. Varga, Z. Kahan, M. A. Deli, G. Safrany, and H. Hegyesi. Low dose cranial irradiation-induced cerebrovascular damage is reversible in mice. *PLoS ONE*, 9(11):e112397, 2014.
- [89] S. C. Baetke, T. Lammers, and F. Kiessling. Applications of nanoparticles for diagnosis and therapy of cancer. *Br J Radiol*, 88(1054):20150207, Oct 2015.